Crystallographic and Magneto-Dynamic Characterization of Thin-Film Spintronic Materials

James Sizeland

Doctor of Philosophy
University of York
Physics

March 2015

Abstract

This thesis sets out to identify and characterise the critical properties of two spintronic materials, the half-metallic Fe_3O_4 and the amorphous rare earth-transition metal alloy GdFe. The critical property of Fe_3O_4 is its crystal ordering, due to the array of exchange and superexchange interactions which define its conductive and magnetic behaviour. A series of post-oxidized Fe_3O_4||MgO (001) thin-films have been produced and the oxide growth has been analyzed by high resolution transmission electron microscopy (HRTEM). The quality of the film has been assessed by magnetometry and critical parameters for the growth of quality films are described. Previous procedures on the (001) orientation turn out to have masked much of the disorder in the films. This meant that judgments of quality based on magnetometry conflicted with optic data. By cutting down the (011) plane this research was able to resolve these conflicts and effectively explain the performance of a film as observed from magnetometry data. Previous work has elucidated the theoretical imperfections that can exist in this material. This work confirms the potential for these defects and has identified others. The characteristic visibility criteria for these crystal defects are confirmed and extended. By contrast the critical property of GdFe is the temperature dependent coupling between rare earth and transition metal sublattices. A measurement system was constructed to resolve the temperature dependence of the magneto-optic Kerr effect at femtosecond time scales. By this method, the theoretical timeline of dynamic behaviour has been experimentally validated and enhanced. Observations of resolved sublattice dynamics have been identified and interpreted, including a clear indication of picosecond ferromagnetic ordering. As such this work corroborates and advances existing techniques for the production, analysis and understanding of these spintronic materials.

Contents

Abstract 2.

Contents 3.

List of Figures 8.

Acknowledgements 21.

Declaration 22.

1 Introduction 23.

1.1 Spintronics 23.

1.2 Origin of Magnetism 26.

1.3 Motivation 27.

1.3 Outline 29.

1.4 References 32.

2 Interpreting Magneto-Optic Dynamics in Thin-film Media 34.

2.1 Introduction 34.

2.2 Magneto-Optical Kerr Effect (MOKE) 36.

Single Detector Signal Calculations 38.

Bridge Detector Signal Calculations 39.

2.3 Ultrafast Magnetization Dynamics 41.

2.3.1 Laser-Induced Ultrafast Demagnetization 41.

2.3.2 Historical Development 45.

2.4 Laser-Induced Coherent Precession 49.

Macrospin Dynamics 49.

Effective Field 50.

Damping and the LLG equation 51.
Interpretation of Precessional Dynamics 53.
2.5 References 55.

3 Materials for Spintronic Applications 58.
3.1 Introduction 58.
3.2 Half-Metals: Magnetite (Fe_3O_4) 58.
3.2.1 Structure & Magnetic Properties 58.
3.2.3 Single Crystal Growth Considerations 62.
3.3 Rare Earth-Transition Metal Alloys: GdFe 64.
3.3.1 Structure & Magnetic Properties 64.
3.3.2 Magneto-dynamic Properties 68.
3.4 Summary 72.
3.5 References 72.

4 Quality Control of Materials 75.
4.1 Introduction 75.
4.2 Growth Techniques 75.
4.2.1 Molecular Beam Epitaxy (MBE) 75.
Growing Epitaxial Fe_3O_4 78.
4.2.2 Sputter Deposition 79.
4.3 Imaging Techniques 79.
4.3.1 Sample Preparation 80.
Cross-section Technique 80.
Plan-View Lift-Off Technique 83.
4.3.2 Transmission Electron Microscopy (TEM) 83.
4.3.3 Electron Diffraction 85.

4.3.4 Dark Field Imaging 88.
4.4 References 90.

5 Building Magnetic Characterization Techniques 91.

5.1 Introduction 91.
5.2 Measuring the Magneto-Optic Kerr Effect (MOKE) 91.
5.3 Time-Resolved MOKE Magnetometry 95.
5.3.1 Stroboscopic Techniques 95.
5.3.2 Femtosecond Laser Operation 97.
Pump Laser 98.
Seed Laser 99.
Regenerative Amplifier 100.
Maintenance 102.
5.3.3 Optics Design Process 103.
Delay Line 104.
Beam Overlap 106.
Beam conditioning 109.
5.3.4 Signal Capture & Electronic Considerations 111.
5.3.5 Design of Software 113.
5.4 References 117.

6 Materials Study of Post-Oxidized Magnetite Thin-Films 119.

6.1 Introduction 119.
6.2 Experimental 120.
6.3 Results 121.
6.3.1 Initial Investigation 121.
6.3.2 (110) Microscopy Investigation 129.

6.3 Fe_3O_4/MgO (100) APB Geometry 133.
6.3.1 Theoretical Review 133.
6.3.2 Experimental Observation 139.
6.4 Summary 142.
6.5 References 143.

7 Ultrafast Magnetization Dynamics Study of GdFe Thin-Films 144.
7.1 Introduction 144.
7.2 Methodology 145.
7.3 Results 146.
7.3.1 Static Hysteresis Measurements 146.
7.3.2 Pump Fluence Series of $Gd_{0.25}Fe_{0.75}$ 148.
Reflectivity 148.
Ultrafast Demagnetization 150.
Magnetization Recovery Time 155.
Magnetic Precessional Frequency 162.
Magnetic Precession Damping 169.
7.3 Summary 171.
7.3.1 Evidence for Magnetization Compensation Temperature 171.
7.3.2 Evidence for Angular Momentum Compensation Temperature 173.
7.4 References 174.

8 Conclusions & Further Work 175.
8.1 Discussion of Post-Oxidized Fe_3O_4 175.

    8.1.2 Further Research 176.

  8.2 Fluence Dependent Magneto-Dynamics in GdFe 177.

    8.2.1 Discussion of Results 177.

    8.2.2 Further Research 179.

  8.3 Concluding Remarks 180.

  8.4 References 180.

Glossary 181.

List of Figures

Figure 1.1: Venn diagram of the three particle interactions which encompass the field of spintronics. 24.

Figure 1.2: Moore's law of exponential improvement in technology showing year on year growth in data storage density in magnetic media. 25.

Figure 2.1: Geometry of a MOKE system showing incident light ray at angle $\alpha$to the surface normal in incident plane. Electric field vectors are defined relative to the incident plane E_P in plane, E_S orthogonal to that. Components of magnetization defined relative to the incident plane and the sample surface. 36.

Figure 2.2: Calculated plots (a) of reflection coefficient K^{Lon} for incident to reflected orientations (s to s, p to p and s to p = p to s) and (b) polarization rotation angle ρ and ellipticity η versus incident angle α. 38.

Figure 2.3: Graph of signals for a single detector scheme. Normalized signal observed for a theoretical isotropically magnetized sample, showing the relative signal amplitude of each Kerr orientation as a function of analyzer angle for incident s and p polarized light source. Signal maximized for 90° angle between polarizer and analyzer. 39.

Figure 2.4: Graph of signals for a two detector scheme. Normalized signal observed for a theoretical isotropically magnetized sample, showing the relative signal amplitude of each Kerr orientation as a function of analyzer angle for incident s and p polarized light source. Signal maximized for 45° angle between polarizer and analyzer. 40.

Figure 2.5: Three thermodynamic reservoirs in a ferromagnetic metal. Each can be initially excited by different mechanisms (e.g. photon injection, magnetic field

change, mechanical stress). This is followed by a relaxation to the other reservoirs dependent on the strength of coupling between each. 41.

Figure 2.6: Time-energy correlation graph, plotting t = h/E. This gives a direct comparison between frequency, time and associated energies. General ranges of interactions are marked. 43.

Figure 2.7: Graphs showing spin (T_s), electron (T_e) and lattice (T_l) temperatures from specific heat calculations on Ni (left) and pump-probe SHG measurements over fluence series 250-1150 μJ/cm^2 also on Ni (right). 46.

Figure 2.8: (a) Time-resolved spin polarization of photo-emitted electrons for Ni films; (b) induced ellipticity (open circles) compared to induced rotation (filled circles) showing a phase shift between them; (c) Polar Kerr hysteresis of $CoPt_3$ alloy at pump delays, showing transient M-H loop evolution. 48.

Figure 2.9: Cartoon of stimulation of magnetic precession. Effective field H_{eff} at equilibrium balances internal anisotropy K with external field H; M aligns with that. A rapid temperature change reduces the internal anisotropy and causes a change in H_{eff} causing a force on M (left). As H_{eff} returns to equilibrium, a torque is applied to M as it returns to equilibrium (right). 52.

Figure 2.10: Plot of damped sinusoidal oscillation equation showing ideal exponential decay envelope from A to M_0. 54.

Figure 3.1: Illustrations of the three most common orientations of the Fe_3O_4 cubic inverse spinel crystal unit cell. The structure is comprised of a fcc O^{2+} lattice ((O), red atoms), equal numbers of Fe^{3+} and Fe^{2+} ions filling half of the octahedral site ((B), dark blue atoms) and Fe^{3+} ions filling ⅛ of the tetrahedral sites ((A), light blue atoms). These orientations provide different visibility of atomic columns. 59.

Figure 3.2: Cartoons of interatomic interactions which exist in crystalline magnetite (left) and example positions of superexchange interactions within the magnetite

unit cell (right), displaying (i) ~90 weakly ferromagnetic superexchange interaction on B sites, (ii) ferromagnetic double exchange interaction on B sites, and (iii) strongly antiferromagnetic superexchange interaction between octahedral and tetrahedral iron sites. 60.

Figure 3.3: Cartoon of (a) Fe_3O_4 (001) unit cell, containing octahedral (dark blue) and tetrahedral (light blue) iron ions, showing superexchange bonds via oxygen (red) sublattice. By comparison, to scale (b) MgO (001) unit cell, containing magnesium (yellow) sublattice bonded to oxygen (red) sublattice. 63.

Figure 3.4: Schematic illustration of APB types with shift vectors (left) showing translational and rotational shifts used to calculate TEM visibility conditions and 220 type TEM dark field images of APBs in Fe_3O_4/MgO (001) films of (a) 6nm, (b) 12nm, (c) 25nm and (d) 50nm thickness (right). 64.

Figure 3.5: Hartree-Fock theoretically calculated radial influence of Gd electron orbitals. The 4f orbital, which carries the magnetic moment, is shielded deep within the ion, affected by the environment only via intra-atomic exchange with the 5p orbital. 65.

Figure 3.6: Schematic guide to the temperature dependence of both individual sublattices along with their combined effect on the net magnetic characteristics of the material. Shows the two compensation temperatures, magnetic (T_M) and angular momentum (T_A) along with the Curie temperature (T_C) these broadly describe the temperature dependent characteristics of a RE-TM material. 67.

Figure 3.7: Schematic demonstration of the energy transfer channels which exist within a RE-TM alloy under laser photon stimulation. 70.

Figure 3.8: (a) Theoretical calculated response rates for Gd5d, Fe3d and Gd4f electron orbitals under pulsed laser stimulation. (b) Cartoon schematics of the two observable modes of spin precession, the FMR coherent mode and the high temperature exchange mode. (c) Experimental observations of temperature and

angular momentum compensation in GdFeCo as well as the observed Gilbert damping. 71.

Figure 4.1: Schematic of MBE system. Sample is positioned at the top of the chamber behind a mechanical shutter. An electron source gun is guided onto a sublimation source in a Hearth, which ejects a molecular beam towards the sample. Various pumps and heat sinks are used to maintain the low pressure environment. A plasma oxygen source is fitted here to introduce molecular oxygen into the chamber for post-oxidation experiments. 77.

Figure 4.2: Iron oxide phase diagram, showing the spectrum of oxides which can be formed under various temperature and oxygen environmental conditions. Pure Fe_3O_4 (magnetite) exists under a very narrow range between ~900-1500° and ~27.5-28.5% oxygen composition by weight. 78.

Figure 4.3: Example images of several stages of polishing a cross-section sample, showing the quality of the interface required for a successful sample. 81.

Figure 4.4: Cartoon schematic of the arrangement of materials combined to make a cross section TEM sample. Slices of a sample are glued face to face (film surfaces together) and backed by Si supports. After thinning one side, a Cu grid is glued to support the sample once it reaches <50 μm thick. 81.

Figure 4.5: After PIPS milling, the sample is considered ready when a clear band of rainbow fringes are observable at the interface. This is due to the thickness of that region being of the scale order of the wavelength of visible light. 82.

Figure 4.6: Schematic showing ray diagram of a standard Transmission Electron Microscope (TEM) setup. Showing the series of lenses which collect and shape the electron beam created at the top of the column. 84.

Figure 4.7: Calculated diffraction pattern for Fe_3O_4 (001) showing the Miller index for each spot corresponding to a plane in the real-lattice. 86.

Figure 4.8: Examples of basic Miller indices for a simple cubic system. 87.

Figure 4.9: Schematic of planar defect geometry used in Howie-Whelan approximation. 88.

Figure 5.1: Schematics showing Kerr rotation of polarization causing a linear increase in the intensity component along the analyzer axis (left) and a simple cross-analyzer detector configuration (right). 93.

Figure 5.2: (a) Design of bridge detector built and used in this investigation showing two trans-impedance photodiode amplification circuits mounted to a rotating frame to detect orthogonal polarization components. Only 400 nm probe light is admitted and the frame is able to rotate around the axis of the probe beam to balance the detectors. The setup allows easy access to variable capacitors to tune the temporal response of each diode independently. (b) A schematic circuit diagram for the trans-impedance circuit built. 94.

Figure 5.3: Difference between bridge detector photodiode 1 and 2 on oscilloscope. Shows an example of a signal spike observed if the detector timings are mismatched. This is adjusted for by changing the detector amplifier capacitance. 95.

Figure 5.4: Historical image of frame by frame observation of a horse in motion by Eadweard Muybridge showing early example of observation of a dynamic event captured faster than real time. 96.

Figure 5.5: Schematic showing the combination of laser instruments to form the high-power, short-rise pulsed laser essential to this investigation. 97.

Figure 5.6: The seed pulse is stretched, reducing its peak power, before amplification and then recompressed to form a short, high power pulse. This allows greater amplification circumventing the power damage threshold of the amplifier. 101.

Figure 5.7: Amplifier regeneration profile observed on oscilloscope. Just the input Pockels cell activated (left) and the output Pockels additionally activated (right). This shows an example of a well-tuned regeneration, points of note: low background interference, sharp build-up, output timing set to output high pulse power. 101.

Figure 5.8: Example of effect of laser stability noise on the detector output shown on oscilloscope for an unstable situation (left) and after optimizing (right). Showing signal from detector 1 (top trace), inverted signal from detector 2 (bottom trace) and the optimized difference between the channels (middle trace). 102.

Figure 5.9: Schematic of the ultimate experimental set-up used in this investigation. The laser output is split into transmitted pump (92%) and reflected probe (8%) by a beam-splitter. The pump beam (red) passes through a delay line, optical chopper and beam reducer before being focused onto the sample. The probe (blue) passes through a BBO wavelength doubling crystal and a polarizer before being focused onto the sample. 104.

Figure 5.10: Alignment of the delay line. A pinhole is mounted on the delay line during alignment to measure the relative deviation in the beam. A one axis translation stage and rotation mount are used to adjust the beam entering the delay line to minimize this deviation. 105.

Figure 5.11: Frame by frame camera capture of the pump beam spot on the sample during a delay line movement using two mirrors. Shows a non-linear drift as the delay line is moved from one end to the other. This is caused by sub-micron unevenness in the delay line tilting the mirrors. 106.

Figure 5.12: Schematic of alignment of the three interdependent lenses required to focus the laser and then obtain a true image of the sample surface. 107.

Figure 5.13: Camera images of alignment of the three interdependent lenses required to observe the sample surface clearly. The image lens is added and moved to focus (left); the reflected lens is added and moved until a wide-field image of the sample surface is in focus (middle); the incident lens is added and moved until the beam focus is observed again. This is done for both pump and probe together and overlapped (right). 108.

Figure 5.14: Ray diagram of geometry for approximating beam focus diameter based on lens focal length, f, and incoming beam divergence, θ_{d1} from a collimated beam. 110.

Figure 5.15: Ray diagram of geometry for calculating change in beam radius and divergence from a collimated beam. 110.

Figure 5.16: LabVIEW software front panel, designed to show a number of useful values such as the applied field strength and runtime information. 114.

Figure 5.17: LabVIEW software settings menu, designed to allow a large amount of control over the experimental settings. Delay line steps are set up here in ranges to allow the time sensitivity to be varied based on the scale of dynamics in each range (middle). A field sweep can also, optionally, be set-up for at each delay step (right). 115.

Figure 5.18: Image showing LabVIEW main experiment ‘For loop’. 116.

Figure 5.19: LabVIEW software pre-run information. Each run is saved with a data sheet containing the useful experimental information and save filenames and folders are then procedurally generated. 117.

Figure 6.1: VSM measurements for three post-oxidized samples. Sample A (green) shows an over oxidized state; sample B (red) shows a more favourable square Fe_3O_4 response; sample C (blue) shows an iron dominated signal for a thicker film with a limited oxidation depth. 121.

Figure 6.2: Table showing growth and magnetometry information for thin over-oxidized sample A; thin less oxidized sample B; thick unoxidized layer-dominated sample C. 122.

Figure 6.3: HRTEM cross-section of 15 minutes oxidation time (top) and 60 minutes oxidation time thin samples (bottom). Showing the substrate, film and vacuum (guide lines have been added to compare with **figure 6.5**). 123.

Figure 6.4: Select area diffraction of 15 minute oxidation time thin-film (top left); 60 minute oxidation time thin-film (top middle); MgO substrate (top right); calculated pattern of Fe_3O_4 (001) (bottom left) and MgO (001) (bottom right). Yellow squares mark out common oxygen sublattice pattern and blue squares mark out Fe_3O_4 unit cell pattern, displaying inverse spinel structure. 124.

Figure 6.5: Bragg filtered images of (a) 60 minute oxidation time thin-film and substrate; (b) 15 minute oxidation time thin-film and substrate. Greater disorder is observable in (a) compared to (b). 125.

Figure 6.6: TEM image showing long range film with sharp interface and uniform depth (left). Select area diffraction (right) shows Fe_3O_4 (100), Fe (110) and MgO (100) crystalline order epitaxially stacked. 126.

Figure 6.7: HRTEM images of Fe_3O_4 (100)||Fe (110) interface (far left) with Bragg filtered image (mid left) and of Fe (110)||MgO (100) interface (mid right) with corresponding Bragg filtered image (far right). Crystal plane dislocations are identified from the Bragg filtered images and circled showing regular predictable mismatch in Fe_3O_4||Fe, but irregular mismatch in Fe||MgO. 127.

Figure 6.8: Illustrations of the three most common orientations in the Fe_3O_4 cubic inverse spinel crystal unit cell. The (110) direction resolves each atomic column independently, unlike the other two. 128.

Figure 6.9: (110) direction HRTEM of (a) 9 minutes post-oxidized sample, showing Fe (100), Fe_3O_4 (110) and substrate. Interface transition takes place over ~5 monolayers. 129.

Figure 6.10: (110) direction HRTEM of (b) 27 minutes, (c) 45 minutes post-oxidized sample, showing Fe (100), Fe_3O_4 (110) and substrate. Interface transition in (b) much sharper than figure 6.9 (a) and (c). 130.

Figure 6.11: Bragg filtered images of 9 minutes (left) and 45 minutes (right) samples. Shows increase in disorder with oxidation time more clearly than **figure 6.5**. 131.

Figure 6.12: Example line contrast profiles of 9 (left) 27 (middle) and 45 (right) minute sample images. These are used to determine the thickness of each film with a rigorous measure. 132.

Figure 6.13: Example of two geometric shifts of the Fe_3O_4 unit cell on the (grey-scale) MgO (100) lattice. They may appear to be unique, but are in fact mirror images. 134.

Figure 6.14: Schematic showing proposed terminating planes of Fe_3O_4 (100) unit cell. Four octahedral (B) iron atoms exist in each plane, notably the oxygen lattice is constant through each plane. 135.

Figure 6.15: In-plane APBs on Fe_3O_4 (100). 136.

Figure 6.16: 1/2 z-shift out-of-plane APBs on Fe_3O_4 (100). 136.

Figure 6.17: 1/4 z-shift out-of-plane APBs on Fe_3O_4 (100). 137.

Figure 6.18: 3/4 z-shift out-of-plane APBs on Fe_3O_4 (100). 137.

Figure 6.19: Non-integer unit cell shifts and visibility criteria, showing the in-plane shifts (grey) and out-of-plane shifts. 138.

Figure 6.20: Images showing example diffraction pattern for 15mins sample (top left); a TEM image of the sample surface (top right); calculated gamma-phase Fe_2O_3 maghemite, observed in plan-view analysis (bottom left) and calculated Fe_3O_4 diffraction pattern (bottom right). 139.

Figure 6.21: Images showing plane-view TEM images of two regions of 15 minute post-oxidized film under [220] dark field conditions which show a large defect density. 140.

Figure 6.22: Images showing plane-view TEM images of 15 minute post-oxidized film under [400] dark field conditions, showing visible defects, as well as Moiré fringes. 141.

Figure 7.1: Normalized static MOKE longitudinal hysteresis measurements showing the anisotropic magneto-optic response. All TRMOKE measurements are undertaken at the in-plane hard axis, 0° here. 147.

Figure 7.2: Amplitude of maximum reflectivity peak (red) compared to equivalent maximum Kerr signal peak (blue) as a function of pump fluence. Reflectivity shows a discontinuity between 37-42 $\mu J/cm^2$ which is not seen in the Kerr signal data. Both curves show a possible gradual saturation at higher fluences. 149.

Figure 7.3: Recovery time constant of the local sample reflectivity, as a function of pump fluence. Two regimes of energy dissipation are observed. For low fluence, this is not energy dependent, but for higher fluence it becomes significantly so. 149.

Figure 7.4: Graph showing ultrafast demagnetization curves for low (a), (black), (23 $\mu J/cm^2$) and high fluence (b), (red), (76 $\mu J/cm^2$). Inset graph shows the picosecond

timescale drop in magnetization and the high frequency artefacts which affect the regime highlighted in the blue dashed region. 151.

Figure 7.5: Ultrafast moment flipping contrast, defined in figure 7.4, shows the strength of the ferromagnetic state as the Gd and Fe moments align for a picosecond above a critical thermal threshold, corresponding to T_{Mcomp}. 152.

Figure 7.6: Schematic timeline of the ultrafast magnetic reversal behaviour. 154.

Figure 7.7: Time for Gd sublattice to reach internal equilibrium, showing 2 critical temperature points (a) and (b) 154.

Figure 7.8: TRMOKE rotation signal as a function of pump fluence for low pump powers. Oscillatory recovery is observed for each, with the first oscillation being gradually absorbed into the long range recovery curve. 155.

Figure 7.9: TRMOKE rotation signal as a function of pump fluence for high pump powers. Oscillatory recovery is all but obscured by the long range recovery curve. 156.

Figure 7.10: Graph showing an example magnetization recovery time curve for low pump fluence (25 μJ/cm^2), with fitted exponential decay; recovery is rapid and strongly oscillatory. 158.

Figure 7.11: Graph showing an example magnetization recovery time curve for high pump fluence (82 μJ/cm^2), with fitted exponential decay; recovery is much slower and oscillatory behaviour is both suppressed and delayed. 159.

Figure 7.12: Graph showing time constant τ as a function of pump fluence (black), showing the recovery time from each maximum demagnetization state; and total recovery time (blue), which includes the time from the initial pump event, showing the total time associated with elevated energy in the spin reservoir. 160.

Figure 7.13: Comparison of energy dissipation from spin reservoir (black), (Kerr signal) and lattice reservoir (red, dominant temperature reservoir over long timescale represented in Reflectivity signal). 161.

Figure 7.14: Schematic showing energy and angular momentum gain and loss channels. Spin lattice relaxation is dependent on the dominant moment's spin-orbit coupling, which is Gd at low temperatures, and swaps to Fe above T_{Mcomp}. 162.

Figure 7.15: Example of magnetic precession residual, after removing recovery slope low fluence measurement (black) (25 μJ/cm^2), with fitted sinusoidal decay (red). 164.

Figure 7.16: Example of magnetic precession residual, after removing recovery slope low fluence measurement (black) (82 μJ/cm^2), with fitted sinusoidal decay (red). 164.

Figure 7.17: Residual for 65 μJ/cm^2 fluence plot. This shows the two frequencies, separated by a temperature boundary. 165.

Figure 7.18: FFT series, showing the gradual growth of lower frequency precession while the dominant frequency begins to fall, followed by the rapid reversal of the frequency dominance, and finally the lower frequency drops again at the highest laser pump fluences. 166.

Figure 7.19: Comparison of FFT frequency vs curve fitted frequency for coherent precession regime. Shows slow increase with fluence followed by a significant drop off after 71 μJ/cm^2, lower frequency oscillation observed at higher temperature becomes stronger at higher fluences. 167.

Figure 7.20: Graph showing resonance amplitudes from FFT as a function of pump fluence for both oscillation frequencies observed. This shows swapping of dominant precessional mode after T_{Mcomp} which is also then quenched at T_{Acomp}. 167.

Figure 7.21: Graphs showing examples of cropped FMR mode precession data with damped sinusoidal fitting. 169.

Figure 7.22: Graph showing Gilbert damping parameter as a function of fluence. Highlighted are the magnetization T_{Mcomp} and angular momentum T_{Acomp} compensation temperatures. 170.

Figure 8.1: Dynamic hysteresis measurements taken at 0.5 ps intervals after pump event 179.

Acknowledgements

It has been a long and educational journey that leads up to the submission of this document. A task that would not have been possible without the support and guidance of so many people at the University of York and beyond. I'd like to take this opportunity to acknowledge Professor Kevin O'Grady for introducing me to the world of research, without this inspiration I would not be where I am today. To my supervisors Dr. Vlado Lazarov and especially Dr. Jing Wu, have opened up new worlds for me. To Professor Rex Godby and Dr Stuart Cavill for your advice and counsel.

I'd like to thank the support staff, particularly Bob Hide, Dave Coulthard, Neil Johnson and Mark Laughton for their guidance and friendship throughout this process. To the students who went before me, from whom I have learned a great deal, Dr. James Naughton, Dr. Andy Vick, and Dr. Tuyuan Chen. And to my fellow students, too numerous to list, who have shared in the triumphs and frustrations which we all faced.

Finally to my family, thank you for supporting me this far.

For Rod.

Declaration

The research present here in this doctoral thesis is the work of the author, James Sizeland, except where explicitly acknowledged or referenced in the text, in accordance with the examination regulations of the University of York. This work has not previously been presented for an award at this, or any other, University.

Chapter 1

Introduction

1.1 Spintronics

Spintronics is an umbrella term for the area of condensed matter physics which deals with the understanding of the electron spin in conjunction with its charge and their interaction with photons, all three of which represent information carriers **[1]**. The major motivations in this area are twofold; enhancement of modern cutting-edge electronics technology and greater appreciation of the fundamental physical principles which inevitably emerge when pushing the limits of both size and speed of functional devices. The name is derived from a portmanteau of spin and electronics.

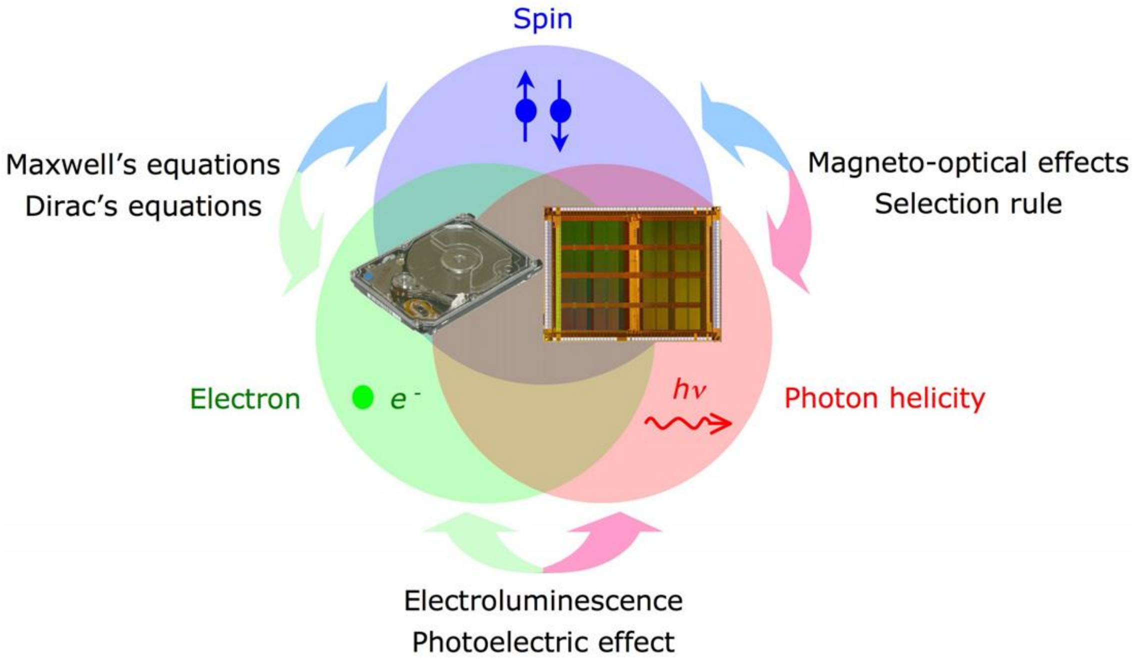

Figure 1.1: Venn diagram of the three particle interactions which encompass the field of spintronics. **[2]**

It is an area covering a large number of specialisms (as shown in **figure 1.1**), covering topics from quantum computing **[3]** and graphene nanostructures **[4]** to year on year improvements in speed and scale of the technology in our pockets and homes **[5]**. By necessity it is a fast moving and rapidly advancing field, fuelled by its eminently applicable nature, producing many exciting developments over a relatively short span of time. The field received a Nobel Prize in Physics in Albert Fert and Peter Grünberg in 2007 for their work on giant magnetoresistance (GMR) **[6] [7]**. Magnetoresistance is employed in a spin-valve structure in the read-heads of the hard disk drives (HDD), found in most personal computers for the last 30 years. It is used to convert the magnetic field of a data bit to an electronic signal. Such information is stored in magnetic bits, where anisotropy limits the magnetization to one of two orientations, read in binary by allocating them as ones or zeroes. The discovery of GMR, and subsequent adoption of materials supporting it, has increased magnetoresistance conversion efficiencies from ~10% to >40% **[8]** allowing even smaller magnetic bits to be used. This is fuelling the growth in areal data density as predicted by Moore's Law (**figure 1.2**).

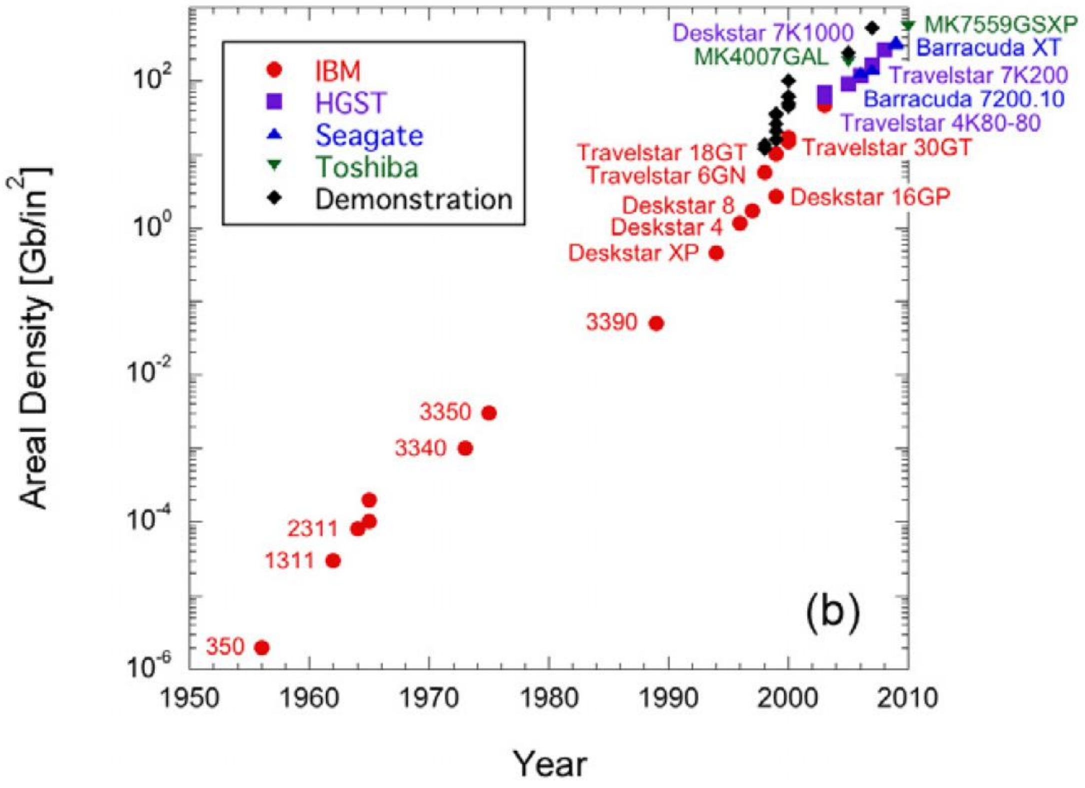

Figure 1.2: Moore's law of exponential improvement in technology showing year on year growth in data storage density in magnetic media. **[2]**

Future efforts are focused on greater improvements in GMR devices, but additionally on technologies such as magnetic random access memory (MRAM) which aim to replace both current HDD and conventional RAM architecture as a "universal memory", offering non-volatility, nanosecond read and write times, competitive density and significant savings in both power and real estate, crucial in mobile devices. That being said, there are equally important fundamental physics questions at stake. Questions like the fundamental timescales of spin coherence. Fundamentally, spin is a quantum-mechanical effect whose interaction with charge and other such phenomena offer invaluable information on matter.

1.2 Origin of Magnetism

Extensive descriptions of magnetism exist in many places and this section will serve to introduce a few of the key points which will be relevant throughout this work. **[9] [10]**.

Two main theoretical approaches exist to apply quantum theory to magnetism, these being the localized model and the band model. The first describes a system dominated by intra-atomic electron-electron interactions, which define atomic moments. Interatomic interactions are small and compete with thermal energy to define magnetic behaviour. The second considers magnetic carriers as itinerant (mobile), heavily influenced by interatomic interactions and forming electron energy bands. Intra-atomic interactions produce ordered magnetic states based on the proportions of electron spins oriented up and down. A spectrum of behaviour exists between these two extremes and both are necessary to fully characterize a range of magnetic material properties. For instance, transition metals, such as iron (Fe) are well described by the band model, whereas rare earths, such as Gadolinium (Gd) require a combined approach.

The magnetism of an atom is fundamentally caused by electron angular momentum, divided into electron spin and orbital magnetic moments, written as **equation 1.1** and **1.2** respectively, these are defined in terms of the Bohr magneton, μ_B, Planck's constant, $\hbar$, and the respective quantum angular momentum operators $< s_z >$ and $< l_z >$. The orbital moment is described by electrons circling the atomic nucleus, while the spin moment is an intrinsic property of the half-integer fermionic nature of electrons, which have projections of $\pm\hbar/2$. The total spin moment is then given by the sum of these (**equation 1.3**) with a so-called g-factor (~2) representing the larger spin moment contribution.

$$< m_o^z > = -(\mu_B/\hbar) < l_z > = \underline{L_e} \tag{1.1}$$

$$< m_s^z > = -2(\mu_B/\hbar) < s_z > = \underline{S_e} \tag{1.2}$$

$$\underline{\mathrm{M}} = \underline{\mathrm{L_e}} + \mathrm{g}\underline{\mathrm{S_e}} \tag{1.3}$$

While conservation of energy is an important factor in all physical processes, modern treatments of magnetism are focused on conservation of angular momentum, which requires the magnitude and vector of $\underline{\mathrm{L_e}}$ and $\underline{\mathrm{S_e}}$ to remain constant unless angular momentum is transferred between them or away to the environment. From here it becomes necessary to mention the three magnetic inter- and intra-atomic interactions which define the magnetic character of a material:

1. The exchange interaction defines a material's spin moment and is a consequence of interatomic electron-electron coulomb interaction. Electrons of neighbouring atoms align parallel (ferromagnetic) or antiparallel (antiferromagnetic), depending on the material dependent sign of the exchange integral $\underline{\mathrm{J_{ex}}}$.

2. The spin-orbit interaction describes the coupling strength between $\underline{\mathrm{L_e}}$ and $\underline{\mathrm{S_e}}$. It is on the order of $10 - 100 \times$ smaller than the exchange interaction for transition metal 3d electron orbitals, but notably larger for rare earth 4f electron orbitals. It also determines the magneto-crystalline anisotropy of a solid material.

3. The Zeeman interaction describes the coupling between a material's total magnetic moment and an externally applied magnetic field.

1.3 Motivation

Both of the materials studied in this project, half-metallic Fe_3O_4 (magnetite) and the rare earth-transition metal alloy GdFe represent important aspects of spintronic research **[11] [12]**. Each material contains its own set of unique challenges and opportunities, from an engineering perspective and equally from a theoretical and experimental scientific perspective.

Magnetite is an abundant, naturally occurring cubic crystal oxide of iron. It is magnetic at room temperature and was thought to have been discovered by the inhabitants of the Magnesia region of ancient Greece, from which the material and the magnetism itself took their names **[13]**. The complex interactions of the atoms within this structure give rise to both ferromagnetic and antiferromagnetic components, due to super-exchange interactions. This results in a net ferrimagnetic material with a relatively high Curie temperature (T_C) of ~860K making it stable within the running parameters of all but the most extreme electronic devices. Magnetite is also an electrical conductor and displays half-metallic properties to the extent that it is theorised to be a 100% spin polarisable material **[14]**. These properties make it a very promising material for application in modern spintronic devices such as spin-valves, characteristically requiring thin-films of a few hundred of nanometres at most **[15]**.

The necessity for pure single crystal growth throws up a range of new challenges, as at this length scale, the well understood bulk behaviour begins to break down, and interfacial effects begin to become much more dominant. So far however such attempts to integrate this material have provided limited success, hindered by low magnetoresistance observations in thin-film prototypes **[16]**. As the magnetic character of Fe_3O_4 is defined by its crystal structure, these limitations have been attributed to the existence of a large number of crystal defects possible within its epitaxial film. Such defects, known as antiphase domain boundaries (APBs) disrupt the population of superexchange interactions. These APBs are locations where the repeating pattern of the crystal structure is interrupted, introducing random interatomic coupling. Advances in molecular beam epitaxy (MBE) deposition techniques as well as more detailed work on the structure and formation process of this material are working to resolve these issues. As such it is important to gather an understanding of the nature and density of defects present within the film, as these will provide a fundamental limit on the efficiency of any spintronic devices.

By contrast GdFe belongs to a group of materials which exist as amorphous alloys, whose magnetic characteristics have been shown to be robustly independent of their microstructure **[17]**. The rare-earth transition metals exist as ferrimagnetic thin-films with two semi-independent magnetic moments, coming from separate electron orbitals. These sublattices critically have very different temperature responses, and exhibit compensation temperatures, at which the barrier to magnetic reversal becomes very large and any stored magnetic information is extremely shielded from unwanted thermal disorder. In order to manipulate the magnetic information then, rapid control of the temperature of the material is needed; to raise it to an unstable state, induce a magnetic reversal and return to rest stability. It has been shown **[18]** **[19]** that this barrier to reversal can be overcome on a sub nanosecond timescale by inducing a coherent magnetic precession (ferromagnetic resonance) and more recently **[20]** **[21]** investigations have reported on mechanisms for even faster reversal via sub picosecond optical excitation from a laser pulse. Laser induced magnetisation reversal investigations are well placed to provide further information on these still poorly understood **[22]** mechanisms.

The key motivations for this investigation were to better understand the critical parameters which affect the magnetic character of these two materials in thin-film. This was achieved by developing and commission a measurement apparatus for spatial and temporally resolved magnetic measurements used to understand temperature dependence of the magnetic behaviour of GdFe as well as investigating techniques to understand the effects of growth and structure on Fe_3O_4.

1.3 Outline

In this thesis, two different methodological techniques of investigating the magnetic character of thin-film media are discussed. These techniques are divided into self-contained chapters based on themes of materials science and magneto-optics. Within this division, each chapter is designed to be as self-contained as possible, which results in some limited restatement of key facts with referential pointers to other sections for greater detail.

Chapter 2: This describes the theoretical background required to understand the magneto-optic work investigated in this thesis. $2.2 Introduces the concept of the Magneto-optic Kerr effect (MOKE) and provides a quantitative discussion of the geometry and analysis of such measurements. $2.3 develops this discussion for the case of ultrafast (<100 ps) optically induced demagnetization and provides a historical contextualization for the technique. Following this, the longer timescale recovery process is discussed in detail in $2.4, including the energy and angular momentum considerations and the Landau-Lifshitz Gilbert (LLG) equation which describes such behaviour.

Chapter 3: Here the theoretical material considerations are presented. $3.2 discusses the nature of magnetite, including its crystallographic qualities and quirks. This presents the necessary framework required for growth and structure investigations of this material, in the context of its magnetic behaviour. $3.3 then discusses the key properties of GdFe and their physical origins. The unique magnetic properties of rare-earth transition metals thin-films are also provided in more detail here.

Chapter 4: Provides the growth and structural characterization techniques required to control the quality of thin-film growth. While this project has not been focused growth method, but rather post-growth characterization, the methods of growth encountered in this investigation are introduced in $4.2 to provide context for the later work. $4.3 then provides details of the experimental and theoretical techniques which were used and developed during the course of this investigation to obtain and analyze high resolution electron microscopy images. This work, along with the results provided in chapter 6 formed the first year and a half of my degree.

Chapter 5: $5.2 provides a background for the detection of the magneto-optic Kerr effect and is provided as a stand-alone technique discussion, or as a supplementary document to the theoretical discussion in chapter 2. $5.3 details the method and understanding required to construct a high powered femtosecond time-resolved MOKE apparatus. This laser system was obtained and commissioned as part of this investigation as was the optical setup and data acquisition programmes also detailed here.

Chapter 6: A critical high resolution transmission electron microscopy (HRTEM) investigation into the quality of magnetite thin-films produced by post-oxidation of epitaxially grown iron films. This investigation begins in $6.3 with cross-sectional HRTEM of 3nm films under varied oxidation times which show very clear differences in the quality of magnetic ordering and the corresponding hallmarks in the material structure. $6.4 then provides a theoretical discussion of allowed ABP defects and their observation criteria in dark field imaging, followed by an experimental observation from plan-view HRTEM imaging.

Chapter 7: Details a magneto-optical investigation of a critical composition ratio GdFe thin-film. It provides a systematic series of measurements in pulsed laser pump energy density (fluence) to identify the critical energy transfer mechanisms taking place on a picosecond timescale. It identifies key temperatures and characteristics of the material and provides an important collection of information with which to feedback to the further growth and optimization of such materials.

Chapter 8: Summarises the key points and provides a discussion of further work which would benefit from this research.

1.4 References

[1] S. A. Wolf, et al., Magn. and Mat., **294**, 1488 (2001)

[2] A. Hirohata and K. Takanashi, J. Phys. D: Appl. Phys., **47**, 193001 (2014)

[3] T. D. Ladd, et al., Nature **464**, 45 (2010)

[4] W. Han, et al., Nature Nanotechnology, **9**, 794 (2014)

[5] S. A Wolf, Proceedings of IEEE, **98**, 2155 (2010)

[6] P. A. Grunberg, Rev. Mod. Phys., **80**, 1531 (2007)

[7] A. Fert, et al., J Magn. Magn. Mat., **140-144**, 1 (1995)

[8] M. N. Baibich, et al., Phys. Rev. Lett., **61**, 2472 (1988)

[9] F. Gautier and M. Cyrot, Magnetism of Metals and Alloys (North-Holland Publishing Company, 1982)

[10] J. Stöhr and H. C Siegmann, Magnetism: from Fundamentals to Nanoscale Dynamics (Springer Verlag, Berlin, 2006)

[11] T. Hauet, et al., Phys. Rev. B, **76**, 144423 (2007)

[12] D. Venkateshvaran, et al., Phys. Rev. B, **79**, 134405 (2009)

[13] F. D. Stacey and S. K. Banerjee, The Physical Principles of Rock Magnetism (Elsevier Science, 2012)

[14] S. M. Thompson, et al. J. Appl. Phys., **107**, 09B102 (2010)

[15] D. Tripathy, et al., Phys. Rev. B, **75**, 012403 (2007)

[16] J-B Moussy, J. Phys. D: Appl. Phys., **46**, 143001 (2013)

[17] S. Mangin, et al., Nature Mat., **13**, 286 (2014)

[18]C. H. Back, et al., Phys. Rev. Lett., **81**, 3251 (1998)

[19] T. Gerrits, et al., Nature (London), **429**, 850 (2002)

[20] K. Vahaplar, et al., Phys. Rev. Lett. **103**, 117201 (2009)

[21] I. Radu, et al., Nature (London) **472**, 205 (2011)

[22] V. López-Flores, et al., Phys. Rev. B, **87**, 214412 (2013)

Chapter 2

Interpreting Magneto-Optic Dynamics in Thin-film Media

2.1 Introduction

Linearly polarized light, incident on a material exhibiting a net magnetization will undergo an ordinary metallic interaction causing an ellipticity in any reflected and transmitted components **[1]**. Alongside this ellipticity, there will be a rotational effect proportional to the net magnetization; this is known as a magneto-optic effect. When referring to the transmitted light, this is known as the Faraday Effect and is proportional to the magnetization in the direction of light propagation. In reflection, the effect is known as the magneto-optic Kerr effect (MOKE). Both the Faraday Effect and MOKE are first-order effects, linear with magnetization, and are described by circular birefringence, whereby left- and right-handed polarizations propagate at different speeds and are selectively absorbed. As linearly polarized light can be considered a superposition of equal left- and right-handed polarizations, the effects can cause the shape and angle of plane-polarized light incident on such a medium to be modified **[2]** **[3]**. Second-order magneto-optic effects, such as the Voigt effect, also exist, which are quadratic with magnetization and produced by second-order linear magnetic birefringence. These effects are only a factor at normal incidence, when net magnetization is applied in the plane perpendicular to the incident light, and will not be treated further here. As the rotation is proportional to the propagation length through the material, the Faraday Effect was historically easier to detect than MOKE, despite being limited by the necessity for transmission through the medium, where MOKE only requires a reflective surface. For a long time the Kerr effect was considered to be 'rather weak and difficult' **[1]** to obtain meaningful information from until background subtraction methods were improved.

The timescales of changes in magnetization, in response to external stimuli, can vary greatly from millions of years in geography, to decades in magnetic storage devices, to nanoseconds in magnetic hard drive read and writing, and further still. Composition, structure and scale of constituent parts play a key role in defining each of these time regimes. Particularly of interest to Spintronics research are three methods of manipulating magnetic ordering on a sub-microscale, namely pulsed field, spin current and pulsed laser stimulation **[4]**. Of these, pulsed laser is the only method able to reach the sub picosecond timescale.

Over the past 20-30 years, the development of pulsed lasers has allowed science and technology to push further into faster and faster magneto-dynamics, down to the timescales of fundamental physical processes **[5] [6]**. The so-called ultrafast regime loosely refers to the timescales below 100 ps, the intrinsic spin-lattice relaxation time, defined by the time-energy correlation. The questions of the fundamental limits of these processes are still as relevant today and with fundamental limits to magnetic pulse technology being reached, alternative sources of magnetization manipulation are all the more relevant in pushing speed limits.

This chapter discusses the current understanding and required knowledge to perform and appreciate magneto-optic characterization experiments, particularly time-resolved, pump-probe Kerr effect magnetometry. It goes into detail on the development of pulsed laser induced dynamics.

2.2 Magneto-Optical Kerr Effect (MOKE)

> "I was led some time ago to think it very likely, that if a beam of plane-polarized light were reflected under proper conditions from the surface of intensely magnetized iron, it would have its plane of polarization turned through a sensible angle in the process of reflection."
>
> **- John Kerr, 1877 [7]**

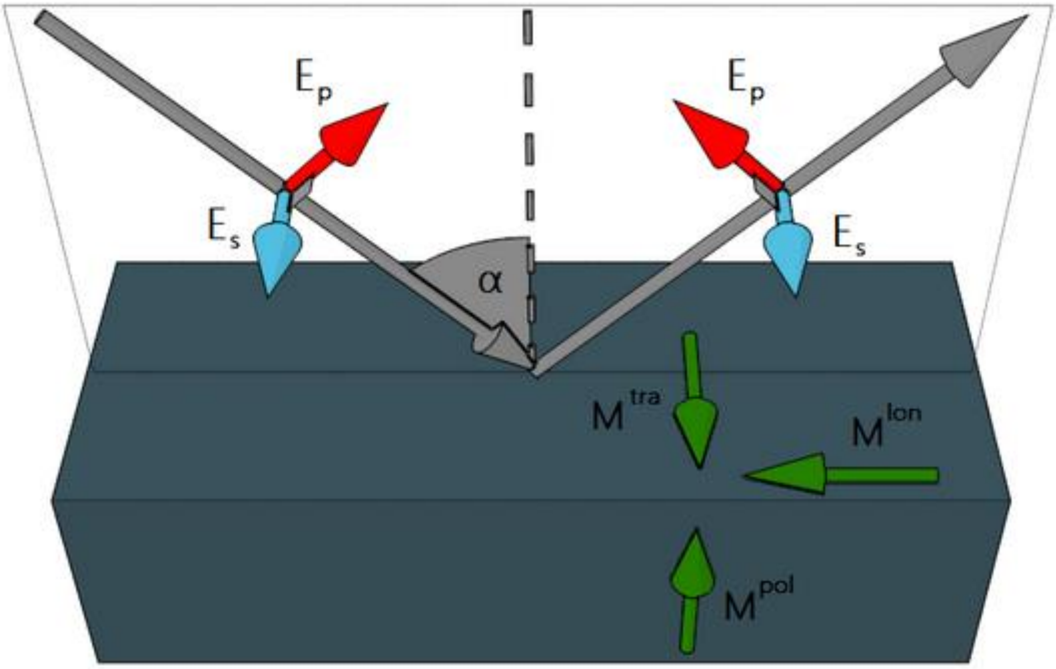

Figure 2.1: Geometry of a MOKE system showing incident light ray at angle α to the surface normal in incident plane. Electric field vectors are defined relative to the incident plane E_P in plane, E_S orthogonal to that. Components of magnetization defined relative to the incident plane and the sample surface.

The Magneto-optical Kerr effect (MOKE) was discovered by Scottish Physicist John Kerr in 1876-8 **[8] [9]**, and is distinct from his other discovery: the electro-optical, nonlinear Kerr effect. It is well described by the dielectric law $\underline{\mathbf{D}} = \underline{\boldsymbol{\varepsilon}\mathbf{E}}$, where $\underline{\varepsilon}$, the dielectric permittivity tensor of a medium relates an incident electromagnetic plane wave of electrical vector, $\underline{\mathbf{E}}$, with a displacement vector $\underline{\mathbf{D}}$ upon interaction with that medium. The dielectric permittivity tensor contains information relating to the magnetization vector of the interacted medium and material specific constants **[10]** **[11]**. It can be expanded to give the following:

$$\underline{D} = \varepsilon(\underline{E} + iQ\underline{M} \times \underline{E}) \qquad (2.1)$$

In **equation 2.1**, ε is the dielectric permittivity constant, $\underline{M}$ is the magnetization vector of the medium and Q refers to the (material dependent) maximum strength of the Kerr effect, which is roughly proportional to M_s, the saturation magnetization of the medium (or sublattice). The cross product relationship between $\underline{M}$and $\underline{E}$ describes a Lorentz force, $\underline{\upsilon_L} = -\underline{M} \times \underline{E}$, and shows the symmetry of the polarization displacement, with respect to $\underline{E}$.

The geometry of a MOKE system is defined relative to the sample surface normal and the incident plane made by the incident and reflected beam; the axis of polarization is referred to as p in the plane of incidence, and s perpendicular to it (see **figure 2.1**). The effect is separated into three distinct orientations; the first of these is referred to as longitudinal MOKE, (M^{Lon}) and is due to the magnetization component in-plane with the material surface and parallel to the plane of reflection **[1]**. A linearly polarized light source incident on the material will cause an oscillation of the electrons in the plane of the material surface and parallel to the polarization vector $\underline{E}$. This regularly reflected light, $\underline{N}$, will remain polarized parallel to $\underline{E}$. Additionally, due to the Lorentz force $\underline{\upsilon_L}$, a small electron oscillation will be induced in-plane with the material surface and perpendicular to $\underline{E}$, causing a fraction of the light to be polarized perpendicular to $\underline{E}$ upon reflection. This fraction is referred to as the Kerr amplitude, $\underline{K}$, and together with $\underline{N}$, causes the rotational effect on the reflected polarization vector, proportional to $|\underline{M}|$. The other two MOKE orientations are known as polar (M^{Pol}) and transverse (M^{Tra}), and refer to the magnetization vector out-of-plane with the material surface, and in-plane but orthogonal to the incident light plane, respectively. Combining the three orientations, relative (to the incident) signal amplitude can be quantified as follows in **equation 2.2**.

$$
\begin{aligned}
S = \; & -N_P\cos\Theta_P\sin\phi_S + N_S\sin\Theta_P\cos\phi_S + \\
& K^{Pol}\cos(\phi_S - \Theta_P)M^{Pol} + \\
& K^{Lon}\cos(\phi_S + \Theta_P)M^{Lon} + \\
& K^{Tra}(\sin\phi_S\cos\Theta_P)M^{Tra}
\end{aligned}
\tag{2.2}
$$

In this equation the subscripts p and s refer, respectively, to components in the plane of incidence and orthogonal to it, and the angles Θ_P and ϕ_S, correspond to the angular deviation from the p and s axis of the incident and reflected polarizers, respectively.

The first two terms describe the regular reflection contribution; the coefficients N_P and N_S are dependent on the incident angle α and the optical properties of the medium, via the Fresnel formulae **[12]**. Analogously, the coefficients K^{Pol}, K^{Lon} and K^{Tra} (referring to the polar, longitudinal and transverse components of the Kerr reflection) are also dependent on incident angle and optical properties of the medium. Simulations performed by MULTILAYER™ and DIFRACT™ programs **[13]** show that the longitudinal signal, of interest here, increases with 0 at α = 0° to peak around α = 65° as shown in **figure 2.2** below.

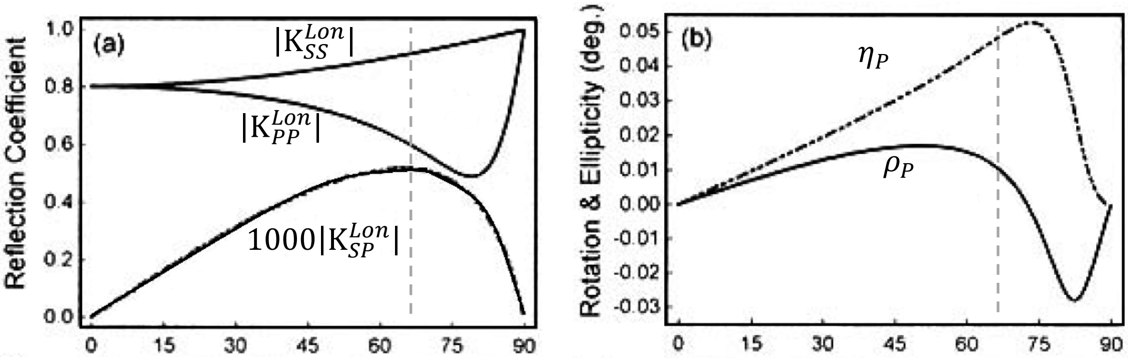

Figure 2.2: Calculated plots (a) of reflection coefficient K^{Lon} for incident to reflected orientations (s to s, p to p and s to p = p to s) and (b) polarization rotation angle ρ and ellipticity η versus incident angle α.

Single Detector Signal Calculations

From **equation 2.2** it is possible to isolate the properties which contribute to the observed signal received by a detector. By setting the polarizer angle to be Θ_P=0, the signal becomes a function of the analyzer angle,ϕ_S as shown in **equation 2.3** below. **Figure 2.3** shows the angular variation in the components of this signal for the incident p-polarized (Θ_P=0) and s-polarized ($\Theta_P = \pi/2$) for an isotropically magnetized sample.

$$S = -N_P \sin\phi_S + K^{Pol}\cos(\phi_S)M^{Pol} + K^{Lon}\cos(\phi_S)M^{Lon} + K^{Tra}(\sin\phi_S)M^{Tra} \tag{2.3}$$

It can be seen that the largest longitudinal and polar signals are received when the analyzer is oriented at 90° to the polarizer angle. This is known as a cross-polarizer, or cross-analyzer arrangement. The regular reflected signal is also minimized at this orientation.

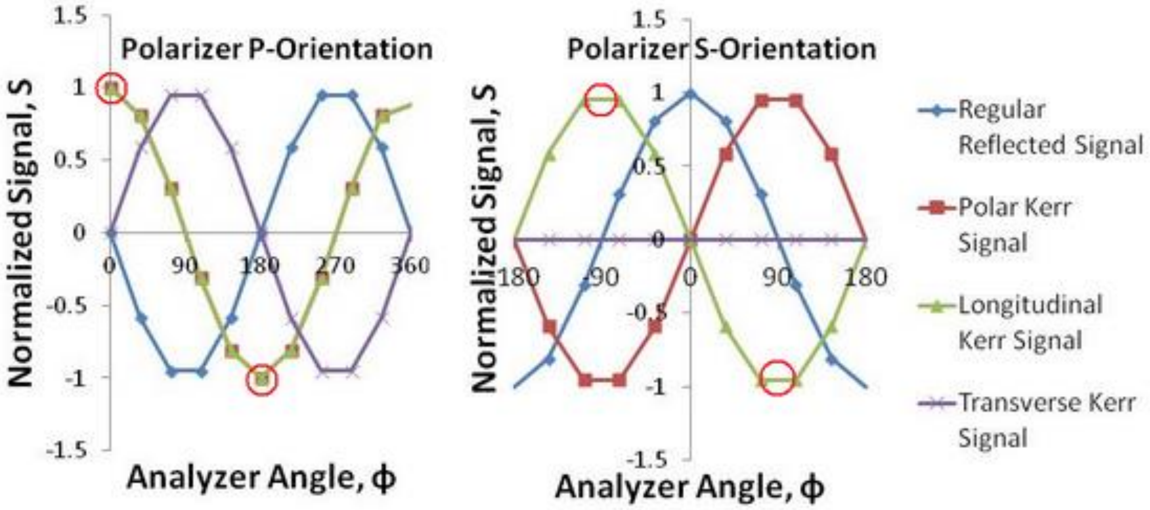

Figure 2.3: Graph of signals for a single detector scheme. Normalized signal observed for a theoretical isotropically magnetized sample, showing the relative signal amplitude of each Kerr orientation as a function of analyzer angle for incident s and p polarized light source. Signal maximized for 90° angle between polarizer and analyzer.

Bridge Detector Signal Calculations

For dynamic measurements involving small signals and requiring reflectivity information, a configuration of two detectors can be introduced to collect all light reflected from a sample, divided into two orthogonal components. This scheme is known as a bridge detector and is arranged with a reference state such that the reflected light intensity is equally split into the two detectors by a rotating polarizing beam splitter (see **chapter 5** for further details on measurement technique). Following **equation 2.2** for a single detector and setting the total signal, $S_{Total} = S_A(\phi_s) + S_B(\phi_s)$, where the angle between $S_A(\phi_s)$ and $S_B(\phi_s)$ is fixed to be 90°, equivalent graphs can be produced for this arrangement (see **figure 2.4**).

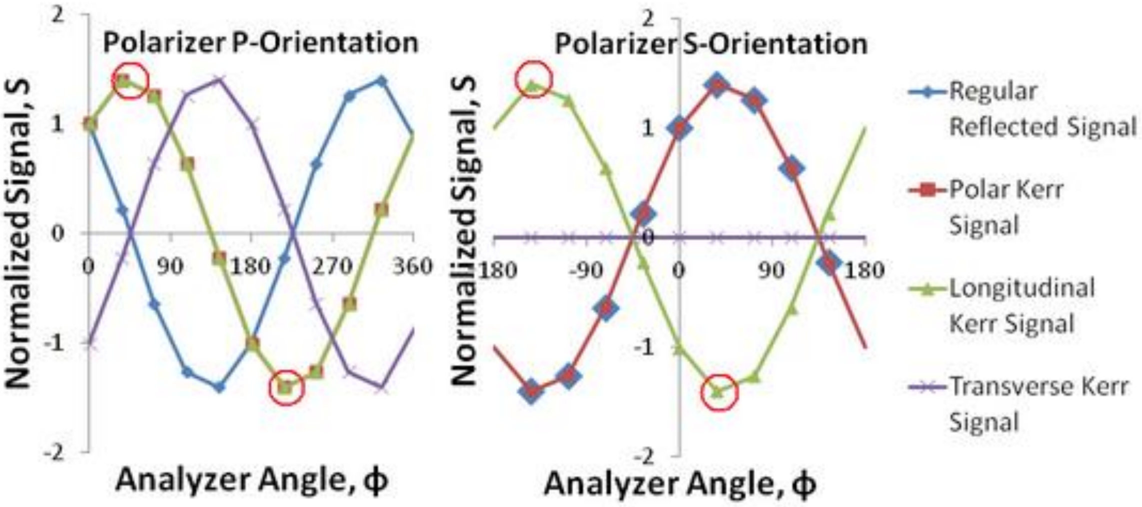

Figure 2.4: Graph of signals for a two detector scheme. Normalized signal observed for a theoretical isotropically magnetized sample, showing the relative signal amplitude of each Kerr orientation as a function of analyzer angle for incident s and p polarized light source. Signal maximized for 45° angle between polarizer and analyzer.

The longitudinal and polar signals are maximized at 45° to the polarizer angle, which is the point at which the two detectors will be balanced. Again the regular reflection is minimized at the same point, but only in the p-polarized incident orientation. For s-orientation, the regular reflection is maximized inverse to the longitudinal signal. It is for this reason that p-polarized incident configuration has been used for all MOKE measurements in this investigation.

At set-up the analyser angle ϕ_s is then fixed at +45° for S_A and -45° for S_B ready to detect variations in ϕ_p caused by changes in the magnetization state of the sample.

The Kerr signal is then found from the difference between detectors: $S_{Kerr} = S_A(\phi_p) - S_B(\phi_p)$. This leads to a voltage output which is linear with Kerr rotation (with the small angle approximation), with an offset signal S_0.

$$S_{Kerr} \approx S_0 \phi_p$$

2.3 Ultrafast Magnetization Dynamics

2.3.1 Laser-Induced Ultrafast Demagnetization

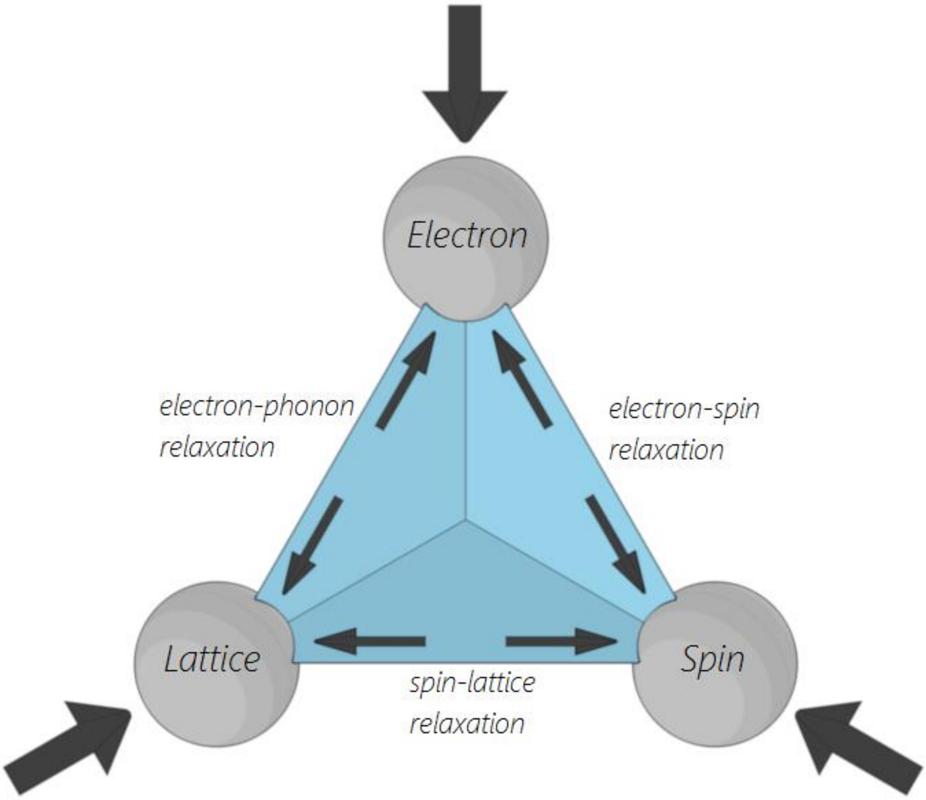

Figure 2.5: Three thermodynamic reservoirs in a ferromagnetic metal. Each can be initially excited by different mechanisms (e.g. photon injection, magnetic field change, mechanical stress). This is followed by a relaxation to the other reservoirs dependent on the strength of coupling between each.

As discussed in the previous section, the magnetization state of a material can change the properties of interacting light. By the same token, the interacting light can also affect the magnetization state of the material in return. The absorption of light by a magnetic material is described by energy transfer and angular momentum transfer **[5]**. This has a direct and indirect effect on its magnetization state, with timescales dominated by that interaction and interplay between three thermodynamic reservoirs, electron, lattice and spin (**figure 2.5**).

The initial interaction between a light source and a metallic system occurs by transfer of energy from photons to the degenerate electron gas creating electron-hole pairs which rapidly thermalize by means of electron-electron interactions **[14]**. The electron reservoir temperature increases extremely (typically >1 kK) and rapidly, due to a low heat capacity, and creates a non-equilibrium with the lattice reservoir. Energy transfer to the lattice via phonons then rapidly cools the electron reservoir and raises the temperature of the lattice reservoir before propagating and dissipating. Thermal equilibrium is reached between the electron gas and lattice within ~1 ps. The specific heat of the lattice is much higher than that of the electron gas, and as such the temperature rise of the lattice is significantly lower. Initial photon energy absorption is well described by the Beer-Lambert law:

$$\mathrm{T} = \frac{\mathrm{I(d)}}{\mathrm{I_0}} = \exp[-\alpha(\omega)\mathrm{d}] \tag{2.4}$$

This equation relates the transmission of light, T, through a material to the angular frequency dependent optical absorption coefficient $\alpha(\omega)$ and the path length through that material, d. The absorption coefficient can be further expressed as:

$$\alpha(\omega) = \frac{4\pi\mathrm{k}}{\lambda} \tag{2.5}$$

It is then related to the wavelength of the incident light, λ, and the imaginary component of the material's complex refractive index, k. The penetration depth, $1/\alpha(\omega)$, for visible light sources (1.5-3 eV) incident on metallic surfaces varies linearly with λ from around 10-30 nm. This depth must be taken into consideration when analysing results from thin-film media, as the effect of any oxide layer or dis-uniformity of the material with depth will be much greater.

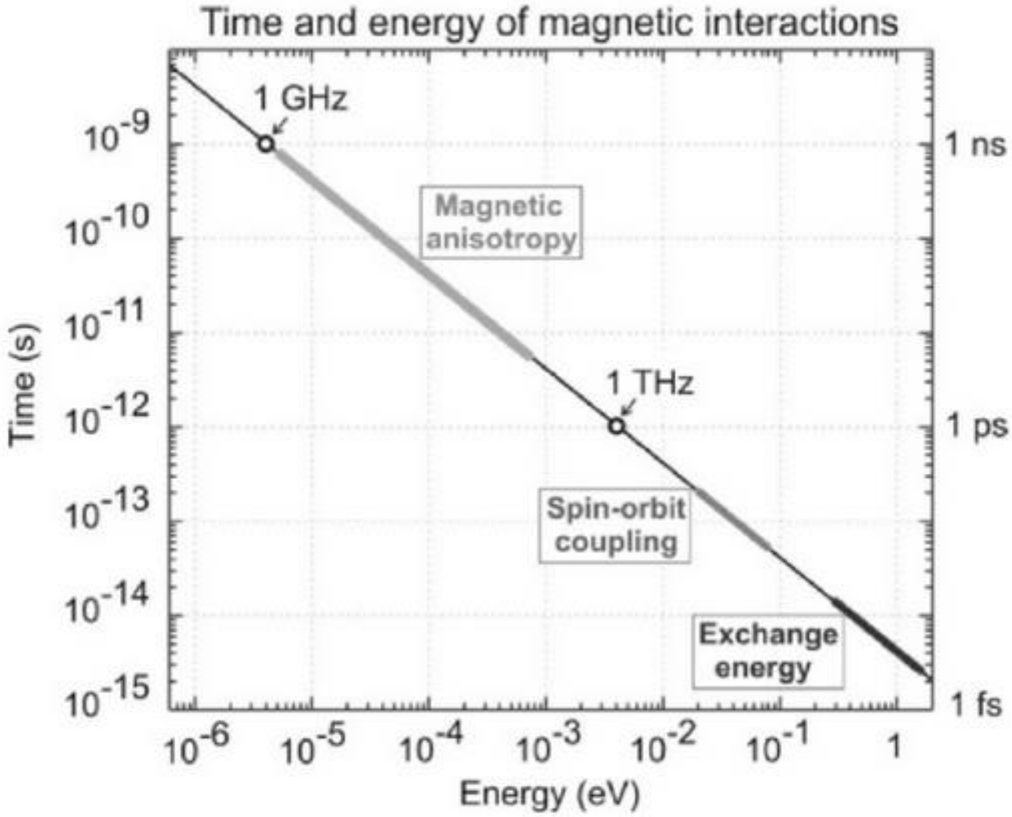

Figure 2.6: Time-energy correlation graph, plotting t = h/E. This gives a direct comparison between frequency, time and associated energies. General ranges of interactions are marked. **[14]**

The speed of these interactions is indicated by the time-energy correlation, $t = h/E \sim 1/\omega$, shown in **figure 2.6 [14]** for 3d (itinerant) metals and the initial absorption of photons followed by electron-electron exchange takes place on a femtosecond timescale. The pulse width of typical modern femtosecond lasers is on the order of ~100 fs, and therefore larger than the limit of electron-electron interactions. It is therefore the case in these experiments, that the initial energy deposition rate is dictated by the laser pulse width. This excitation and the subsequent exchange of energy to the lattice reservoir are observable as a change in the transient reflectivity (see **chapter 5** for measurement technique). The reflectivity represents a two temperature system, combining the electron and lattice temperatures. High frequency pulses can sometimes be observed in this information (on the order of 10's of picoseconds) corresponding to the propagation of stress waves. For a known thickness, the speed of sound of the sample material can be calculated from the round trip time. Energy transfer is constrained by the (material dependent) strength of electron-phonon coupling, defined by the degrees of freedom of scattered electrons and those at the Fermi surface.

Crucially for the investigation of magneto-dynamics, is the existence and influence of spin ordering. After the initial photon-electron interaction, the electron reservoir is in general raised to temperatures above the Curie temperature, T_C. Energy is dispersed by electron-phonon coupling to the lattice system, but also to the spin system. This transfer can either be by rapid direct electron-spin coupling or by much slower spin-lattice coupling and it is pertinent to ask:

- How quickly can energy transfer into and out of the spin reservoir take place and how quickly can the spontaneous magnetization respond to such a transfer?

In order to approach this question, it is useful to consider the conservation of angular momentum, which can be expressed by the Hamiltonian:

$$J = L_e + S_e + L_p + L_\omega \tag{2.6}$$

$$\Delta L_e + \Delta S_e + \Delta L_p + \Delta L_\omega = 0 \tag{2.7}$$

These equations relate the total angular momentum to the orbital momentum of the electron system, L_e, the total electron spin momentum, S_e, the lattice angular momentum, L_p, and that of the excitation photons, L_ω. The local system can be considered closed on the sub-picosecond timescale.

It has been argued **[15]** that ΔL_P in the above **equation 2.7** might be too slow to be included as in general spin-lattice interactions are considered to occur on the ~100 ps timescale. ΔL_ω is agreed to be negligible due to the degree of circular polarization contributed by the photons being small. The remaining major components belong to the electron system, $J_e = L_e + S_e$, and as the total magnetic moment can defined as $M = L_e + gS_e$ (where $g \approx 2$) this implies that magnetic dynamics are caused by a redistribution of electron orbital and spin angular momentum. In 3d transition metals at rest, $S_e >> L_e$; transfer from $S_e \rightarrow L_e$ would cause an increase, rather than a decrease, in magneto-optic (MO) response with laser heating, which has not been reported. As a result, some fast contribution from coherent phonon spin-lattice exchange cannot be neglected entirely and must be considered. This also highlights how important the conservation of angular momentum is to any dynamic magnetic process.

In order to manipulate the spin system both the transfer of energy and angular momentum must be involved. Due to the tighter restrictions on angular momentum exchange therefore the above questions can be reframed as:

- How quickly can angular momentum be exchanged to and from the spin system and from which reservoirs is this most dominant?

In order to approach this question however, one must also ask:

- How quickly and how precisely can we measure magneto-dynamics at this extreme timescale?

2.3.2 Historical Development

The experimental study of ultrafast magneto-dynamics began with relatively simple metallic systems, such as Fe and Ni, and developed alongside the evolution of short-pulse lasers. The photon energy of a laser pulse can be used to ‘pump’ energy into a magnetic medium, causing both thermal and non-thermal effects. Early experiments **[16-19]** were restricted by the limitations of pulsed lasers which, at 60 ps - 10 ns, were on the timescale or slower than the spin-lattice relaxation of the systems they wished to explore.

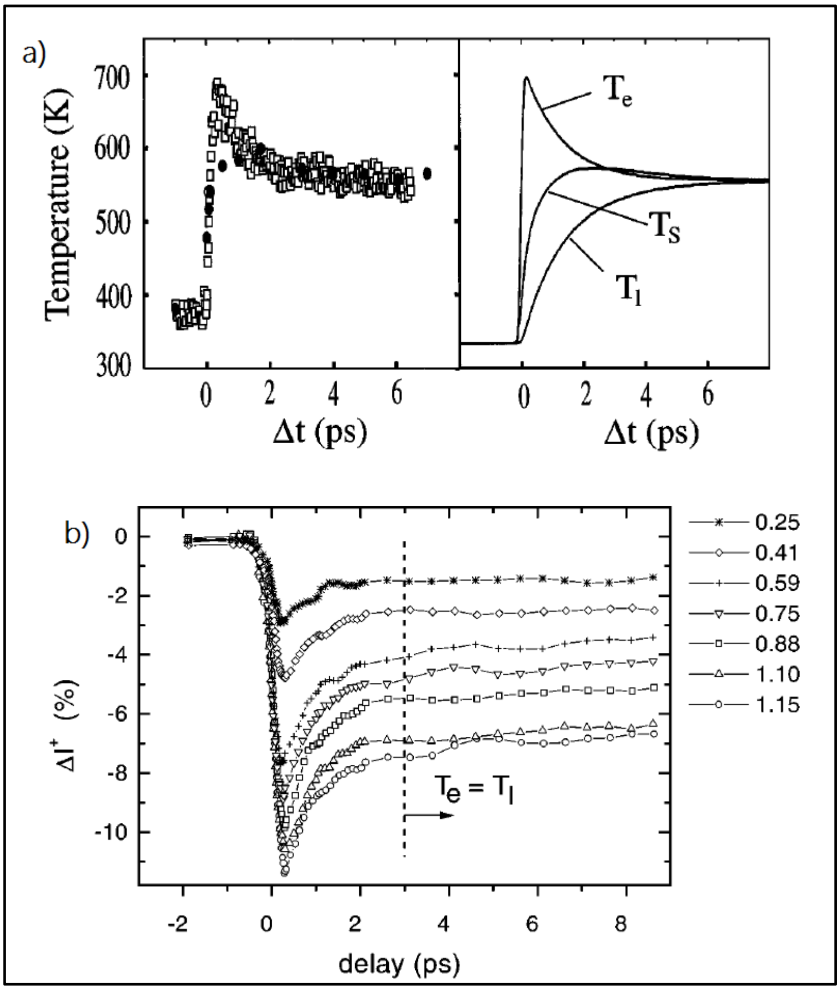

Figure 2.7: Graphs showing spin (T_s), electron (T_e) and lattice (T_l) temperatures by **[20]** from specific heat calculations on Ni (a) and pump-probe SHG measurements over fluence series 250-1150 µJ/cm^2 by **[21]**, also on Ni (b).

It was not until 1996, (Beaurepaire et al. **[20]**) that experimental observations were possible in which the laser pulse fall-off was sharp enough that the system relaxation did not simply follow the excitation curve of the laser pulse and instead reached non-equilibrium conditions. Beaurepaire et al. used a 60 fs pulsed laser to observe MOKE of 22nm Ni thin-films (see **figure 2.7**), due to it having the lowest T_C of the transition metals. The work observed an electron thermalization time of ~260 fs by measuring the transient reflectivity and calculated an electron temperature decay of around 1 ps, while observing a maximum spin temperature (from hysteresis) only within 2 ps, supporting the case for separate spin and electron reservoirs. Following on from this work, Hohlfeld et al. **[21]** reported a year later on pump-probe second harmonic generation, also on Ni thin-films, with a 150 fs pulsed laser. This work corroborated the electron thermalization time of Beaurepaire et al., but additionally observed that beyond ~300 fs electron and spin reservoirs had equilibrated such that local magnetization was governed by the electron temperature. They also showed the first series of pump fluence measurements on this timescale, showing that a classical M(T) graph could be reproduced even before electron-lattice thermal equilibrium has been reached. Critically both studies indicated magnetization change faster than spin-lattice relaxation time. In the same year Scholl et al., **[22]** using 170 fs pump-probe two-photon photoemission, reported observation of two separate demagnetization processes. Attributed to electron-electron "Stoner excitations" and spin-lattice (phonon-magnon) scattering, these were ~300 fs and >500 ps respectively and stated that the electron system is 'inextricably coupled' to the local spin moment for itinerant ferromagnets. Despite numerous attempts, this separation has not been reproduced and the true origin of the observation remains ambiguous.

Following this collection of early papers, a sceptical treatment of the experimental findings was developed by, notably, Koopmans et al. **[23]**. This work on Cu/Ni/Cu wedges challenged the previous assumption that a direct relationship exists between sample magnetization and measured magneto-optic response. Koopmans demonstrated, by polar time-resolved (TR)MOKE, an optically induced non-magnetic component in the initial Kerr response. They showed that during the first 500 fs, a delay between the evolution of Kerr ellipticity and Kerr rotation existed, which also showed no external applied field dependence. It was concluded that while ultrafast dynamics does occur, reported observations of <100 fs (e.g. Aeschliman et al. **[24]**) after photon injection were unlikely to be magnetically derived, though contested by Wilks et al. **[25]** This detachment between true magnetization dynamics and observed magneto-optics was further corroborated by ab initio calculations in Ni by Oppeneer and Liebsch **[26]** who showed that the conductivity tensor, and thus the complex Kerr angle, can be significantly distorted under a non-equilibrium electron distribution. These papers concluded that due to state-blocking effects, magneto-optic observations before the first picosecond cannot be reliably interpreted as representing the true magnetization.

Notably however, further work by e.g. Beaurepaire et al. **[27]**, Guidoni et al. **[28]**, Bigot et al. **[29]** showed 'true' support for ultrafast demagnetization from $CoPt_3$ films. Beaurepaire measured transient hysteresis (M-H) loops which showed the ferromagnetic - paramagnetic phase transition occurred within 600 fs (see **figure 2.8**) and as such the demagnetization occurred within the timescale of the electron thermalization. An extra point in favour of this observation was that when repeated in a reverse bias applied field, the resulting recovery was also reversed.

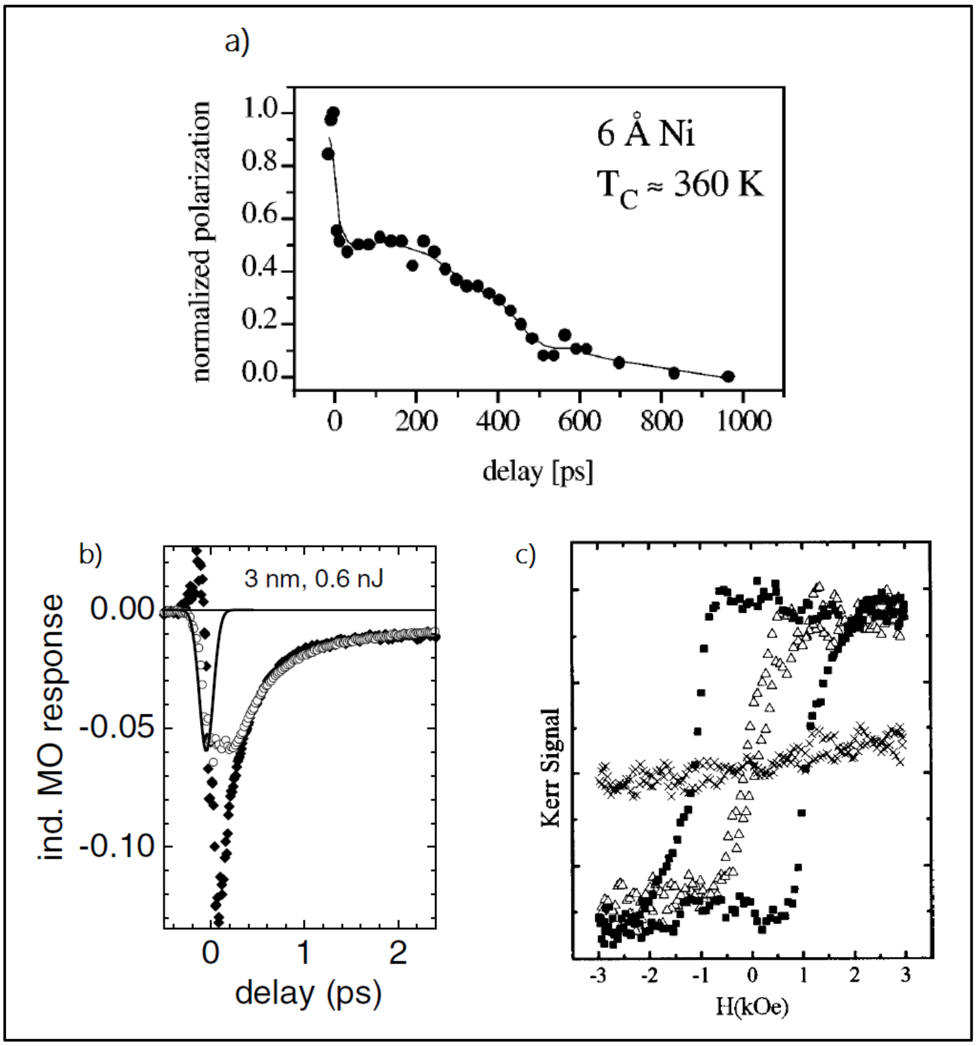

Figure 2.8: (a) Time-resolved spin polarization of photo-emitted electrons for Ni films by **[22]**; (b) induced ellipticity (open circles) compared to induced rotation (filled circles) by **[23]** showing a phase shift between them; (c) Polar Kerr hysteresis of $CoPt_3$ alloy at pump delays, showing transient M-H loop evolution, by **[27]**.

Due to the complexity of the processes involved, the exact origin of ultrafast magneto-dynamics remains uncertain. What is known is that laser-induced ultrafast demagnetization (with a sufficiently short laser pulse) can occur on a sub 300 fs timescale and that this is brought about by the exchange between three thermal reservoirs through electron-spin and lattice-spin interactions.

2.4 Laser-Induced Coherent Precession

Over a picosecond time-scale, thermal equilibrium between the electrons and lattice is reached, but the lattice temperature remains elevated in relation to the environment and most likely the local magnetization is out of equilibrium. In this regime, within a small volume, spin contributions can be considered as a coherent macrospin, due to the tight binding effect of the exchange interaction. In this regime a coherent magnetic precession, known as a ferromagnetic resonance (FMR), can occur. Phenomenologically this is described by the Landau-Lifshitz Gilbert (LLG) equation **[30]**. Time-resolved measurements of this precession can provide quantitative information regarding the anisotropy, switching and damping characteristics of a given magnetic material.

Macrospin Dynamics

The process dictating the path back to magnetic equilibrium can be treated semi-classically starting generally with Newton's second law of motion, relating angular momentum $\underline{L}(t)$ to the torque $\underline{\tau}(t)$ (**equation 2.8**). Specifically in the case of a magnetic material this torque is caused by an angular difference between $\underline{M}(t)$ and $\underline{H_{eff}}$ as shown in **equation 2.9**:

$$d\underline{L}(t)/dt = \underline{\tau}(t) \tag{2.8}$$

$$d\underline{M}(t)/dt = -\gamma\left[\underline{M}(t) \times \underline{H_{eff}}\right] \tag{2.9}$$

$$\gamma = 2\pi g \mu_B / h \tag{2.10}$$

$$\omega = \gamma \underline{H_{ext}} \tag{2.11}$$

Here, $\underline{M}(t)$ is the summation of the magnetic dipole moments of the individual spins within a ferro- (or ferri-) magnetic system and $\underline{H_{eff}}$, is the total effective magnetic field. γ is the gyromagnetic ratio (**equation 2.10**), which relates the local system magnetic moment to its angular momentum and is quantum mechanical in nature. In this equation, g is the spectroscopic splitting Lande factor, μ_B the Bohr magneton and h, Planck's constant.

These equations lead to a precessional dynamic motion of $\underline{M}(t)$ around $\underline{H_{eff}}$ at an angular frequency, ω, determined by that effective field and the gyromagnetic ratio (**equation 2.11**). As an order of magnitude estimate, for a free electron spin, $\gamma \approx 2\pi(28)$ GHz/T, which gives a precessional period of ~360 ps (frequency of 2.8 GHz) in a 0.1 T (1 kOe) external field.

Effective Field

The effective magnetic field vector $\underline{H_{eff}}$ represents the minimization of the competing energy terms associated with the local system. This energy is generally considered to be made up of contributions from four sources: Zeeman energy E_{Zee}, exchange energy E_{ex}, (magnetocrystalline) anisotropy energy E_{ani} and demagnetizing energy E_{dem} in the form:

$$\underline{H_{eff}} = -(1/\mu_0)\left[\partial(E_{eff})/\partial\underline{M}\right] \tag{2.12}$$

The Zeeman energy (**equation 2.13**) is the interaction between the magnetization, $\underline{M}$ and the external field, $\underline{H_{app}}$, and is minimized when they are aligned.

$$E_{Zee} = -\mu_0 \int_V \underline{M} \cdot \underline{H_{app}} dV \tag{2.13}$$

The exchange energy (**equation 2.14**) comes from the interatomic quantum mechanical exchange interaction due to electron charge distributions, discussed in more detail in **chapter 3**. It is generally minimized by uniform spatial distribution of the magnetization and proportional to the exchange constant, A. This term is only applied in the case of larger areas, where spatial variation is more important.

$$\mathrm{E_{ex}} = \mathrm{A}\int_{\mathrm{V}} \left(|\nabla \mathrm{M_x}|^2 + \left|\nabla \mathrm{M_y}\right|^2 + |\nabla \mathrm{M_z}|^2\right)(1/\mathrm{M_S^2})\mathrm{dV} \qquad (2.14)$$

The anisotropy energy (**equation 2.15**) comes from the spin-orbit interaction, producing directional energy variation based on the crystal geometry of the material. It is minimized by the magnetization aligning along an easy axis and is proportional to the anisotropy constant, K and a geometry dependent anisotropy field, $\underline{\mathrm{H_K}}$.

$$\mathrm{E_{ani}} = \mathrm{K}\int_{\mathrm{V}} \left(\underline{\mathrm{M}} \cdot \underline{\mathrm{H_K}}\right)^2 (1/\mathrm{M_S^2})\mathrm{dV} \qquad (2.15)$$

The demagnetizing energy (**equation 2.16**) is the effect of the magnetic fields created by the magnetization itself. This acts to minimize the total magnetic energy, by forming closed loops of magnetization and attempting to inhibit flux leakage and is heavily dependent on the macroscopic shape of the sample.

$$\mathrm{E_{dem}} = -(\mu_0/2)\int_{\mathrm{V}} \underline{\mathrm{M}} \cdot \underline{\mathrm{H_{dem}}}\mathrm{dV} \qquad (2.16)$$

The equilibrium state of the total effective field direction is a balance between the external applied field $\underline{\mathrm{H_{app}}}$ and the internal fields.

Damping and the LLG equation

In addition to the precessional frequency, an energy dissipation channel (viscous damping term) must be introduced to avoid the unphysical case of perpetual motion. This causes the magnetization, over time, to come to rest aligned with the effective field. In its simplest form, this is done by assuming that the damping is linear and isotropic and achieved by including an extra time varying dissipation term to the effective field with an expression in the form of **equation 2.17** in which α is the dimensionless phenomenological damping constant (so-called Gilbert damping parameter **[31]**):

$$\underline{H_{\mathrm{eff}}}(t) = \underline{H_{\mathrm{eff}}} - (\alpha\gamma^{-1}M_S^{-1})d\underline{M}(t)/dt \tag{2.17}$$

When combined with **equation 2.9**, this produces the standard form of the precessional magnetisation dynamics equation known as the Landau-Lifshitz Gilbert (LLG) equation:

$$d\underline{M}(t)/dt = -\gamma\left[\underline{M}(t) \times \underline{H_{\mathrm{eff}}}(t)\right] + \alpha M_S^{-1}\left[\underline{M}(t) \times d\underline{M}(t)/dt\right] \tag{2.18}$$

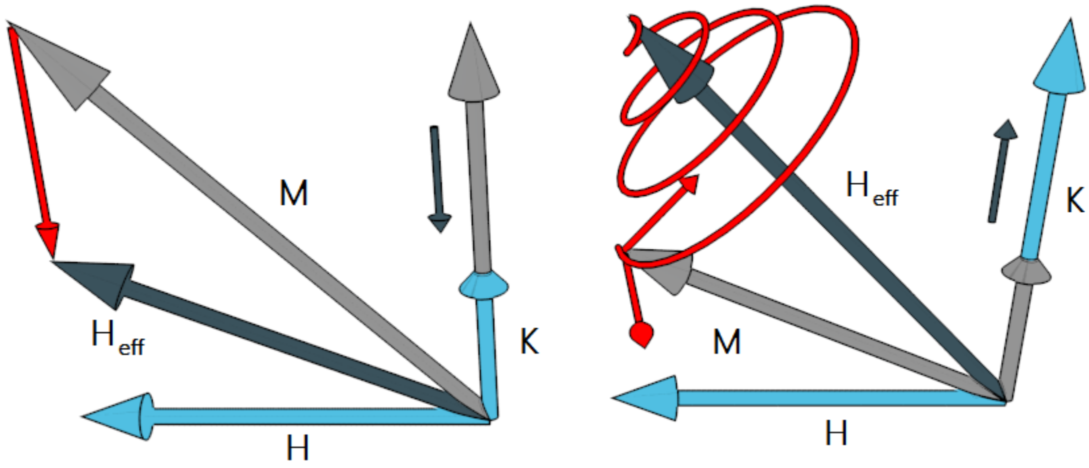

Figure 2.9: Cartoon of stimulation of magnetic precession. Effective field H_{eff} at equilibrium balances internal anisotropy K with external field H; M aligns with that. A rapid temperature change reduces the internal anisotropy and causes a change in H_{eff} causing a force on M (left). As H_{eff} returns to equilibrium, a torque is applied to M as it returns to equilibrium (right).

At rest, the magnetization vector tends to align with the effective field vector, representing the balance of the internal and external energies. An excitation event, such as a sufficiently rapid laser photon impulse, disturbs this energy balance and creates an angular contrast between $\underline{M}$ and $\underline{H_{\mathrm{eff}}}$ as shown in **figure 2.9** above. From **equation 2.9**, this induces a torque and the magnetization spirals around the new effective field direction. In compliance with the law conservation of angular momentum, during the recovery, angular momentum must be exchanged away from the spin system. This is mediated by direct spin-orbit coupling to the local lattice system; indirect spin wave coupling (e.g. magnon scattering); impurity relaxation mechanisms and even magnetic damping caused by free conduction electron eddy currents. However to a first approximation, the strength of the Gilbert damping parameter, α, determines the rate of exchange due to the strength of the spin-orbit coupling.

Some criticism of the applicability of the LLG equation to ultrathin-films comes from (e.g.) Mills and Arias **[32]** and Lindner, et al. **[33]** where FMR linewidth measurements diverged from linear, LLG predictions. Their work championed a two-magnon mechanism, introduced by Kittel **[34]**, as the major contributor to the spin damping for ultrathin-films with in-plane magnetization. Magnons are quantized spin waves; propagating disturbances in the magnetic order which cause damping by redistributing energy in the local system. A precessional mode can be defined as magnons with infinite wavelength, wavevector = 0. Scattering events created at interfaces, grain boundaries and defect sites can cause magnons which have matching frequency but differing wavevector, causing a destructive interference which will grow over time. They argue that, in particular for the case of large amplitude spin motion, a clear understanding of the damping phenomenology is still lacking.

Interpretation of Precessional Dynamics

As previously stated, interpretation of the precessional dynamics can provide information about the anisotropy, damping and switching characteristics of a material, critical in predicting spintronic device performance. Demonstrations have shown that excitation of homogeneous mode spin precession is one of the fastest mechanisms for overcoming the energy barrier to macrospin reversal **[35] [36]**.

One method of determining the damping parameters of a particular measurement, as described by (e.g.) T. J. Silva, et al. **[37]** is to fit a damped sinusoidal function to the data as shown in **equation 2.19** and schematically in **figure 2.10**.

$$M_p(t) = M_0 + A\exp(-t/\tau_d) \times \sin(2\pi f(t - \varphi_0)) \tag{2.19}$$

In this function, M_0 refers to the equilibrium magnetization state offset, generally zero in the case of a normalized data set. A is the amplitude of the decay envelope and φ_0, a phase shift factor. The two factors of particular interest however are τ_d, the exponential decay damping factor and f, the oscillation frequency.

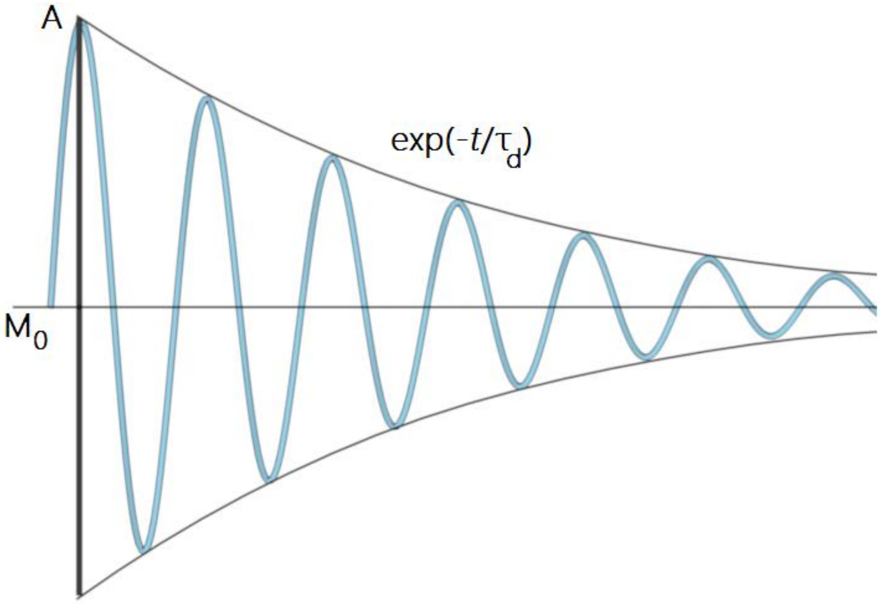

Figure 2.10: Plot of damped sinusoidal oscillation equation showing ideal exponential decay envelope from A to M_0.

This equation is an approximate solution to the LLG equation for small perturbations forming circular precession. The oscillation frequency, f, and the exponential decay constant τ_d relate to the Gilbert damping parameter α by **equation 2.20**. This becomes unphysical for $|\alpha| \geq 1$.

$$\alpha = 1/(2\pi f \tau_d) \tag{2.20}$$

The precessional frequency can also be determined from a fast Fourier transform (FFT) calculation **[38]**. This provided an independent verification method and was capable of identifying multiple resonant frequencies which may exist within the data, as well as the strength of a given frequency, represented by the amplitude of the frequency spectrum peak **[39]**. These FFTs were calculated using Origin Lab's signal processing functions, with a Hamming filter and fixed sampling intervals. Amplitude, frequency and full-width half-maximum data was produced from this and used in conjunction with the damped sinusoidal fit.

2.5 References

[1] Alex Hubert and Rudolf Schäfer, Magnetic Domains: The Analysis of Magnetic Microstructures (Springer Verlag, Berlin, 1998)

[2] Petros N. Argyres, Phys. Rev. **92**, 334 (1955)

[3] Oliver S. Heavens and Robert W. Ditchburn, Insight into Optics (Wiley, Chichester, 1991)

[4] Fabio Pulizzi, Spintronics, Nature Materials Insight **11**, 367 (2012)

[5] Andrei Kirilyuk, Alexey V. Kinel, and Theo Rasing, Rev. Mod. Phys. **82**, 2731 (2010)

[6] M. Djordjevic, et al., Phys. Stat. Sol. **3**, 1347 (2006)

[7] John Kerr, Phil. Mag., **3,** 321 (1877)

[8] P. Weinberger, Phil. Mag. Lett., **88**, 897 (2008)

[9] John Kerr, Phil. Mag., **5**, 161 (1878)

[10] J. C. Maxwell, Phil. Trans R. Soc. Lond., **155**, 459 (1865)

[11] M. Mansuripur, The Principles of Magneto-Optical Recording (Cambridge University Press, Cambridge, 1995)

[12] David J. Griffiths, Introduction to Electrodynamics. 3rd Ed. (Pearson Education, Inc., 2008)

[13] M. Mansuripur, The Magneto-Optical Kerr Effect, (Optics & Photonics News, 2000)

[14] Joachim Stöhr, Hans C. Siegmann, Magnetism, (Solid-State Sciences Springer Verlag, Berlin, 2006)

[15] Bert Koopmans, Topics Appl. Phys. **87**, 253 (2003)

[16] M. B. Agranat et al., Sov. Phys. JETP **59**, 804 (1984)

[17] A. Vaterlaus et al., J. Appl. Phys. **67**, 5661 (1990)

[18] A. Vaterlaus et al., Phys. Rev. Lett. **67**, 3314 (1991)

[19] A. Vaterlaus et al., Phys Rev. B. **46**, 5280 (1992)

[20] E. Beaurepaire, et al., Phys. Rev. Lett. **76**, 4250 (1996)

[21] J. Hohlfeld, et al. Phys. Rev. Lett. **78**, 4861 (1997)

[22] A. Scholl, et al., Phys. Rev. Lett. **79**, 5146 (1997)

[23] B. Koopmans, et al., Phys. Rev. Lett. **85**, 844 (2000)

[24] M. Aeschlimann, et al., Phys. Rev. Lett. **79**, 5158 (1997)

[25] R. Wilks, et al., J. Appl. Phys. **95**, 7441 (2004)

[26] P. M. Oppeneer and A. Liebsch, J. Phys.: Condens. Mat. **16**, 5519 (2004)

[27] E. Beaurepaire, et al., Phys. Rev. B, **58** 12134 (1998)

[28] L. Guidoni, et al., Phys. Rev. Lett., **89**, 017401-1 (2002)

[29] J-Y. Bigot, et al., Phys. Rev. Lett. **93**, 077401 (2004)

[30] Y. Tserkovnyak, et al., Rev. Mod. Phys. **77**, 1375 (2005)

[31] T Gilbert, IEEE Trans. Mag. **40**, 3443 (2004)

[32] D.L. Mills and R. Arias, Physica B **384**, 147 (2006)

[33] J. Lindner, et al., Phys. Rev. B, **68**, 060102(R) (2003)

[34] M. Sparks, R. Loudon and C. Kittel, Phys. Rev. **122**, 791 (1961)

[35] C. H. Back, et al., Science **285**, 864 (1999)

[36] T. Gerrits, et al., Nature (London) **418**, 509 (2002)

[37] T. J. Silva, et al., J. Appl. Phys., **85**, 7849 (1999)

[38] A. Mekonnen, et al. Phys. Rev. Lett., **107**, 117202 (2011)

[39] E. Brigham, The Fast Fourier Transform and its Applications (Englewood Cliffs, 1988)

Chapter 3

Materials for Spintronic Applications

3.1 Introduction

The core of any spintronic application is the choice of materials. Understanding this foundation is prerequisite to any meaningful developments in device fabrication and functionality and the list of useful materials is vast and diverse. This thesis and this chapter have been focused on two such materials of current interest: the half-metal, Fe_3O_4 (magnetite), and the rare-earth transition metal GdFe. This chapter will detail the physical properties of both of these materials which make them interesting and useful.

3.2 Half-Metals: Magnetite (Fe_3O_4)

3.2.1 Structure & Magnetic Properties

Bulk magnetite exists as an inverse spinel cubic structure of lattice constant 0.8397 nm consisting of Fe^{2+} and Fe^{3+} ions surrounding an fcc O sublattice **[1]**. The Fe ions are arranged in tetrahedral (A) and octahedral (B) sites within the lattice, with 8 Fe^{3+} ions on A sites and 16 $Fe^{2+/3+}$ ions occupying B sites to give a resultant charge here of $Fe^{2.5+}$. Being a cubic structure, the three most common orientations to find it are (001), (011) and (111) as displayed in profile in **figure 3.1** below. The lattice unit cell consists of 8 planes along the <100> direction, alternately containing A sites and B sites, with the oxygen sublattice sitting along the planes containing the B site iron **[2]**. As can be seen here, the (011) orientation is the only one which fully resolves the oxygen (red) from the iron atoms (blue).

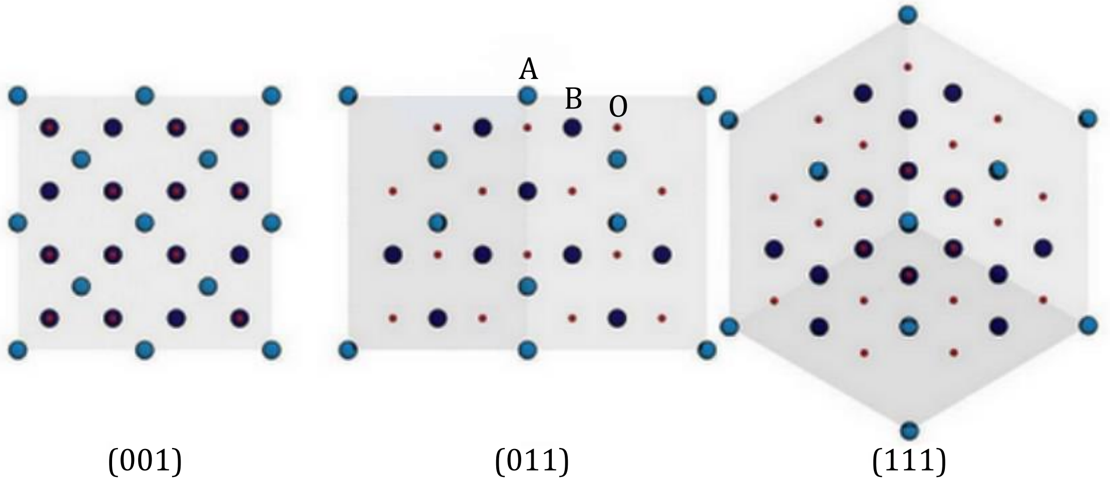

Figure 3.1: Illustrations of the three most common orientations of the Fe_3O_4 cubic inverse spinel crystal unit cell. The structure is comprised of a fcc O^{2+} lattice ((O), red atoms), equal numbers of Fe^{3+} and Fe^{2+} ions filling half of the octahedral site ((B), dark blue atoms) and Fe^{3+} ions filling ⅛ of the tetrahedral sites ((A), light blue atoms). These orientations provide different visibility of atomic columns.

Bonding between neighbouring ions in a magnetite crystal lattice is described by the exchange interaction. This can occur as cation-cation bonding and cation-anion-cation bonding; corresponding to Fe-Fe and Fe-O-Fe bonding and is described by the Heisenberg exchange Hamiltonian as follows:

$$H_{ex} = -\sum_{ij} \underline{J}_{ex}\underline{S}_i \cdot \underline{S}_j \tag{3.1}$$

In the above equation $\underline{S_n}$ represents the spin angular momentum of ion i or j. $\underline{J_{ex}}$ is the effective exchange integral, dependent on the angle, distance, spin and electronic configuration of neighbouring ions i and j. A set of semi-empirical rules were laid out in the 1950s by Goodenough and Kanamori **[3] [4]** determining the properties of each of these interactions. They take into consideration the electronic symmetry and occupancy of overlapping atomic orbital wave functions and generally allow a quick prediction of the net magnetic exchange. However in the case of magnetite there exists a more complicated system involving competing direct and superexchange interactions, which define its magnetic character.

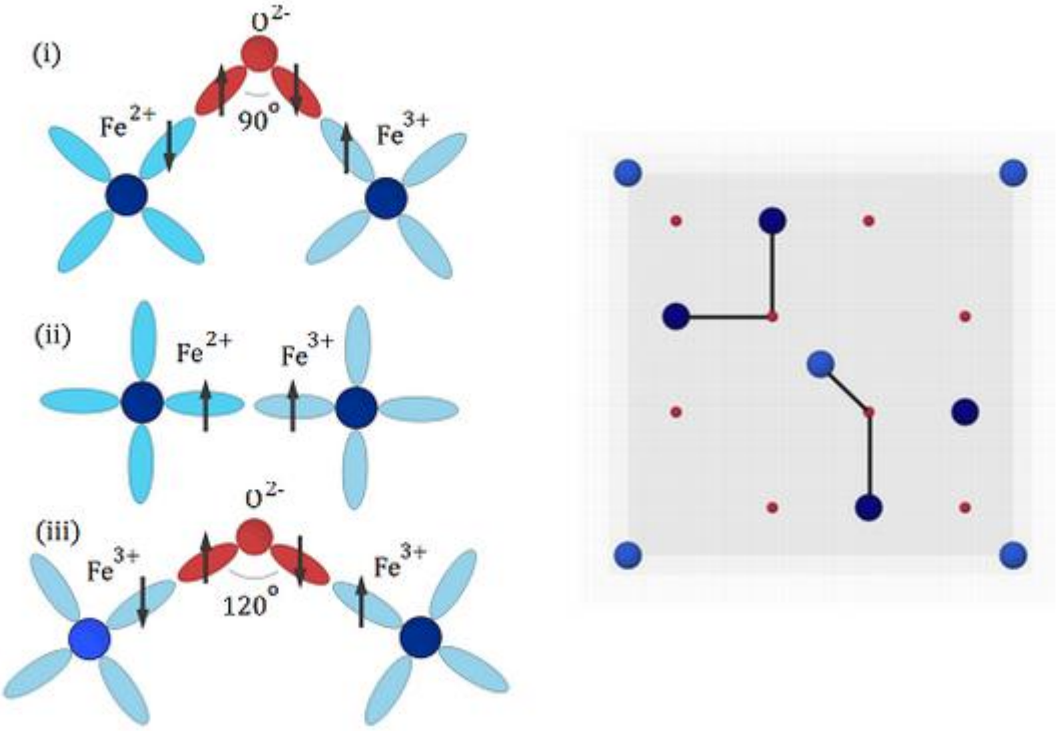

Figure 3.2: Cartoons of interatomic interactions which exist in crystalline magnetite (left) and example positions of superexchange interactions within the magnetite unit cell (right), displaying (i) ~90 weakly ferromagnetic superexchange interaction on B sites, (ii) ferromagnetic double exchange interaction on B sites, and (iii) strongly antiferromagnetic superexchange interaction between octahedral and tetrahedral iron sites.

These interactions in magnetite occur due to the arrangement of Fe^{2+} and Fe^{3+} ions which have, respectively, $3d^6$ and $3d^5$ electronic configurations. The Fe^{3+} ions have five unpaired 3d electrons forming a closed subshell and the Fe^{2+} ions have an extra electron which results in four 3d electrons unpaired. A local double exchange interaction exists between the B site Fe^{2+} and Fe^{3+} ions whereby the direct exchange of an electron to the empty d level in Fe^{3+} results in a weak ferromagnetic contribution. This is mostly masked by much stronger indirect superexchange interactions, which occur between next nearest neighbour (NNN) Fe ions via a 'go-between' O^{2-}. As there are now three particles involved, the angle between them becomes an important factor in determining the strength and sign of the interaction. Super-exchange occurs only between overlapping orbitals with similar symmetry types and in magnetite there are three 2p orbitals on the O^{2-} ions which can contribute, consisting of two with π-type and one with σ-type symmetry. On the Fe ions, there are five 3d orbitals, three with π-type and two with σ-type symmetry, so when these respectively overlap with the corresponding orbitals of the O^{2-} ions, the interaction takes place. The σ-type symmetry is generally larger and more dominant **[5]**. The two main superexchange interactions in bulk magnetite which must be considered are: ~120° FeB-O-FeA (strongly antiferromagnetic) and ~90° FeB-O-FeB (weakly ferromagnetic) as shown in **figure 3.2**.

There are 3 classes of spin-polarisation and magnetite belongs to the second **[6]**, type IIB, due to it exhibiting hopping within the minority spin band. The conduction occurs across the B site Fe ions, between the Fe^{2+} and Fe^{3+} charges. As discussed previously, the 5 d-orbital electrons form a closed subshell, leaving the single 6th electron from the Fe^{2+} with an opposite spin and in a higher energy level. This single electron state forms the conduction band at the Fermi level and as such the conduction is theoretically 100% spin-polarised for a perfect inverse spinel structure. Literature suggests that magnetite behaves under the itinerant electron model more so than the localised electron model **[7]**. A complete understanding of the complex band structure of magnetite is still unknown, consisting of hybridised bands of overlapping wave functions. As a material is grown as a nanoscale film, the properties of the substrate become important and surface effects begin to dominate the overall characteristics of the material. Surface properties can be significantly different from those of the bulk, perhaps exhibiting persisting order beyond the Curie temperature **[8]**. Theoretical calculations of thin-film systems are possible, but can be notoriously difficult. Any mismatch in the lattice parameter between film and substrate becomes critical as this can cause defects within the film which also alter the bulk properties.

3.2.3 Single Crystal Growth Considerations

Iron oxide is stable across a significant range of stoichiometry **[9]**. A solid solution group exists with Fe_3O_4 at one end and γ-Fe_2O_3 (maghemite) at the other via FeO (wüstite) and α-Fe_2O_3 (hematite), following the formula $Fe_{3-\delta}O_4$ ($\delta = 0 \leftrightarrow 1/3$). wüstite exists in the form $Fe_{1-x}O$, in a halite (rock-salt) crystal structure whose lattice parameter is 0.433 nm. It is insulating and antiferromagnetic, with a Néel temperature (T_N) of only 198 K. Hematite exists in an insulating Rhombohedral lattice structure like Corundum which exhibits antiferromagnetic behaviour (T_N~955 K) and has a band gap of ~2 eV.

Critically maghemite and magnetite share a very similar spinel structure, difficult to distinguish in structural investigation. Maghemite is a ferrimagnetic insulator with a band gap of ~2.5 eV and a moment of ~1.2μ_B. By contrast, magnetite has a very small band gap of ~0.1 eV **[10]** and about 20% larger magnetic moment of ~1.4μ_B. As a consequence of the shared structure between magnetite and maghemite, altering oxidization conditions can change the occupation on the octahedral sites of the spinel lattice from Fe^{2+} ions to Fe^{3+} ions and vacancies. This range of conditions will have a significant effect on the performance of the material as both its ferrimagnetism and spin polarization rely on the existence of the Fe^{2+} ions on the octahedral sites.

For epitaxial single crystal growth, the lattice match between the magnetite unit cell and that of the chosen substrate must have a very low mismatch. This investigation will focus on the insulating rock salt, magnesium oxide, MgO (001), which boasts a, close to, ideal mismatch to Fe_3O_4 of 0.3%. The lattice constant of MgO is 0.4212 nm, **[11]** compared to Fe_3O_4 of 0.8397 nm, which results in four MgO unit cells matching to each Fe_3O_4 unit cell face and continuing the oxygen sublattice. These unit cells are shown to scale below in **figure 3.3**.

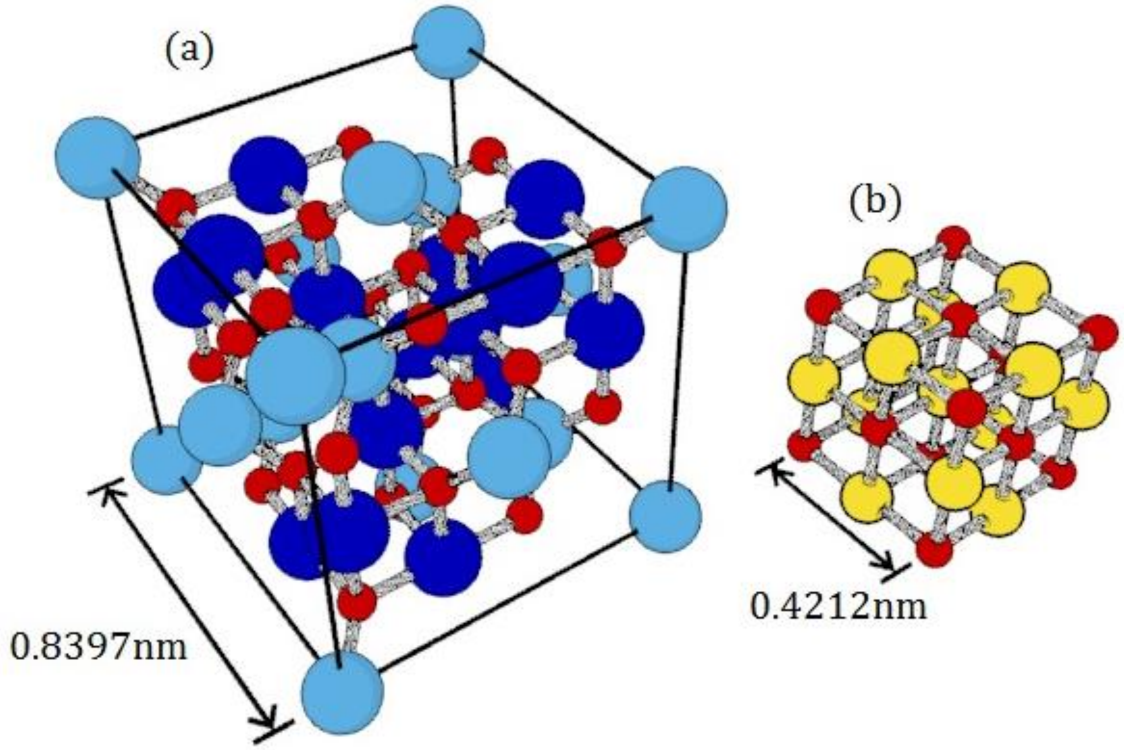

Figure 3.3: Cartoon of (a) Fe_3O_4 (001) unit cell, containing octahedral (dark blue) and tetrahedral (light blue) iron ions, showing superexchange bonds via oxygen (red) sublattice. By comparison, to scale (b) MgO (001) unit cell, containing magnesium (yellow) sublattice bonded to oxygen (red) sublattice.

During epitaxial growth, the film is deposited on the substrate piecemeal, at a rate determined by the sublimation of a growth source. As clusters of Fe_3O_4 form, they lower the local surface potential, resulting in island growth with multiple unrelated nucleation sites. This naturally results in regions of the film where the Fe_3O_4 unit cell cannot be tessellated perfectly. The boundaries where these islands meet cannot always match and defects are formed. These defects are referred to as anti-phase domain boundaries (APBs) which introduce a greater antiferromagnetic coupling component **[12]**. They exist in Fe_3O_4/MgO (001) for two reasons: the half-sized unit cell of MgO means that islands can form half a unit cell mismatched, and the lower order of rotational symmetry of Fe_3O_4 allows islands to meet 90° rotated with respect to each other. A crystallographic study of this is reported by S.Celotto, W. Eerenstein and T. Hibma **[13]**, which discusses the type of defects which are allowed to occur and their electron microscopy visibility criteria, as calculated by the Howie-Whelan visibility criteria (**equation 3.2**) and shown in **figure 3.4**. These criteria are discussed in more detail in **chapter 4.**

$$2\pi\underline{g}.\,\underline{R} = (2N + 1)\pi \tag{3.2}$$

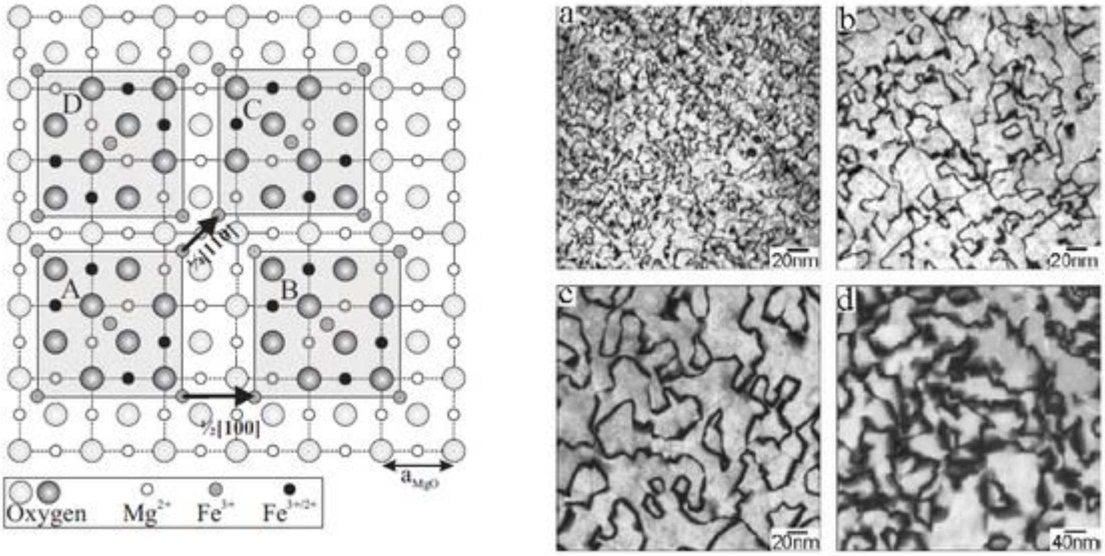

Figure 3.4: Schematic illustration of APB types with shift vectors (left) showing translational and rotational shifts used to calculate TEM visibility conditions and 220 type TEM dark field images of APBs in Fe_3O_4/MgO (001) films of (a) 6nm, (b) 12nm, (c) 25nm and (d) 50nm thickness (right).

3.3 Rare Earth-Transition Metal Alloys: GdFe

3.3.1 Structure & Magnetic Properties

Rare earth-transition metal (RE-TM) alloys have enjoyed dedicated study within the magnetic storage industry for over 40 years, following the ground-breaking paper of P. Chaudhari, et al. in 1972 **[14]**. This industrial development brought RE-TM alloys to market in the first commercial magneto-optic storage devices as the now superseded ‘bubble memory’. This non-volatile storage technology was considered very promising as a potential 'universal memory' in the 1970s, but was overtaken by semiconductor and hard disk drive (HDD) technologies in speed and density respectively. The search for a versatile universal memory, a non-volatile, fast access, high density media, still continues in the form of Magnetic Random Access Memory (MRAM), with commercial focus on smaller and smarter devices, this goal has never been more relevant **[15]**. MRAM promises to provide cheap, low power consumption, resilient components, with RE-TM alloys as a major contributing element.

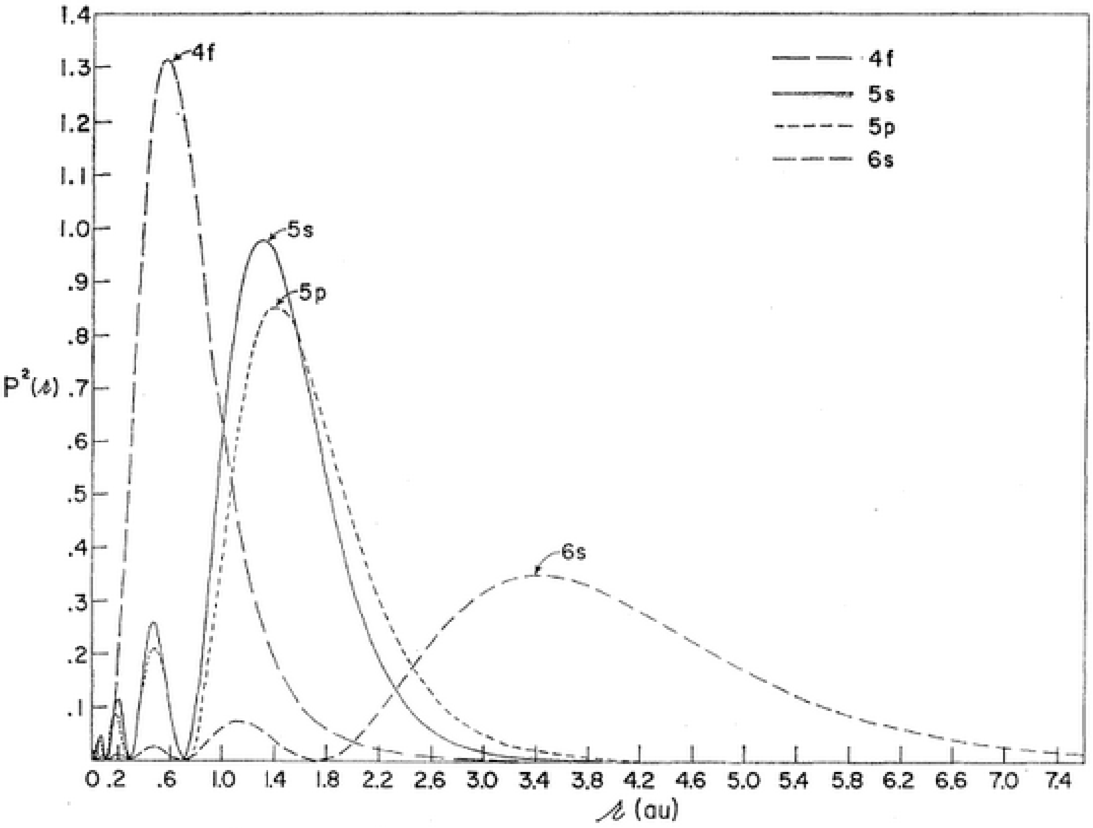

Figure 3.5: Hartree-Fock theoretically calculated radial influence of Gd electron orbitals. The 4f orbital, which carries the magnetic moment, is shielded deep within the ion, affected by the environment only via intra-atomic exchange with the 5p orbital. **[17]**

There are 17 rare earth metals (REs), the 15 lanthanides (Lanthinum, z=57 to Lutetium, z=71) along with Scandium and Yttrium, which share similar chemical properties **[16]**. These elements have a general electronic configuration of

$4f^n\ 5s^2\ 5p^6\ 5d^1\ 6s^2$. The magnetisation is defined by the spin moment of the 4f electron shell, however it has a relatively small radial extent (as demonstrated for Gadolinium in **figure 3.5 [17]**) and is significantly shielded from external influence by the filled 5s and 5p shells; external interactions are mediated through an exchange interaction with the single 5d electron. For greatest stability electrons will preferentially single-fill all available orbitals before pairing up, as stated by Hund's rule, resulting in the orbital moment and spin moment coupling antiparallel for up to half filled shells, and parallel for the rest. This leads to an orbital moment > spin moment for light REs, with the total moment antiparallel to the spin moment; this is reversed for the heavier elements.

Gadolinium, Gd, is the chosen rare-earth for this investigation due to its unique position within the lanthanide group. It has a ground state electronic configuration with a half-filled 4f orbital, which according to Hund's rule, gives it the largest number of majority spin carriers allowed and no minority spin carriers. It also has an isotropic S-state character, which makes it a soft magnet, useful for experimental practicality, while not compromising its real world applicability.

The 4f electron spin moment of a RE couples antiparallel (via 4f-5d internal exchange and then 5d-3d interatomic exchange) to the 3d electron spin moment of a transition metal (TM). As such, in an alloy with a TM (such as iron), the lighter rare earths (Lanthanum <-> Samarium) exchange couple ferromagnetically; the heavier rare earths, which have more than half filled f-electrons, (≥Gadolinium) exchange couple antiferromagnetically. This antiferromagnetic coupling, which generally displays as a ferrimagnet due to any imbalance in the total spin moment of the two sublattices, provides the interesting behaviour in these alloys from a magneto-dynamic perspective **[18] [19]**. The dominance of either sublattice can be tuned in the growth process by altering the concentration ratio between the two elements, generally with concentrations of rare earth in the alloy of between 15-25%.

With these ferrimagnetic RE-TM alloys, the magnetic properties are highly temperature dependent due to, typically, a large contrast between the temperature dependences of the two sublattices. Transition metals, such as iron or cobalt, have a high Curie temperature (1043 K, 1400 K respectively) compared to that of the rare earths. Due to the separate origins of the magnetization in RE and TM (4f shell and 3d shell respectively), the magnetic moments of each sublattice retain separate temperature dependencies. The localized 4f shell moment produces a larger temperature dependence than that of the itinerant 3d shell; as a result, at low temperatures, typically, the magnetic moment of the RE will dominate that of the TM, and vice versa for high temperatures.

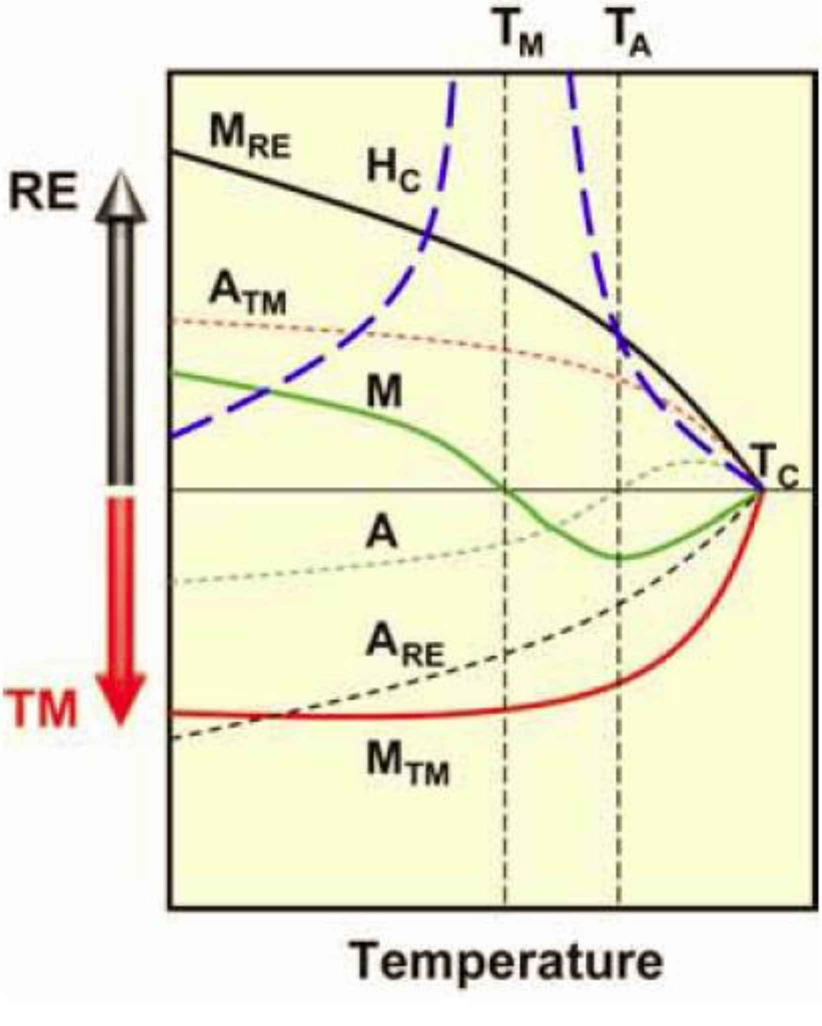

Figure 3.6: Schematic guide to the temperature dependence of both individual sublattices along with their combined effect on the net magnetic characteristics of the material. Shows the two compensation temperatures, magnetic (T_M) and angular momentum (T_A) along with the Curie temperature (T_C) these broadly describe the temperature dependent characteristics of a RE-TM material. **[20]**

The temperature at which the RE and TM spin moments are balanced is referred to as the magnetization compensation temperature, T_{Mcomp} and will generally be reduced with increased RE concentration in the alloy. At this point (as shown in **figure 3.6**) there is a divergence in the coercive field, H_c, required to switch the magnetization, which is due to the relationship $H_c = 2K/M_S$ **[21]** and the observation that at this point there is a drastic reduction in net magnetic moment, M, without loss of intrinsic magnetic anisotropy, K. This means that around this temperature, it becomes extremely energetically expensive to manipulate the magnetic ordering of the alloy. For spintronic applications, alloys with T_{Mcomp} around or just above room temperature are ideal as at this point, the magnetic state, and thus the stored information, is greatly resistant to unwanted stray fields.

Analogously to T_{Mcomp} an angular momentum compensation temperature T_{Acomp} can be defined where the contributions of the two sublattices are equal and opposite, cancelling each other. This compensation is due to the composition dependence of each sublattice's gyromagnetic ratios (which relate the magnetic moment to angular momentum) and will vary relative to T_{Mcomp} for different elements and composition ratios. As discussed in **chapter 2** it is the angular momentum contribution which significantly impacts on magneto-dynamic rates and is thus a critical parameter for any applied technology.

3.3.2 Magneto-dynamic Properties

A general theory of laser-induced ultrafast demagnetisation considers a unified material with a single temperature dependence (see **chapter 2**). Experimental evidence **[22]** however suggests that in the special case of a ferrimagnetic multi-sublattice material, such as GdFe, the two sublattices undergo distinct ultrafast dynamic behaviour. Experimental and theoretical evidence has been reported **[23]** **[24]** in which magnetic switching is achieved using linearly polarized light, caused by a transient "ferromagnetic-like state" in which the RE and TM sublattices align parallel on a picosecond timescale. Recent work by Mentink et al. **[25]** attributed this to an additional angular momentum exchange between the sublattices, not possible in a single sublattice material. In this treatment, the two-temperature model of electron and lattice thermal reservoirs is accepted and defines three regimes of dynamics relative to the electron temperature: $T_e >> T_c$, $T_e \sim T_c$ and $T_e < T_c$. Above the Curie temperature, the system is paramagnetic; the interaction between sublattices can be considered negligible and their dynamics independent. Crucially, this initial relaxation rate is calculated to be dependent on the atomic magnetic moment. Once the temperature drops to the vicinity of T_c, angular momentum exchange between the sublattices begins to occur alongside intra-sublattice relaxation, and gradually comes to dominate the dynamics. This leads to the conclusion that the interplay between two antiferromagnetically bound sublattices causes a mutual acceleration of the demagnetization process.

Further treatment of RE-TM dynamics came from Wienholdt et al. (2013) **figure 3.7 [26]** who proposed an "orbital-resolved spin model" separating the dynamics of the 4f and 5d electrons within the RE sublattice. As discussed previously, it is the 4f electrons that carry the most (92%) magnetic moment in a RE, but are buried deep beneath the Fermi energy accessible only through exchange with the 5d electron shell. This 5d shell can be thermally excited by laser heating, but the 4f cannot.

After laser heating and electron thermalization, strong spin non-equilibrium will exist between the directly accessible transition metal 3d spins and the shielded rare earth 4f spins. In order to maximize entropy, as the exchange interaction begins to compete, angular momentum transfer will occur not only between the two sublattices but also within the RE sublattice. The TM sublattice will reach its (laser fluence dependent) maximum demagnetization state after ~1 ps while the RE sublattice is still demagnetizing, leading to a transient state in which both spin systems are aligned. This leads to a faster demagnetization process than single sublattice relaxation.

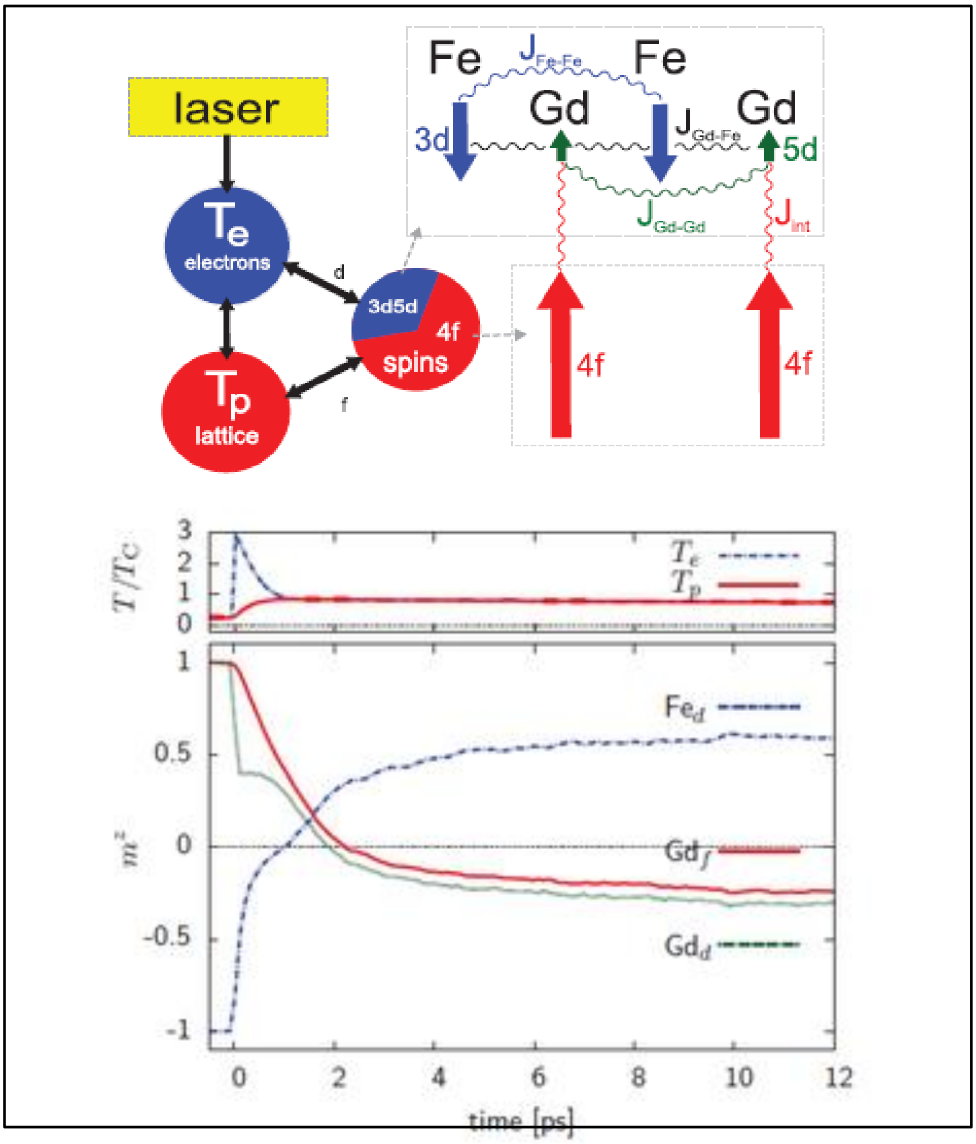

Figure 3.7: Schematic demonstration of the energy transfer channels which exist within a RE-TM alloy under laser photon stimulation and theoretical calculated response rates for Gd5d, Fe3d and Gd4f electron orbitals. **[26]**

Recent work by Stanciu et al. (2006) **figure 3.8(c) [27]** and Mekonnen et al. (2011) **figure 3.8 (b) [28]** has reported fluence dependent investigations on RE-TM alloys, providing experimental evidence of the inter-sublattice exchange occurring. These papers show that the frequency of precessional spin motion is related to the strength of the coupling between the sublattices and their ability to transfer energy and angular momentum. In this work, the coherent macrospin precession (referred to as the ferromagnetic resonance FMR mode) is shown to clearly respond to the compensation temperatures. It is also shown to be degraded at higher temperatures in favour of an exchange mode precessional motion **[29]**. This mode represents the strength of inter sublattice exchange. As temperature rises, the effective fields of rare earth and transition metal sublattices diverge and precess around their own respective field terms. A frequency for this exchange mode is given by the following **equation 3.3**. This is related to the inter-sublattice exchange coupling λ_{RE-TM}, the respective gyromagnetic ratios γ_{RE} and γ_{TM}along with the relative magnetization based on the concentration ratio between the two elements.

$$f_{ex} = \lambda_{RE-TM}\gamma_{RE}\gamma_{TM}[xM_{TM}/\gamma_{TM} - (1-x)M_{RE}/\gamma_{RE}] \tag{3.3}$$

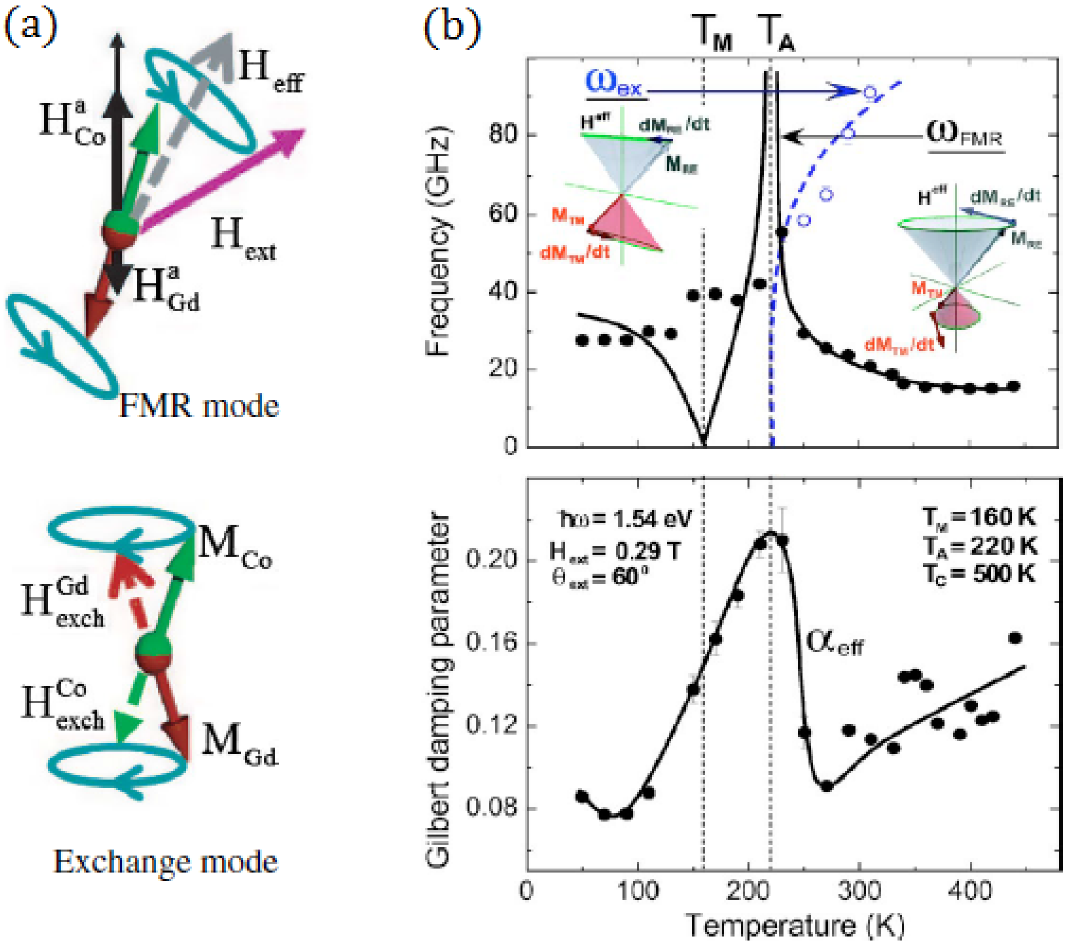

Figure 3.8: (a) Cartoon schematics of the two observable modes of spin precession, the FMR coherent mode and the high temperature exchange mode **[28]**. (b) Experimental observations of temperature and angular momentum compensation in GdFeCo as well as the observed Gilbert damping **[27]**.

3.4 Summary

In summary, the magnetic properties of Fe_3O_4 are highly dependent upon its crystallographic ‘purity’ making the growth process a very key aspect of any quality refinement. The crystal benefits from a high spin-polarizability and high Curie temperature, while requiring only cheap and abundant elements. These make this a worthwhile cause. The quality of the material can be analysed in detail by electron microscopy and provide feedback to the growth process.

The RE-TM alloy, by contrast, has no restriction on crystal geometry and as such is easier to produce and alter the composition ratio for material performance optimization. Their angular momentum and magnetization compensation points make them ideal for long term stable storage of magnetic information and make temperature dependent studies an informative method of characterization.

3.5 References

[1] A. Koblischka-Veneva, et al., J. Appl. Phys. **103**, 07E505 (2008)

[2] V. K. Lazarov, et al., Phys. Rev. B, **72**, 195401 (2005)

[3] J. B. Goodenough, Phys. Rev., **100**, 564 (1955)

[4] J. Kanamori, J. Phys. Chem. Solids **10**, 87 (1959)

[5] K. Yosida, Theory of Magnetism (Springer-Verlag, Berlin, 1996)

[6] G. M. Müller, Nature Mat., **8**, 56 (2009)

[7] M. Kallmeyer, et al. J. Appl. Phys., **103**, 07D715 (2008)

[8] L. M. Falicov, Thin Solid Films, **216**, 169 (1992)

[9] M. Paul et al. J. Appl. Phys., **110**, 073519 (2011)

[10] R. M. Cornell and U. Schwertmann, The Iron Oxides: Structure Properties, Reactions, Occurrences and Uses, (Wiley-VCH 2003)

[11] R. J. Beals, et al., J. Am. Ceram. Soc., **40**, 279 (1957)

[12] D.T. Margulies, et al., Phys. Rev. Lett., **79**, 5162 (1997)

[13] S. Celotto, W. Eerenstein, and T. Hibma, Eur. Phys. J. B, **36**, 271 (2003)

[14] P. Chaudhari, et al., Appl. Phys. Lett., **22**, 337 (1973)

[15] US patent US 7531830 B2 “Spin-polarization devices using rare earth-transition metal alloys” (2007)

[16] G. R. Giesbrecht and J. C. Gordon, Dalton Trans. 2387 (2004)

[17] A. J. Freeman and R. E. Watson., Phys. Rev., **127**, 2058 (1962)

[18] M. Mansuripur, The Physical Principles of Magneto-Optical Recording (Cambridge University Press, Cambridge, 1995)

[19] X. Jiang, et al., Phys. Rev. Lett., **97**, 21702 (2006)

[20] C. D. Stanciu, Laser-Induced Femtosecond Magnetic Recording (PhD Thesis, Radboud University, Nijmegen, The Netherlands, 2008)

[21] J. D. Livingston, J. Appl. Phys. **52**, 2544 (1981)

[22] C. Stamm et al., Nature Mater. **6**, 740 (2007)

[23] I. Radu, et al. Nature (London) **472**, 205 (2011)

[24] T. A. Ostler, et al. Nat. Commun. **3**, 666 (2012)

[25] J. H. Mentink, et al., Phys. Rev. Lett., **108**, 057202 (2012)

[26] S. Weinholdt, et al., Phys. Rev. B, **88**, 020406(R) (2013)

[27] C. D. Stanciu, et al., Phys. Rev. B, **73**, 220402(R) (2006)

[28] A. Mekonnen, et al., Phys. Rev. Lett., **107**, 117202 (2011)

[29] J. Kaplan and C. Kittel, J. Chem. Phys., **21**, 760 (1953)

Chapter 4

Quality Control of Materials

4.1 Introduction

This chapter discusses the techniques and principles necessary to produce and characterize the material quality of a test sample and has been subdivided by discipline. Molecular beam epitaxy growth method and technique used to produce thin-film Fe_3O_4 samples for this project in the Department of Physics at York are discussed, along with a brief comparison to sputter deposition used undertaken by collaborators for GdFe alloy thin-films also investigated. Facilities available at the York-Jeol Nanocentre for electron microscopy imaging of thin-films, as well as the techniques used and developed over the course of this project are then detailed.

4.2 Growth Techniques

4.2.1 Molecular Beam Epitaxy (MBE)

As implied by the name, MBE employs concentrated beams of molecules or atoms, which are liberated from a source by sublimation heating and directed through an ultra-high vacuum (UHV) ($<10^{-9}$ mbar) to an atomically flat crystalline substrate.

This beam, with a low flux, creates a uniform film one layer at a time. Originally applied to compound semiconductor growth, today it is used to produce thin-films of a large number of material types. The UHV environment maintains the purity of the substrate surface and because the mean free path of the beam is much greater than the distance between source and substrate, it will be extremely uniform in energy and incidence angle. Furthermore, any scattered molecules will be captured by the walls of the chamber and removed from the growth. A raised temperature of the substrate allows arriving molecules the thermal energy required to shift across its surface onto lattice sites, facilitating the underlying crystal structure to translate to the grown film. If the crystalline structure of the substrate translates to that of the film, it is considered to be epitaxial. A mechanical shutter is used to produce sharp start and end times to film deposition, in this manner numerous film layers of differing constitution can be grown on top of one another and each time the molecular beam flux can be tuned to a desired deposition rate before the substrate is exposed. **Figure 4.1** shows a schematic of the growth chamber.

Samples are loaded into the chamber via a fast entry load lock and manoeuvred into position above the sublimation sources. The base pressure in the growth chamber is kept below 10^{-10} mbar, which can rise as high as 10^{-5} mbar during growth. Deposition can be controlled to an accuracy of 0.05 nm/min and the substrate can be heated to above 1000°C via a tungsten filament and electron beam heating. All substrates were thoroughly cleaned, prior to insertion into the growth chamber, using acetone, then ethanol.

The important differentiating factor between this method and other growth systems is the rate of deposition; which is much lower here than in, for example, plasma sputtering systems. This slower rate, in theory, allows more precise control over the thickness of the film over a range from 1-100 nm and, more importantly, epitaxial single-crystal growth. In order to accommodate this slower growth rate which would allow more impurity collisions, the apparatus must be contained within a proportionally higher vacuum system.

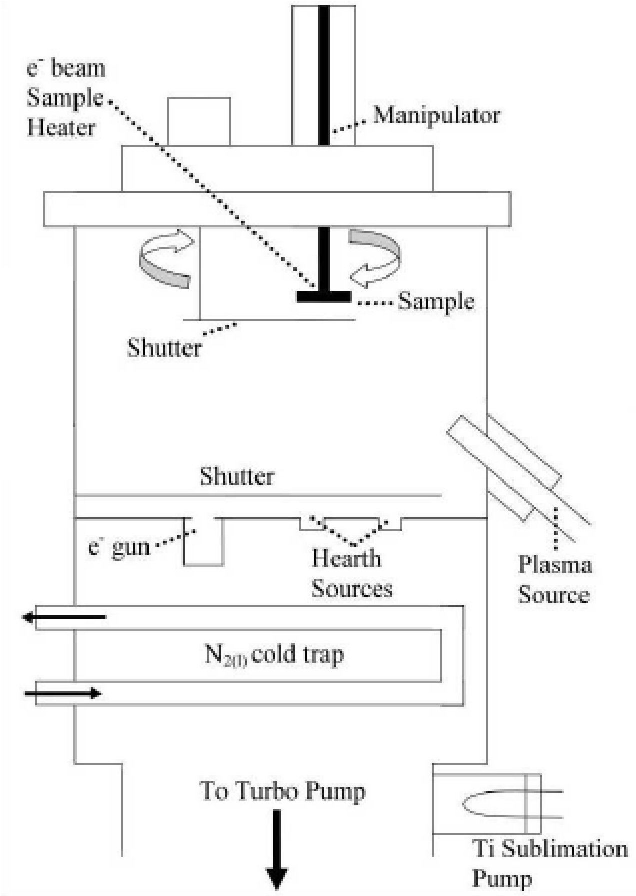

Figure 4.1: Schematic of MBE system. The sample is positioned at the top of the chamber behind a mechanical shutter. An electron source gun is guided onto a sublimation source in a Hearth, which ejects a molecular beam towards the sample. Various pumps and heat sinks are used to maintain the low pressure environment. A plasma oxygen source is fitted here to introduce molecular oxygen into the chamber for post-oxidation experiments.

A piezoelectric quartz crystal rate monitor is used to measure the rate of deposition during a growth procedure. As the vibrational frequency of the crystal is proportional to its mass, it is placed in position to receive an equivalent amount of deposited material as the substrate. By referring to the molecular mass of the sublimation source, it is possible to track the thickness of a grown film quite accurately, to within one or two monolayers.

Growing Epitaxial Fe_3O_4

There are two methods of epitaxial Fe_3O_4 growth by MBE. These are simultaneous oxidation and post-oxidation. Simultaneous oxidation involves the introduction of atomic oxygen into the growth chamber during the deposition of an iron film. This is performed by an oxygen plasma source, which introduces additional complications to the growth by requiring the iron growth conditions and oxidation conditions to be mutually non-exclusive. Post-oxidation consists of first depositing the iron film, under suitable growth conditions, before producing the correct growth conditions for oxidation and then admitting atomic oxygen into the chamber at a controlled rate. Both of these methods were investigated during the preliminary stages of this project however it was decided to focus on the post-oxidation technique, which was found to be more robust and reliable.

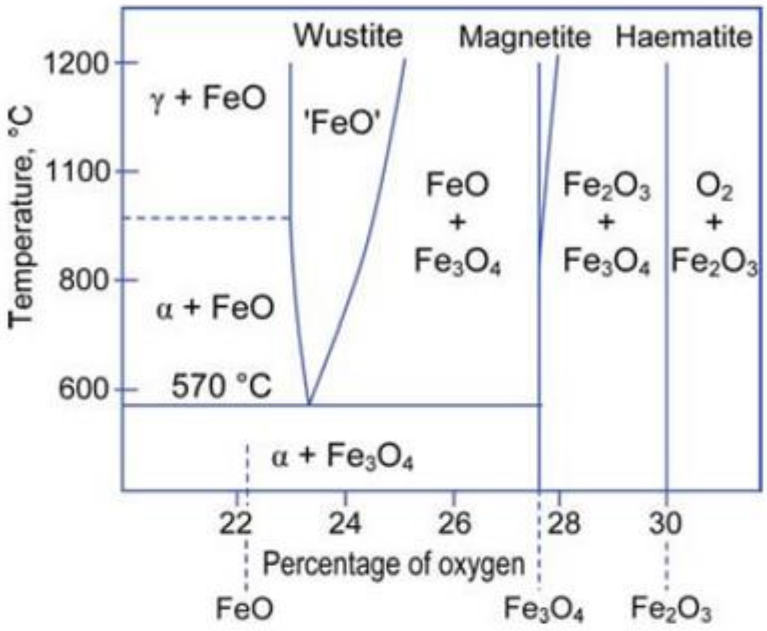

Figure 4.2: Iron oxide phase diagram, showing the spectrum of oxides which can be formed under various temperature and oxygen environmental conditions. Pure Fe_3O_4 (magnetite) exists under a very narrow range between ~900-1500°C and ~27.5-28.5% oxygen composition by weight. **[1]**

The factors which contribute to the oxide formation are iron deposition rate, growth temperature, oxygen partial pressure, oxidation temperature and time **[1]**. As discussed in more detail in chapter 3, there is a spectrum of iron oxides which can be formed during this growth process. **Figure 4.2** shows the temperature vs oxygen percentage chart, which gives an idea of the challenge associated with growing pure single phase Fe_3O_4, under a very narrow combination of temperature and pressure conditions.

4.2.2 Sputter Deposition

A number of sputtering techniques exist, but what they all have in common is a relatively high growth rate, producing polycrystalline thin-films rather than single crystals. This method particularly excels over MBE growth in its ability to deposit materials with high melting points, which would otherwise be difficult to evaporate. It is a desirable technique for rare earth-transition metal alloy deposition because of its ability to produce denser films **[2]**. Factors which affect the growth are the choice of sputtering gas and gas pressure, as well as deposition rate and temperature.

Rare earth-transition metal samples created during this investigation were grown to 20 nm thickness on cleaved 5x10 mm Si substrates at room temperature and 1×10^{-7} mbar base pressure. This growth was by direct current magnetron co-sputtering from elemental targets, using Ar gas at a pressure of ~0.005 mbar, at Nanjing University, China. The samples were finished with a 5 nm Au cap for oxidation protection. Composition ratios of Gd:Fe were then controlled by tuning the relative deposition rates, monitored by quartz crystal rate monitoring.

4.3 Imaging Techniques

With a sample offcut, or once non-invasive characterizations have been undertaken, investigation of the atomic structure of a sample can give an essential insight into the physical properties of a thin-film system. As Fe_3O_4, like many other materials, is dominated by crystalline structural ordering, particularly of material interface boundaries, a large amount of qualitative and quantitative information can be gathered from a few images. The imaging discussed here is almost exclusively transmission electron microscopy (TEM) on cross-sections of thin-films samples.

4.3.1 Sample Preparation

Cross-section Technique

For many experimental physics techniques the quality of data provided by an experiment relies heavily on the quality of the initial preparation; for TEM this is even truer. Due to the nature of transmission electron microscopy, each sample must be made sufficiently thin such that a large enough electron flux is not absorbed after the beam has interacted with it. The method described here is one of a number which were learned by the author, and was found to be most effective on the metrics of quality and consistency for cross section samples, though this is a subjective opinion.

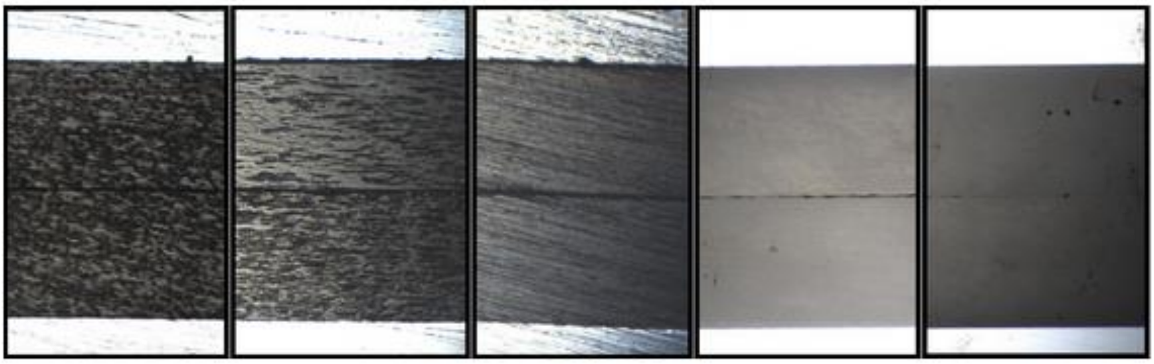

Figure 4.3: Example images of several stages of polishing a cross-section sample, showing the quality of the interface required for a successful sample.

Depending on the amount of sample available to work with, a cut was made to give approximately a 1 mm x 5 mm slice, with the desired zone axis to be imaged along the long edge. A sample would be prepared for cutting by first submerging it face down in heated crystal bond wax, which melts above 80°C, on a glass (1” x 3”) microscope slide, and allowed to cool to be frozen in place. This supported the delicate substrates which were prone to shattering and disintegrating even with this protection. Using a diamond tipped circular saw at a low RPM and low constant pressure, regular cuts could be made along any crystal orientation desired for imaging.

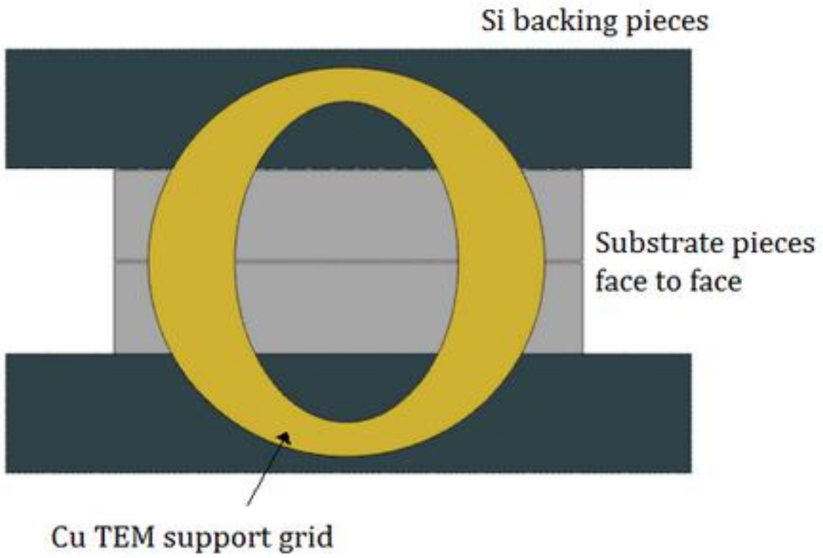

Figure 4.4: Cartoon schematic of the arrangement of materials combined to make a cross section TEM sample. Slices of a sample are glued face to face (film surfaces together) and backed by Si supports. After thinning one side, a Cu grid is glued to support the sample once it reaches <50 μm thick.

Once manually thinned, the final stage was completed using an Argon Precision Ion Polishing System (PIPS). Guns focused onto the region of interest of the sample are used to thin a small area to a thickness of a few atoms. This process produces a thickness gradient towards a hole in the sample, around which are areas of thicknesses appropriate for various characterizations under the TEM. A sample was considered ready for the microscope when there was a clear band of 'rainbow fringes' as shown in **figure 4.5** surrounding a section of the interface, which indicated this region was on the order of thickness of the wavelength of visible light.

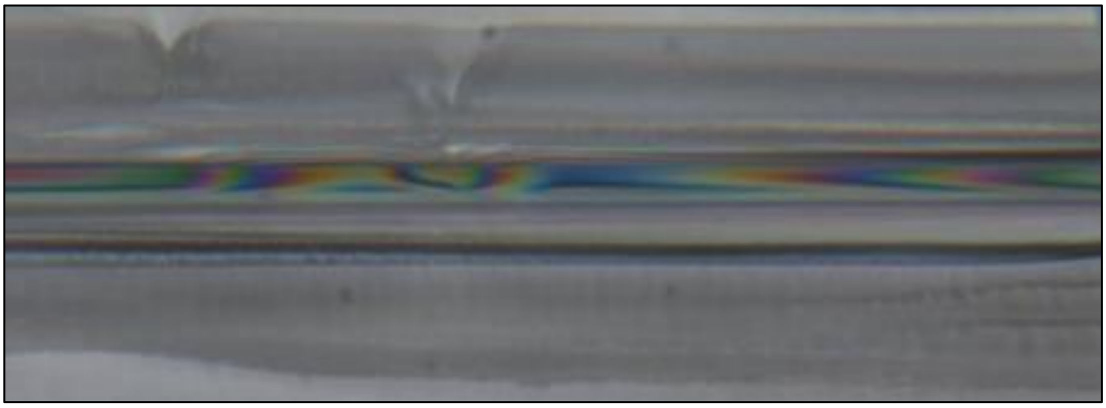

Figure 4.5: After PIPS milling, the sample is considered ready when a clear band of rainbow fringes are observable at the interface. This is due to the thickness of that region being of the scale order of the wavelength of visible light.

Plan-View Lift-Off Technique

Information from a sample surface can be useful alongside the cross-section. This view, especially, gives an advantageous position from which to view the effects of the island growth and the density of APBs throughout the film. This technique was developed during the PhD of Dr. Wilma Erenstein **[3]** as an alternative to a more traditional plan-view preparation technique detailed above for cross-section. The method involves the chemical removal of the film from the MgO substrate using ammonium sulphate ($(NH_4)_2SO_4$) solution. This allows the film to be retrieved on a Cu fine mesh grid and placed directly into the microscope. For this process a 10% solution was made and then used to fill petri dishes suspended in a heat bath. 1x1 mm pieces of a specimen were placed floating on the solution film-side up and the process was left to run for 24 hours at 70°C. The grid was prepared by soaking in ethanol and drawing out impurities onto filter paper. After this time, the substrate had slightly dissolved and detached itself from the film, which was left floating on the surface of the solution. This process did not yield 100% success, but the quality of successful samples was very good. Generally the film fragmented and small samples of this were collected. It was important at this point to carefully wash the sample in ethanol from a pipette, to reduce the contaminants which otherwise degraded the quality of TEM images obtainable.

4.3.2 Transmission Electron Microscopy (TEM)

Transmission electron microscopy is a technique which allows the detailed probing of structures down to the atomic scale. The concept was formulated in the early 20th century and the principles of the pioneering apparatus are very similar to the microscopes used today. The technique shares many similarities with visible light optics; with the photon source replaced by an electron source, and the physical lenses replaced with electromagnetic coils. Electron optics allows the probing of much smaller structures, due to a much smaller de Broglie wavelength. They are also more strongly interacting with matter due to Coulombic interaction and are easily channelled because of their charged nature. The main conceptual difference between electron and light optics comes in the way the resulting images are produced, relying on diffracted and reflected flux respectively. This requirement makes sample preparation very important, as the sample must be made thinner than the penetration depth of the electron beam for any information to be obtained at all. This depth is dependent on the energy of the beam and the density of the target sample but is generally on the order of a few nanometres.

A schematic of the electron optics is shown in **figure 4.6** above. The electron source at the top of the column is a tungsten filament, which is shielded on all sides except for an opening which directs a diffuse beam down through the instrument. Each lens is an electromagnetic coil encircling the beam line and the condenser lenses begin by collecting and focusing the beam down onto the sample. At this stage the intensity and diffuseness of the beam can be controlled by adjusting the microscope’s focal plane. From this point the beam, carrying the information from the specimen, passes through the objective lens where it is collected and focused into a coherent image. Lastly, intermediate and projector lenses refine and direct the beam onto a phosphor viewing screen or CCD camera system for observation and recording.

All of the lenses are subject to aberrations due to the engineering challenge of constructing perfect cylinders to the length scale required, as tiny defects in the system can have a large impact on the image fidelity. This is rectified by manipulating the magnetic fields of each coil to correct for any astigmation. In order to produce an undistorted image, a trade-off is made between the brightness of a captured image and the incident angle of electrons on the sample. The least distorted real-space image is made in the limit where the incident angle of electrons goes to zero, known as the parallel beam condition. Apertures can then be used to isolate parts of and manipulate exposure of the sample.

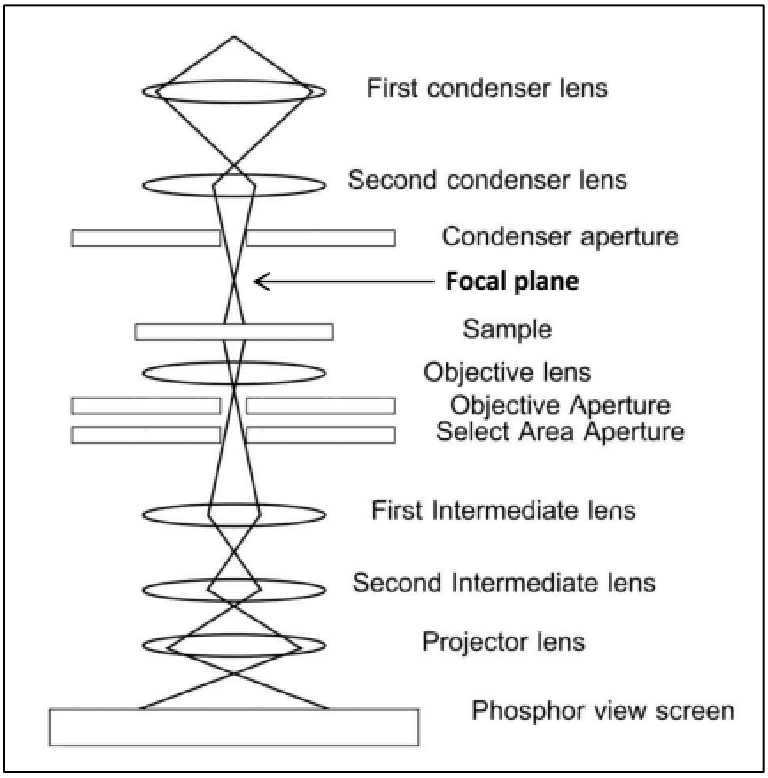

Figure 4.6: Schematic with ray diagram of a standard Transmission Electron Microscope (TEM) setup. Showing the series of lenses which collect and shape the electron beam created at the top of the column.

4.3.3 Electron Diffraction

An important technique for characterising samples is electron diffraction. From this, quantitative data can be extracted, answering questions such as the crystallinity, lattice parameters, orientation and, to an extent, the chemical makeup of the sample. Diffraction spots are the result of an interference pattern due to the wave-like nature of electrons **[4]**. The regular periodicity of a crystal structure is analogous to a diffraction grating in 3-dimensions and using the same mathematics it becomes possible to make quantified measurements of the dimensions of the repeating units of that crystal structure. Bragg's law (**equation 4.1**) gives a starting point for understanding this process, for the case where probing electron beams are parallel and at discrete distances, d, apart. A Bragg peak is produced where reflections from given crystal planes interact constructively as expressed by the following equation, in which n is an integer, λ is the wavelength of the incident electrons and Θ is the angle between incident and scattered rays:

$$\mathrm{n\lambda = 2dsin\Theta} \qquad \textbf{(4.1)}$$

These Bragg peaks are, in practise, the spots seen in a diffraction pattern and the spacing between these spots correspond directly to reciprocal distances in the crystal lattice. The theory talks about reflections; however the real life situation in a TEM is based on diffraction, which provides extra complexity due to multiple planes being involved, with some existing in the lattice but having 'forbidden reflections'. Calculating the real space dimensions of a crystalline structure becomes straight forward for a known camera length using **equation 4.2**:

$$\mathrm{d_x = ((nl_{hkl}^{MgO})/(4l_x)).\, d_{hkl}} \qquad \textbf{(4.2)}$$

For example the calibration at 30cm camera length to convert pixels into a real distance is:

$$\mathrm{d_x = ((18.6961 \times 0.2105)/(4 \times l_x)).\, d_{hkl}}$$

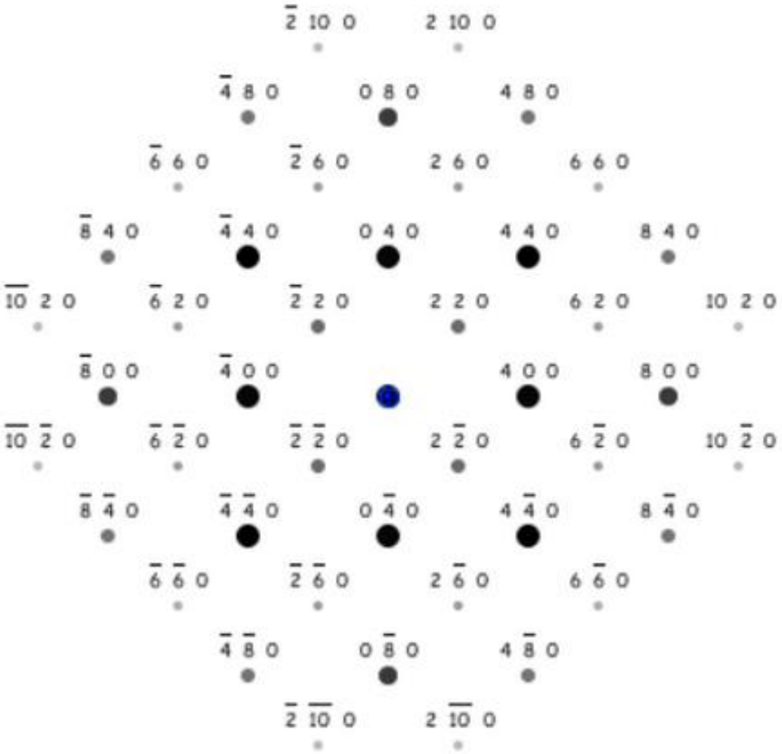

Figure 4.7: Calculated diffraction pattern for Fe_3O_4 (001) showing the Miller index for each spot corresponding to a plane in the real-lattice. **[5]**

The simulated diffraction pattern of Fe_3O_4 (001) is shown in **figure 4.7**, produced by the software package JEMS **[5]**. This crystallography and electron microscopy software suite is a database of crystal structures and their associated characteristics. This was used as a characterisation tool to help with identification of TEM images and diffraction patterns by facilitating the identification of specific lengths and angles in crystal structures in different orientations.

Miller indices are given for each spot, indicating the lattice planes they correspond to (**figure 4.8**). In a cubic system, these are given an x,y,z vector coordinate (hkl) and the plane referred to is the one orthogonal to that vector.

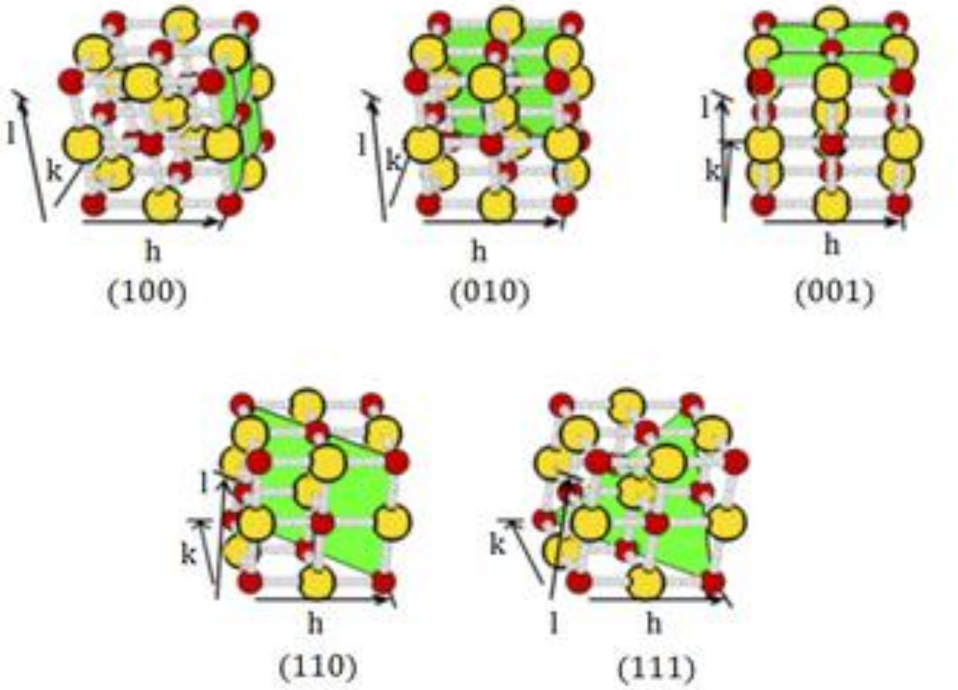

Figure 4.8: Examples of basic Miller indices for a simple cubic system.

The Digital Micrograph software suite was used to collect and then analyse TEM images. It provides the means to study scale calibrated images to accurately measure distances and angles within them. A number of processing tools are available within the software, for example allowing the user to mask and isolate sections of an image. It is possible to take a simulated diffraction image from a High-Resolution TEM (HRTEM) image using a fast Fourier transform (FFT) calculator. This has benefits and drawbacks based on actual imaging of a diffraction pattern; the image quality must be high, resolving atomic planes and thickness contrast artefacts can be unwantedly introduced.

This technique was extremely useful for observing and identifying defects in the structure of the film, especially around interfaces. Once an HRTEM image was taken, an FFT was calculated for the entire image. A mask was applied to this, isolating spots corresponding to the planes under investigation (as a mirrored pair around the zero-spot). An inverse Fourier Transform (IFFT) was then taken of this, producing an image which contained only those planes, making defects much easier to spot.

4.3.4 Dark Field Imaging

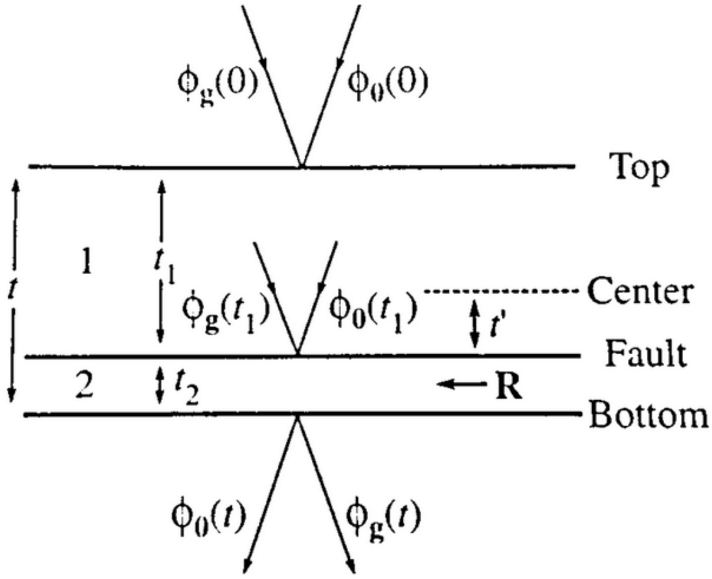

Figure 4.9: Schematic of planar defect geometry used in Howie-Whelan approximation.

In order to observe APBs, a dark field imaging technique was employed. As mentioned in **chapter 3,** ABPs are produced by the translation of an island of growth in the film with respect to another; this produces a diffraction contrast map. This contrast occurs due to the interaction of Bloch waves within the crystal. The visibility of a defect is determined by the relationship between its translational shift vector, R, and the beam vector of the diffraction spot used, g. The column approximation is made in order to produce the Howie-Whelan equations (**4.3, 4.4**), meaning that only the direct beam (0) and the first diffracted beam (g) are considered, as is shown schematically in **figure 4.9**.

$$d\Phi_{0(sub)}/dz = (\pi i/\varepsilon_g)\Phi_{g(sub)}\exp(i\alpha) \qquad \textbf{(4.3)}$$

$$d\Phi_{g(sub)}/dz = (\pi i/\varepsilon_g)\Phi_{0(sub)}\exp(-i\alpha) + 2\pi i s\Phi_{g(sub)} \qquad \textbf{(4.4)}$$

In these equations, Φ_0 is the amplitude of the direct beam (g=0), Φ_g is the amplitude of the diffracted beam for reflection G and ε_g is the characteristic length for reflection g, known as the 'extinction distance'. Planar defects exist when the phase term, α, is non-zero, which can be rewritten as

$$\alpha = 2\pi\mathbf{g}.\mathbf{R} \qquad \textbf{(4.5)}$$

This condition is created experimentally by locating an area of interest on the sample and then tilting the crystal away from the zone axis so only one strong diffracted beam remains. This is known as the 'two-beam condition'. At this point an objective aperture is used to mask all inclusions except those from this diffracted beam. The defect free areas of the film remain bright and slightly over saturated, fulfilling the Bragg condition, while locations containing defects bend the beam away from the beamline and so appear very dark.

The visibility criteria of an APB, as described by W. Eerenstein **[3],** are as follows:

$$2\pi\underline{g}.\underline{R} = (2N+1)\pi \qquad \textbf{(4.6)}$$

This is approximately the same as for a stacking fault planar defect. In this equation, $\underline{g}$ is the diffraction vector of the electron beam, $\underline{R}$ is the translation vector of the planar defect as a fraction of the Fe_3O_4 unit cell. N indicates visibility of an APB for a chosen diffraction spot if it is an integer and invisibility otherwise.

4.4 References

[1] D. R. Lide, Handbook of Chemistry and Physics (88th edition, CRC Press, New York, USA, 2007)

[2] M. Mansuripur, The Physical Principles of Magneto-Optical Recording (Cambridge University Press, Cambridge, 1995)

[3] W. Eerenstein, Spin-dependent transport across anti-phase boundaries in magnetite films (Ph.D Thesis, University of Groningen, 2003)

[4] D. B. Williams and C. B. Carter, Transmission Electron Microscopy: II Diffraction (Plenum Press, New York, 1996)

[5] JEMS crystallographic analysis software package
http://cimewww.epfl.ch/people/stadelmann/jemsWebSite/jems.html

Chapter 5

Building Magnetic Characterization Techniques

5.1 Introduction

During the course of this project, one major set-up was developed; a femtosecond time-resolved optically-induced pump-probe magneto-optic Kerr effect (MOKE) apparatus. This work spanned from design of a new lab and commissioning of a Spectra-Physics femtosecond laser system to a full plan and build of the optics and construction of detectors and software. Alongside this work, design and improvement of a number of other instruments, including static high-resolution MOKE was completed.

5.2 Measuring the Magneto-Optic Kerr Effect (MOKE)

While a number of magneto-optic (MO) effects exist, they are all associated with the propagation and interaction of an electromagnetic wave with a medium under the influence of a static or quasi-static magnetic field, producing an observable change in polarization **[1] [2]**. Where this wave is able to propagate through the medium, it is said to have undergone a Faraday Effect rotation, named for its discoverer Michael Faraday in 1845 who succeeded in providing the first piece of experimental evidence of the relationship between light and magnetism. In the case where the electromagnetic wave is reflected rather than transmitted through the medium, it is referred to as the Kerr Effect, named for its discovery by John Kerr in 1877 and commonly abbreviated to MOKE.

A linearly polarized beam of light, incident on magnetized material experiences an imbalance in the propagation rate of right and left rotating polarizations, resulting in a net shift in the polarization angle of the wave. A degree of ellipticity is induced as the principal axis is rotated relative to the incident beam. The effect is generally small (~1/1000 rad) so it is critical that the experiment is set up with precision and stability in mind. It is important to note that the penetration depth of the beam is on the order of 10 nm - 20 nm and that for films thinner than this, the signal will decrease proportionally to the thickness.

Within the topic of the Kerr effect, it is necessary to make a further distinction based on the direction of the magnetization vector, M, of the sample relative to the plane of incidence. The effect is separated into three: longitudinal, transverse and polar, representing M in-plane with the plane of incidence and reflection surface; orthogonal and in-plane; and orthogonal and out-of-plane respectively. Each effect provides different information about the sample and it is important to be aware which effects are present in a particular measurement and sample. A more detailed treatment can be found in **chapter 2**.

A number of MOKE detection methods exist, based on directing the reflected light onto a photodiode, which registers a change in intensity as a voltage. The simplest system relies on a single detector in a configuration known as a cross-analyzer. A pair of high extinction ratio (>100,000:1) linear polarizers are set at orthogonal polarizations to each other, one in the incident beam path, and one in the reflected beam path. These are referred to as polarizer and analyzer, respectively (see **figure 5.1**). In the case where the magnetization vector of the sample is negligible, the reflected light is completely extinguished by the analyzer and the detector registers baseline voltage. From this state, any change in the angle of polarization is detected as an increase in the intensity of light reaching the detector. This detection is blind to the polarity of that rotation and is susceptible to any external noise introduced into the system.

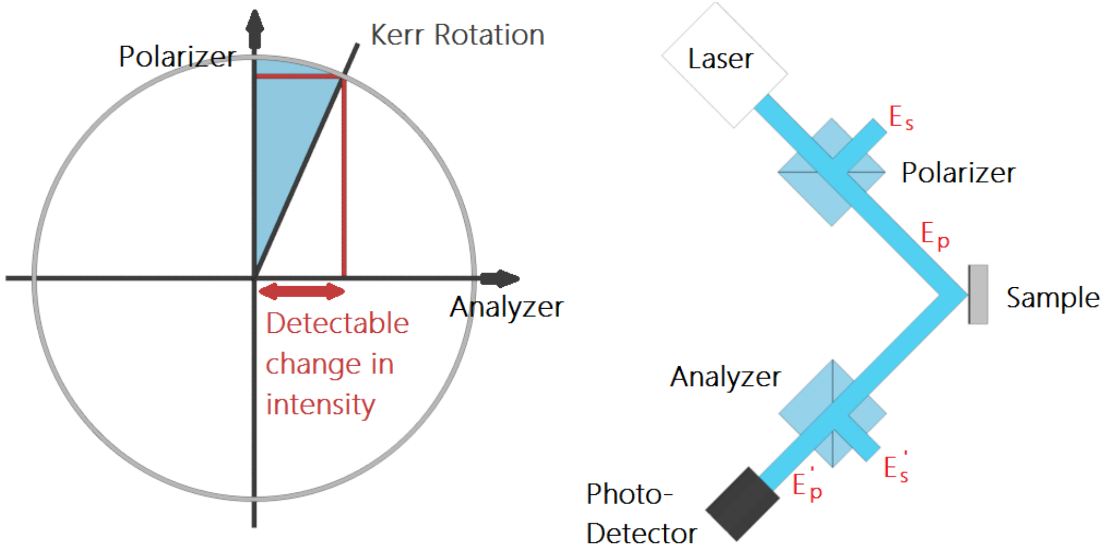

Figure 5.1: Schematics showing Kerr rotation of polarization causing a linear increase in the intensity component along the analyzer axis (left) and a simple cross-analyzer detector configuration (right).

In order to improve on the limitations of the single detector system, a second detector can be introduced to form a 'bridge detector'. This involves capturing both the components in-plane and orthogonal to the incident polarization and taking the difference between the two. This provides a direct feedback between the detectors and the laser intensity, negating any intensity fluctuations and is, by the nature of the arrangement, able to detect the polarity of the Kerr rotation. This detector is either mounted on a rotating frame about the centre of the polarizer, with detectors fixed rigid to this frame, or is mounted statically and uses a half-wave plate as a relative polarization rotator in the beamline before the analyzer. In either case, the two detectors must be balanced prior to a measurement so that again, the initial state is the baseline voltage. A benefit of this technique is the ability to measure the surface reflectivity simultaneously by taking a summation of the two detector readings. This is unnecessary for a static MOKE measurement, but is a very insightful addition to the data produced by a time-resolved MOKE measurement as it provides an indication of the temporally and spatially-resolved surface temperature corresponding to the combined activity of the local electron and lattice thermal reservoirs.

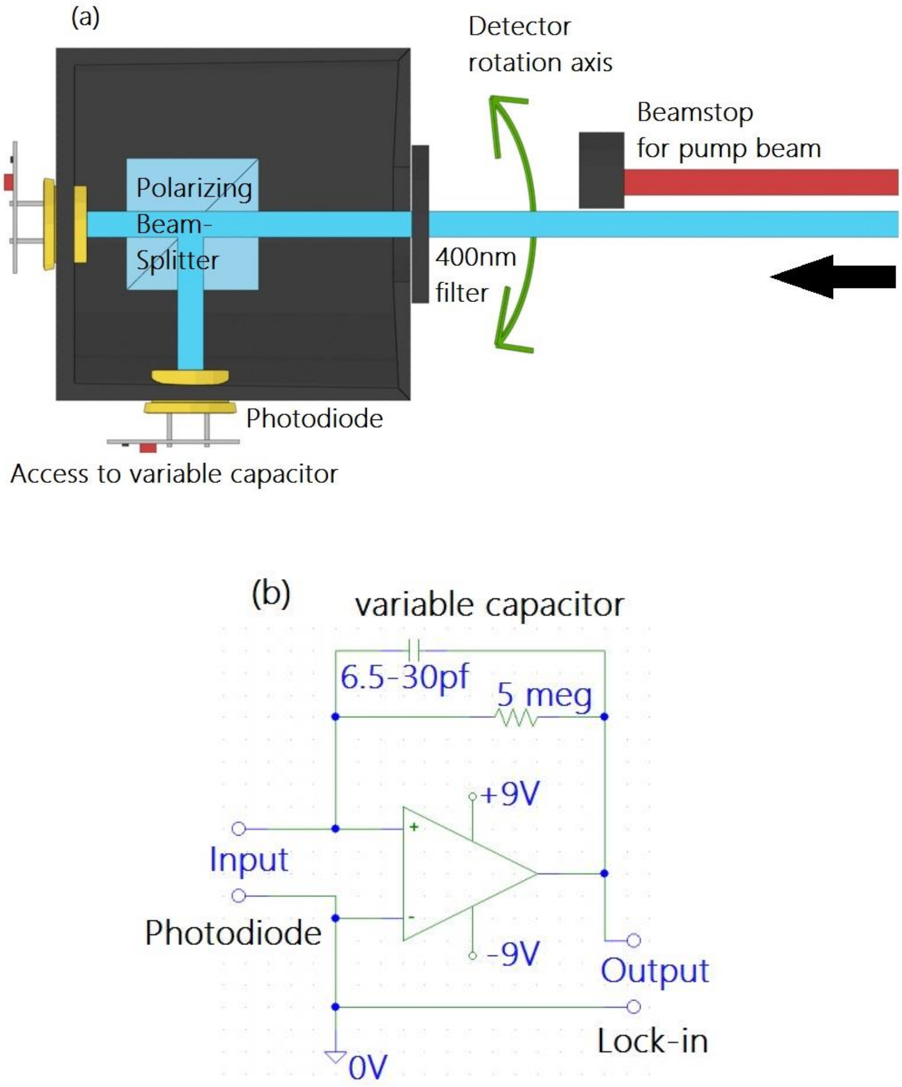

Figure 5.2: (a) Design of bridge detector built and used in this investigation showing two trans-impedance photodiode amplification circuits mounted to a rotating frame to detect orthogonal polarization components. Only 400 nm probe light is admitted and the frame is able to rotate around the axis of the probe beam to balance the detectors. The setup allows easy access to variable capacitors to tune the temporal response of each diode independently. (b) A schematic circuit diagram for the trans-impedance circuit built.

Detectors were constructed based on improvements to the design used by previous student Dr C. Bunce **[3]** using single low noise, reverse biased Si S1226-44BK photodiodes, and a low noise 'trans-impedance' amplification circuit using OPA124 op-amps. See **figure 5.2** for further details. This detection scheme is very sensitive to small rotations in polarization but can be susceptible to differential drift between the individual photodiode amplifiers. This can be compensated for by signal modulation as described later in this chapter using a lock-in amplifier. Additionally, as the measured signal is the difference between the two detectors, the time response of each circuit is critical. A slight difference in the path length to each detector can shift the pulses out of phase enough to cause large signal spikes (see **figure 5.3** below), which affect the output signal-to-noise ratio (SNR). This was solved by using a variable 'trimming' capacitor in each amplifier circuit which allowed the response time of each detector to be altered enough to minimize the phase difference.

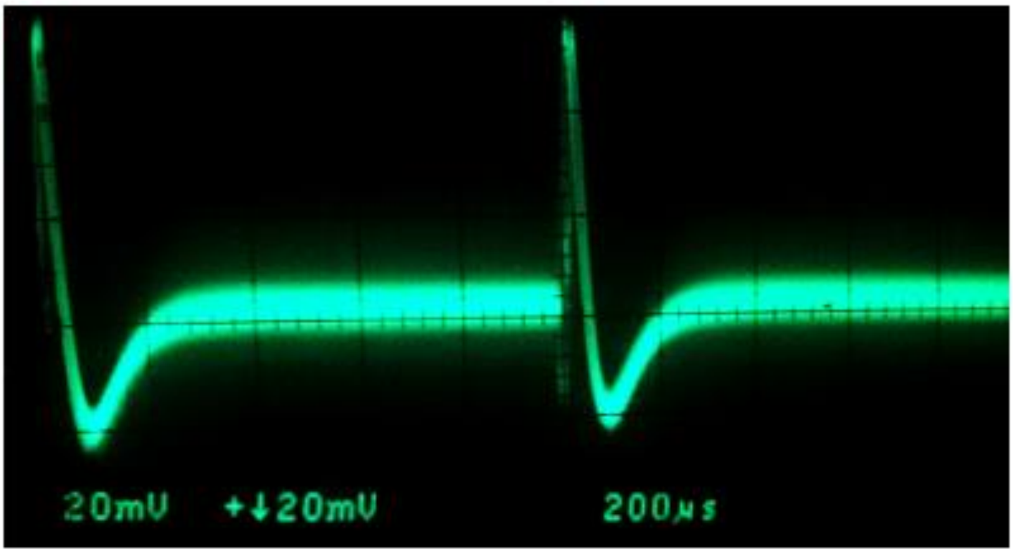

Figure 5.3: Difference between bridge detector photodiode 1 and 2 on oscilloscope. Shows an example of a signal spike observed if the detector timings are mismatched. This is adjusted for by changing the detector amplifier capacitance.

5.3 Time-Resolved MOKE Magnetometry

5.3.1 Stroboscopic Techniques

Due to limitations in the capture time of detector systems available today, it is not possible to observe ultrafast dynamic magnetic phenomena directly, which occur on timescales on or below the nanosecond. However a way around this is possible, using techniques descended from those pioneered by Eadweard Muybridge, an American photographer who was commissioned to study the weight distribution of a horse in motion. This early attempt as shown in **figure 5.4** was achieved by rigging a series of cameras along a track with triggers to set off each camera as the horse passed. The technique was successful and sparked interest in further development of the field.

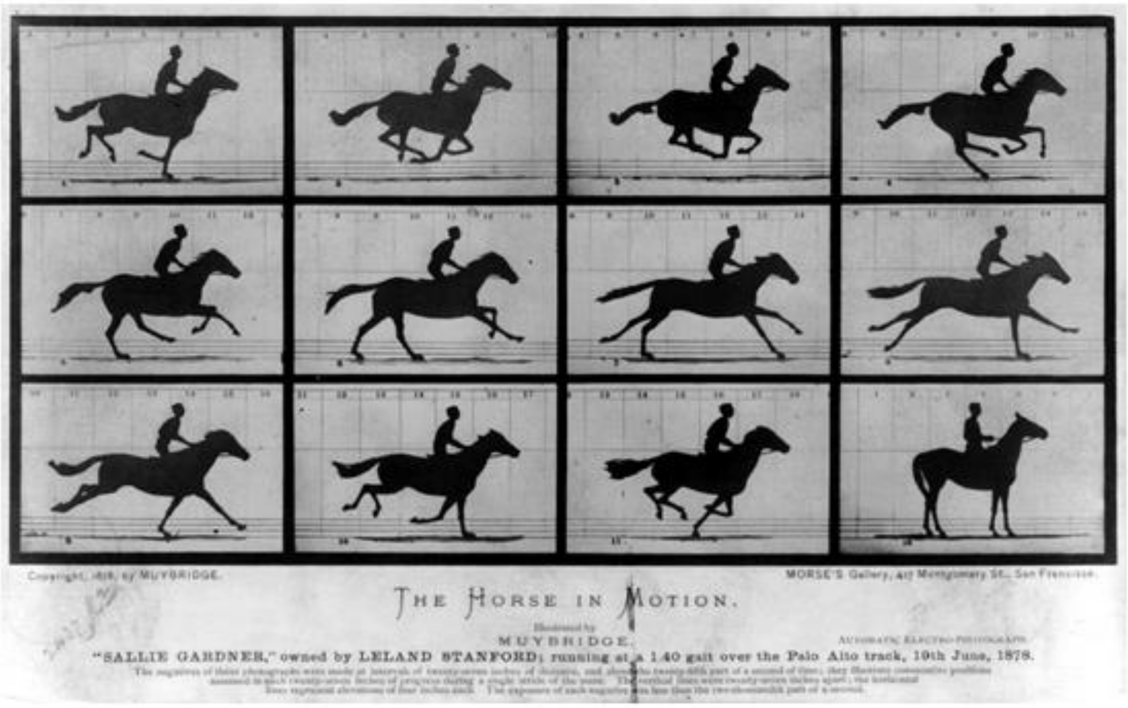

Figure 5.4: Historical image of frame by frame observation of a horse in motion by Eadweard Muybridge showing early example of observation of a dynamic event captured faster than real time. **[4]**

The technique, attributed to Awschalom, et al. in 1985 **[5]**, used to observe magneto-dynamics on the sub nanoscale is considerably more advanced, but still to some extent analogous. It is known as a pump-probe technique, where a pulsed laser is divided into two beams of unequal intensity; the higher intensity beam is known as the pump and the lower intensity beam is the probe. These beams are spatially overlapped on the surface of interest.

Temporal resolution is achieved by varying the travel length, and thus the phase of one beam with respect to the other. In the analogy, if the horse was running on the spot and a single camera was used with a variable trigger, you could build up a picture of the dynamics over the course of many 'runs'. The important point to bear in mind here is that over the course of the experiment, any movements that were not repeatable would be blurred out and lost and only repeatable dynamics would be visible. So it is with pump-probe magneto-optics, the data captured represents the change and resetting of the dynamics, probably many thousands of times. In this manner it is important to bear in mind that the repetition rate of the observation system (laser pulse) must be significantly slower than the duration of the event (magnetic dynamics), so that each repetition finds a completely reset system.

5.3.2 Femtosecond Laser Operation

The femtosecond pulsed laser referred to in this work is a Spectra-Physics Femto Spitfire system, comprised of three units and configured as shown in **figure 5.5**:

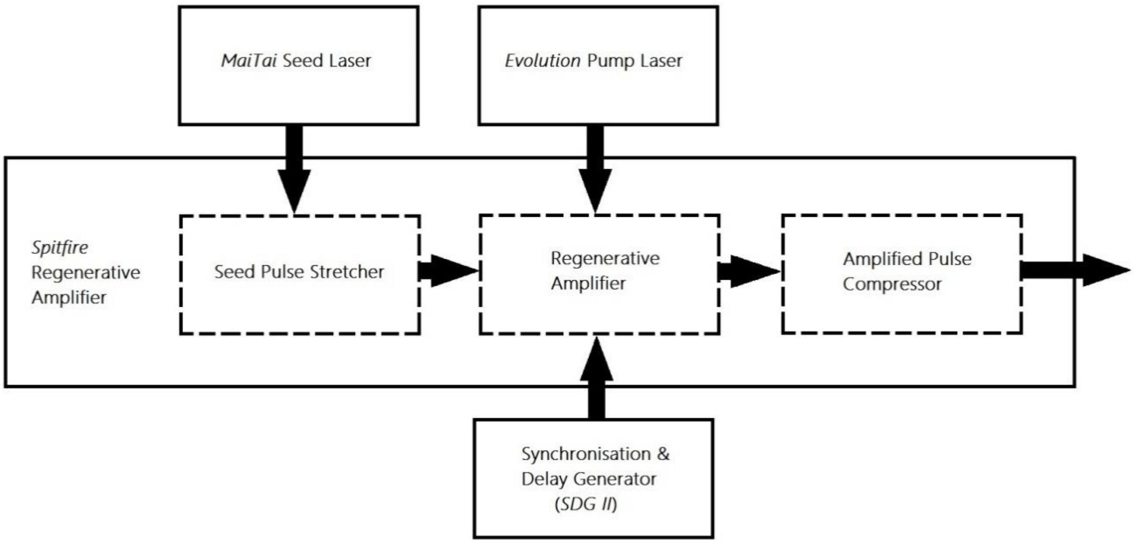

Figure 5.5: Schematic showing the combination of laser instruments to form the high-power, short-rise pulsed laser essential to this investigation.

- 21W 527nm diode-pumped, 1kHz Q-switched, Intra-cavity doubled Nd:YLF Pump Laser ‘Evolution-30’. **[6]**

- 1.5W 800nm diode-pumped, 1MHz mode-locked Ti:Sapphire Seed Laser ‘Mai-Tai’. **[7]**

- 2W Ti:Sapphire 800nm Regenerative Amplifier ‘Spitfire’. **[8]**

Pump Laser

The Evolution has an output wavelength of 527 nm and uses an array of twelve AlGaAs laser diodes to excite its Nd:LiYF$_4$ gain medium at 1053 nm. This medium is chosen for its high thermal conductivity and natural birefringence making it a stable medium for high pulse energy, low frequency lasers. The narrowband emission of laser diodes makes them efficient compared to more traditional broadband arc-lamp sources, which produce extra undesired thermal effects such as depolarization and thermal lensing. The laser resonator is acousto-optically Q-switched at 1 kHz with pulses lasting 100 ns. The Q-switching is achieved by periodically propagating an ultrasonic wave through an optically transparent material (sometimes known as a Bragg cell), manipulating its optical refractive index through the photo-elastic effect to periodically deflect a portion of the beam energy out of the cavity. While the ultrasound is applied, the Q (quality) factor is significantly reduced and lasing is interrupted. During the intervals, the gain medium is rapidly saturated again, producing a high Q-factor and restarting lasing, resulting in high energy pulses. Finally an intra-cavity frequency-doubling (also known as 2nd-harmonic generating (SHG)) Lithium Triborate (LBO) crystal is used to double the pulse energy by halving the wavelength to 527 nm output. The output mirror is selected to be 100% reflective for the fundamental wavelength (1053 nm) and partially transmitting at the 2nd-harmonic (527 nm), so as to output only the higher energy photons.

Seed Laser

The Mai-Tai seed laser is comprised of a continuous wave (CW) pumping chamber followed by a pulsed conversion chamber. The first chamber features a diode-pumped, intra-cavity, frequency-doubled, solid-state Nd:YVO$_4$ 523 nm laser. The second chamber is a mode-locked (Titanium) Ti:Sapphire cavity.

The pumping chamber uses a diode laser to pump Neodymium (Nd^{3+}) ions doped in an Yttrium Vanadate (YVO$_4$) gain crystal. At normal operating temperature, the most likely emission is at 1064 nm, which is then selected with optics. This wavelength is then converted to visible light by interaction with a non-linear frequency-doubling LBO crystal, which is temperature regulated. The output power of this 2nd-harmonic ($P_{2\omega}$) is given by the following:

$$P_{2\omega} \propto \left(d_{eff}^2 P_\omega^2 l^2 [\Phi]\right) / A \tag{5.1}$$

Equation 5.1 contains d_{eff} the effective nonlinear coefficient, P_ω the power of the fundamental input frequency, l the effective length of the SHG medium, [ϕ] a phase-matching factor and A representing the cross-sectional area presented by the beam. As the output power depends on the square of the input power, this is maximised here by positioning the SHG inside the laser cavity. The pump chamber outputs a green 532 nm beam and achieves high power stability through the superposition of many longitudinal laser modes averaging out the effect of 'beating'.

The second (pulsing) chamber is a long cavity using an active acousto-optic modulator (AOM) to mode-lock the laser beam and amplify it with a Ti:Sapphire gain medium. This process shares some small similarities with Q-switching, both involving the interference of an acoustic wave with an optically transparent medium. A standing wave is produced in the AOM resulting in a time varying refractive index grating perpendicular to the beam propagation. A fixed phase relationship is produced between the propagating laser modes by synchronising the frequency of this acoustic wave, ω_{mL}, with the frequency of the laser repetition rate c/2L, where L is the cavity length. It can then be seen that light which is initially in phase with ω_{mL} will continue to be in phase as it round trips the cavity and is progressively amplified, while out of phase light will be deflected. This produces a time varying loss building modulation sidebands which progressively lock subsequent longitudinal modes in phase with one another. Once in phase these modes, periodically, constructively interfere producing a rapid pulse whose duration is dependent on the bandwidth of locked modes and can produce pulses with rise time and falloff on the order of femtoseconds.

Regenerative Amplifier

The Spitfire system employs a state-of-the-art ‘chirped pulse amplification’ (CPA) technique, pioneered by Mourour & Strickland (1985) **[9]** to circumvent the maximum energy limitations in solid-state amplifiers due to the optical damage threshold (for Ti:Sapphire this is <10 GW/cm^2). As shown in **figure 5.6**, the seed pulse is temporally stretched prior to entering the amplifying cavity, reducing its peak power. This is achieved by multiple passes through a pair of optical gratings such that the pulse experiences a frequency-dependent path length gradient, drawing its duration out by a factor of 10^3 or more. This is known as group velocity dispersion (GVD) or chirp.

The Ti:Sapphire amplifier crystal is excited to population inversion by the pump laser pulse allowing the stretched seed laser pulse to initiate stimulated emission, amplifying its energy without changing its wavelength profile. A seed pulse is selectively retained within the amplifier with a pair of Pockels cells, electro-optical ‘voltage-controlled waveplates’, reducing the repetition rate of the output by a factor of 10^3 to concentrate the energy per pulse. Under an appropriately applied voltage these Pockels cells rotate the beam polarization by precisely 90° per pass, and otherwise allow the beam to pass unaffected.

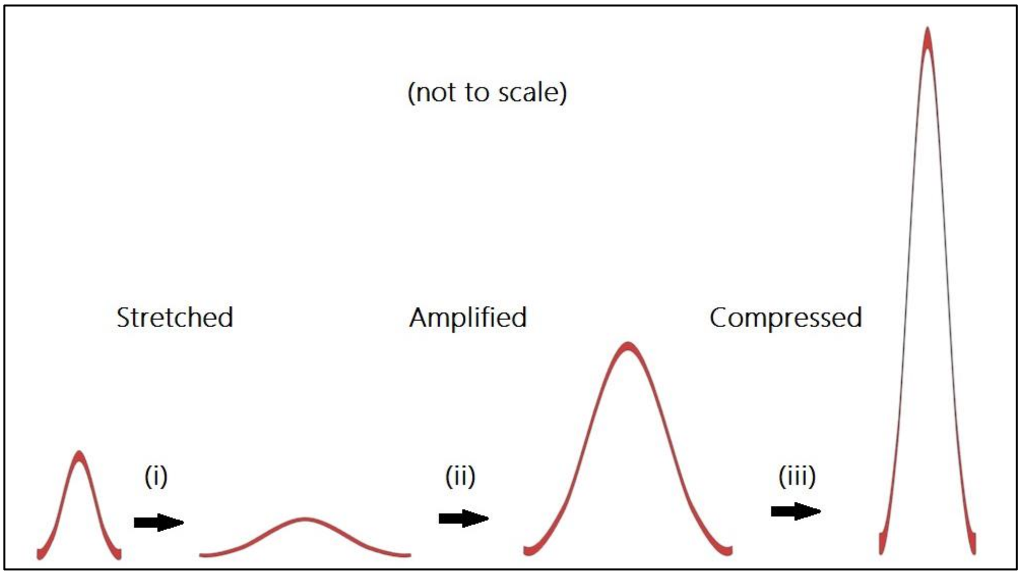

Figure 5.6: The seed pulse is stretched, reducing its peak power, before amplification and then recompressed to form a short, high power pulse. This allows greater amplification circumventing the power damage threshold of the amplifier.

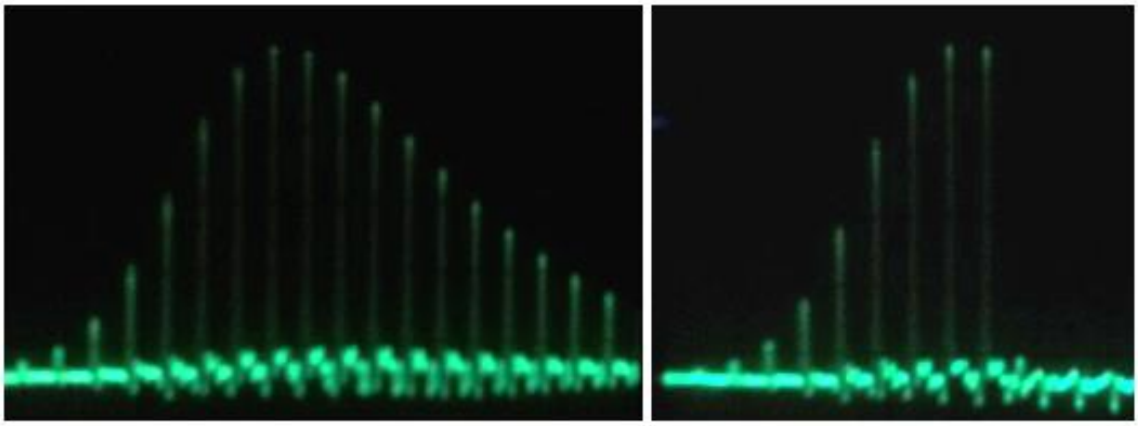

Figure 5.7: Amplifier regeneration profile observed on oscilloscope. Just the input Pockels cell activated (left) and the output Pockels additionally activated (right). This shows an example of a well-tuned regeneration, points of note: low background interference, sharp build-up, output timing set to output high pulse power.

In the Spitfire system, these devices are controlled by a Synchronisation and Delay Generator (SDG II) controller, which is synchronised to an output square wave from the MaiTai and only active when the seed is reliably mode-locking. The first cell is timed to capture a single seed pulse which can pass 20 or more times through the cavity before saturating the gain medium, the second cell is timed to eject this pulse as after that saturating pass. This was tuned by observing a photodiode within the amplifier and adjusting the relative timing so that the last visible pulse was the highest energy as demonstrated in **figure 5.7**.

Maintenance

Careful maintenance of this system is crucial for maximising the signal-to-noise ratio of any measurements and can save hours on each measurement. As demonstrated in **figure 5.8**, below, the stability of the output energy can be affected significantly if the laser is not operating correctly. This has particularly been attributed to the seed laser stability.

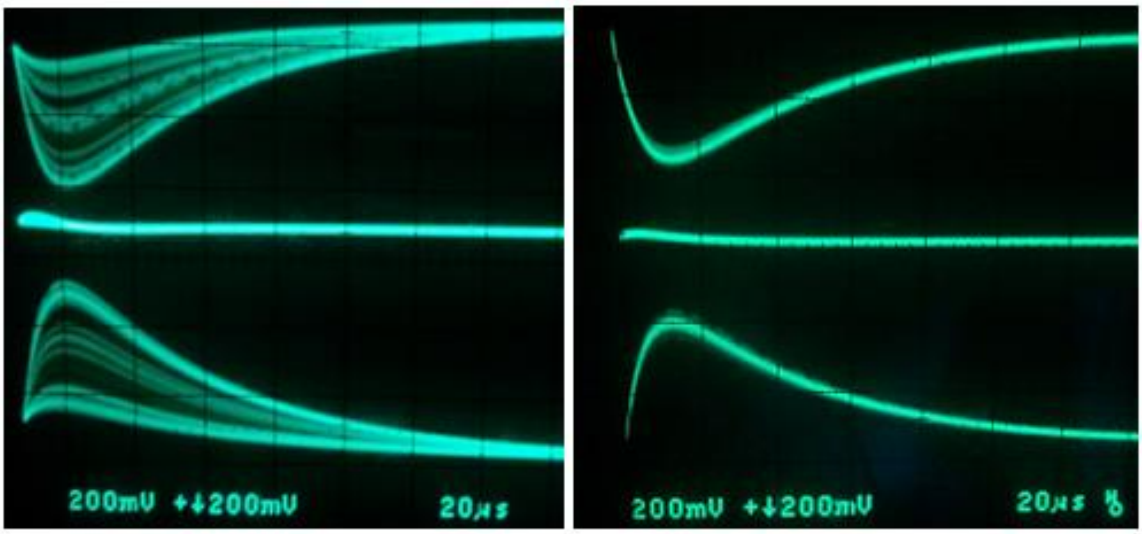

Figure 5.8: Example of effect of laser stability noise on the detector output shown on oscilloscope for an unstable situation (left) and after optimizing (right). Showing signal from detector 1 (top trace), inverted signal from detector 2 (bottom trace) and the optimized difference between the channels (middle trace).

While the MaiTai is a closed system designed to inhibit dust ingress its mode-locking capability still degrades with time, and this can be temporarily offset by manually increasing the output power. This is a method of diminishing returns however and eventually thorough cleaning of key mirrors and windows is necessary.

5.3.3 Optics Design Process

The experimental set-up went through a number of iterations during the course of this project, investigating the pros and cons of various configurations. While some of this will be detailed here, this section will focus on the ultimate design, detailed in **figure 5.9**. When setting up the pump-probe instrument, the major points to bear in mind were as follows:

- The pump beam path length is varied relative to the probe by way of a delay line of 300 mm (2 ns round trip).

- The pump and probe beam paths are equalized to towards the start of the delay line - to maximize the post overlap time.

- The delay line is well aligned to minimize any spatial overlap drift between the beam spots on the sample.

- The beam spots are overlapped with the aid of a webcam and lens system.

- The reflected probe is directed into the detector and any other light is rejected.

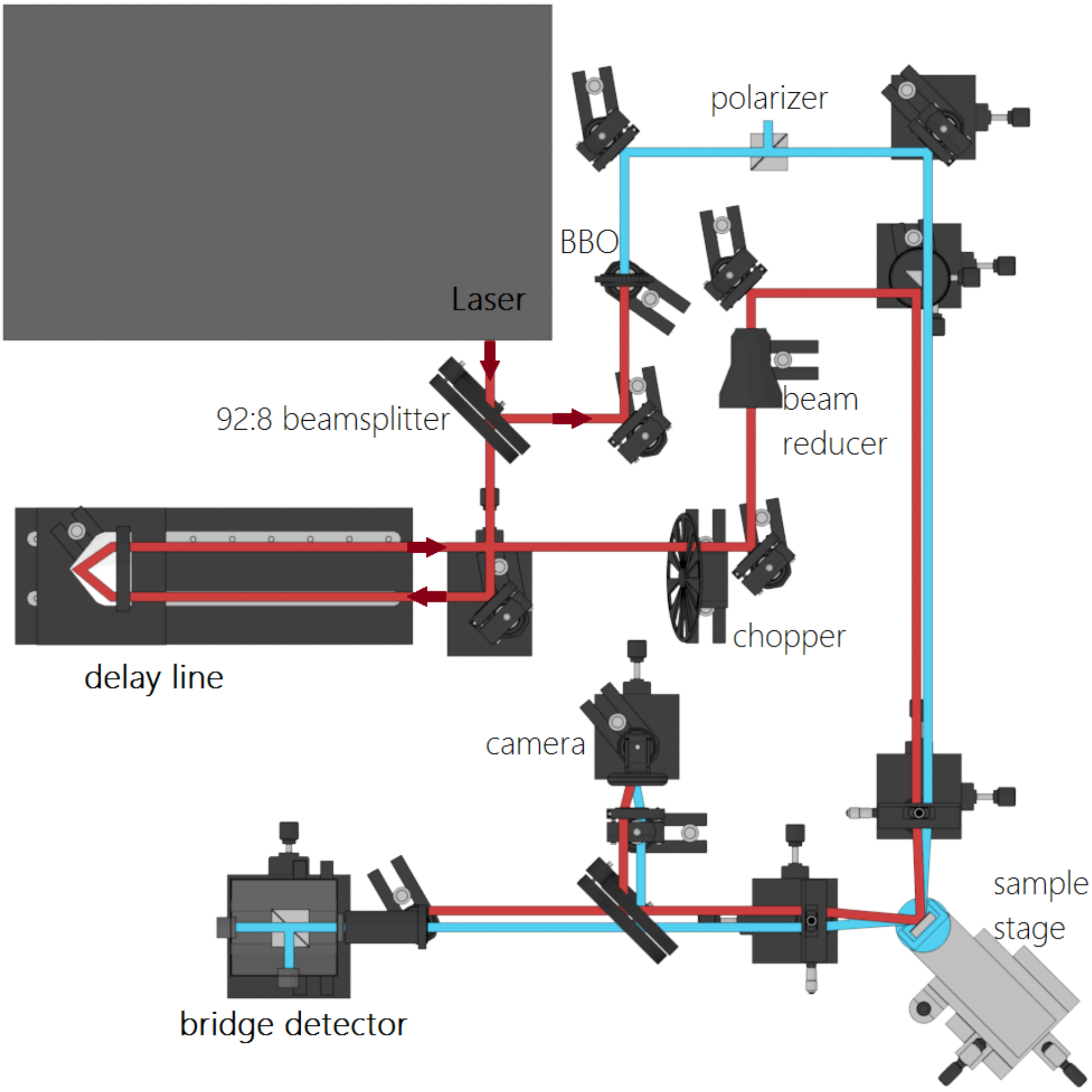

Figure 5.9: Schematic of the ultimate experimental set-up used in this investigation. The laser output is split into transmitted pump (92%) and reflected probe (8%) by a beam-splitter. The pump beam (red) passes through a delay line, optical chopper and beam reducer before being focused onto the sample. The probe (blue) passes through a BBO wavelength doubling crystal and a polarizer before being focused onto the sample.

Delay Line

The femtosecond laser was first attenuated to 120 mW and split 92:8 to produce pump and probe beams. The pump path was then aligned down one side of the delay line with an x-translation stage, a rotatable mirror and a pinhole (see **figure 5.10**).

This was a very effective method for making sure that the beam was aligned with the translation path of the delay line in both horizontal and vertical axes independently. The delay line was a stepper motor driven screw-thread based translation stage with a full travel of 300 mm and a step resolution of 2.5 μm corresponding to 16.7 fs.

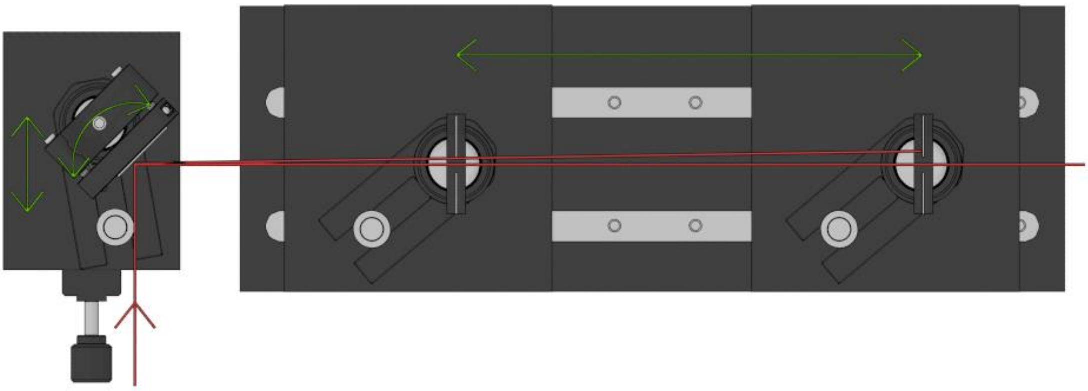

Figure 5.10: Alignment of the delay line. A pinhole is mounted on the delay line during alignment to measure the relative deviation in the beam. A one axis translation stage and rotation mount are used to adjust the beam entering the delay line to minimize this deviation.

The beam was then redirected back along the delay line, parallel to the incoming beam. Originally this was achieved with a pair of mirrors set at right angles to each other, using a similar method of shifting a pinhole and adjusting the mirror tilt to minimize any deviation. It became clear however later that this alignment left the system very sensitive to minor unevenness in the delay line itself, making it impractical when exaggerated through the rest of the system. The effect of this is demonstrated in **figure 5.11** below, which shows a frame by frame observation of the pump spot position on the sample surface as the delay line travels from start to end. Linear drift in the spot position can be corrected for, but a non-linear drift was observed. The alternative was to use a trihedral 'retroreflector' prism (corner cube) which employs total internal reflection to return the beam, parallel to the incident, to within 14 μrad. This effectively removed any drift caused by delay line unevenness. With a retroreflector the trajectory of the reflected beam is shifted unless it is directed at the centre of the prism. This can be dealt with independently for the vertical and horizontal axes and in fact this is a useful property for the horizontal axis, but had to be carefully corrected for in the vertical axis.

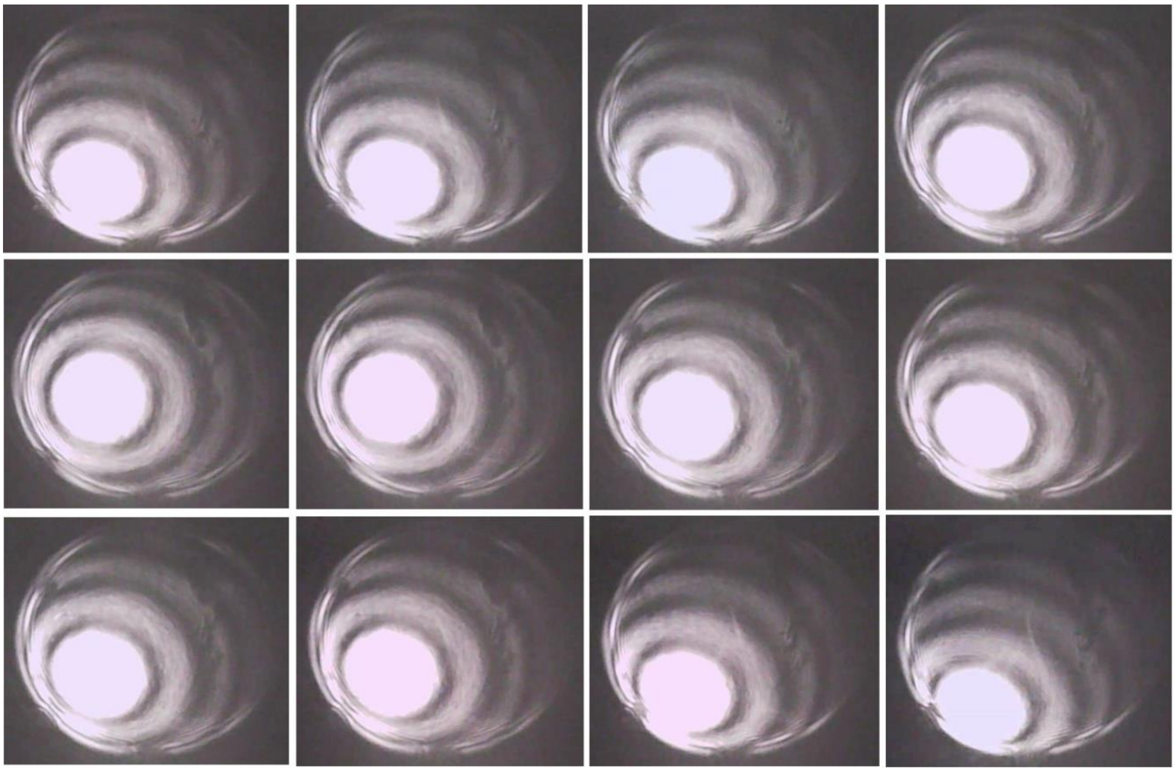

Figure 5.11: Frame-by-frame camera capture of the pump beam spot on the sample during a delay line movement using two mirrors. Shows a non-linear drift as the delay line is moved from one end to the other. This is caused by sub-micron unevenness in the delay line tilting the mirrors.

Beam Overlap

It was critical that the beams should be spatially overlapped on the sample, a non-trivial matter due to the small margin of error (<1 μm). Initially, the experiment was set up with a separate lens for the pump beam set normal to the sample surface. A CCD camera placed in the pump path was unable to detect the probe beam spot, and when placed in the probe path the true position of the pump beam spot was obscured. This was discovered by increasing the pump fluence to the point of burning the sample, which left a mark consistently a few microns to the left of the apparent position. This resulted in a setup redesign to bring the incident pump beam collinear with the probe beam which provided a much more consistent overlap for the price of a slightly more complicated alignment.

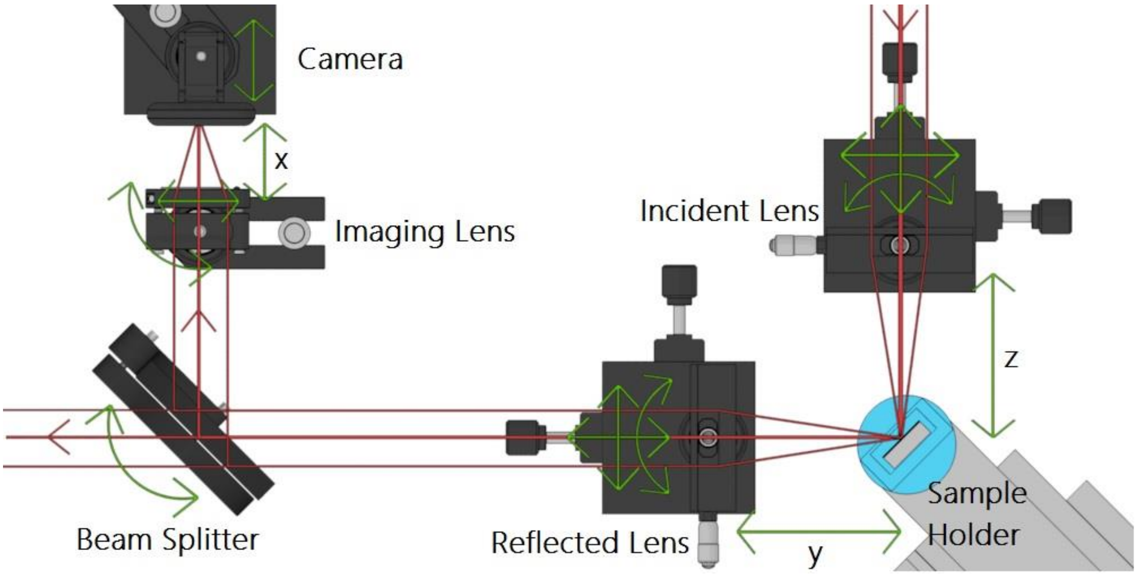

Figure 5.12: Schematic of alignment of the three interdependent lenses required to focus the laser and then obtain a true image of the sample surface.

In order to see a representative image of the sample surface to make these judgements, three interdependent lenses had to be carefully aligned. These are referred to as incident lens, reflected lens and the imaging lens (see **figure 5.12**). For a relatively high fluence, considering spatial limitations caused by the electromagnet, an incident lens focal length of 150 mm was used. This was then matched by the reflected lens to re-collimate the reflected beam. The imaging lens focal length was chosen to be double that of the reflected, for a practical magnification of image. In order to produce a true image, these lenses were added in reverse order, as each preceding lens affects the beam focus. Critically, all three lenses were achromatic doublets so that the focal length was wavelength independent. These lenses also benefit (over singlet lenses) from minimized spherical aberration and greater insensitivity to incident beam angle.

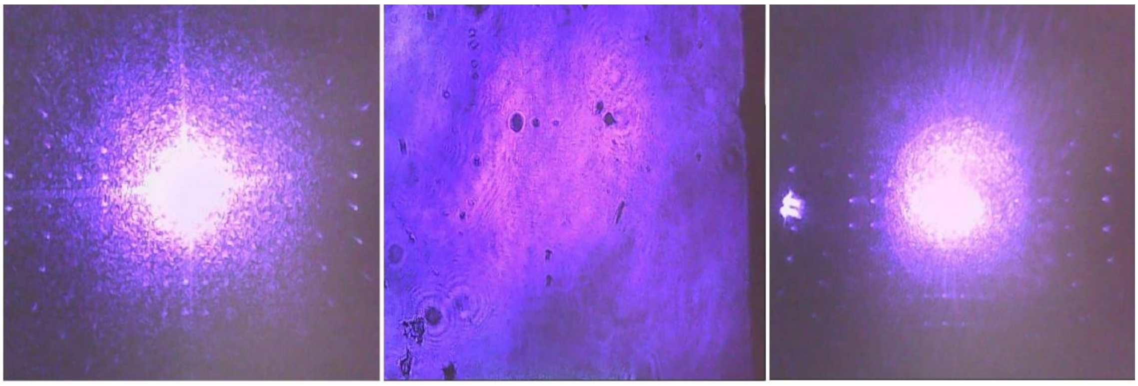

Figure 5.13: Camera images of alignment of the three interdependent lenses required to observe the sample surface clearly. The image lens is added and moved to focus (left); the reflected lens is added and moved until a wide-field image of the sample surface is in focus (middle); the incident lens is added and moved until the beam focus is observed again. This is done for both pump and probe together and overlapped (right).

1. The pump and probe beams were aligned parallel, to within 2 mm over 6 m (0.3 mrad).

2. With no lenses inserted, the two laser beams were directed at 45° onto the sample surface and reflected off towards the detector (which was positioned based on this beam line).

3. 8% of the beam was split off at 90° and onto the camera CCD active area, centred with the live image feed - at this point, the image was of the illuminated sample surface.

4. The imaging lens was inserted and aligned so that distance x is the image lens focal length - the image became beam spots and focus was found by tuning until diffraction spots were observable from both pump and probe beams (see **figure 5.13**).

5. After next inserting the reflected lens, its position was adjusted until distance y was equal to its focal length whereupon the image once again becomes that of the illuminated sample surface.

6. Finally the incident lens was inserted and positioned so that z equalled its focal length - the image is now again of the pump and probe spots and any deviation in their paths could be observed and corrected for.

At this point a true image of the position and focus of the beam spots was observable and fine alignment of the delay line and overlap was possible.

Beam conditioning

As the pump beam was many times more intense than the probe, it was necessary to selectively inhibit it from the detector, which was achieved by wavelength doubling the probe beam after the beam splitter. A barium borate (BBO) crystal, which has a strong negative uniaxial birefringence, was used as an SHG to drop the wavelength of the pump beam from 800 nm to 400 nm. A 400 nm narrowband filter was placed after the BBO crystal and directly before the detector, so that all probe energy was at 400 (±2) nm and no other light source contributed to a measurement. In addition a beam block was inserted to catch the reflected pump beam prior to the detector filter. By intermittently manually blocking the incident probe beam, it was possible to observe the background intensity picked up by the detector to ensure no pump was being detected.

Considering the collimated laser beam geometrically, an approximate laser beam spot radius after focusing, r_2 can be related to the initial beam radius r_1, its divergence θ_{d1} (in radians) and the focal length, f of the focal lens **[10]**. This is shown schematically in **figure 5.14** and **equation 5.2**.

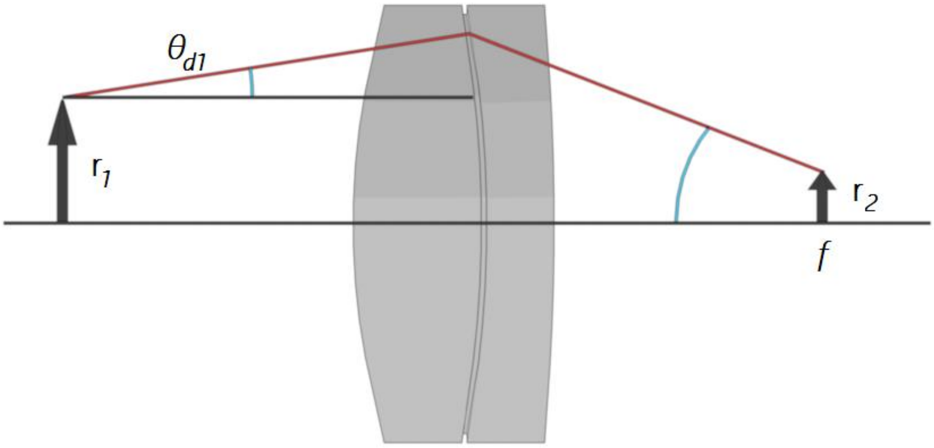

Figure 5.14: Ray diagram of geometry for approximating beam focus diameter based on lens focal length, f, and incoming beam divergence, θ_{d1} from a collimated beam.

$$\mathbf{r_2 = f\theta_{d1}} \tag{5.2}$$

By setting the focal length as a constant for both pump and probe beams, the relative radii of the beam spots was altered by increasing the divergence of the pump beam. This was achieved using a 5x beam reducer placed in the pump beamline, which has a directly proportional effect on the resultant beam divergence via the following relationship from a collimated state **(equation 5.3)** and shown schematically in **figure 5.15**.

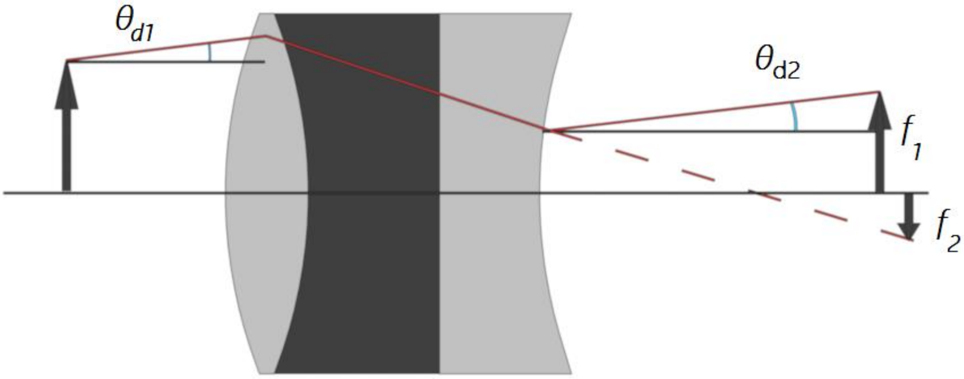

Figure 5.15: Ray diagram of geometry for calculating change in beam radius and divergence from a collimated beam.

$$\theta_{d2} = \theta_{d1}\ f_2/|-f_1| \tag{5.3}$$

Beam power was then converted to fluence (**equation 5.4**) for a more physically meaningful measure of the energy associated with the pump beam. This is provided by the following straightforward relationship, and is quoted here in μJ/cm^2.

$$\text{Fluence} = \text{Laser pulse energy} / \text{Effective focal spot area} \tag{5.4}$$

5.3.4 Signal Capture & Electronic Considerations

As the signal strength is very low in TRMOKE experiments of this type (especially in the longitudinal configuration), maximizing the signal-to-noise ratio (SNR) is very important. This was achieved by a combination of techniques detailed here.

All coaxial cables used to transfer data were double shielded to minimize electrical interference and a two detector bridge configuration was used to eliminate thermal signal drift. Before each measurement, the signal from the detectors was first routed through a fast response (1 MHz) digital oscilloscope to evaluate the signal. At this point, the Pockels cells timings, probe intensity, background light leakage, detector balance and temporal overlap were checked.

The signal is then passed through a lock-in amplifier which allows the detection of a real signal buried within noise, which may be of the same magnitude or even larger **[11]**. In order to achieve this, an optical beam chopper is placed in the pump path to provide an external reference frequency of a few hundred hertz on top of the experiment's driving force. This is necessary as the repetition rate of the laser is too high to be used. The lock-in amplifier then employs a technique known as phase-sensitive detection (PSD) to selectively respond only to the signal which occurs at that reference frequency with a fixed phase relationship. This acts like a very narrow bandpass filter centred on the external reference frequency. The lock-in produces its own internal reference signal (**equation 5.5**), with an amplitude V_L, frequency ω_L and locked to Θ_{ref} the phase of the external reference. The input signal (**equation 5.6**) is amplified and multiplied by the reference frequency to produce two AC signals (**equation 5.7**), one at the difference frequency ($\omega_{\mathrm{sig}} - \omega_{\mathrm{L}}$), and one at the sum ($\omega_{\mathrm{sig}} + \omega_{\mathrm{L}}$). The highly desirable DC signal, V_{DC}, is then extracted using a low pass filter to form the lock-in output (**equation 5.8**), proportional to the amplitude of the input signal.

$$\text{Internal reference signal} = \mathrm{V_L}\sin(\omega_{\mathrm{L}}\mathrm{t} + \Theta_{\mathrm{ref}}) \tag{5.5}$$

$$\text{Input signal} = \mathrm{V_{sig}}\sin\left(\omega_{\mathrm{sig}}\mathrm{t} + \Theta_{\mathrm{sig}}\right) \tag{5.6}$$

$$\begin{aligned} \mathrm{V_{AC}} = {} & \tfrac{1}{2}\mathrm{V_{sig}}\mathrm{V_L}\cos\left[(\omega_{\mathrm{sig}} - \omega_{\mathrm{L}})\mathrm{t} + \Theta_{\mathrm{sig}} - \Theta_{\mathrm{ref}}\right] \\ & -\tfrac{1}{2}\mathrm{V_{sig}}\mathrm{V_L}\cos\left[(\omega_{\mathrm{sig}} + \omega_{\mathrm{L}})\mathrm{t} + \Theta_{\mathrm{sig}} + \Theta_{\mathrm{ref}}\right] \end{aligned} \tag{5.7}$$

$$\mathrm{V_{DC}} = \tfrac{1}{2}\mathrm{V_{sig}}\mathrm{V_L}\cos\left(\Theta_{\mathrm{sig}} - \Theta_{\mathrm{ref}}\right) \tag{5.8}$$

With the delay line set to a point after the pump-probe temporal overlap, it is possible to observe the signal quality directly from the lock-in. The low pass filter was chosen to have a time constant (TC) no longer than necessary, which was judged, by preliminary measurements, to be in the region of 2 seconds as an acceptable compromise of speed and accuracy. This was dependent on the stability of the laser and quality of alignment. This filter then essentially averaged the response from 20,000 pump events to form the output. Finally the lock-in gain was increased until the signal filled approximately 40% of the dynamic range (~20-100 dB) which left sufficient room for larger signals.

From this point, the signal was passed via a high performance Data Acquisition NI-DAQ card to LabVIEW software to be recorded. Further SNR improvements were necessary by averaging the result of a large number of demagnetization events. In order to achieve an acceptable signal-to-noise ratio (>20) it was necessary to average each time delay point for at least 30 seconds, in addition to allowing a 4 ×TC settling time (8 seconds) after any change of the delay line to avoid blurring of the signal. Optimizing the SNR could save hours on a complete measurement which generally consisted of >300 data points.

5.3.5 Design of Software

LabVIEW software was created to run the TRMOKE experiments. This programme was designed to be modular and was improved and added to regularly by the author over the course of the project. The programme was built using a state machine structure. As the magneto-dynamics occur over a number of vastly different timescales throughout the experiment, the programme was constructed with a settings menu (**figure 5.17**) which allowed the delay line time array to be set to five different step sizes, and could be set by mm or ps. An electromagnet set-up was added to allow for dynamic hysteresis loops and multiple runs over a series of external field strength to be produced.

In order to standardize the measurement documentation, a set of experimental protocols were produced, requiring the user to go through a check-list of parameters prior to initializing an experiment (**figure 5.19**). This improved record keeping between group members and ensured a comprehensive list of parameters exist for each experiment.

This was particularly important for the lock-in parameters as this information repeatedly became relevant weeks or more after a measurement had been taken. Software settings were automatically imported into the parameter save file and save file and folder names were generated procedurally to maintain a consistent recording style.

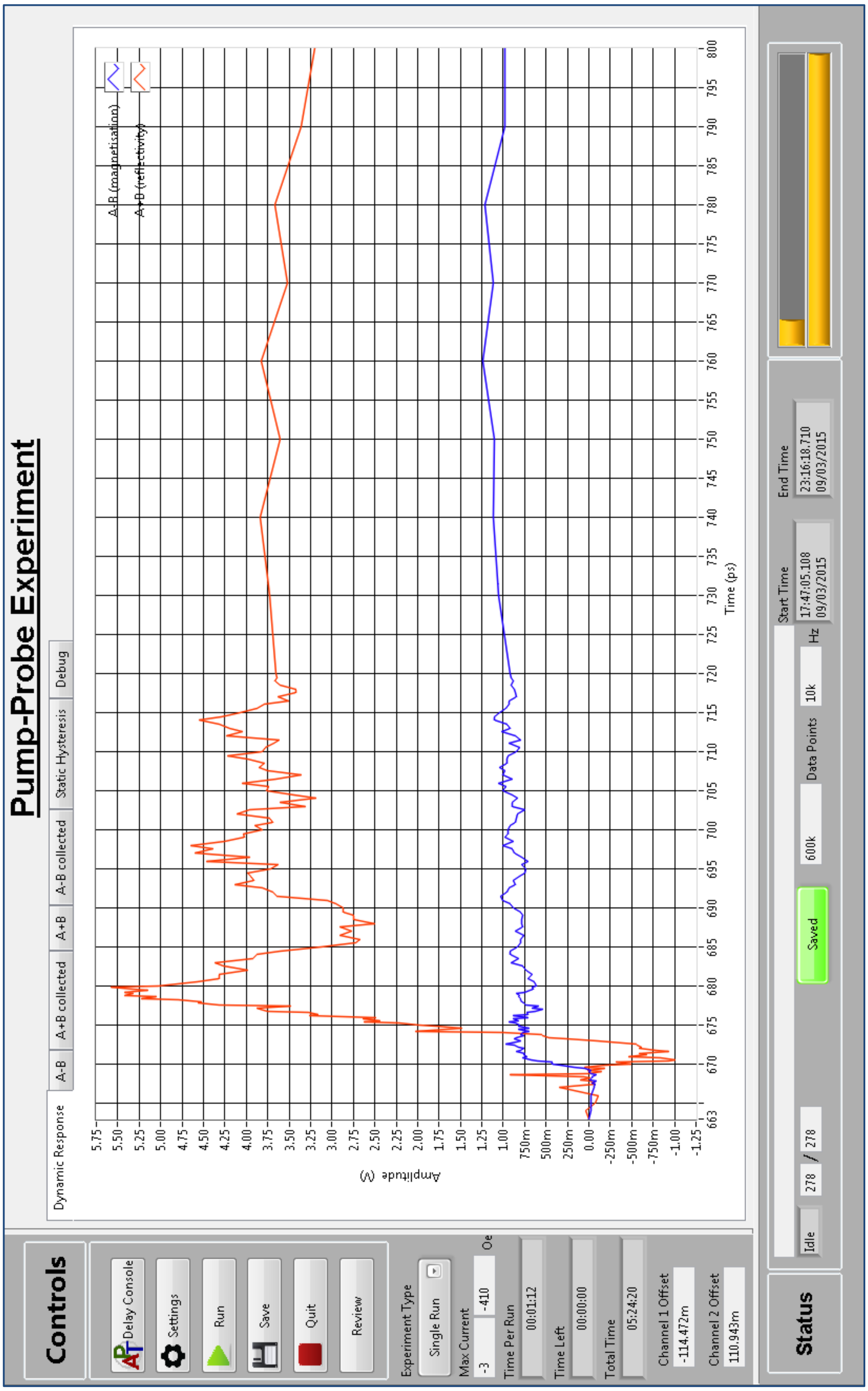

Experiment Type: Single Run

Max Current: -3 -410 Oe

Time Per Run: 00:01:12

Time Left: 00:00:00

Total Time: 05:24:20

Channel 1 Offset: -114.472m

Channel 2 Offset: 110.943m

Idle 278 / 278

Saved

600k

Data Points 10k Hz

Start Time 17:47:05.108 09/03/2015

End Time 23:16:18.710 09/03/2015

Figure 5.16: LabVIEW software front panel, designed to show a number of useful values such as the applied field strength and runtime information.

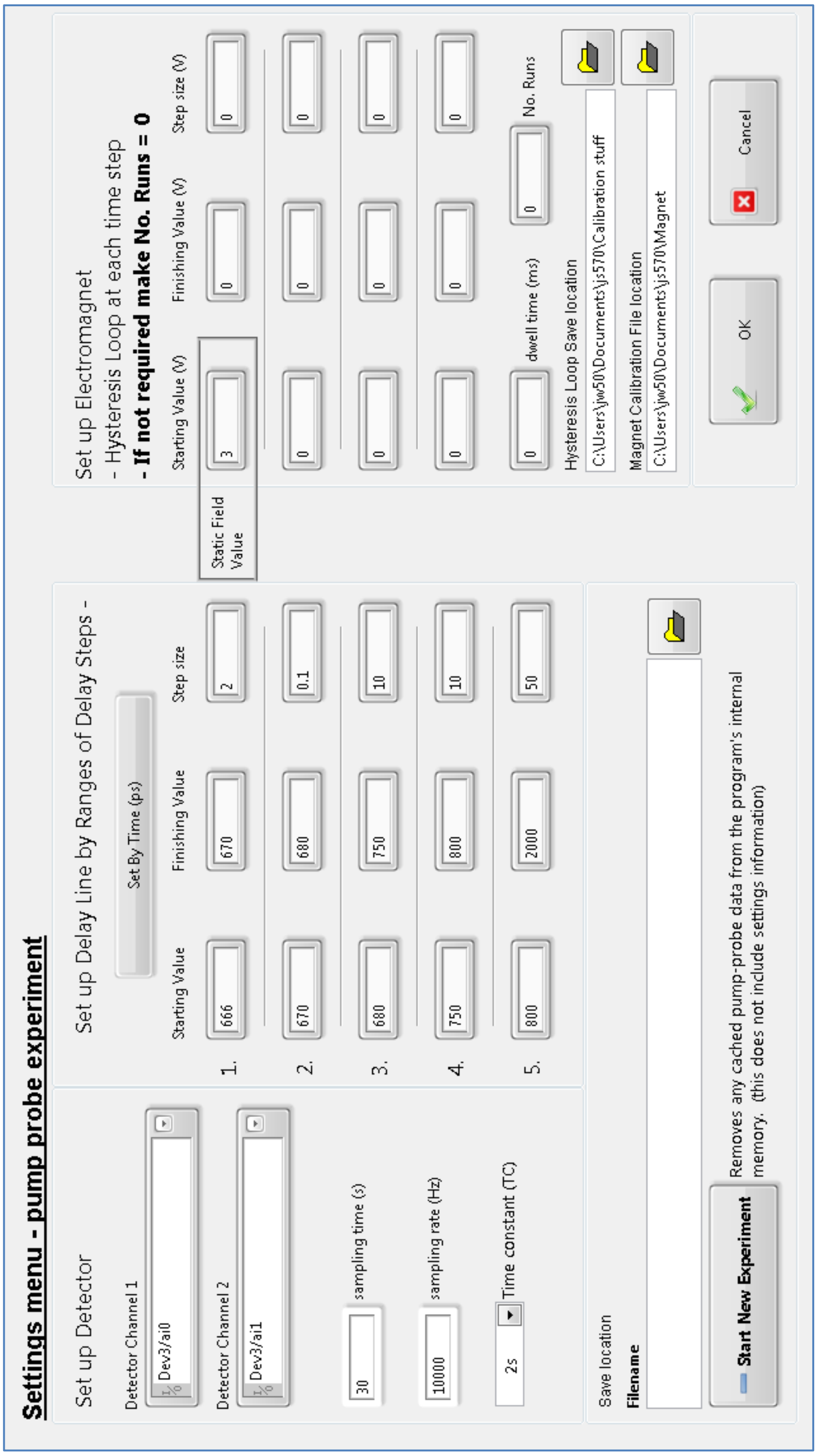

Settings menu - pump probe experiment

Set up Detector

Detector Channel 1: Dev3/ai0

Detector Channel 2: Dev3/ai1

sampling time (s): 30

sampling rate (Hz): 10000

Time constant (TC): 2s

Set up Delay Line by Ranges of Delay Steps -

Set By Time (ps)

	Starting Value	Finishing Value	Step size
1.	666	670	2
2.	670	680	0.1
3.	680	750	10
4.	750	800	10
5.	800	2000	50

Set up Electromagnet
- Hysteresis Loop at each time step
- **If not required make No. Runs = 0**

	Starting Value (V)	Finishing Value (V)	Step size (V)
Static Field Value	3	0	0
	0	0	0
	0	0	0
	0	0	0

dwell time (ms): 0

No. Runs: 0

Hysteresis Loop Save location: C:\Users\jw50\Documents\js570\Calibration stuff

Magnet Calibration File location: C:\Users\jw50\Documents\js570\Magnet

Save location

Filename

Removes any cached pump-probe data from the program's internal memory. (this does not include settings information)

Figure 5.17: LabVIEW software settings menu, designed to allow a large amount of control over the experimental settings. Delay line steps are set up here in ranges to allow the time sensitivity to be varied based on the scale of dynamics in each range (middle). A field sweep can also, optionally, be set-up for at each delay step (right).

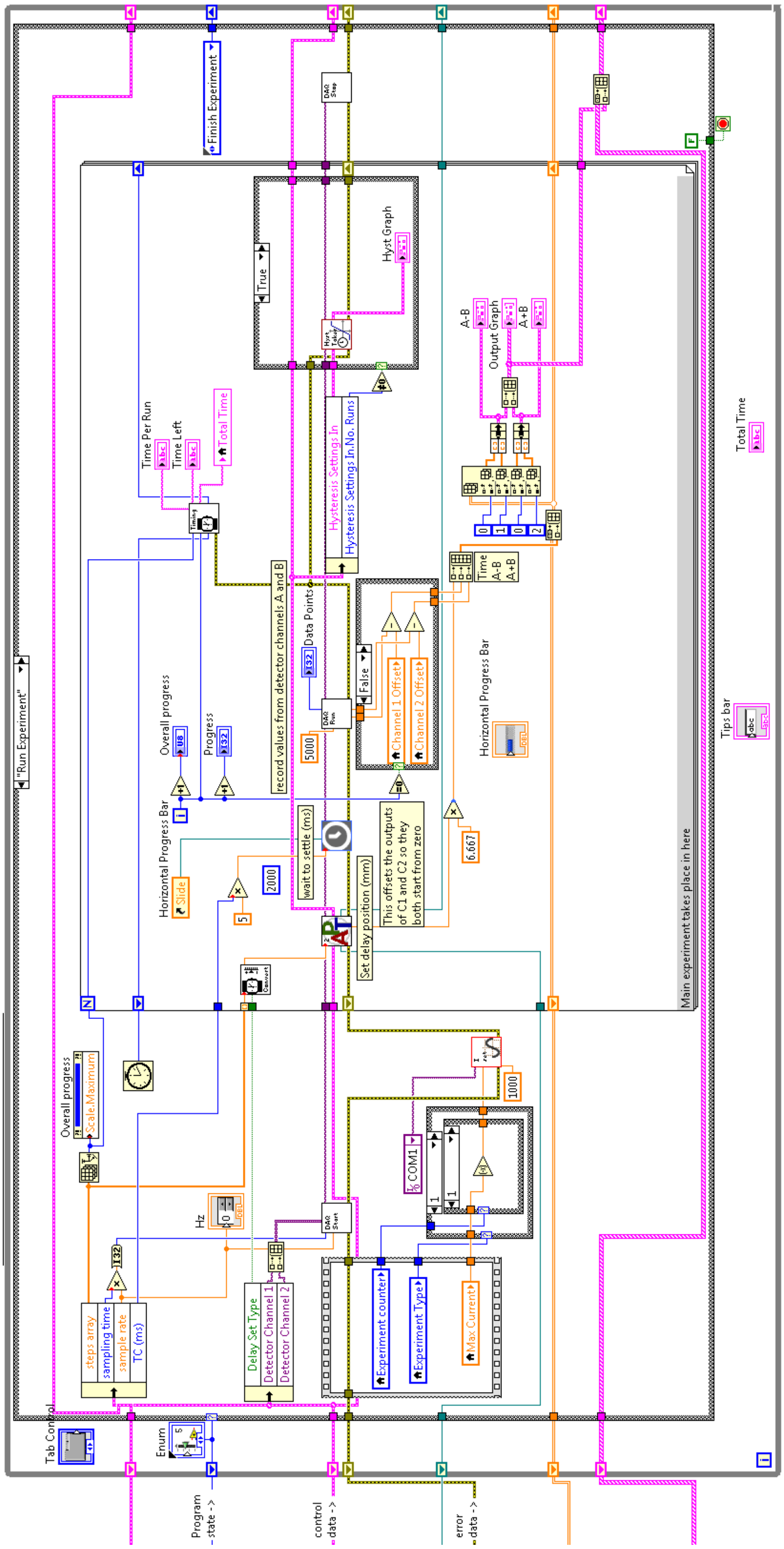

Figure 5.18: Image showing LabVIEW main experiment ‘For loop’.

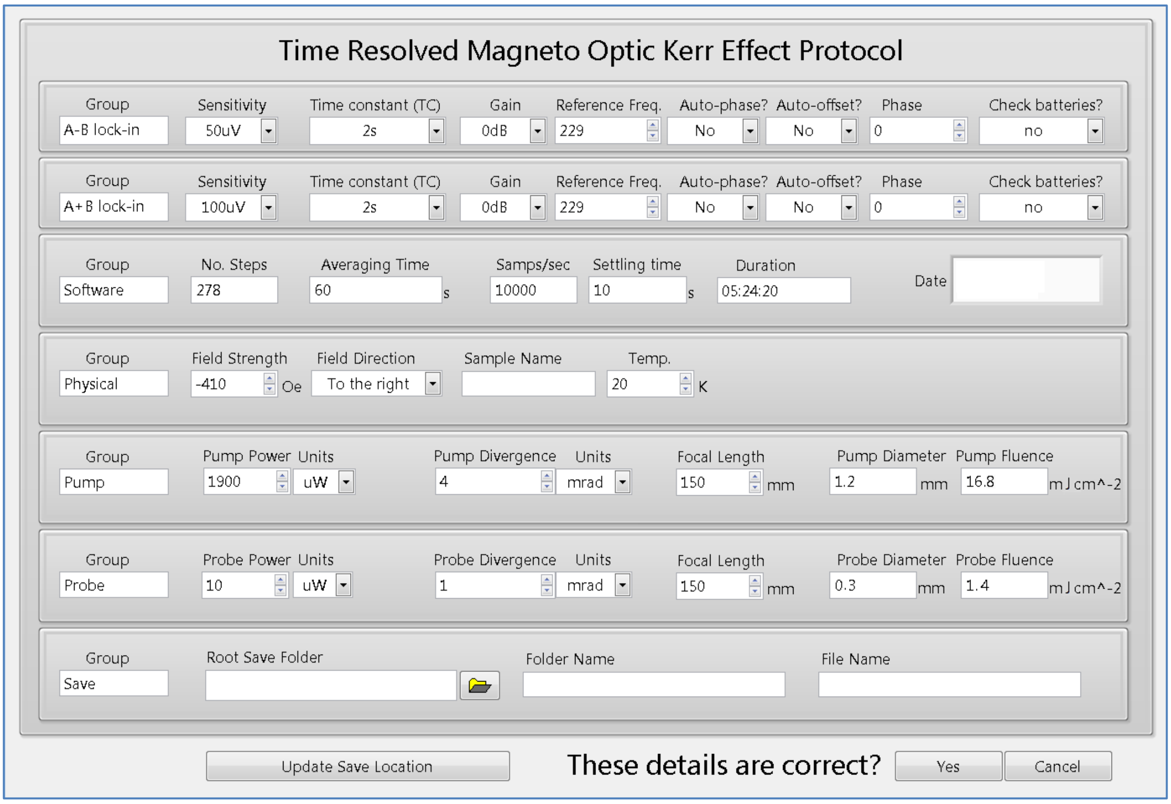

Time Resolved Magneto Optic Kerr Effect Protocol

Group	Sensitivity	Time constant (TC)	Gain	Reference Freq.	Auto-phase?	Auto-offset?	Phase	Check batteries?
A-B lock-in	50uV	2s	0dB	229	No	No	0	no

Group	Sensitivity	Time constant (TC)	Gain	Reference Freq.	Auto-phase?	Auto-offset?	Phase	Check batteries?
A+B lock-in	100uV	2s	0dB	229	No	No	0	no

Group	No. Steps	Averaging Time	Samps/sec	Settling time	Duration	Date
Software	278	60 s	10000	10 s	05:24:20	

Group	Field Strength	Field Direction	Sample Name	Temp.
Physical	-410 Oe	To the right		20 K

Group	Pump Power	Units	Pump Divergence	Units	Focal Length	Pump Diameter	Pump Fluence
Pump	1900	uW	4	mrad	150 mm	1.2 mm	16.8 mJ cm^-2

Group	Probe Power	Units	Probe Divergence	Units	Focal Length	Probe Diameter	Probe Fluence
Probe	10	uW	1	mrad	150 mm	0.3 mm	1.4 mJ cm^-2

Group	Root Save Folder	Folder Name	File Name
Save			

These details are correct?

Figure 5.19: LabVIEW software pre-run information. Each run is saved with a data sheet containing the useful experimental information and save filenames and folders are then procedurally generated.

5.4 References

[1] P. N. Argyres, Phys. Rev., **97**, 334 (1955)

[2] J. Stöhr, H. C. Siegmann, Magnetism, (Solid-State Sciences Springer Verlag, Berlin, 2006)

[3] C. Bunce, Magnetization Dynamics in Thin-films, (Ph.D Thesis, University of York, 2008)

[4] Collections of University of Pennsylvania Archives

[5] D. D. Awschalom, et al., Phys. Rev. Lett., **55**, 1128 (1985)

[6] Spectra-Physics Evolution-30 (User Manual, 2003)

[7] Spectra-Physics Mai Tai (User's Manual, 2002)

[8] Spectra-Physics Spitfire (User's Manual, 2004)

[9] D. Strickland and G. Mourou, Optics Comm. **56**, 219 (1985)

[10] M. Born and E. Wolf, Principles of Optics: Electromagnetic Theory of Propagation, Interference and Diffraction of Light (Pergamon Press, 1959)

[11] About Lock-In Amplifiers (Stanford Research Systems)
http://www.thinksrs.com/downloads/PDFs/ApplicationNotes/AboutLIAs.pdf

Chapter 6

Materials Study of Post-Oxidized Magnetite Thin-Films

6.1 Introduction

Half-metals have been cited as a valuable asset to the field of spintronics for a number of years, due to the potential improvements to spin transport densities afforded by 100% spin polarization within the conduction band. Magnetite (Fe_3O_4) in particular is considered a promising material for room temperature device function because of its high Curie temperature (~848 K) **[1]** and relatively low coercivity. It is a cheap, commonly available ferrimagnet which forms an inverse spinel structure with a high lattice matchup to other oxide formations, such as the insulator magnesium oxide (MgO) appropriate for producing a tunnelling barrier. The roadblock to large-scale adoption falls with the difficulty of producing and controlling the properties of high quality thin-films, especially the density and type of anti-domain phase boundary (APB) defects.

This chapter will discuss growth of epitaxial single crystal magnetite thin-films on MgO (001) substrate, focusing on identification and characterisation after growth. The tiny mismatch of ~0.3%, between the relaxed lattice of the film and substrate, means MgO (001) is an excellent template on which to discuss magnetite growth relatively independently.

6.2 Experimental

All samples detailed were grown by initial molecular beam epitaxy (MBE) deposition of an iron film, on an MgO (001) substrate, via e-beam heating of an iron source at a base pressure of 10^{-9} mbar and the growth rate was fixed at 0.42 nm/min. This was followed by a period of in-situ exposure to atomic oxygen at an elevated temperature of 320 °C. A chamber pressure of 5×10^{-5} mbar was maintained for the duration of the oxidation. Samples were cooled to room temperature before removing from vacuum. This was the responsibility of Dr. Chris Kelley and Dr. Siew Wai Poon, with the assistance of Dr. Ben Murphy and the author.

An initial pair of samples was produced at contrasting oxidation times of 15 minutes and 60 minutes for initial iron film thicknesses of approximately 3 nm. A third was also grown, sharing the 15 minute oxidation time, but for an initial iron thickness of $\sim$20 nm. A further set of samples was then grown under the same growth conditions for thick (20 nm) iron films under a series of oxidation times of 9-45 mins. Magnetometry data was taken by vibrating sample magnetometry (VSM), a high-accuracy magnetometry technique which measures the net magnetic response of the entire sample, including substrate, by oscillating it within a variable magnetic field and measuring the response. Following this, electron transparent cross-section samples were prepared by mechanical grinding and argon ion milling. This was followed by plasma cleaning and optical baking to suppress contamination artefacts. High resolution transmission electron microscopy (HRTEM) analysis was undertaken using a JEOL FS-2200 aberration corrected electron microscope and a JEOL 2011 electron microscope.

6.3 Results

6.3.1 Initial Investigation

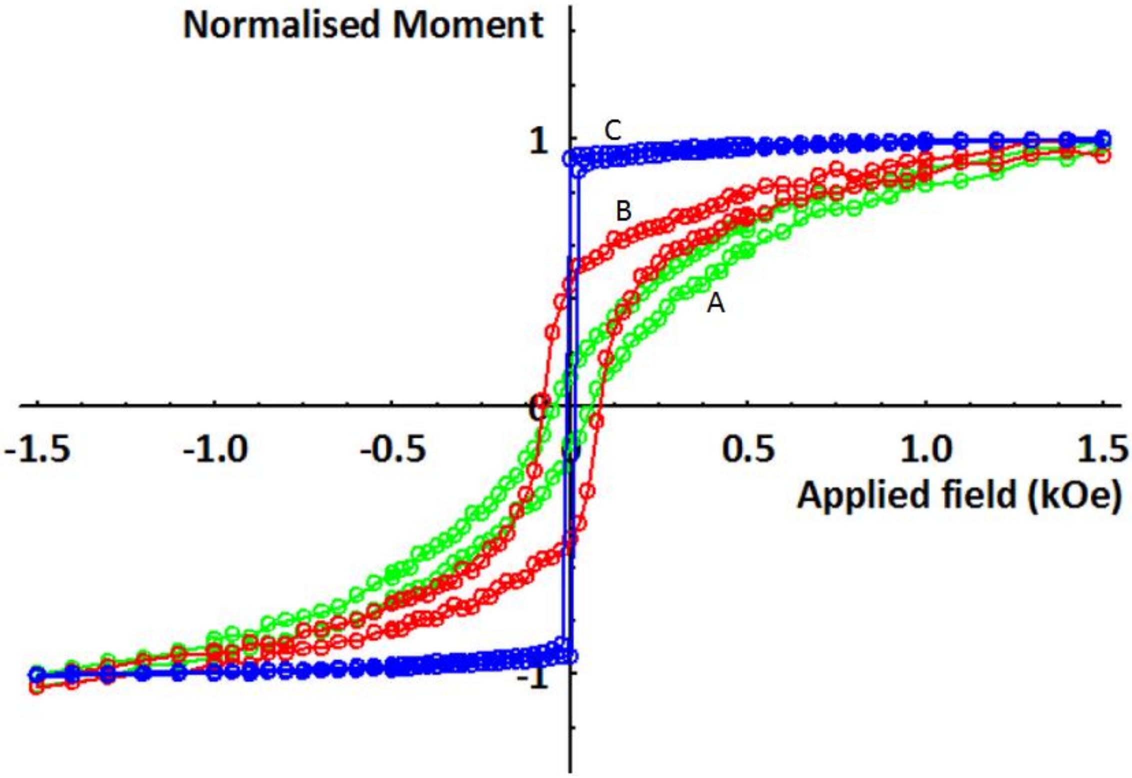

Figure 6.1: VSM measurements for three post-oxidized samples. Sample A (green) shows an over oxidized state; sample B (red) shows a more favourable square Fe_3O_4 response; sample C (blue) shows an iron dominated signal for a thicker film with a limited oxidation depth.

Other than a visual colour inspection, VSM magnetometry was the first characterization technique used on these samples, being the most straightforward and least invasive technique available. The data gives a quick indication of the film quality. In order to compare the magnetic character of these samples, they have been displayed normalized to unity in **figure 6.1** and a summary table has been provided in **figure 6.2**. The 20 nm sample C stands out next to the thinner films as being dominantly iron-like, with a very low coercivity of 13 Oe and a very high remanence to saturation ratio (M_R/M_S) of ~0.95. By contrast the other two samples have a much lower M_R/M_S of ~0.1 and ~0.5 for A and B respectively, corresponding to the higher and lower oxidation conditions. Along with a drop in remanence, the increased oxidation also results in a drop in coercivity of 34% from 79 Oe to 51 Oe. Sample B showed a relatively ordered magnetization reversal and sample A show a much more disordered reversal.

Absolute values of saturation magnetisation can be useful in characterizing a material when volume normalized. For samples A, B and C the measured saturations were respectively 0.00028 emu, 0.0003 emu and 0.002 emu. As each sample was measured from a 1 x 1 cm substrate wafer, the film volume can be approximated along with its thickness of approximately 6nm, 6nm, and 20nm. This provides estimated volume corrected saturations of 467 emu/cc, 500 emu/cc and 1010 emu/cc, respectively.

From literature **[2]**, an iron film is expected to show in the region of 1700 emu/cc, whereas for a magnetite film it should be close to 480 emu/cc. The inaccuracy comes in estimating precisely the volume of film present in the measurement, as is recognised by literature. It would however imply that an uncompensated iron contribution may still exist within the 15 min sample. Substrate effects have been removed from these samples, and represent a ~0.01% contribution. Expected value for coercivity for iron is around 4 Oe and between 30-100 Oe for magnetite. This data suggests an over-oxidation taking place, where the oxidized film from A to B is losing coherence and experiencing increased domain wall pinning.

Sample	Nominal Thickness (nm)	Oxidation Time (min)	Coercivity, H_C (Oe)	Absolute Magnetization M_S (emu/cc)	Normalized Remanence M_R/M_S
A	3	60	51	467	0.1
B	3	15	79	500	0.5
C	20	15	13	1010	0.9

Figure 6.2: Table showing growth and magnetometry information for thin over-oxidized sample A; thin less oxidized sample B; thick unoxidized layer-dominated sample C.

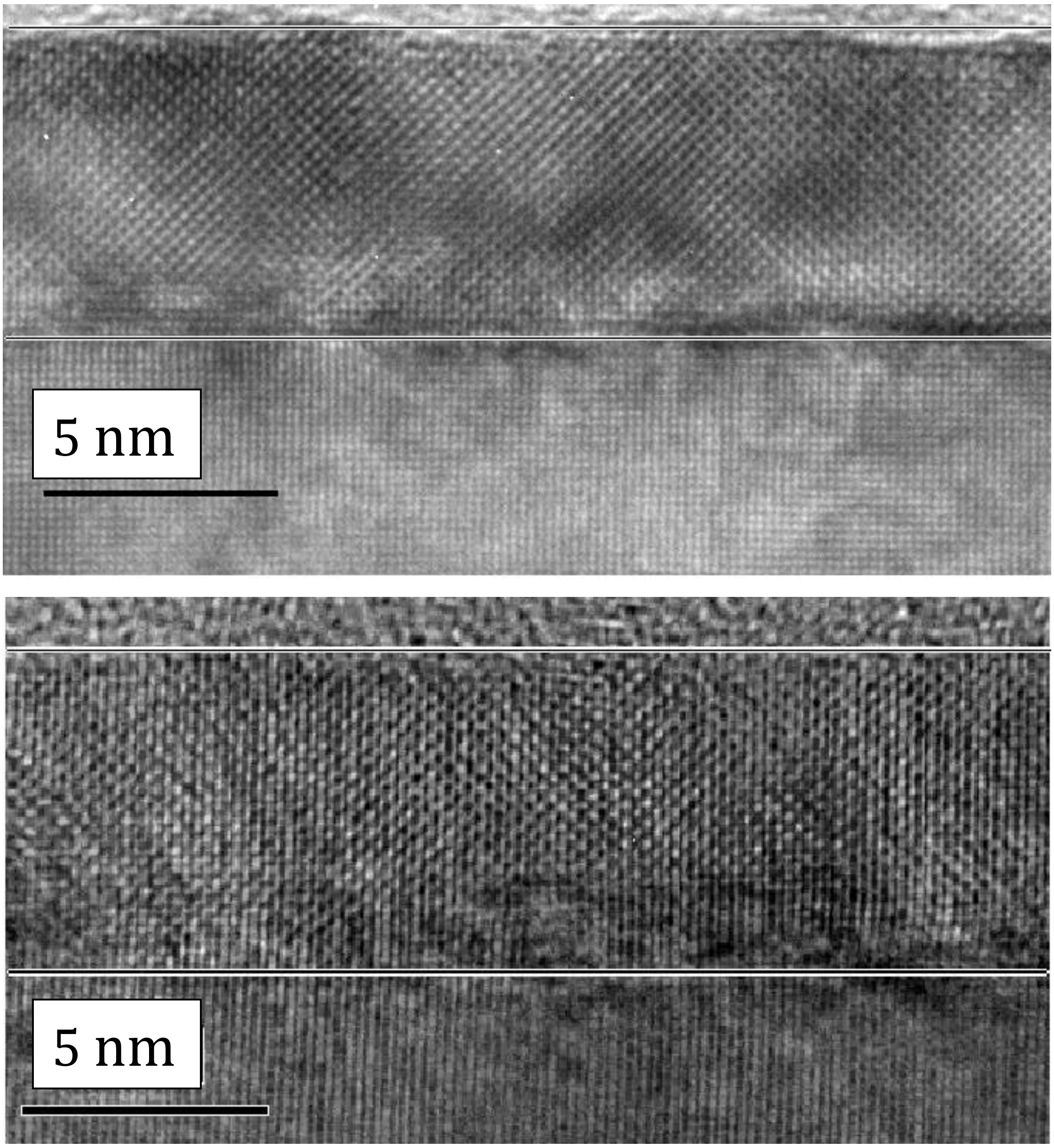

Figure 6.3: HRTEM cross-section of 15 minutes oxidation time (top) and 60 minutes oxidation time thin samples (bottom). Showing the substrate, film and vacuum (guide lines have been added to compare with **figure 6.5**).

Further investigation of the difference between the oxidation times was performed by taking a cross-section of the samples in the (100) direction, as is a standard characterization technique. HRTEM of samples (a) and (b), shown in **figure 6.3,** reveal the difficulty in interpreting the magnetization data. Very little difference can be observed between the two, which both show high quality single crystal spinel structure with the characteristic 45° planes. Select area diffraction (SADIFF) imaging of the films, seen in **figure 6.4,** indicates highly regular spinel structure and confirms the epitaxial nature of the film to substrate.

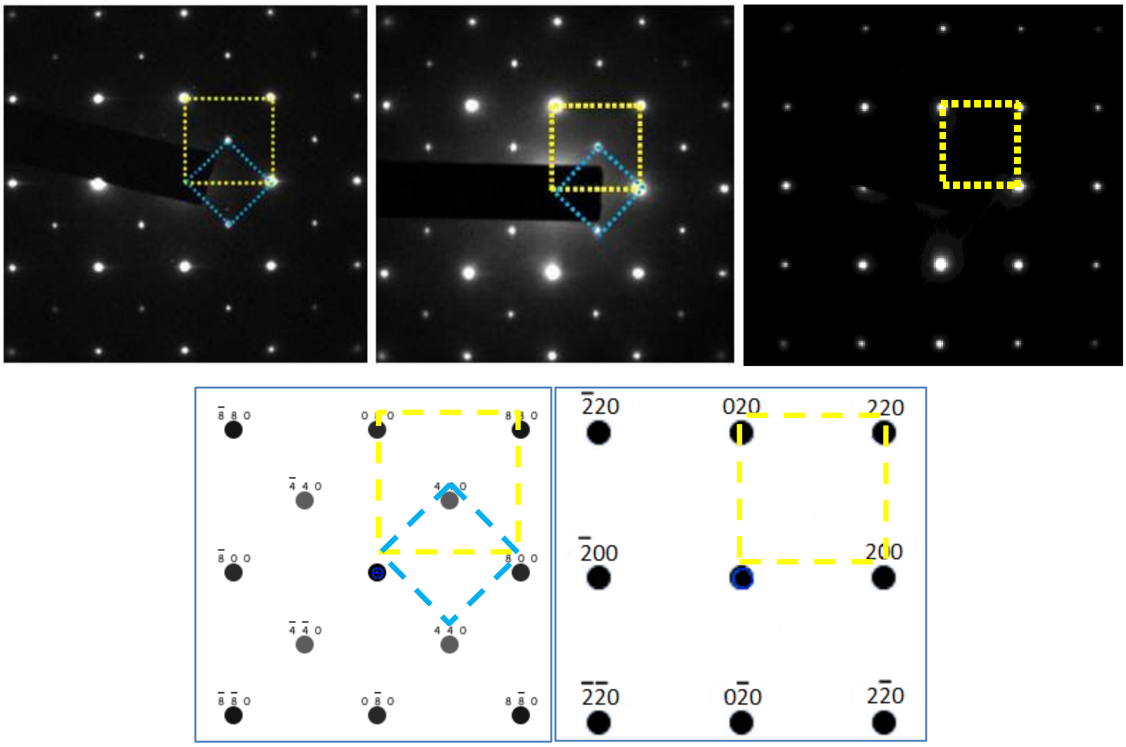

Figure 6.4: Select area diffraction of 15 minute oxidation time thin-film (top left); 60 minute oxidation time thin-film (top middle); MgO substrate (top right); calculated pattern of Fe_3O_4 (001) (bottom left) and MgO (001) (bottom right). Yellow squares mark out common oxygen sublattice pattern and blue squares mark out Fe_3O_4 unit cell pattern, displaying inverse spinel structure.

All SADIFF images were taken on the JEOL 2011 microscope with an electron wavelength (λ) of 0.0253 Å at a camera length (L) of 500 mm. Using the MgO (001) substrate diffraction image as a reference, it is possible to check the calibration of the images using the equation $\lambda L = d_{hkl} R_{hkl}$ where d_{hkl} is the distance between lattice planes and R_{hkl} is the observed spot spacing on the image. As MgO and Fe_3O_4 share an oxygen sublattice, the substrate diffraction image appears similar to that of the film but missing the additional atomic planes formed by the iron sublattice. Measuring from the $0\bar{2}0$ to the 020 spots on the image gave a distance of half a unit cell at 6.006 ±0.005 mm, giving a calculated lattice parameter of 4.212 ±0.003 Å compared to the actual spacing of 4.212 Å. Continuing this analysis for the film gives an equivalent lattice spacing of 3.014 ±0.005 mm from $\overline{22}0$ to 220 which becomes 8.394 ±0.014 Å compared to 8.397 Å in bulk Fe_3O_4.

The epitaxial relationship between the film and substrate can be shown by comparing the oxygen sublattice spacing to that of the substrate. For sample A, at 6.001 mm this works out to be 4.216 ±0.04 Å with a 0.9 (±0.8) % lattice mismatch. Similarly for sample B at 5.998 ±0.005 mm this gives 4.218 ±0.04 Å with a 1.4 (±0.8) % lattice mismatch. This is evidential of the expected epitaxial relationship, close to the expected 0.3 % lattice mismatch.

It is possible to further analyze the quality of these films by isolating the {220} planar contributions to each image, which only exist in the spinel structure. The result of this is shown in **figure 6.5** and gives some limited extra insight into the level of disorder in the two films. Horizontal lines have been added as a guide to the eye to indicate where the film||substrate and film||vacuum interfaces occur.

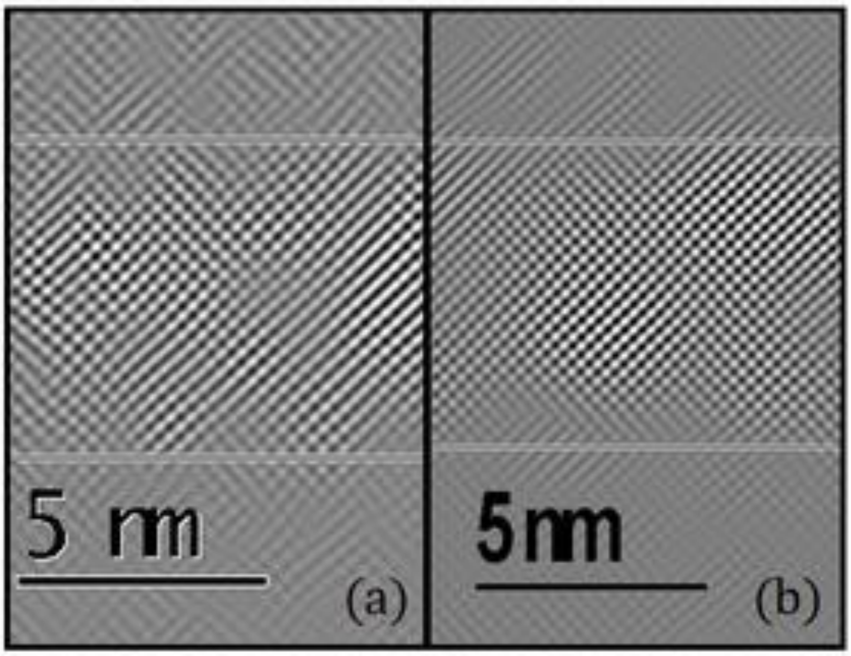

Figure 6.5: Bragg filtered images of (a) 60 minute oxidation time thin-film and substrate; (b) 15 minute oxidation time thin-film and substrate. Greater disorder is observable in (a) compared to (b).

HRTEM images alongside the Bragg filtered images show that an elevated state of disorder existed in the sample with increased oxidation time, consistent with magnetometry. Both samples exhibited one or two atoms roughness on the surface and both samples also showed some roughness to film||substrate interface, with intermixing occurring over, again, one or two atomic planes. The disorder in sample (b) was greater than for sample (a). The third sample (c) was grown much thicker (~20 nm) so as to investigate the penetration depth of the oxide layer and observe the oxide||iron and iron||substrate interfaces. As mentioned previously, the magnetometry revealed that the film was dominated by the iron contribution and the microscopy corroborated this as shown in **figure 6.6** below. The immediate striking observation was that the oxide/iron interface was almost atomically flat and that both layers showed long range crystalline order.

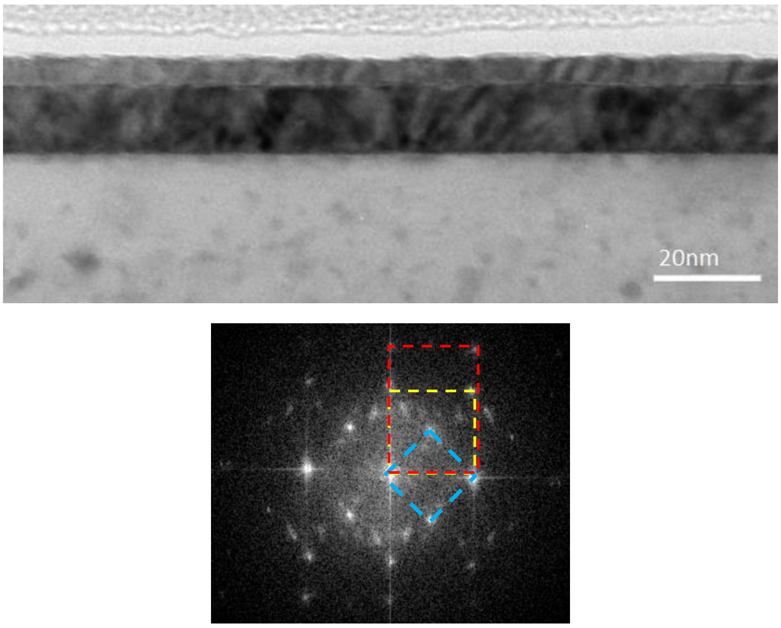

Figure 6.6: TEM image showing long range film with sharp interface and uniform depth (left). Select area diffraction (right) shows Fe_3O_4 (100), Fe (110) and MgO (100) crystalline order epitaxially stacked.

Diffraction analysis showed evidence of Fe_3O_4 (100), MgO (100) and Fe (110) existing epitaxially together in this arrangement. By resolving the sample, shown in **figure 6.7(a), (c)**, it was possible to see what could be a 'freeze-frame' of the growth process and how sharp the interface between oxide and iron layers was. Following the same processing technique used on the previous samples: Bragg filtering just the vertical {200} planes (see **figure 6.4 (c)**), it was possible to observe the effect of the lattice mismatching between the three layers (see **figure 6.7(b), (d)**).

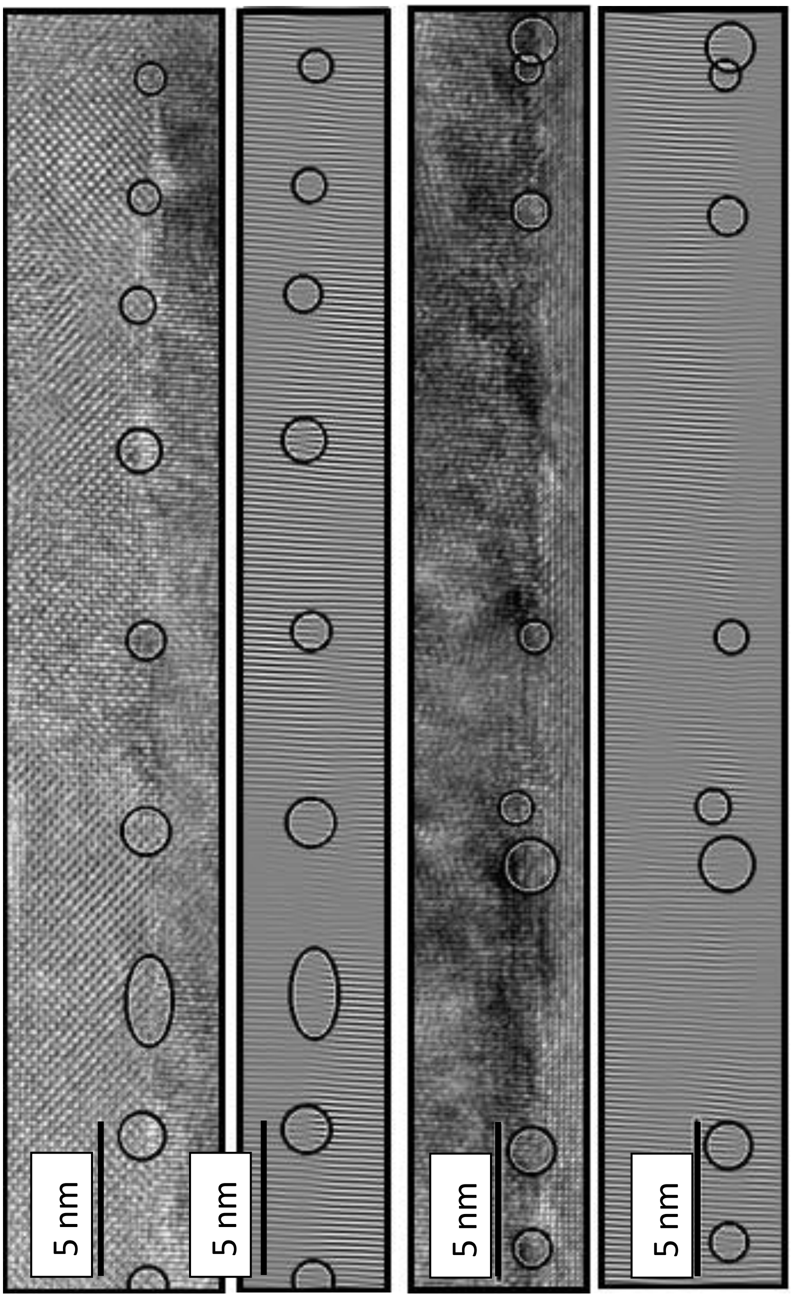

Figure 6.7: HRTEM images of Fe_3O_4 (100)||Fe (110) interface (far left) with Bragg filtered image (mid left) and of Fe (110)||MgO (100) interface (mid right) with corresponding Bragg filtered image (far right). Crystal plane dislocations are identified from the Bragg filtered images and circled showing regular predictable mismatch in Fe_3O_4||Fe, but irregular mismatch in Fe||MgO.

The lattice mismatch between MgO (100) and Fe_3O_4 (100) is ~0.3% **[3]**, low enough for strain relaxation to take place without causing many misfit dislocations. The mismatch between these and Fe (100) however is on the order of 36% **[4]** and as a consequence it is unsurprising that the iron film observed was rotated 45° to produce Fe (110) and a mismatch of ~3.6% to both.

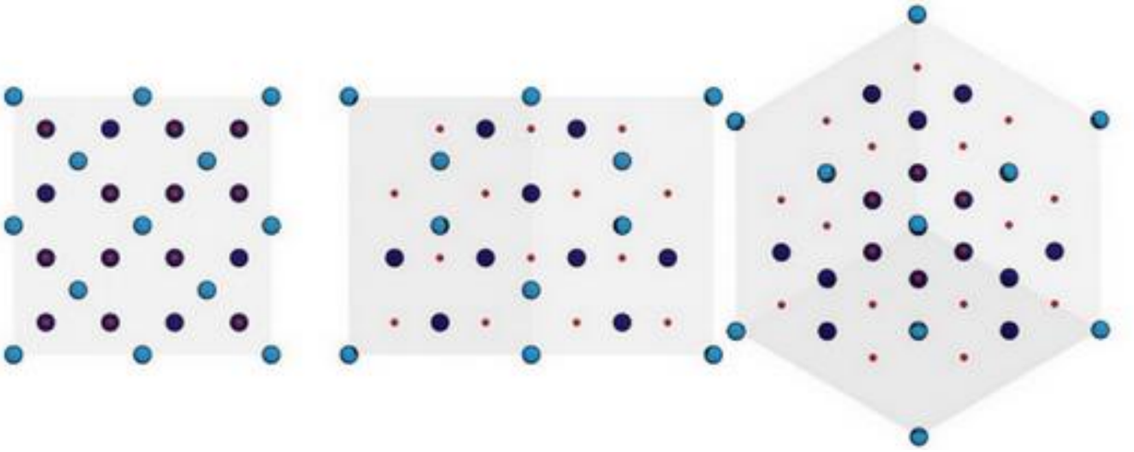

(001) (011) (111)

Figure 6.8: Illustrations of the three most common orientations in the Fe_3O_4 cubic inverse spinel crystal unit cell. The (110) direction resolves each atomic column independently, unlike the other two.

High resolution study of the interface between the iron and the iron oxide layers confirms the sharpness of the transition, which is not atomically sharp but appears to have completely transitioned after two or three monolayers. It is interesting to note then that, although the lattice mismatch between MgO (100) and Fe (110) is approximately equal to that between Fe (110) and Fe_3O_4 (100), the observed misfit dislocation periodicity was quite different. It could be argued that the crystallinity of the substrate will be greater than that of the grown Fe, which would further suggest that this interface should be more regular; however this was not borne out in the investigation. The observed Fe (110)||Fe_3O_4 (100) dislocations occurred approximately every 15 and 30 planes, which would be consistent with the mismatch percentage, however the MgO (100)||Fe (110) dislocations occurred much more randomly. This may be due to differences in the potential strain of each of these films, and the fact that there is a smaller difference between the Young's modulus of Fe and Fe_3O_4 (2.8%) than between MgO and Fe (14.7%) **[5]**.

Ultimately, the loss of magnetic order is not fully accounted for by the small increase in disorder observed from the (100) direction microscopy. As previously discussed, a continuum of oxidation states exists for the iron oxide spinel, based on the state of the B site iron. The inverse spinel structure, as shown again above in **figure 6.8**, is partially obscured in the (100) direction, and also in the (111) direction, which are the most common orientations observed. This limitation does not exist in the (110) direction, which might then prove a superior orientation for characterising the film order.

6.3.2 (110) Microscopy Investigation

A set of samples was grown following the same growth conditions as above, again varying the post growth oxidation time, but all with thick initial iron growth. These samples were oxidised for 9, 27 and 45 minutes. Magnetometry of these samples was inconclusive because of the large iron signal dominating any effect from the oxide layer. For this set, cross-section sample preparation was performed at 45° to the wafer orientation, to view the (110) direction. High resolution TEM images for these samples are shown below in **figures 6.9, 6.10**. (Images courtesy of Dr. Daniel Gilks)

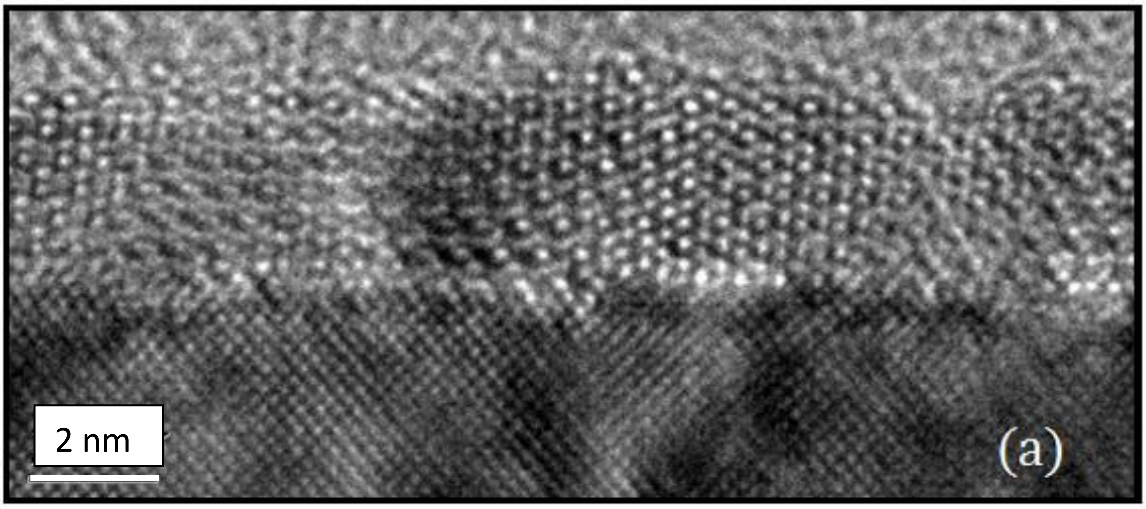

Figure 6.9: (110) direction HRTEM of (a) 9 minutes post-oxidized sample, showing Fe (100), Fe_3O_4 (110) and substrate. Interface transition takes place over ~5 monolayers.

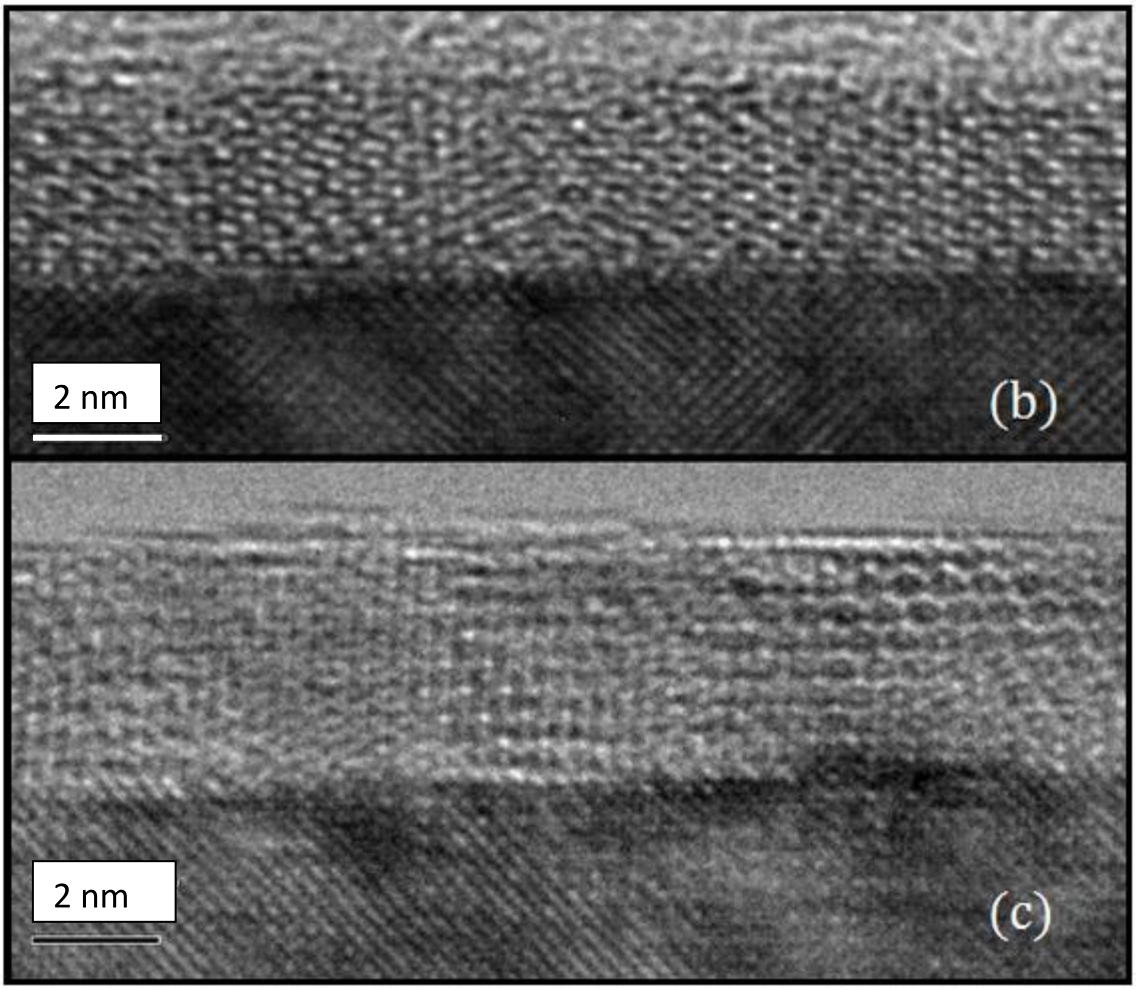

Figure 6.10: (110) direction HRTEM of (b) 27 minutes, (c) 45 minutes post-oxidized sample, showing Fe(100), Fe_3O_4 (110) and substrate. Interface transition in (b) much sharper than **figure 6.9 (a)** and **(c)**.

The increased level of disorder caused by the extended oxidation times was much more visible in this orientation. The 9 minute oxidation sample showed a high level of ordering, with some discontinuities. Its interface with the unoxidized layer was significantly rougher than that of the other two samples, which might mean that this film is actually under-oxidized. The 27 minute oxidation sample showed a heightened level of disorder, where order existed in more 'granulated' regions, and had a much sharper interface. The 45 minute oxidation sample continued the trend, with order existing in much smaller regions. The interface here was also, for the most part, atomically sharp. The extent of the contrast in order was highlighted further by Bragg filtering similarly to that done in **figure 6.5**; this is shown in **figure 6.11** for 9 minutes and 45 minutes.

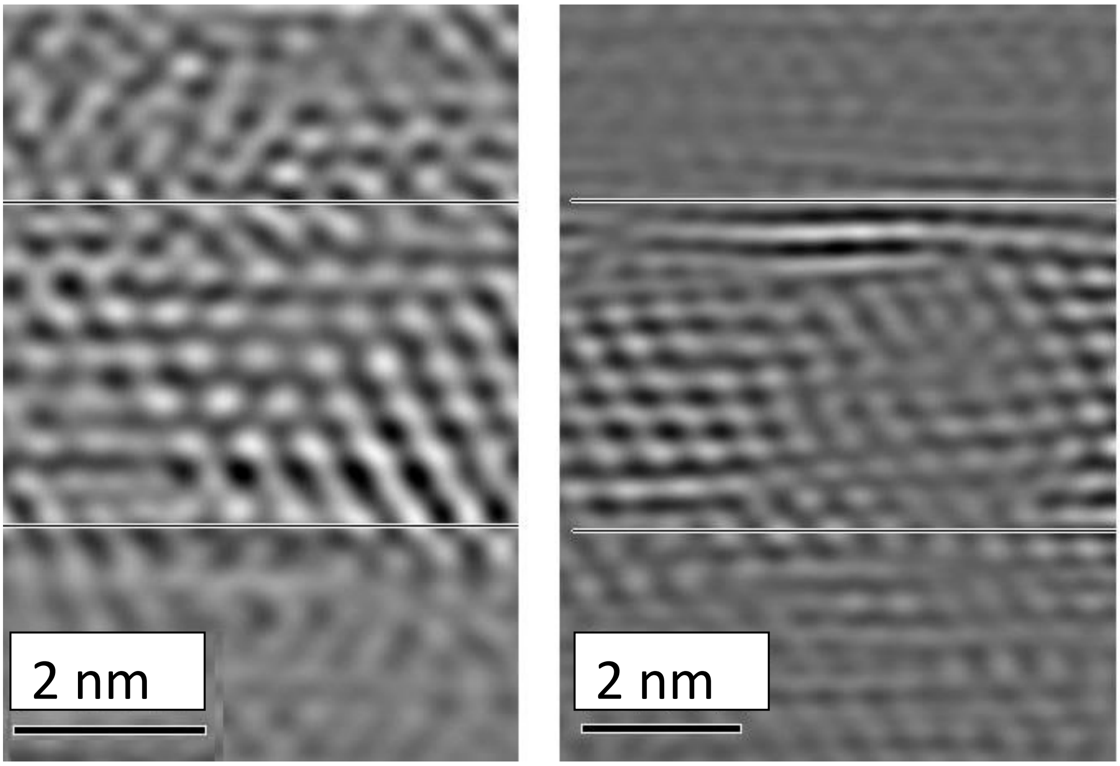

Figure 6.11: Bragg filtered images of 9 minutes (left) and 45 minutes (right) samples. Shows increase in disorder with oxidation time more clearly than **figure 6.5**.

The average thickness of each film was measured by an intensity line profile averaged horizontally over 2.5 nm and defined by the distance between the first and last resolved atomic peak in each profile. An example for the 9 minute sample is shown in **figure 6.12**. These averaged thicknesses were measured to be 3.115 ±0.05 nm, 3.395 ±0.05 nm and 3.839 ±0.05 nm in order of increasing oxidation time. The oxide layer appears to reach a skin-depth, as described by Cabrera-Mott oxidation **[6]**, between 3-4 nm. Although this skin-depth is dominated by both the oxygen partial pressure and the temperature **[7]** it is also minimally dependent on the oxidation time. The oxide layer appears to nucleate rapidly and any further increase in film thickness is minimal. This suggests that tuning the film's oxidation time could be a method of maximizing the quality output of the film.

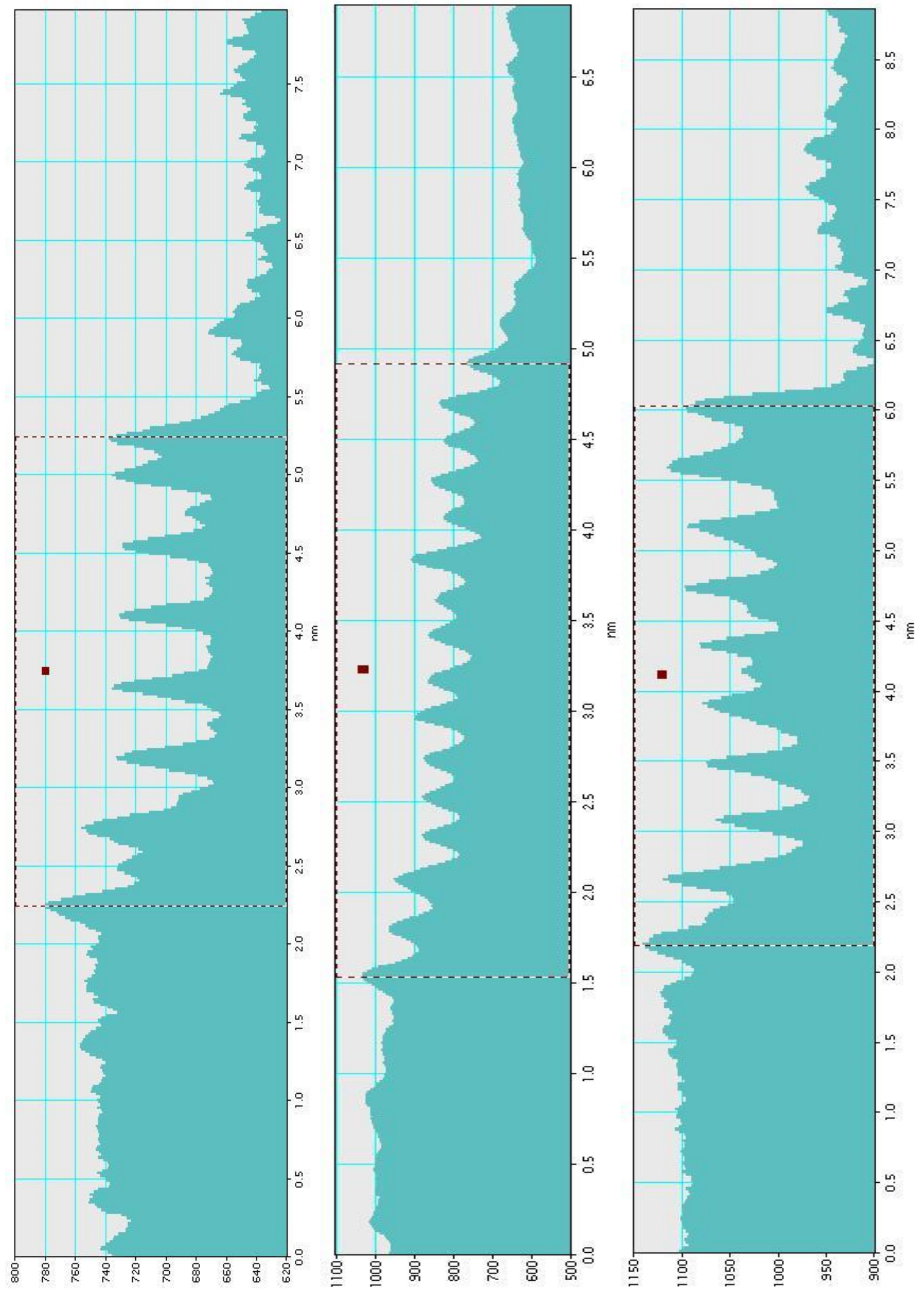

Figure 6.12: Example line contrast profiles of 9 (left) 27 (middle) and 45 (right) minute sample images. These are used to determine the thickness of each film with a rigorous measure.

6.3 Fe_3O_4/MgO(100) APB Geometry

6.3.1 Theoretical Review

An incomplete study of the possible APBs exists for the MgO/Fe_3O_4 (001) system **[8]**. In order to properly identify these defects it is necessary to investigate and catalogue the geometrical non-integer shifts made possible by the relationship between the MgO (001) surface and the possible terminating planes in magnetite. This has been carried out to both characterise the APB visibility from experimental imaging and then to provide geometric data for theoretical calculations of net superexchange interactions taking place within each system.

Following the work of W. Eerenstein et al. **[9]** the possible non-integer shifts have been recalculated for (001) taking the postulate that the magnetite unit cell has several unique terminating planes. This gives the possibility of more APBs existing than have previously been reported, without requiring the case of uneven substrate surface. These defects are reported here along with visibility criteria using the Howie-Whelan equations.

The magnetite film will lie most naturally with the O sites on top of the Mg sites on the substrate. This continues the crystal structure with the least disturbance, and is considered to be the lowest energy state. This work considers a flat MgO surface termination, with all steps being relative steps in the magnetite unit cell. In characterising all of the possible non-integer shifts, it is necessary to be aware that not all geometrically unique shifts are physically unique. It is possible to characterise a shift which will not tessellate with a second shift, but is essentially identical and exists as, for example, a mirror image, such as is shown in **figure 6.13**. In these cases the listed available superexchange interactions will be the same, and so one or the other shift can be discounted as trivial.

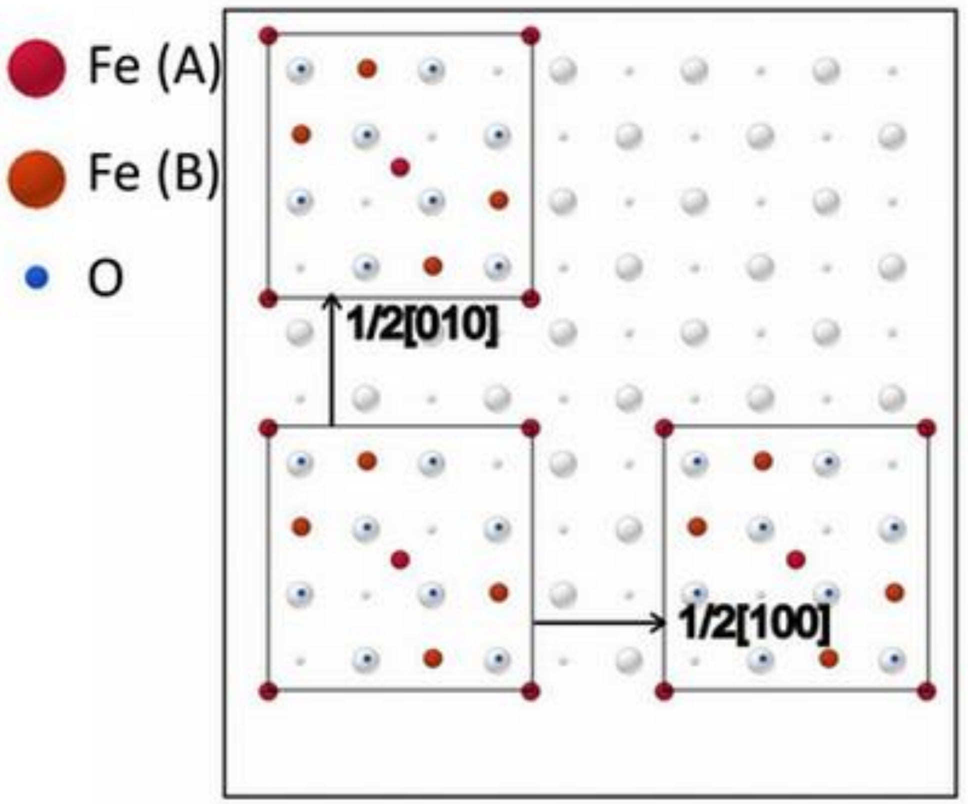

Figure 6.13: Example of two geometric shifts of the Fe_3O_4 unit cell on the (grey-scale) MgO (100) lattice. They may appear to be unique, but are in fact mirror images.

There are multiple O planes within the magnetite unit cell in each orientation, and it is proposed that the film exhibits no bias as to which of these planes the film will terminate on. These planes for (100) orientation are shown in **figure 6.14**; each contains 8 O atoms and 4 Fe atoms, giving a possible out-of-plane non-integer shift component of 1/4[001], 1/2[001] and 3/4[001]. This is on top of rotational shifts, as the film has rotational symmetry, which in (100) also corresponds to a 3/4[001] shift. The starting reference plane and orientation is arbitrarily assigned for the reasons discussed. Additionally vector shifts that can be made up of a combination of two or more characterised vectors are considered to be trivial and can be discounted.

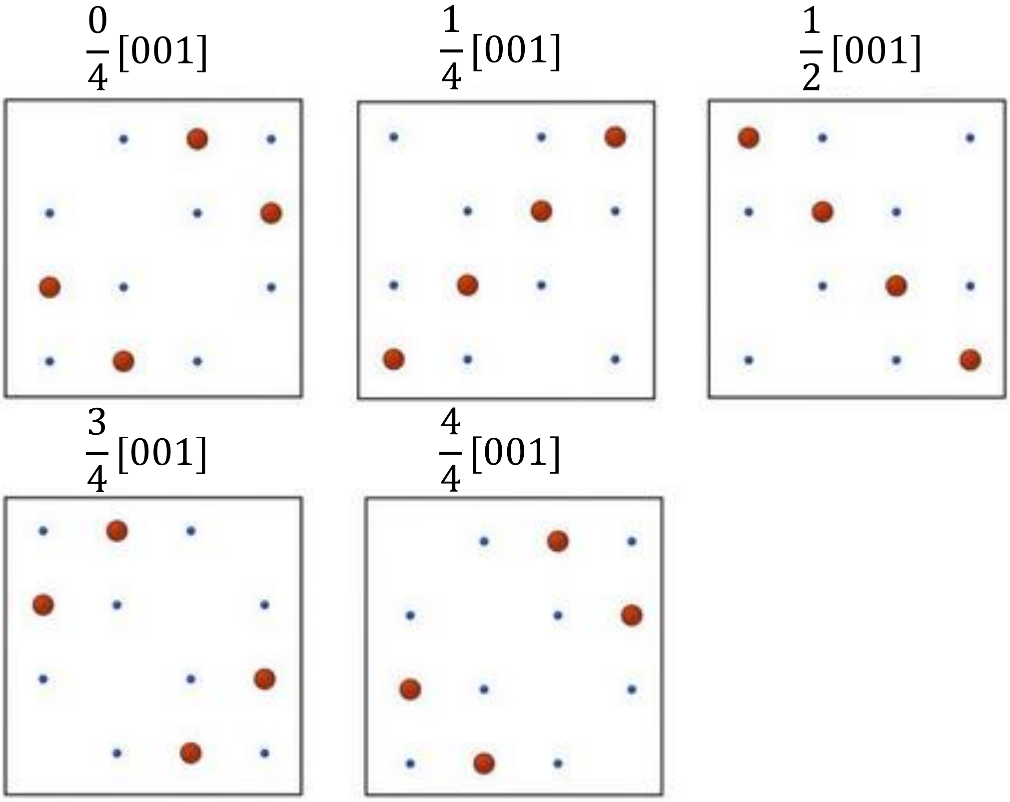

Figure 6.14: Schematic showing proposed terminating planes of Fe_3O_4 (100) unit cell. Four octahedral (B) iron atoms exist in each plane, notably the oxygen lattice is constant through each plane.

Figure 6.15 shows the in-plane shifts. The 1/4[-110] and 1/4[110] are unique as they translate over different geometry on the substrate beneath. These have been previously reported by Eerenstein et al. These shifts will be invisible from a plan-view of the film. **Figures 6.16, 6.17** and **6.18** show the out-of-plane-shifts produced by this geometry, with the breakdown of some of the vectors shown. In-plane shifts, 1/4[-110] and 1/4[110] for example, are unique as they are shifted over different geometry of the underlying lattice; one is shifted across a Mg atom, and the other across an O atom. Things become more complicated when looking at out-of-plane shifts, and full calculations of the interactions involved would be needed to deduce how many of these shifts are in-fact unique.

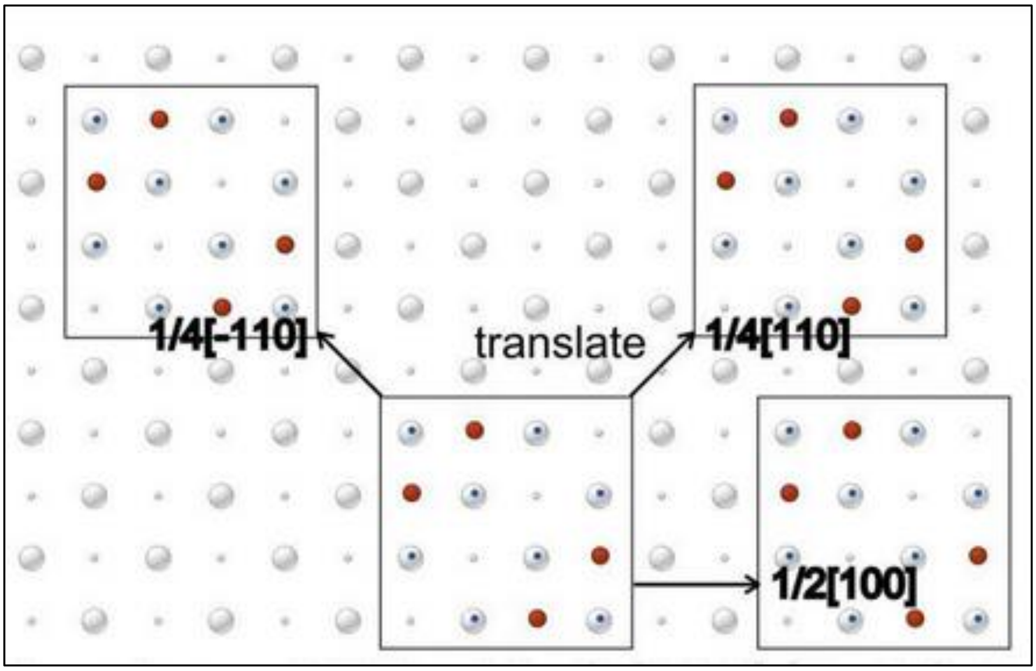

Figure 6.15: In-plane APBs on Fe_3O_4 (100).

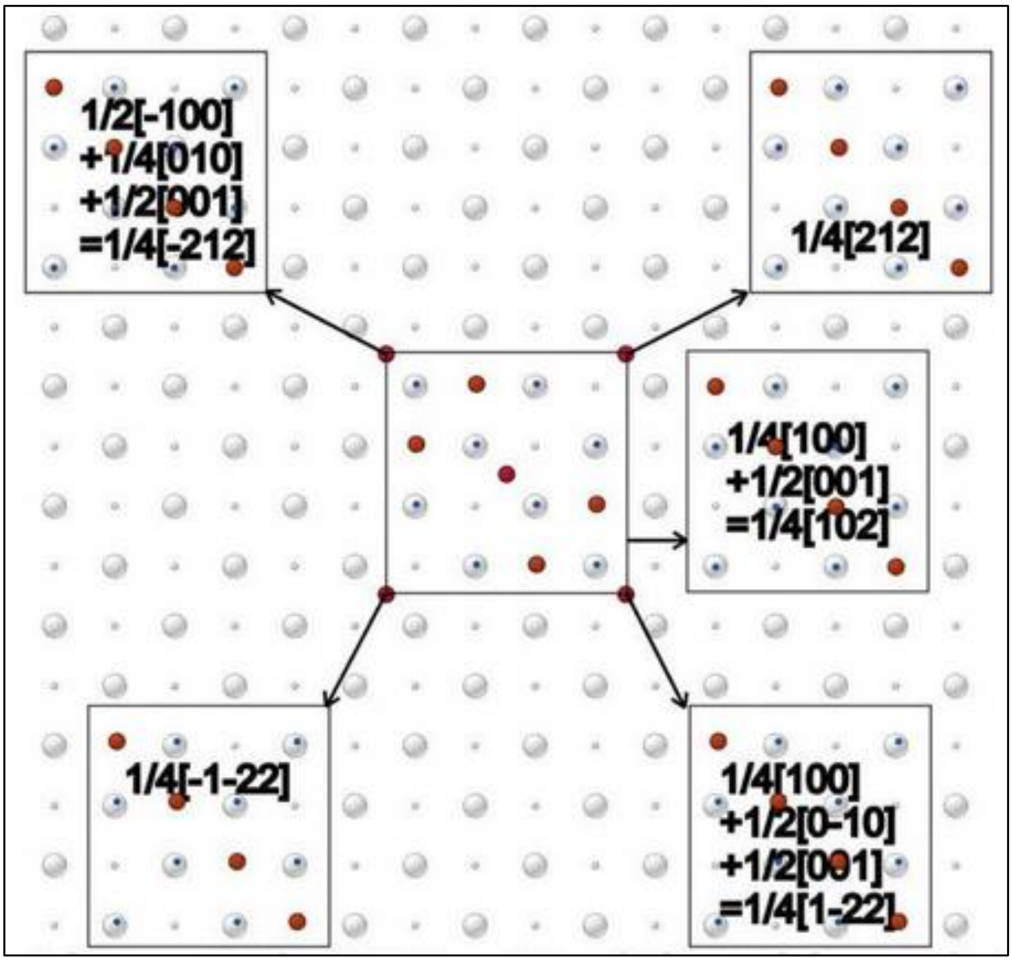

Figure 6.16: 1/2 z-shift out-of-plane APBs on Fe_3O_4 (100).

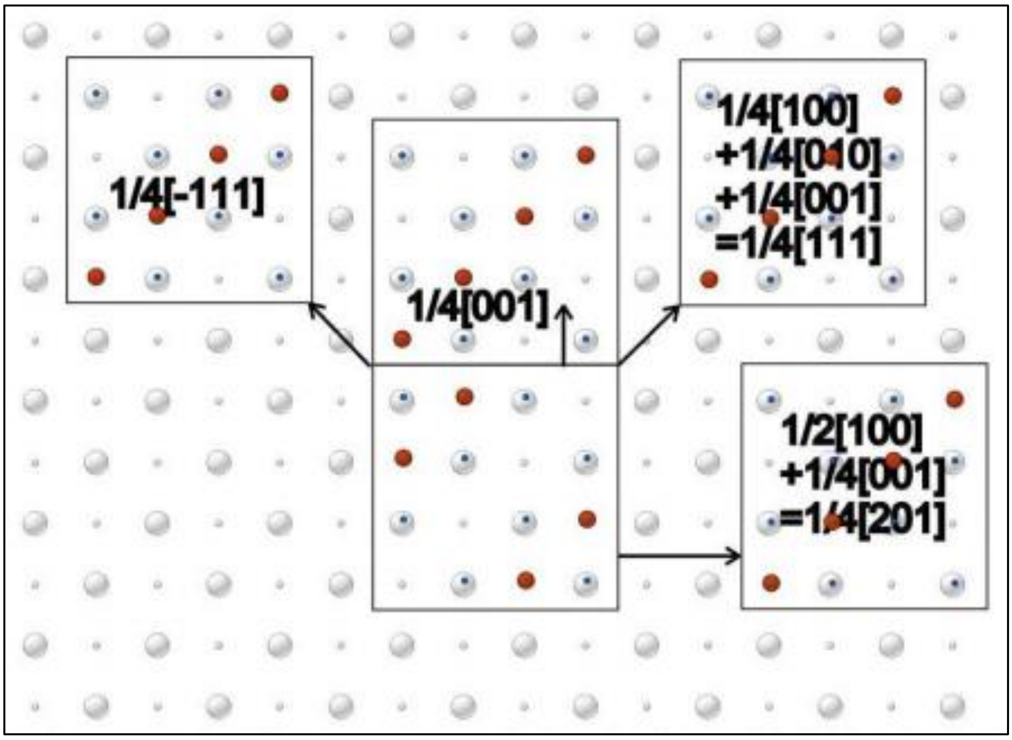

Figure 6.17: 1/4 z-shift out-of-plane APBs on Fe_3O_4 (100).

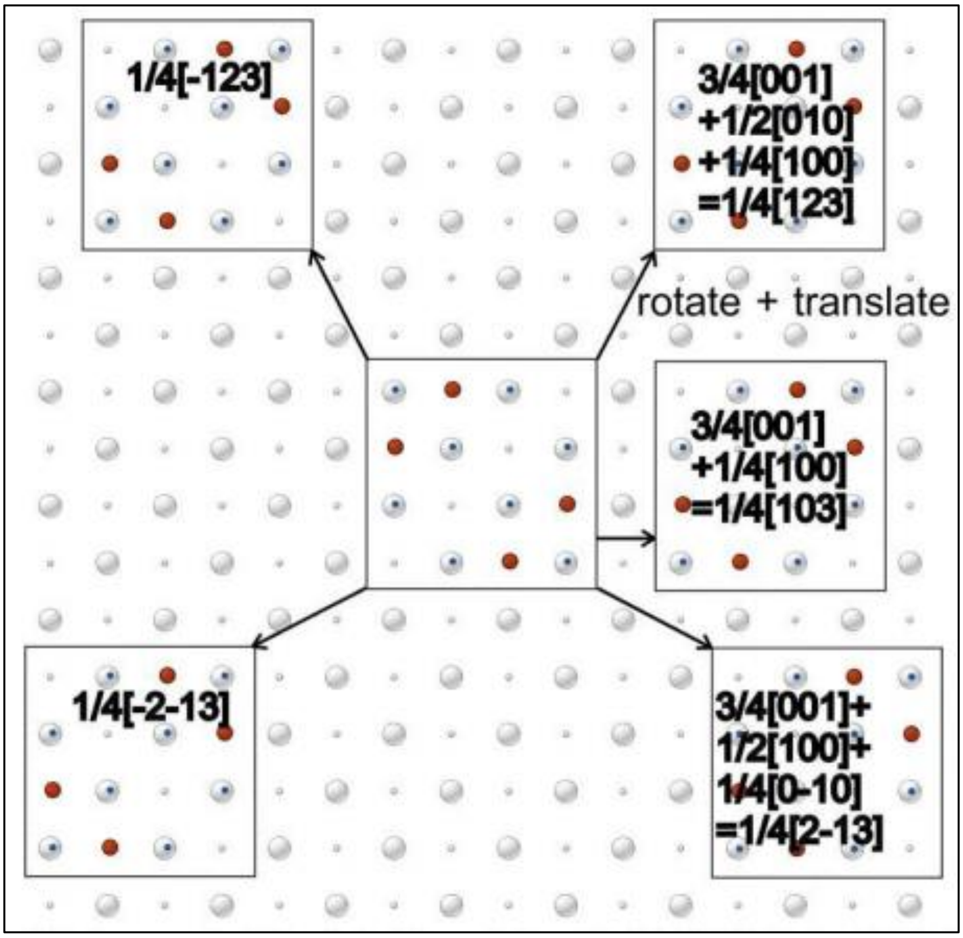

Figure 6.18: 3/4 z-shift out-of-plane APBs on Fe3O4 (100).

Using the Howie-Whelan APB visibility criteria equation, discussed in **chapter 4** and restated here in **equation 4.6**, it is possible to calculate the visibility conditions for these shifts for the first zone of diffraction spots; (220)-type and (400)-type. As can be seen from **figure 6.19**, approximately half of the identified shifts are observable under a (220) dark field condition, and none should be observed under a (400) dark field condition.

$$2\pi \underline{g}.\underline{R} = (2N+1)\pi \tag{4.6}$$

This condition is approximately the same as for a stacking fault planar defect. In this equation, $\underline{g}$ is the diffraction vector of the electron beam, $\underline{R}$ is the translation vector of the planar defect as a fraction of the Fe_3O_4 unit cell size. N indicates visibility of an APB for a chosen diffraction spot if it is an integer and invisibility otherwise.

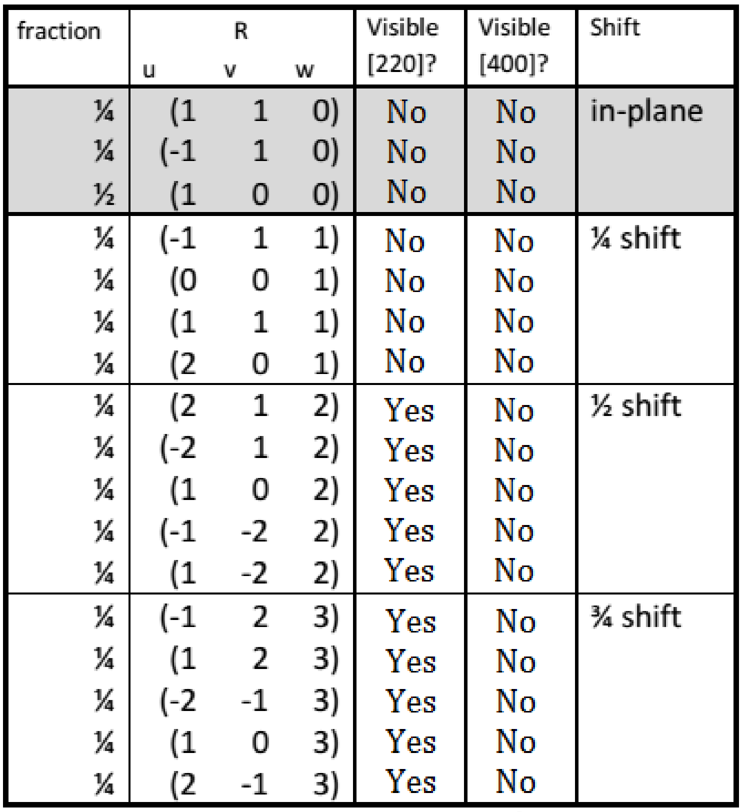

fraction	R			Visible [220]?	Visible [400]?	Shift
	u	v	w			
¼	(1	1	0)	No	No	in-plane
¼	(-1	1	0)	No	No	
½	(1	0	0)	No	No	
¼	(-1	1	1)	No	No	¼ shift
¼	(0	0	1)	No	No	
¼	(1	1	1)	No	No	
¼	(2	0	1)	No	No	
¼	(2	1	2)	Yes	No	½ shift
¼	(-2	1	2)	Yes	No	
¼	(1	0	2)	Yes	No	
¼	(-1	-2	2)	Yes	No	
¼	(1	-2	2)	Yes	No	
¼	(-1	2	3)	Yes	No	¾ shift
¼	(1	2	3)	Yes	No	
¼	(-2	-1	3)	Yes	No	
¼	(1	0	3)	Yes	No	
¼	(2	-1	3)	Yes	No	

Figure 6.19: Non-integer unit cell shifts and visibility criteria, showing the in-plane shifts (grey) and out-of-plane shifts.

6.3.2 Experimental Observation

A brief investigation of a plan-view slide of the 15 minutes post-oxidized sample was produced by the lift-off method, detailed in **chapter 4**, and imaged in the 2011 JEOL TEM. This sample was chosen as the best of the samples grown which had been oxidized entirely to the substrate. Standard TEM imaging shows a rough surface with no obvious inhomogeneity (**figure 6.20** right), however diffraction imaging (**figure 6.20** left) shows an extra crystal structure overlaid on top of the inverse spinel of the Fe_3O_4. On inspection this is a signal from gamma-phase Fe_2O_3 maghemite.

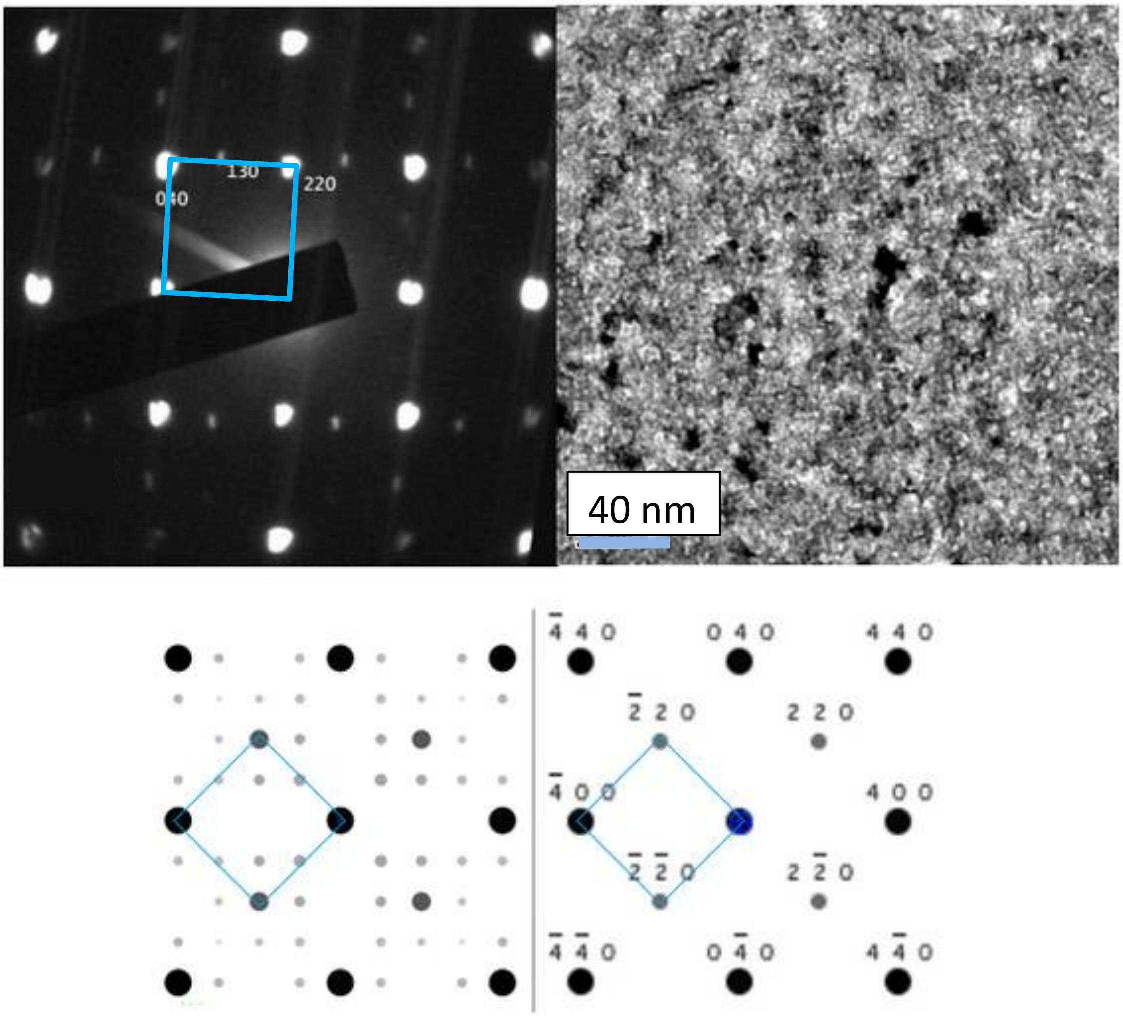

Figure 6.20: Images showing example diffraction pattern for 15mins sample (top left); a TEM image of the sample surface (top right); calculated gamma-phase Fe_2O_3 maghemite, observed in plan-view analysis (bottom left) and calculated Fe_3O_4 diffraction pattern (bottom right).

Dark field image observations were made under the two beam condition to increase image contrast. Images were taken of the APBs observed, isolating a (220) and (400) spot individually (see **figure 6.21, 6.22**).

APBs are clearly visible in **figure 6.21** which shows the sample in plan-view looking in the (001) direction under the [220] dark field condition. The defect density is surprisingly high considering the quality of the cross-section information. They appear to be restricted in their direction of propagation in a way that was not apparent in W. Eerenstein's **[9]** simultaneously oxidized films. This disorder will cause the reduced quality of the magnetic response.

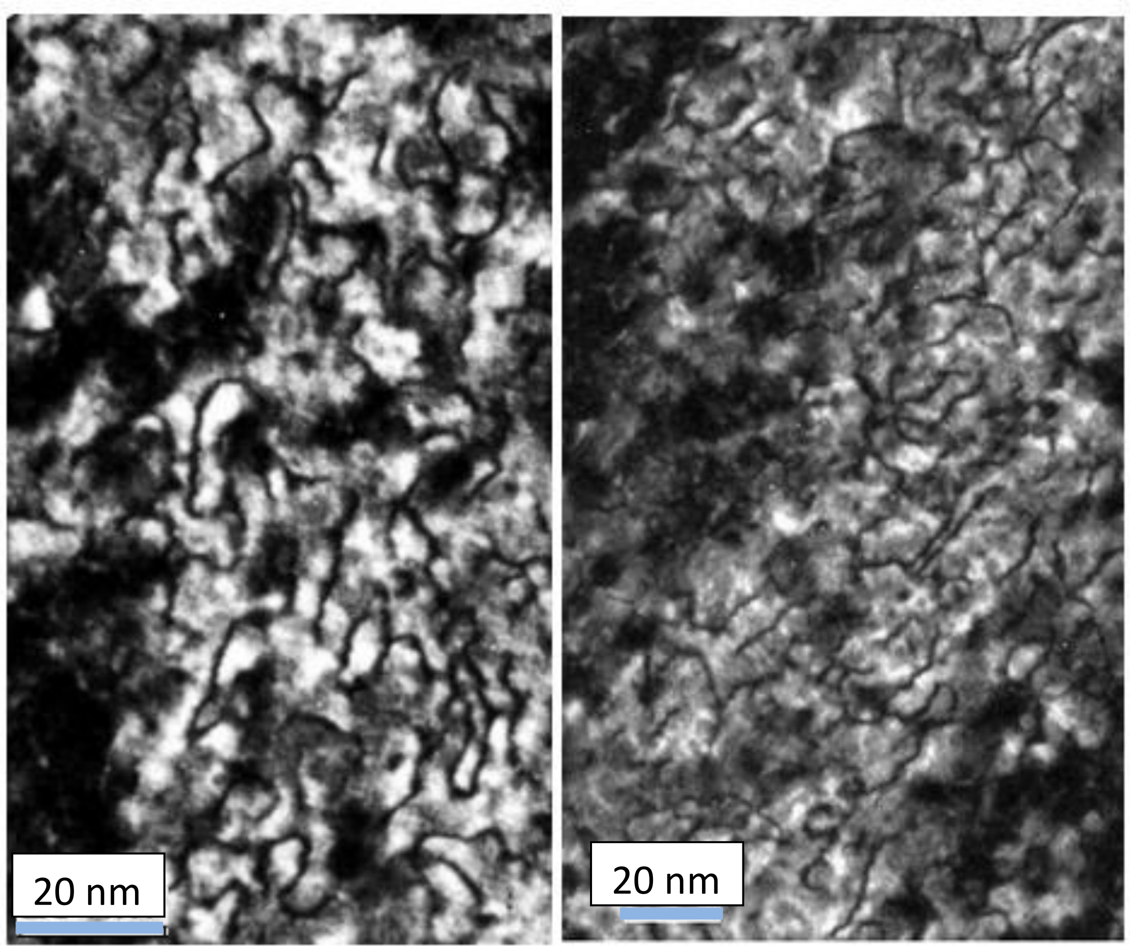

Figure 6.21: Images showing plane-view TEM images of two regions of 15 minute post-oxidized film under [220] dark field conditions which show a large defect density.

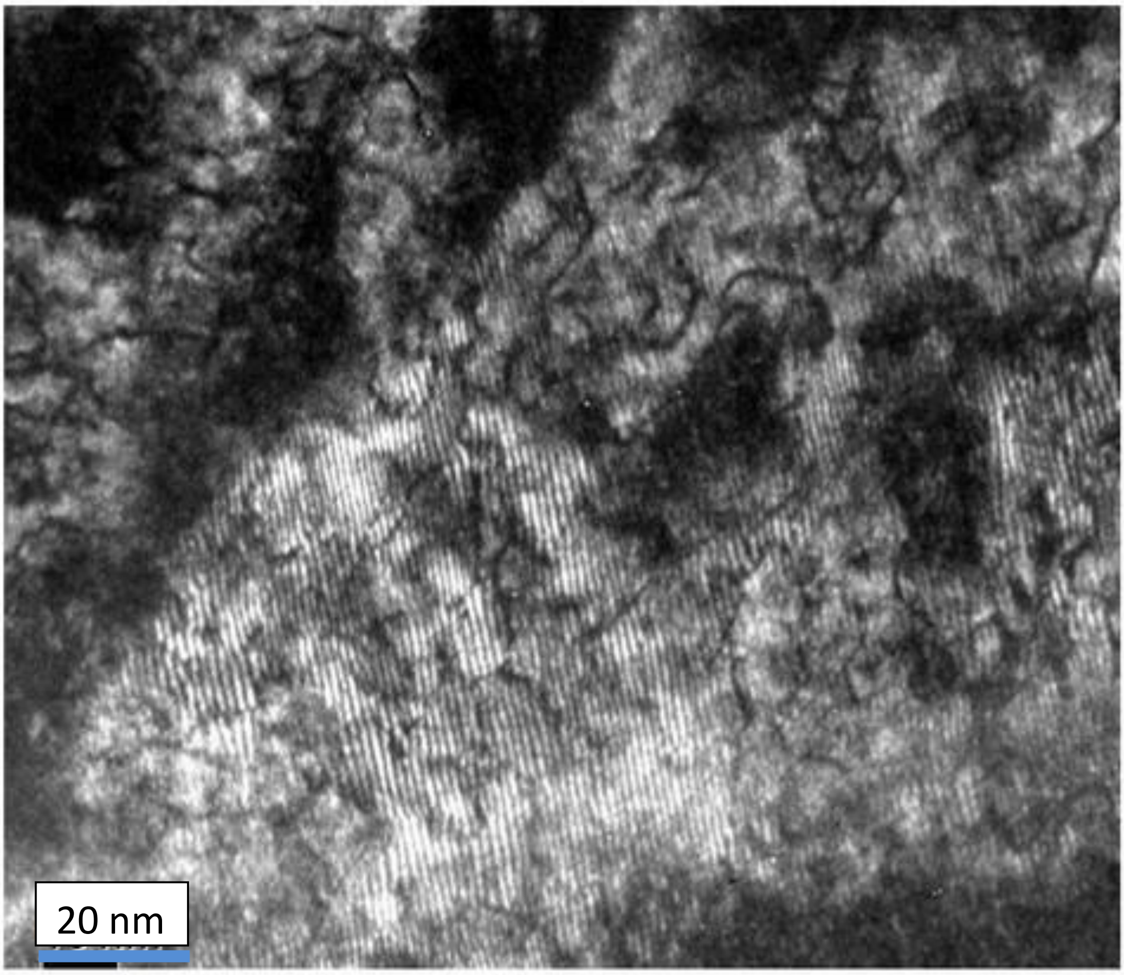

Figure 6.22: Images showing plane-view TEM images of 15 minute post-oxidized film under [400] dark field conditions, showing visible defects, as well as Moiré fringes.

Isolating the area around a [400] spot in the post-oxidised film gave images such as **figure 6.22**. As these films have maghemite signal in plan-view, this dark field image also contains contributions from the [130] type spot which is very close to the [400] as seen in **figure 6.20**. This observation is interesting firstly because it contains APBs, when this spot is considered to highlight none. These are potentially due to the contribution of the maghemite spot making more defects visible. The fringe patterns in this image are the second point of interest. These are too widely spaced to be atomic planes and are in fact Moiré interference patterns **[10]**, observed when two lattices of differing period or orientation interfere with each other. This is a further indication that there is a surface layer of over-oxidised iron on this film, not present in the cross-section and is likely due to the instability of the film surface to further oxidation during the lift-off process.

6.4 Summary

A pair of $Fe_3O_4||MgO$ (001) samples have been grown by MBE by post-oxidizing 3 nm thin-films of epitaxial Fe. Increased oxidation time from 15 minutes to 60 minutes has shown a significant reduction in magnetic quality metrics of coercivity (~35%) and remanence (~80%). Investigation of the crystal structure by cross-section HRTEM in the standard (001) direction has shown the difficulty of identifying any increased film disorder and would suggest both films are of equivalent quality.

Further investigation of a series of 9, 27 and 45 minutes post-oxidized samples has shown that the disorder exists on the B site Fe ions in the lattice, by HRTEM observation in the (011) direction. This disorder is strongly dependent on the oxidation time, while the inverse spinel structure is more robust than expected.

20 nm Fe films, post-oxidized for 9, 27 and 45 minutes show a skin depth to the oxidation, of 3-4 nm for the chosen temperature and pressure. This was seen to be only very weakly dependent on oxidation time.

By taking another look at the geometry of the magnetite unit cell, a number of potential extra APB defects have been identified. Looking at the layers of the unit cell in the given orientation, it was theorized that a number of unique surfaces existed on which the film could terminate. As the growth conditions presume island growth, this could lead to z-shifts between neighbouring islands of Fe_3O_4 previously unappreciated in the literature.

As the visibility criteria suggest that approximately half of the shifts are viewable in plan-view, the actual density can be approximated from experimental data as being twice that observed. It is interesting that the defects appear to be clearly grouped based on their z-shift component, despite it having no direct contribution to the calculation for either [220] or [400] vectors.

APBs have been experimentally observed under both spot conditions. It has been seen that even the 15 minute post-oxidized sample contains a dense APB network, which explains the undesired reduction in remanent magnetization from an ideal square loop.

6.5 References

[1] Vescovo et al., J. Appl. Phys., **98**, 084507 (2005)

[2] Y. Cao, et al., J. Magn. Magn. Mat. **395**, 361 (2015)

[2] R. J. Beals, et al., J. Am. Ceram. Soc., **40**, 279 (1957)

[3] W. Zhong, et al., Phys. Rev. B, **47**, 95 (1993)

[4] H. M. Ledbetter and R. P. Reed, J. Phys. Chem. Ref. Data, **2**, 531 (1973)

[5] N. Cabrera and N. F. Mott, Rep. Prog. Phys., **12**, 163 (1949)

[6] T-M Lu et al. J. Appl. Phys., **95**, 4346 (2004)

[7] S. K. Arora, J. Appl. Phys., **100**, 073908 (2006)

[8] W. Eerenstein, et al. Eur. Phys. J. B., **36**, 271 (2003)

[9] D. B. Williams and C. B. Carter, Transmission Electron Microscopy: II Diffraction (Plenum Press, New York, 1996)

Chapter 7

Ultrafast Magnetization Dynamics Study of GdFe Thin-Films

7.1 Introduction

As discussed previously in **chapter 3**, rare-earth transition-metal alloys (RE-TM), including GdFe, have been of interest to industrial and commercial applications for decades **[1]**. It is as exciting today with the development of new non-volatile, high density, fast access devices under the umbrella of magnetic random access memory (MRAM). They are important because of the interaction between their two sublattices giving these materials the desirable extreme stability and high magnetic anisotropy under operating conditions. Data recording is required to reach frequencies into the GHz regime and beyond and field pulsed techniques are physically limited to the tens of picoseconds. The development of ultrafast pulsed laser systems since 1996 has opened up new avenues of exploration into methods of manipulating and observing the dynamic behaviour of these magnetic materials and, despite high levels of interest, the underlying mechanisms are still the subject of significant debate **[2]**. Ultrafast laser stimuli have been applied to explore coherent spin precession without using a pulsed magnetic field. The ability to carefully control the spin state of a magnetic material through optical interaction could have a significant impact on the world of micro/nano-electronics **[3]**. Further research is still necessary to understand these interactions with materials.

An initial series of GdFe amorphous alloy thin-film samples, of varying Gd concentration, is studied here by static magnetometry. The focus is to investigate the temperature dependencies of each. Pump fluence dependent laser-induced magnetization dynamics is then investigated, in a selected concentration of Gd, using the time-resolved magneto-optic Kerr effect (TRMOKE) apparatus whose design and construction is detailed in **chapter 5**.

7.2 Methodology

Samples used in this investigation were grown by direct current magnetron co-sputtering onto cleaned Si (001) substrates by collaborators in Nanjing, China using the Ar gas, magnetron co-sputtering. Details of this procedure are documented in **chapter 4.** A series of Gd concentration was produced, with total film thickness of ~20 nm and Gd concentration of 10%-25%. From this set, the 25% Gd concentration sample was chosen to perform a time-resolved dynamic measurement investigation.

Laser-induced, pump-probe, room temperature TRMOKE in a longitudinal configuration was used to optically induce and measure a demagnetization event. A reference magnetization state was provided by a (>sample coercivity) 1 kOe in-plane external magnetic field perpendicular to the sample's magnetic easy axis. Ultrafast (~100 fs) regenerative Ti:Sapphire laser light with a repetition rate of 1 kHz was used for both pump and probe beams. A central wavelength of 800 nm was used for the pump beam and 400 nm for the probe. Pump and probe beams were linearly polarized orthogonal to each other, in s and p orientation respectively, and both incident to the sample surface at ~45°. The overlap of both beams was carefully aligned with precision optics and a magnified digital camera image through a shared focal lens of f=150 mm. A 4x beam reducer was included in the pump beam to modify the relative spot sizes of pump and probe to improve the overlap margin of error. Further details can be found in **chapter 5**. Pump power was varied from 350 μW to 1450 μW, which corresponds to a fluence range of 20 μJ/cm^2 to 82 μJ/cm^2, over twelve increments. Due to the risk of permanent damage to the measured sample area, the lowest fluence measurement was undertaken first, and then proceeding from there until saturation was reached.

Note on MOKE measurement calibrations

Values of Kerr rotation and reflectivity are given in internally consistent figures of voltage linearly proportional to change in magnetization and temperature (respectively). While it would be ideal to calculate the scaling factors for each, this is necessarily an empirical process, requiring calibration points for a particular sample. To calibrate for magnetization requires that the sample is at rest in a saturated state for the detector balancing, and that a second state of full demagnetization is recorded under the same laser, lock-in and detector conditions. This is possible to do by pumping the sample with sufficient fluence as to detect a full demagnetization without burning the sample. This can be difficult to define however and an alternative method using a variable electromagnet to detect a state of fully saturated reversal is better. This author was in the process of establishing this method during the writing of this document. A reliable temperature calibration is more complicated still, and would require calibration of reflective surfaces of know temperatures. This could be done with a cryostat system which is also being commissioned.

7.3 Results

7.3.1 Static Hysteresis Measurements

Static MOKE measurements at varying in-plane orientations of the sample (**figure 7.1**) show that it has strong in-plane anisotropy. The in-plane anisotropy tells us that there is a degree of crystalline order in the sample film, as an amorphous film would not produce this effect. Additionally as the substrate is diamond cubic Si(001), a completely epitaxial film would present a four-fold rotational symmetry, with its hard axis at 45° (in-plane) to its easy axis.

For the TRMOKE measurements, to stimulate precessional dynamics, it is necessary to apply the external field along the hard axis, making the resultant change in the effective field direction as large as possible, increasing the signal strength. An external field of 1 kOe was chosen to be >>H_c, the coercivity, which was ~25 Oe at the hard axis.

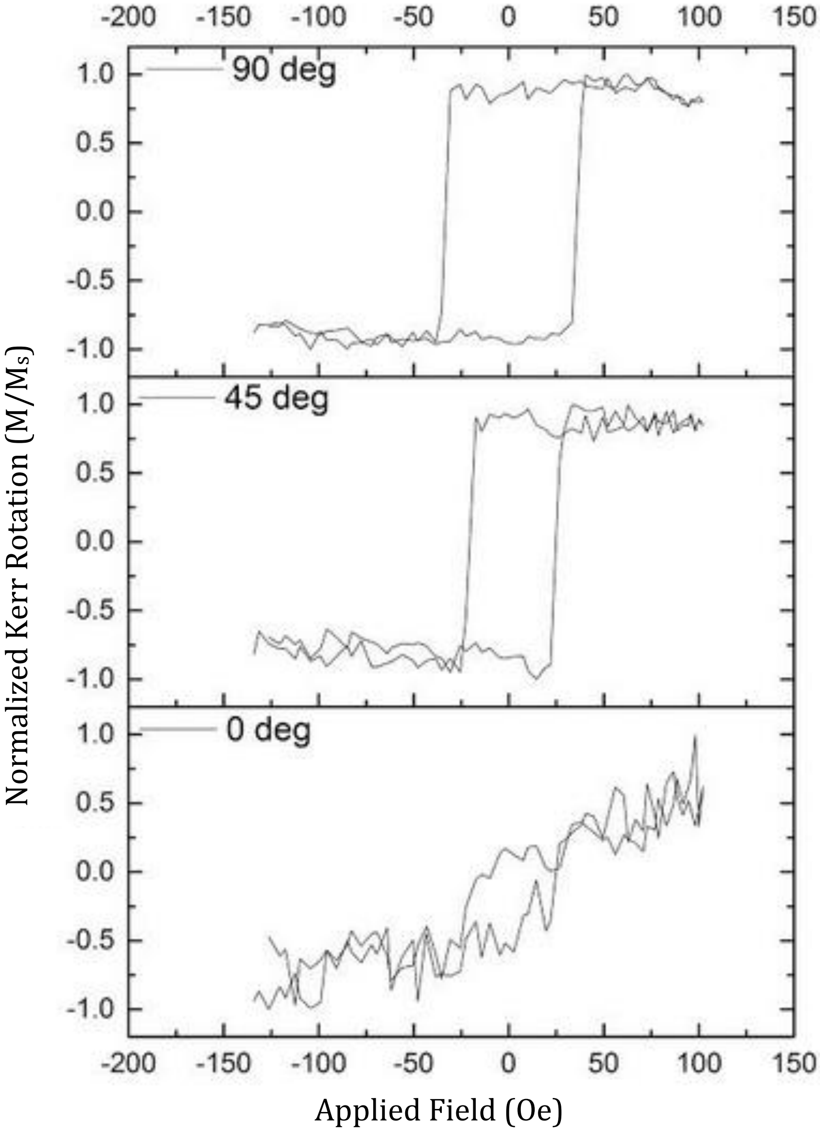

Figure 7.1: Normalized static MOKE longitudinal hysteresis measurements showing the anisotropic magneto-optic response. All TRMOKE measurements are undertaken at the in-plane hard axis, 0° here.

7.3.2 Pump Fluence Series of $Gd_{0.25}Fe_{0.75}$

Fluence is an important factor in understanding the behaviour of a material, especially one as complex as GdFe **[4]**. From a technological standpoint, the power requirements of a laser system to perform magnetic manipulation are also critical for bringing a product to a state of commercial feasibility.

Reflectivity

Time-resolved reflectivity data was produced for the series of twelve pump fluence measurements from the sum of the detector signal intensities, representing the total energy reflected from the sample and is proportional to the combined temperature of the local electron and lattice reservoirs. The noise level was higher in this data than for the Kerr rotation data detailed later. This is due to the nature of the measurement technique meaning that instead of negating any laser intensity fluctuations, they are instead doubled. This does not detract from the meaningfulness of this data however as the signal-to-noise ratio (SNR) is still >10 at each peak reflectivity. Slightly higher laser instability was present for the latter, higher fluence measurements. The reflectivity is seen to consistently increase, over the course of 2 ps in response to the pump photon injection, independent of fluence. This initial rise in surface temperature is due to a rapid photon-electron energy transfer followed by electron-electron thermalization.

The height of the reflectivity peak corresponds to the magnitude of the energy initially transferred into both the electron and lattice reservoirs and is presented alongside the equivalent data for the Kerr rotation (which shows the same for the spin reservoir) in **figure 7.2**. Errors for both data sets represent the effect of the instability of the laser hence, as previously mentioned, the Kerr signal data has a significantly lower average error. The amplitude of the reflectivity peak shows a significant step at pump fluence between 37-42 μJ/cm^2 from a shallow linearly increasing relationship to a second steeper regime. This second regime appears to tend towards saturation above ~70 μJ/cm^2. By comparison, the amplitude of the maximum Kerr signal shows no discontinuity, but progresses from a linear regime to a gradual saturation after ~54 μJ/cm^2.

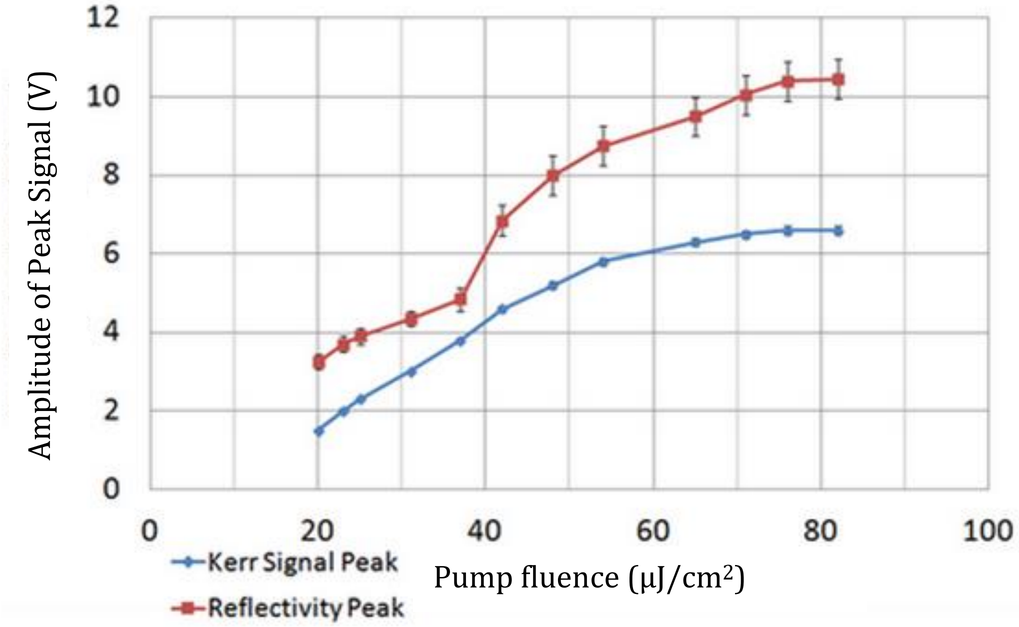

Figure 7.2: Amplitude of maximum reflectivity peak (red) compared to equivalent maximum Kerr signal peak (blue) as a function of pump fluence.

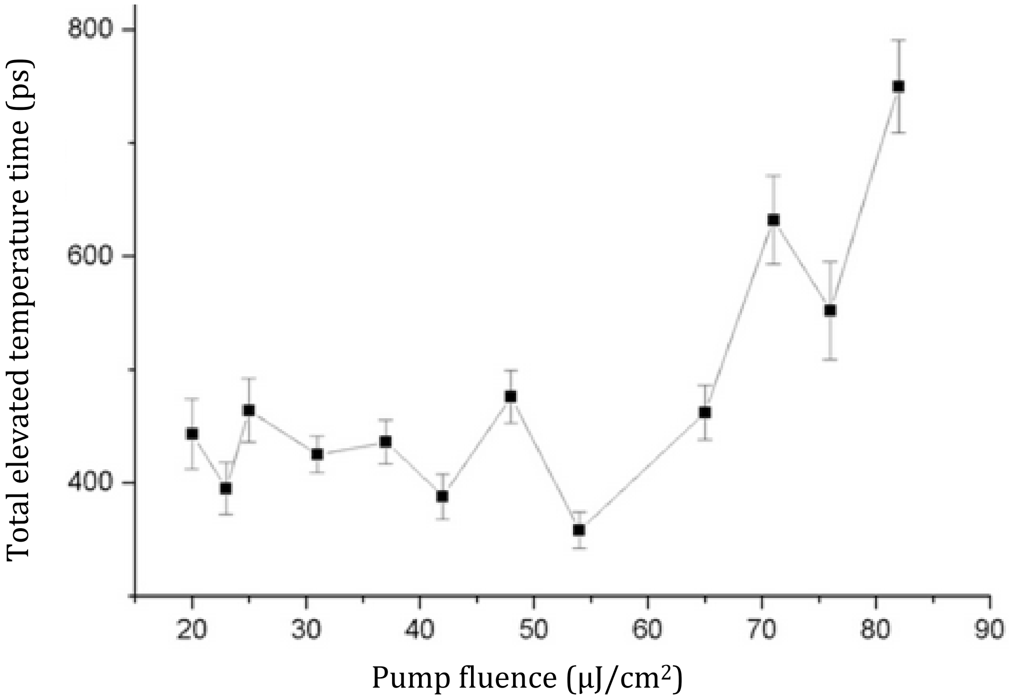

Figure 7.3: Recovery time constant of the local sample reflectivity, as a function of pump fluence. Two regimes of energy dissipation are observed. For low fluence, this is not energy dependent, but for higher fluence it becomes significantly so.

Following the ultrafast rise in reflectivity, there is a period of exponential decay back to equilibrium conditions as the energy is gradually distributed to the environment; this total time of elevated temperature can be seen in **figure 7.3**. For the lower fluence measurements, this took place on the order of 400 ps independent of fluence, but for the higher inputs an increase in the dissipation time was observed as a function of fluence. This regime change corresponds to the step in the peak reflectivity and indicates that an additional mechanism has been activated. Energy is being transferred within the local system for longer and/or more often before being dissipated to the environment. The coupling between the lattice and the environment is considered to be constant, with the dissipation occurring most strongly to the substrate rather than to the neighbouring film, as the area of the laser stimulation is on the microscale, while the film thickness is nanoscale. The mechanism that extends this dissipation time becomes more apparent later, when compared to the spin system recovery time.

Ultrafast Demagnetization

As discussed in detail in **chapter 2**, interpretation of ultrafast magnetization dynamics must be undertaken with caution as optical artefacts can provide misleading information. This section will discuss some of the observations made in this series and their interpretations.

Shown in **figure 7.4** is an example of the initial TRMOKE signal observed for a pair of low and high fluence values, 23 and 76 μJ/cm^2. Each measurement consists of a baseline value, corresponding to the rest magnetization, which is normalized to zero volts by the data acquisition program. Any change in magnetization is relative to this; change in the positive direction is demagnetization. Within this baseline it is possible to observe the noise floor, which should be <5% of the peak signal for the smallest fluence, for a SNR of >20. Following this, for each measurement, there is an apparent short strengthening of the magnetization which occurs consistently over the course of ~1 ps (see **figure 7.4 inset**). This negative peak is slightly fluence dependent. Additional high frequency oscillations were detected in the first few picoseconds following the initial rapid demagnetization. The frequency of some of these oscillations are dependent on the data acquisition sampling parameters and are as such discredited as true signal, however some persistent behaviour is observable.

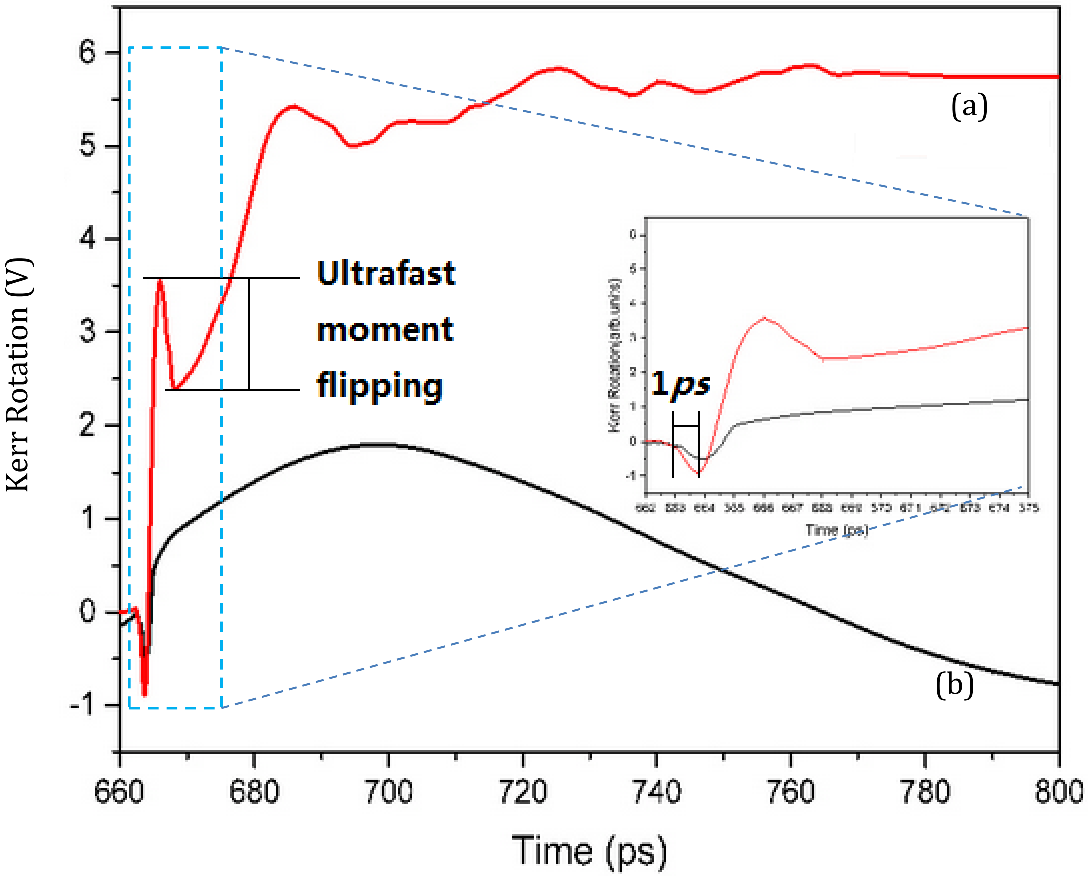

Figure 7.4: Graph showing ultrafast demagnetization curves for low (a), (black), (23 μJ/cm^2) and high fluence (b), (red), (76 μJ/cm^2). Inset graph shows the picosecond timescale drop in magnetization and the high frequency artefacts which affect the regime highlighted in the blue dashed region.

As discussed in **chapter 2**, the energy associated with $\underline{H_{eff}}$ is $E_{eff} = E_{Zee} + E_{ex} + E_{ani} + E_{dem}$ and each of these energies have associated field vectors which are balanced at equilibrium but respond at different rates based on the time-energy correlation, t=h/E. This time scale is dominated by the exchange energy term, E_{ex}. From **chapter 3**, the behaviour of GdFe comes from the separate sublattice dynamics of Fe and Gd, which can be assigned their own distinct $\underline{H_{eff}}$ vectors. The difference between these two effective fields is dependent on the strength of the exchange coupling between Gd and Fe, which is highly temperature dependent.

During the ultrafast demagnetization process, the two sublattices undergo separate temperature dependent dynamics. Photon energy is transferred from the laser pulse event to the electron thermal reservoir to the 3d spin orbitals of the Fe atoms and the 5d orbitals of the Gd atoms. Both orbitals experience rapid thermalization; however it is the 3d contribution which responds first and as the subordinate partner in the antiferromagnet, its initial reduction actually results in a momentary increase in net magnetization. Following this, further change in the Kerr signal is dominated by the destruction of magnetic ordering of the Gd, as intra-atomic exchange between its 5d and 4f orbitals takes place. The requirement of this second exchange to reach the magnetic information held in the Gd sublattice is critical.

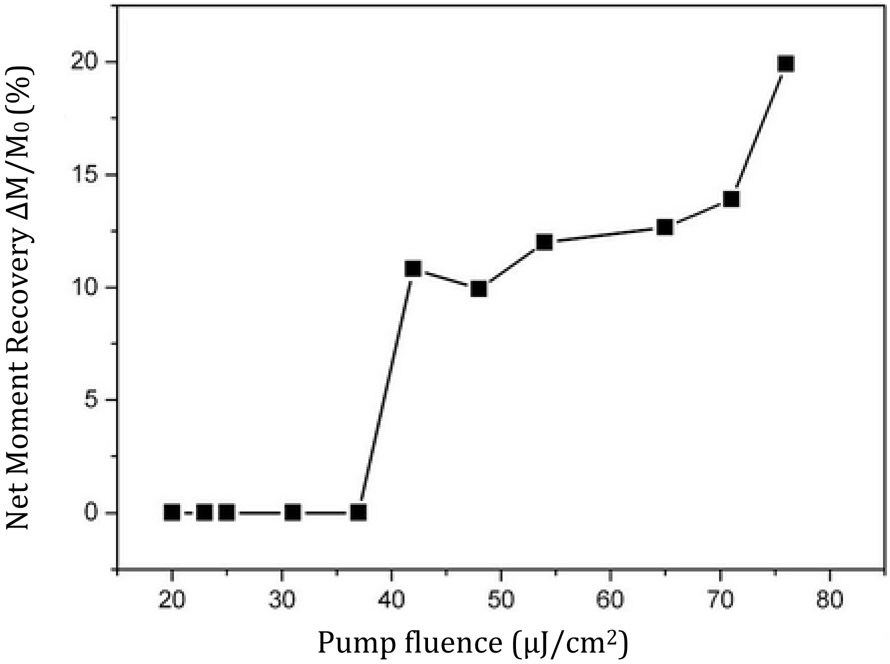

Figure 7.5: Ultrafast moment flipping contrast, defined in figure 7.4, shows the strength of the ferromagnetic state as the Gd and Fe moments align for a picosecond above a critical thermal threshold, corresponding to T_{Mcomp}.

At lower pump fluences this explanation is simple enough however seen in the example of 76 μJ/cm^2 is again the rapid Fe demagnetization, but this is interrupted by a short-lived recovery before the second demagnetization phase. This was observed to occur for all curves above the 37 μJ/cm^2 fluence point. The corresponding height contrast between these turning points, (marked on **figure 7.4** as the ultrafast moment flipping differences) is plotted in **figure 7.5**. A clear phase transition can be observed above 37 μJ/cm^2 which is a point already noted from the reflectivity data. A transient ferromagnetic state has been theorized, but not experimentally observed in RE-TM systems such as this. The interpretation of this behaviour, summarized in **figure 7.6**, is as follows:

1. Energy is transferred from the electron thermal reservoir to the 3d and 5d spin orbital thermal reservoirs, which exchange energy with each other to remain close to equilibrium, but with negligible dissipation to the lattice.

2. The magnetic order associated with the 3d reservoir begins to decay rapidly, causing a picosecond strengthening of the net magnetic moment.

3. a. The 5d reservoir is also able to exchange energy away to the 4f reservoir and does so rapidly following the 3d head-start. The large 4f magnetic order begins to decay and the net magnetic moment reduces rapidly.

   b. At some point the 5d and 4f reservoirs reach equilibrium with each other and the rate of decay of the net magnetic moment slows.

4. If the energy available is sufficient the 3d magnetic moment will reach full demagnetization and begin to reverse due to conservation of angular momentum. This results in a momentary ferromagnetic-like alignment of the magnetic moments causing a short-lived recovery of net moment.

5. The 4f magnetic moment is still decreasing and the net moment begins to fall again until the net moment reaches a minimum.

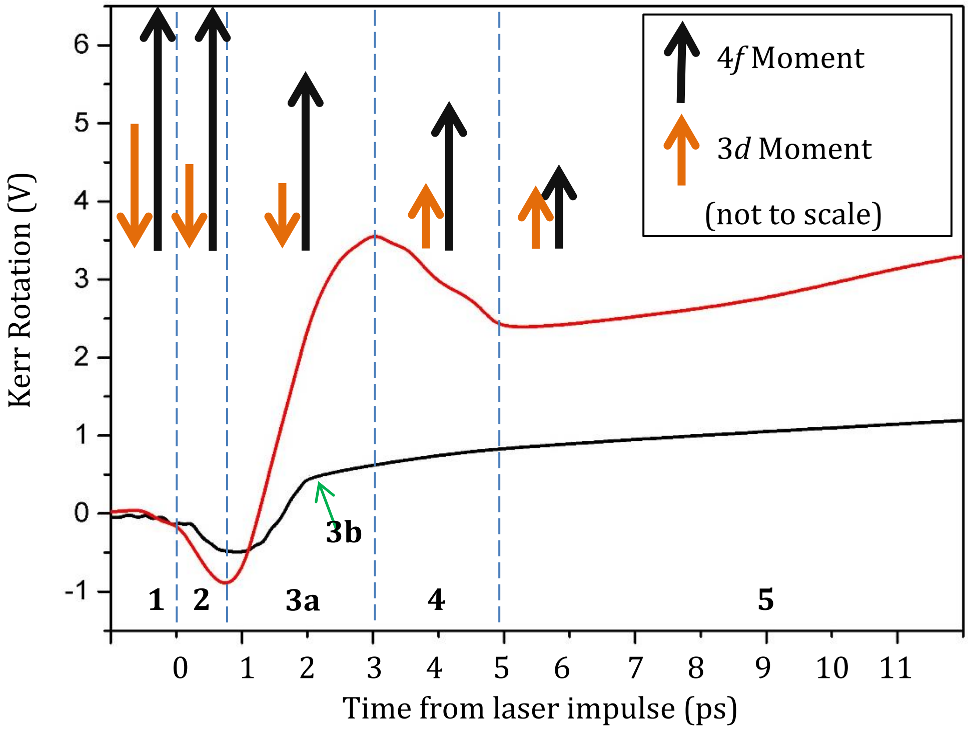

Figure 7.6: Schematic timeline of the ultrafast magnetic reversal behaviour.

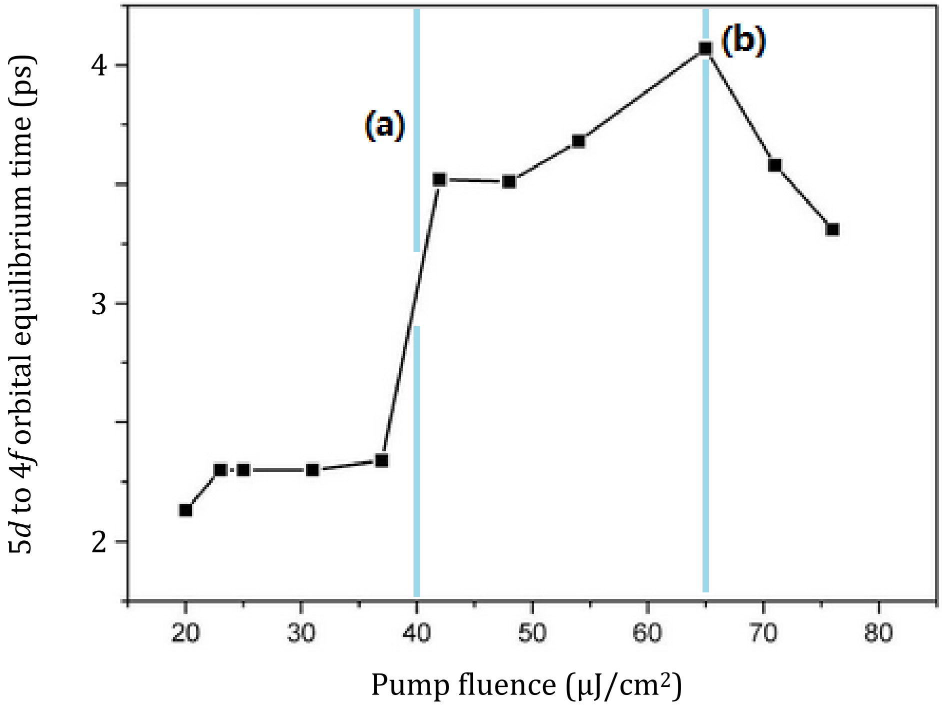

Figure 7.7: Time for Gd sublattice to reach internal equilibrium, showing 2 critical temperature points (a) and (b).

Lastly a fluence dependence was observed in the ultrafast demagnetization time, defined as the time taken for the 5d and 4f (and therefore 3d and 4f) spin orbitals to equilibrate (**figure 7.7**). Below 37 μJ/cm² this occurs in <1.3 ps, after which a large increase in the demagnetization time is accounted for by the ferromagnetic transient state. A second turning point appears around 65 μJ/cm², after which point the demagnetization speeds up again. This second turning point is noted and will be discussed again in relation to further data in the following sections.

Magnetization Recovery Time

Following the ultrafast demagnetization, the recovery of the magnetic order is an essential observation in understanding the mechanisms at work within any material. **Figures 7.8** and **7.9** show the full time-resolved Kerr rotation signals, taken simultaneously alongside the reflectivity data; these plots have been y-offset for clarity.

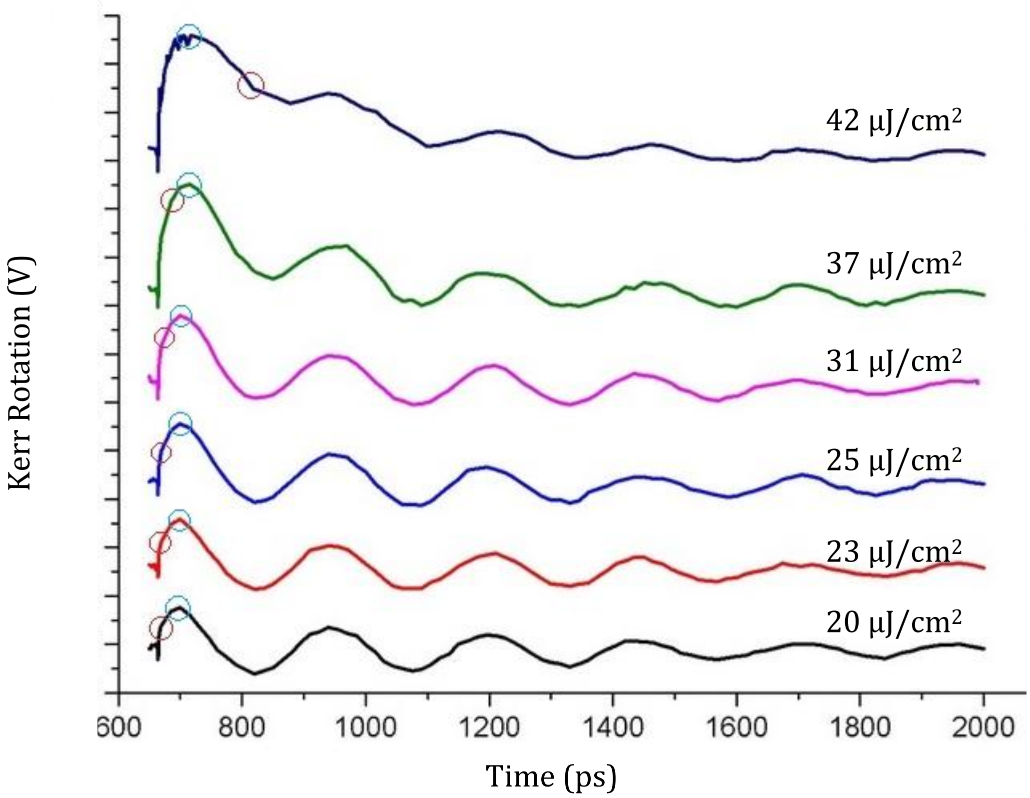

Figure 7.8: TRMOKE rotation signal as a function of pump fluence for low pump powers. Oscillatory recovery is observed for each, with the first oscillation being gradually absorbed into the long range recovery curve.

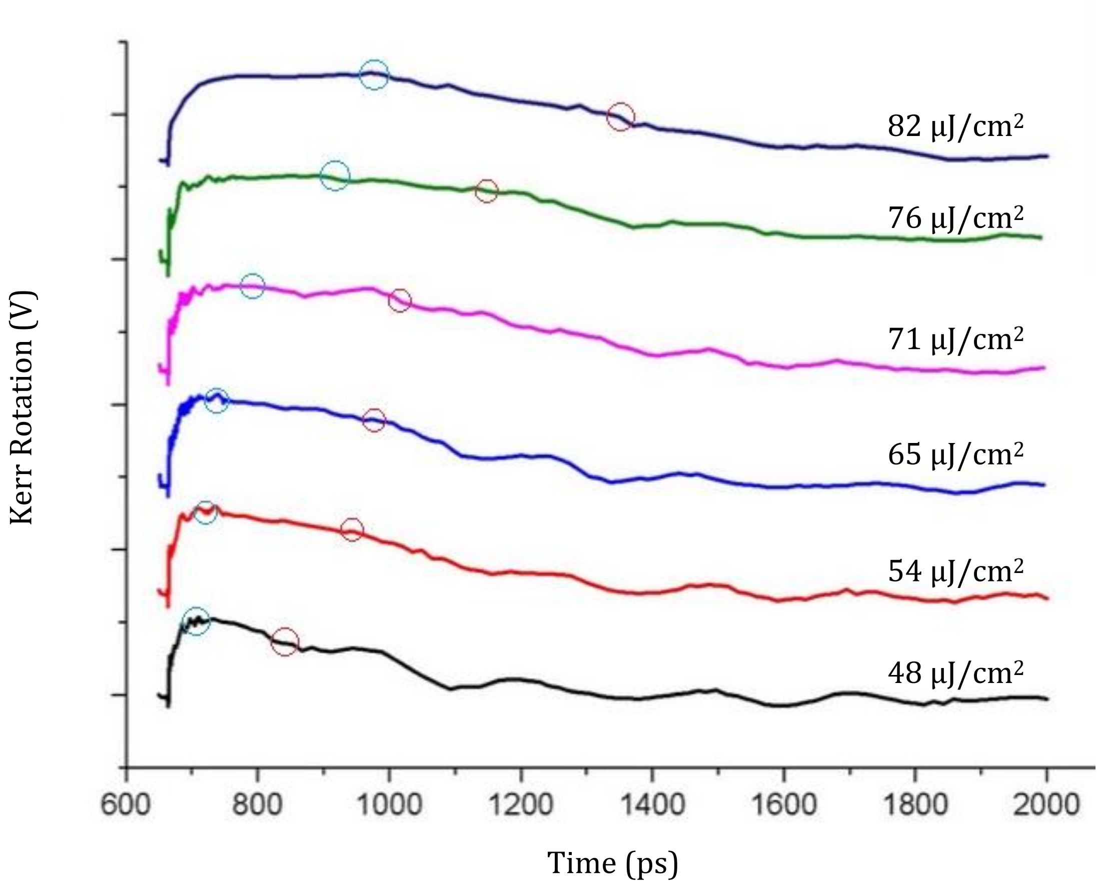

Figure 7.9: TRMOKE rotation signal as a function of pump fluence for high pump powers. Oscillatory recovery is all but obscured by the long range recovery curve.

A few observations are immediately apparent: For all low power measurements (<42 μJ/cm^2), after the initial ultrafast demagnetisation, clear coherent oscillations begin almost immediately. As there is an angle between the external field vector and the internal anisotropy field vector of this sample, these oscillations are attributed to the stimulation of damped magnetization precession. A reduction in the clarity of the oscillations begins to be seen above ~42 μJ/cm^2 corresponding to the point of discontinuity in the reflectivity data; this is despite the maximum signal height showing no correlation. By the end of the series, these oscillations are almost completely lost. Along with this loss in amplitude, the start of the precession is delayed further with increasing fluence as the rate of recovery drops.

In order to calculate the magnetization recovery time, a definition of the starting point of the recovery was required. This was initially set to the point of maximum

Kerr signal used to plot **figure 7.2**, however this did not give a consistent representation across the series, as the highest fluence plots display an increasingly broad plateau of stable magnetization (which indicates that the stimulated area of the sample has reached a full demagnetization condition). This initial setting distorted later analysis which relied on this measurement, so an alternative systematic point had to be identified. It was postulated that the beginning of the recovery was directly linked to a local sample temperature, so by looking at the higher fluence curves, an approximate point at which the gradient the graph reached maximum, following the peak signal, was found from derivative calculations. This required some nuance for the higher fluences as noise and the overlying precession made a direct automatic calculation inaccurate. This point was found to have a reasonably consistent correspondence to the time at which the reflectivity data reached a value of ~4 (arbitrary units representing the voltage from the detector offset from the reference equilibrium). It is shown on **figures 7.7** and **7.8** by the red circles. This observation then related back to the discontinuity in the reflectivity data, as the lower fluence measurements did not reach or were on the order of this value. For the lowest pump fluence curves (20, 23, 25 μJ/cm^2) another starting point was required, which was chosen to be the time delay corresponding to the maximum reflectivity signal.

For rigorous testing, a second definition of the start of the recovery was also used (indicated by the blue circles in **figures 7.7** and **7.8**). This was the point at which the trend of each curve turned negative. This provided a poorer exponential fit, but did highlight an extra aspect of the precessional dynamics, which will be detailed later in this section.

A measure of the magnetization recovery time was then empirically quantified by fitting an exponential expression $M_r(t) = M_0 + M_1 \exp(-(t - t_0)/\tau)$ for each fluence curve. These were fitted to originate from the start of the recovery (as defined above), M_1, with offset values M_0 representing the equilibrium reference magnetization state and t_0 the time offset of M_1. These plots can be seen in **figures 7.9** and **7.10** which show how the recovery time increases as a function of pump fluence as well as showing a decrease in the clarity of the precessional behaviour, in part due to the low amplitude compared to the noise floor. From this data, a value for the recovery time, τ, was plotted with a standard error associated with the fitting (**figure 7.12**). This time constant corresponds to the mean lifetime of the recovery, the time taken for it to decay to 1/e of its maximum value. This recovery time appears to show a linear relationship with anomalous values at 48 μJ/cm², and 76 μJ/cm², the former falling within the previously identified transitional region. Additionally it shows no saturation, which is to be expected if this recovery is dictated by local energy dissipation.

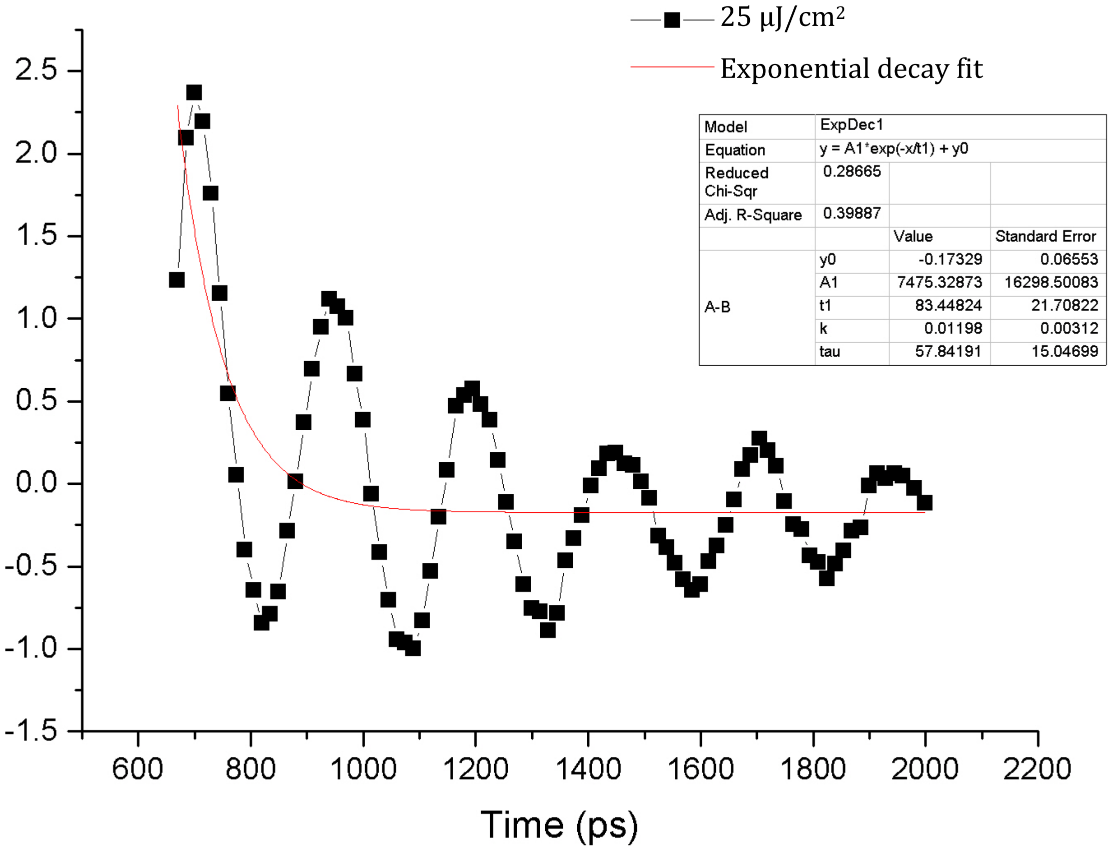

Model	ExpDec1		
Equation	y = A1*exp(-x/t1) + y0		
Reduced Chi-Sqr	0.28665		
Adj. R-Square	0.39887		
		Value	Standard Error
A-B	y0	-0.17329	0.06553
	A1	7475.32873	16298.50083
	t1	83.44824	21.70822
	k	0.01198	0.00312
	tau	57.84191	15.04699

Figure 7.10: Graph showing an example magnetization recovery time curve for low pump fluence (25 μJ/cm²), with fitted exponential decay; recovery is rapid and strongly oscillatory.

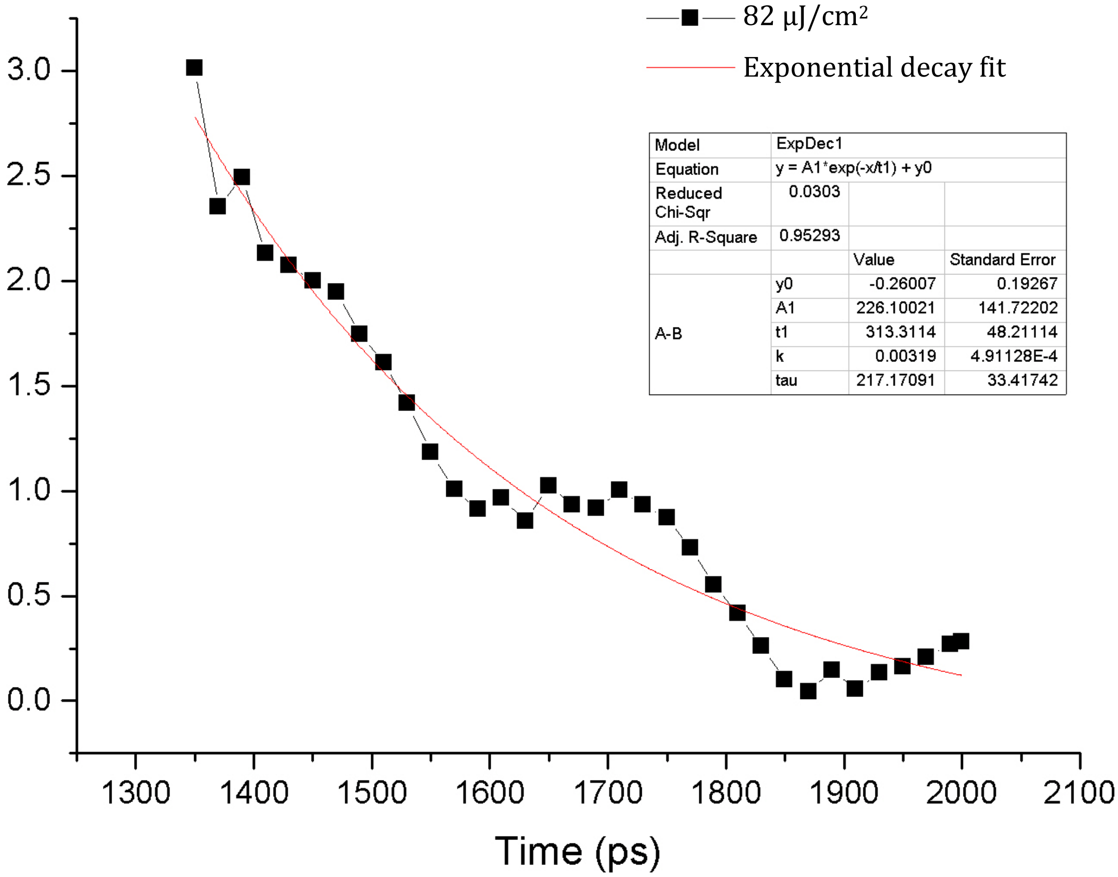

Model	ExpDec1		
Equation	y = A1*exp(-x/t1) + y0		
Reduced Chi-Sqr	0.0303		
Adj. R-Square	0.95293		
		Value	Standard Error
A-B	y0	-0.26007	0.19267
	A1	226.10021	141.72202
	t1	313.3114	48.21114
	k	0.00319	4.91128E-4
	tau	217.17091	33.41742

Figure 7.11: Graph showing an example magnetization recovery time curve for high pump fluence (82 μJ/cm^2), with fitted exponential decay; recovery is much slower and oscillatory behaviour is both suppressed and delayed.

Also plotted on **figure 7.12** is the full recovery time, defined as the time interval between pump photon injection and the end of the recovery at which point the local area has returned to its reference magnetization state. This data again doesn't show saturation at higher fluence (potentially the opposite) but in light of the lack of an anomaly at 72 μJ/cm^2 and the lower calculated error in this measurement, it does show the discontinuity again around 48 μJ/cm^2. Without the saturation present in **figure 7.2**, it is possible to see more clearly that these are actually two linear regimes with a very similar slope, with a step discontinuity between them.

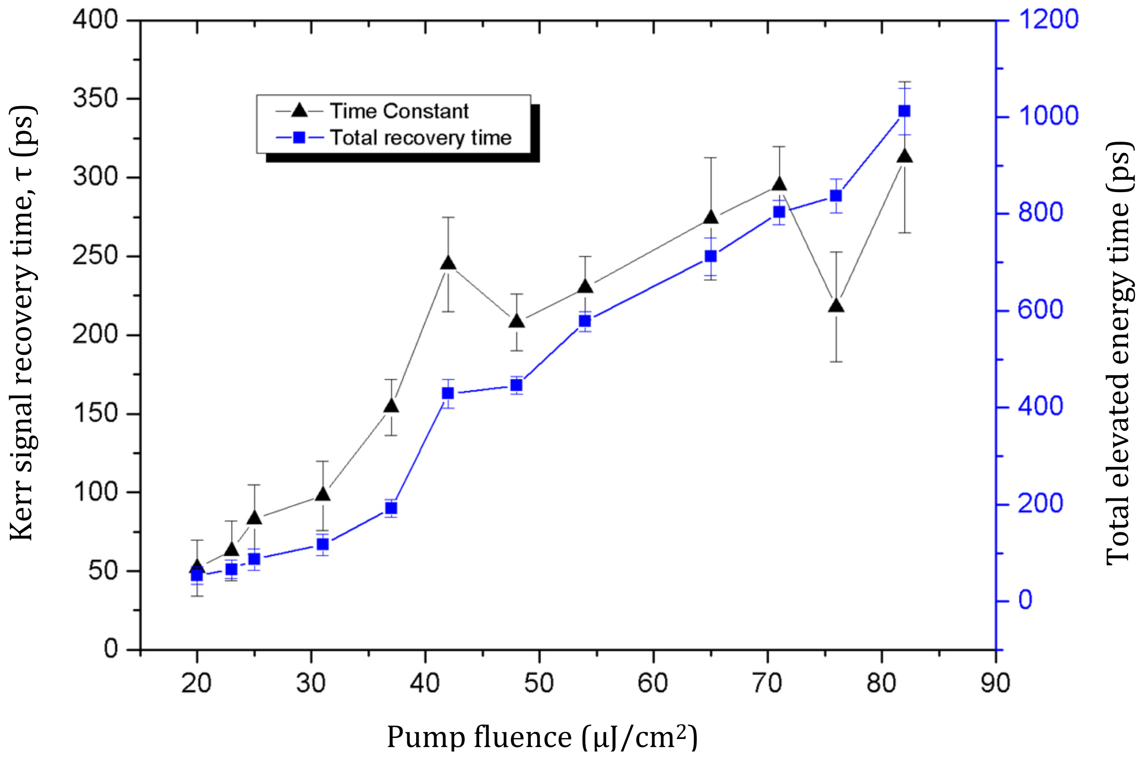

Figure 7.13: Graph showing time constant τ as a function of pump fluence (black), showing the recovery time from each maximum demagnetization state; and total recovery time (blue), which includes the time from the initial pump event, showing the total time associated with elevated energy in the spin reservoir.

This recovery represents the time taken for the effective field vector $\underline{H_{\mathrm{eff}}}$ to return to its equilibrium minimum energy state. This timescale is dominated by the change in the magnetic anisotropy energy, E_{ani} and the demagnetization energy, E_{dem} as well as a transfer of angular momentum. The relaxation takes place by the transfer of energy and angular momentum to the environment and to the lattice reservoir. Relaxation to the environment will occur primarily to the surrounding GdFe rather than to the substrate, due to stronger coupling. As the surface area of the laser stimulated region is much smaller than the volume this will be a limited, but constant, energy sink. Relaxation from spin to the lattice is dependent on the spin-orbital coupling between them. This can be analyzed by comparison between the dissipation curves for lattice and spin reservoirs shown from the total Kerr signal recovery time (displayed in **figure 7.13**) and the reflectivity recovery time (displayed in **figure 7.3**). The relationship between the two recovery mechanisms becomes more obvious when replotted against each other in **figure 7.13**.

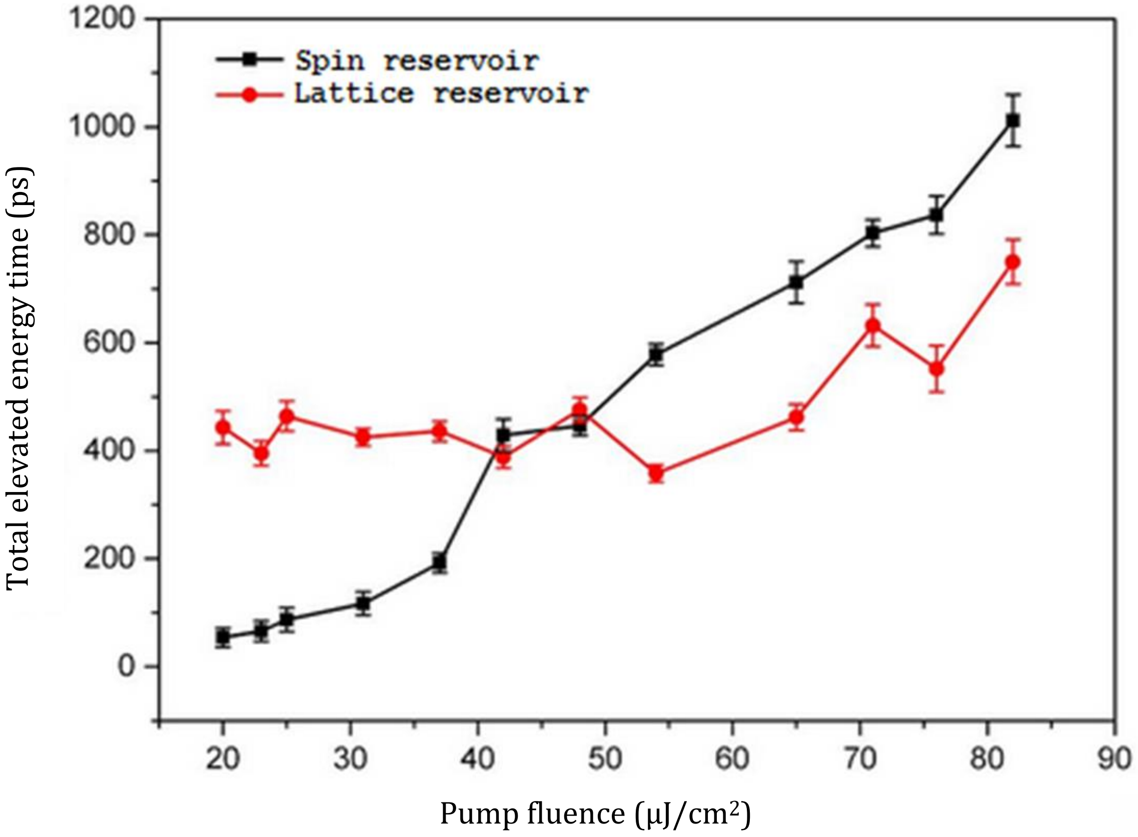

Figure 7.13: Comparison of energy dissipation from spin reservoir (black), (Kerr signal) and lattice reservoir (red, dominant temperature reservoir over long timescale represented in Reflectivity signal).

For low fluence, the magnetization recovery is significantly faster than the reflectivity recovery, by ~8x (400 ps). It can be inferred from this data that angular momentum loss from the lattice to the environment is limited at ~400 ps, and its capacity to dissipate at this rate is not at all challenged; angular momentum transfer from the spin to lattice is fast enough that it can be dissipated too. At ~42 μJ/cm^2 an equivalent time scale is reached, and the relaxation of spin plateaus. As this has already been identified as the magnetization compensation temperature, this behaviour can be attributed to the stimulated region losing net moment and its recovery being dominated by the spin-lattice relaxation. Above T_{Mcomp} the dominant moment has reversed, and the spin-orbital coupling to the Fe is now most important.

As this is lower in Fe, **[5]** it follows that the spin-lattice relaxation is weaker, reducing the rate of dissipation of the spin reservoir but also of the lattice reservoir, which is now 'drip-fed' energy and angular momentum. This is shown in **figure 7.14**. After a certain time, the lattice reservoir reaches equilibrium with the environment, and the spin reservoir consistently takes ~200 ps longer to finally dissipate. This will be due to a combination of fast dissipation of a lower energy density from the lattice (once the energy from the initial electron-lattice relaxation has dissipated) and an increased importance of the spin-environment loss channel.

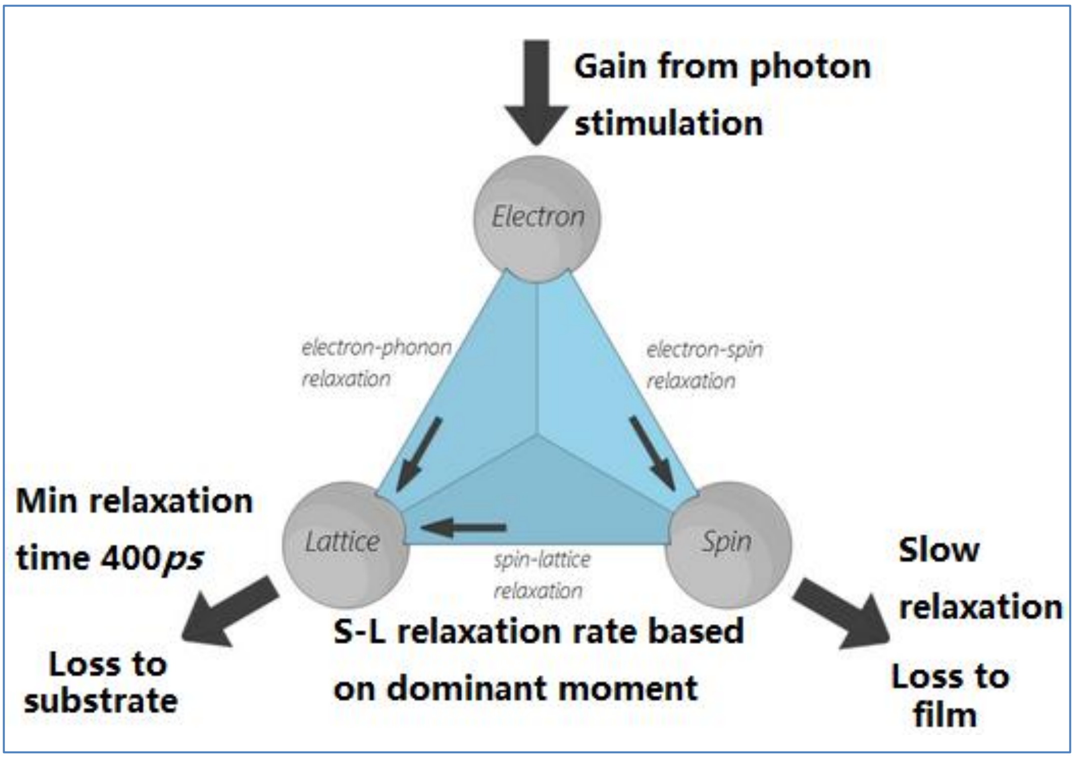

Figure 7.15: Schematic showing energy and angular momentum gain and loss channels. Spin lattice relaxation is dependent on the dominant moment's spin-orbit coupling, which is Gd at low temperatures, and swaps to Fe above T_{Mcomp}.

Magnetic Precessional Frequency

In order to analyse the precessional information more accurately, it was necessary to extract it from the underlying recovery curve. Where that recovery represents the vector orientation of the effective field, $\underline{H_{eff}}$, relative to its initial state, the procession details the motion of the net magnetization vector, $\underline{M}$. To isolate this information, the recovery curve, obtained above (from the red circles in **figures 7.8** and **7.9**), was subtracted from each plot**;** this is referred to as the residual. An example of this result is shown in **figures 7.15** and **7.16**. Each residual was analysed following two contrasted methods, and compared. Also shown is the first method: a damped sinusoidal curve fit plotted against the residual data following **equation 2.16** (more details in **chapter 2**). Of particular interest are the damping factor, τ_d and f, the frequency of oscillation, which are related to the damping constant in the Landau-Lifshitz Gilbert (LLG) equation (written again here in **equation 2.18)**. For low temperatures, this equation represents the combined coherent precession of the net moment of both sublattices, which remain fixed relative to each other by their exchange coupling. For higher temperatures, this approximation becomes less physical as the sublattices decouple and begin to precess around their own separate effective field vectors.

$$\mathrm{M_p(t) = M_0 + A\exp(-t/\tau_d) \times \sin(2\pi f(t - \varphi_0))} \qquad (2.19)$$

$$\mathrm{d\underline{M}/dt = -\gamma\left[\underline{M} \times \underline{H}_{eff}\right] + \alpha M_S^{-1}\left[\underline{M} \times d\underline{M}/dt\right]} \qquad (2.18)$$

It can be seen here that each residual showed an oscillatory waveform, which took at least half an oscillation to reach a maximum before behaving similarly to a damped sinusoid even at the highest fluence, despite being particularly obscure in the raw data. As can also be seen, the superimposed sinusoidal fits are not adequately representative to draw conclusions for the damping parameter, but are able to provide a set of values for frequency, plotted below in **figure 7.19** and discussed further later.

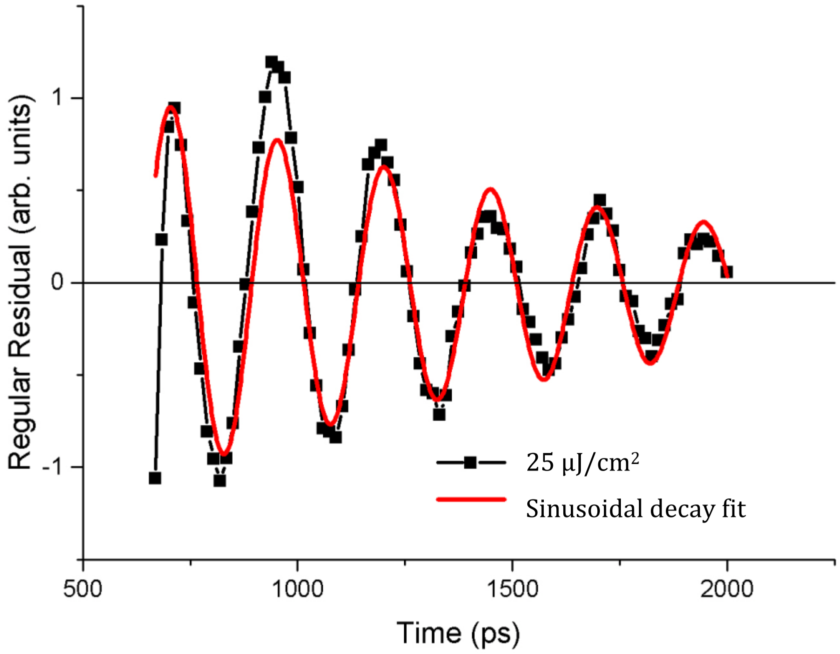

Figure 7.15: Example of magnetic precession residual, after removing recovery slope low fluence measurement (black) (25 μJ/cm^2), with fitted sinusoidal decay (red).

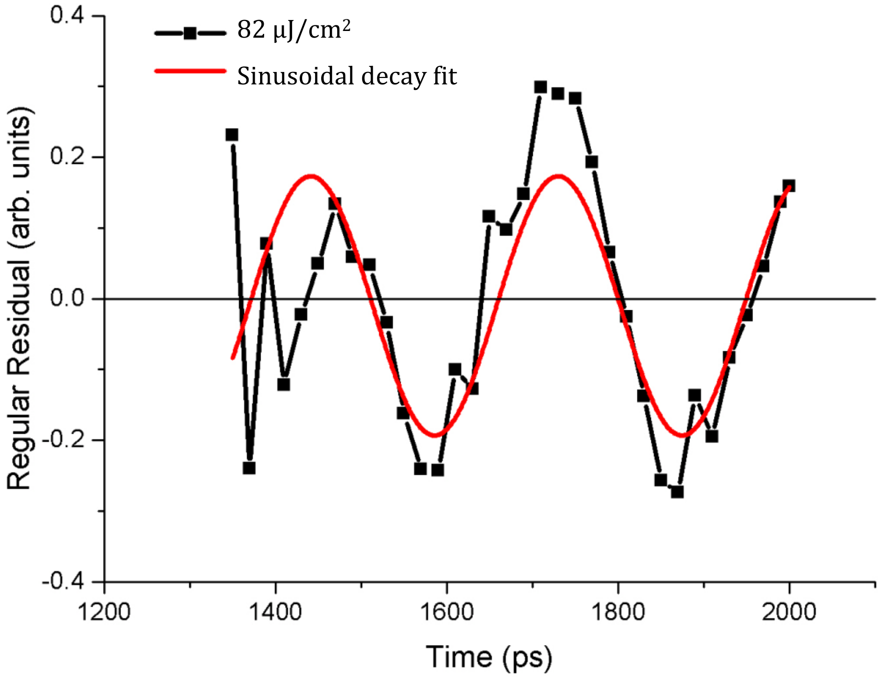

Figure 7.16: Example of magnetic precession residual, after removing recovery slope low fluence measurement (black) (82 μJ/cm^2), with fitted sinusoidal decay (red).

Additionally this technique was undertaken from the second definition of recovery time, previously discussed and highlighted in **figures 7.8** and **7.9** as blue circles. This gave further confirmation of the significance of the temperature point associated with ~4 (arb. units) reflectivity, by showing a sharp transition in oscillation frequency at this time/temperature. An example is shown in **figure 7.17** below for 65 μJ/cm^2.

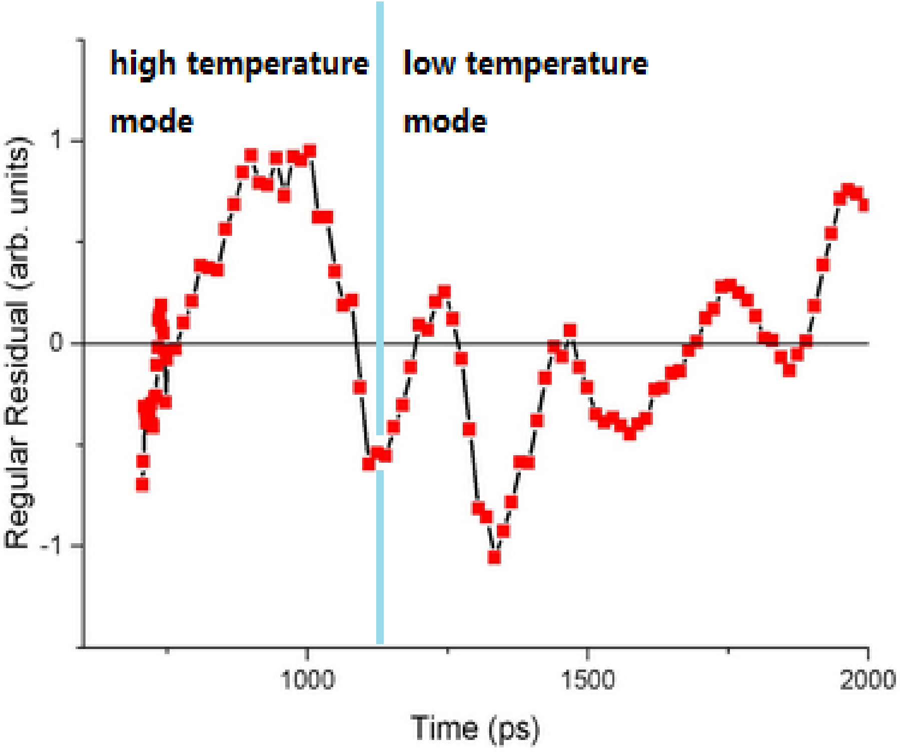

Figure 7.17: Residual for 65 μJ/cm^2 fluence plot. This shows the two frequencies, separated by a temperature boundary.

This recovery time also correlated well with a second reflectivity value of ~6.25. This second set of residuals was used to then calculate fast Fourier transforms (FFTs) to analyse these oscillations further in the frequency domain. A peak finding function then provided the resonance frequencies with amplitudes, along with their full width half maxima (FWHM) which provided the associated error. For the series, a pair of frequencies was observed, shown in **figure 7.18**. These are plotted alongside the equivalent frequency, f, obtained from the curve fitting method in **figure 7.19**.

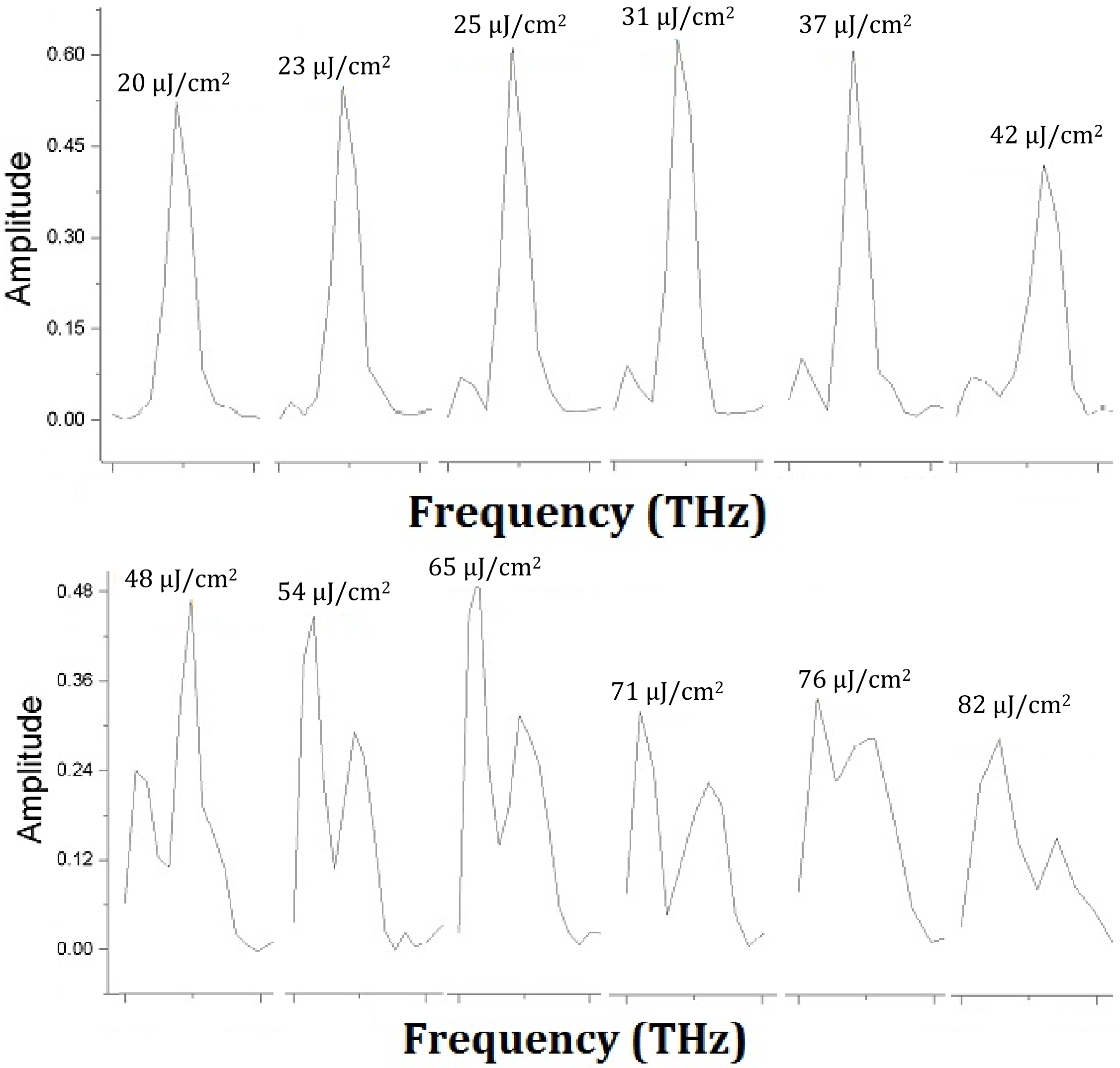

Figure 7.18: FFT series, showing the gradual growth of lower frequency precession while the dominant frequency begins to fall, followed by the rapid reversal of the frequency dominance, and finally the lower frequency drops again at the highest laser pump fluences.

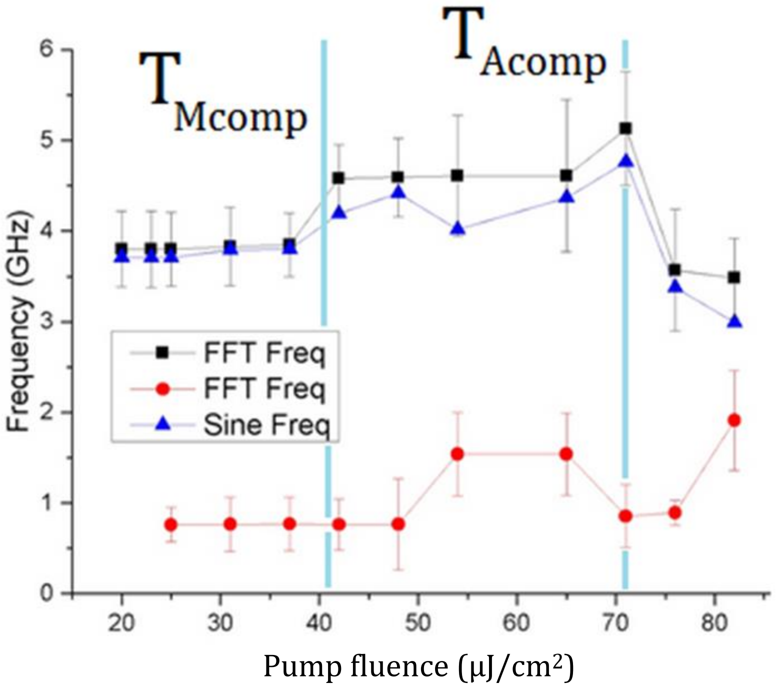

Figure 7.19: Comparison of FFT frequency vs curve fitted frequency for coherent precession regime. Shows slow increase with fluence followed by a significant drop off after 71 μJ/cm^2, lower frequency oscillation observed at higher temperature becomes stronger at higher fluences.

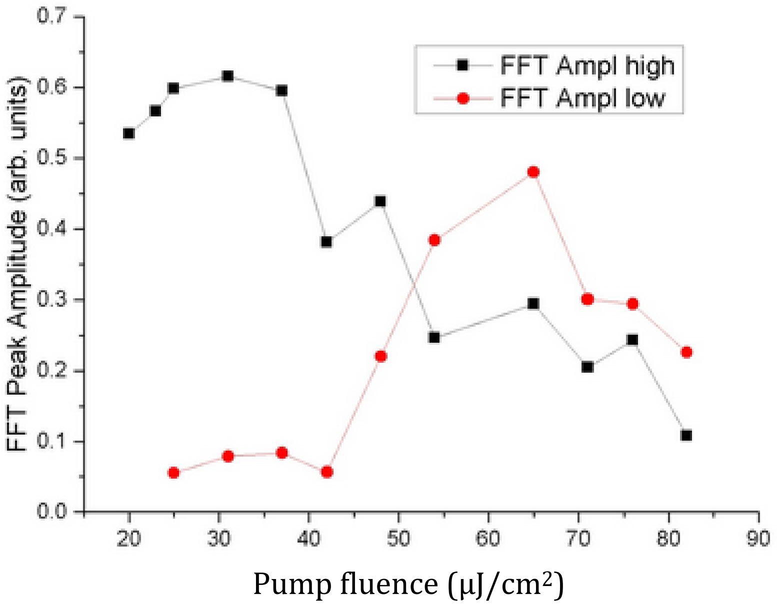

Figure 7.20: Graph showing resonance amplitudes from FFT as a function of pump fluence for both oscillation frequencies observed. This shows swapping of dominant precessional mode after T_{Mcomp} which is also then quenched at T_{Acomp}.

These frequencies are separated by a temperature boundary as defined by the reflectivity of ~4. The higher frequency (referred to here as f_1) exists below this temperature boundary, while the higher frequency, f_2, occurs only above it. **Figure 7.19** shows f_1 calculated by two separate methods and f_2 from the FFT alone. **Figure 7.20** shows the resonance amplitudes of f_1 and f_2. Both FFT and sine curve fitted data of f_1 suggest a general upward trend of increasing frequency as a function of pump fluence, until after 72 μJ/cm^2 when a significant reduction is observed. The change in frequency and amplitude can be related to the torque applied to the local macrospin, discussed in **chapter 2** and reprinted here in **equation 2.9**.

$$\mathrm{d}\underline{\mathrm{M}}(\mathrm{t})/\mathrm{dt} = -\gamma\left[\underline{\mathrm{M}}(\mathrm{t}) \times \underline{\mathrm{H}_{\mathrm{eff}}}\right] \qquad (2.9)$$

In order to interpret this data, it is important to consider the relative dynamic behaviour of the two sublattices within the different regimes, which can be divided into three based on the temperatures reached: low fluence (20-31 μJ/cm^2), intermediate fluence (31-54 μJ/cm^2) and high fluence (65-82 μJ/cm^2).

- At low temperature, the the Gd and Fe sublattices are exchange coupled and coherent precession with little reduction in $\underline{M}(t)$ is observed. As this region is below the magnetization compensation temperature T_{Mcomp}, the Gd sublattice moment dominates the magnetism. This results in lower frequency, higher amplitude oscillations for f_1, while f_2 is very weak.

- Once the fluence is high enough to increase the local lattice temperature above T_{Mcomp}, the Fe sublattice dominates, and the net moment flips, altering the frequency. Explanations for why this goes up, rather than down (due to larger moment) have been discussed by Stanciu et al. **[6]** but with no conclusive explanation. This may be due to distortion of the frequency in the vicinity of the two compensation temperatures. As the temperature increases in this region, the exchange coupling between the sublattices begins to weaken and f_2 begins to become more prominent.

- At very high fluence, the exchange coupling reaches a minimum as the amplitude of f_2 maximizes. Here there is a divergence of frequency f_1 which corresponds to the angular momentum compensation temperature T_{Mcomp}. The exchange mode is similarly quenched at this fluence, but grows again at higher temperatures, as the frequency f_1 begins to rapidly drop away, corresponding to the loss of the FMR mode.

Magnetic Precession Damping

The final property of use which can be obtained from this series, is the damping of the spin precession, which allows a direct calculation of the Gilbert damping parameter used in the LLG equation to describe spin orbit relaxation.

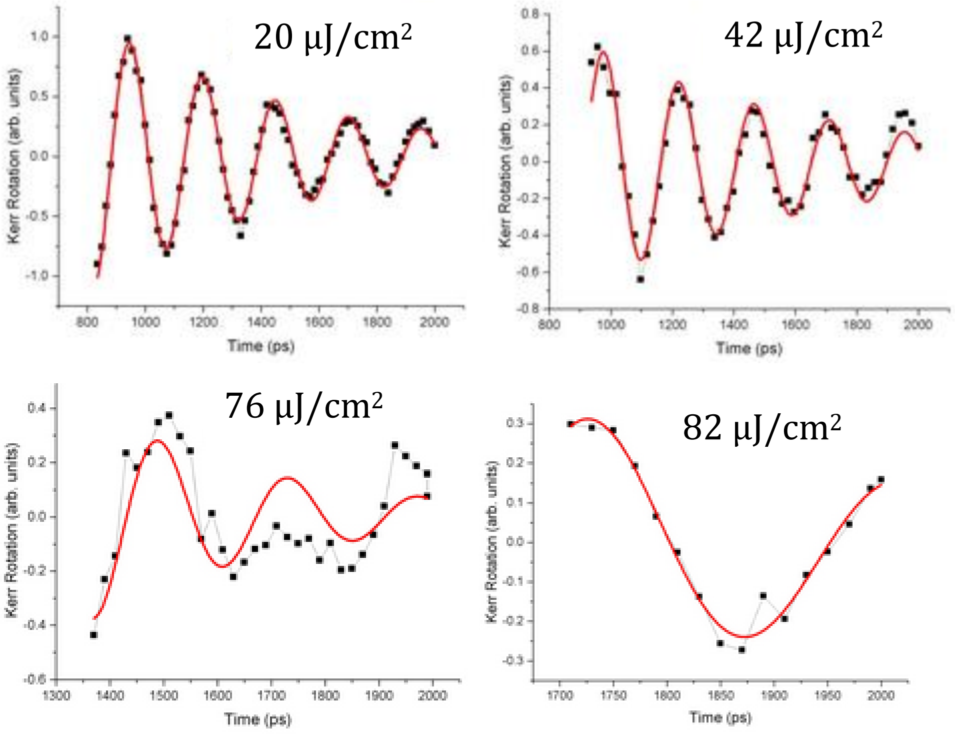

Figure 7.21: Graphs showing examples of cropped FMR mode precession data with damped sinusoidal fitting.

In order to more accurately calculate the precession damping, the residual data collected into **figures 7.4** and **7.16** was selectively refitted, specifying a new starting time to coincide with the start of the largest oscillation. This initial growth in the oscillation amplitude could be related to the re-coherence of the macrospin as the thermal instability decreases. As the TRMOKE signal detected is the average of a large number of repeat events, any incoherence will have a net effect of reducing the observed signal.

Damped sinusoidal curve fitting to this new data provides a much closer fit and also helps to highlight where the data cannot be described as accurately by this method. **Figure 7.21** shows examples of the new fit for two low fluence graphs, and the higher fluence curves, which have lower SNR and are more distorted.

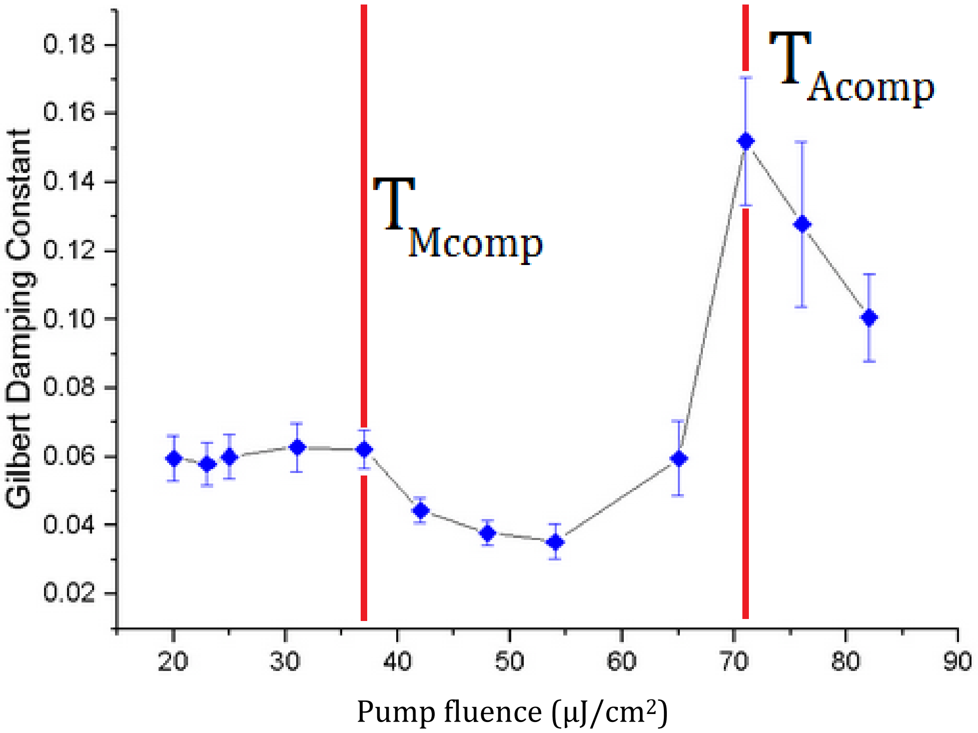

Figure 7.22: Graph showing Gilbert damping parameter as a function of fluence. Highlighted are the magnetization T_{Mcomp} and angular momentum T_{Acomp} compensation temperatures.

$$\alpha = 1/(2\pi f\tau_d) \tag{2.20}$$

From the FMR mode frequency f_1 and exponential sine damping coefficient, τ_d, the Gilbert damping parameter, α, was calculated with **equation 2.21**, detailed in **chapter 2**. This data provides a systematic method of measurement and is shown in **figure 7.22** above. This plot confirms the analysis of the precession frequencies in the previous section, showing both the angular momentum, T_{Acomp}, and magnetization, T_{Mcomp}, compensation temperatures clearly.

7.3 Summary

A series of increasing pump fluence magneto-optic measurements has been analyzed to extract the characterizing features of a chosen composition ratio of the rare earth-transition metal alloy GdFe. These features provide an important insight into both the energy and angular momentum transfer interactions occurring on a picosecond timescale between the electron, lattice and spin thermodynamic reservoirs associated with an irradiated region of the sample. Several nonlinearity features have been observed, which together build up a detailed timeline of the dynamics. At each step these have been related back to the local lattice temperature, proportional to the reflectivity response.

7.3.1 Evidence for Magnetization Compensation Temperature

During the demagnetization process a critical reflectivity of ~4V has been identified, which has been attributed to the spin reservoir transitioning up through the magnetization compensation temperature T_{Mcomp} by three observations:

- Above this temperature, a short lived magnetization recovery is observed. This corresponds to the transient ferromagnetic state reported theoretically by other groups **[7] [8]** and recently observed experimentally in X-ray Magnetic Circular Dichroism (XMCD) data **[9],** but not reported in experimental time resolved MOKE.

- The time taken for the 4f Gd and 3d Fe spin orbital thermal reservoirs to equilibrate increased by as much as 175% at this temperature.

- At this temperature a step change in the peak reflectivity is observed, indicating a sudden increase in peak temperature experienced by the sample area.

During the recovery, more evidence that the reflectivity of ~4V corresponds to T_{Mcomp} is provided by the following observations:

- A significant transition between non- and highly fluence dependent regimes is observed in the lattice relaxation time for fluences which raise the temperature above this point. This is due to a change from Gd dominated to Fe dominated spin-orbital coupling to the lattice. The smaller coupling offered by Fe results in a slower 'drip fed' transfer of energy and angular momentum which causes the slowing of its recovery.

- A sharp transition in precessional modes is observed at this threshold. A lower frequency exchange mode is observed above the threshold, and a higher frequency FMR mode coherent precession is consistently observed below. The exchange mode is caused by higher temperatures weakening the exchange coupling between the sublattices and causing them to precess around divergent effective field vectors. It is seen to grow in strength from this temperature.

- The coherent precession FMR mode is seen to decrease in strength dramatically from this point and show a limited increase in frequency in agreement with observations reported by Stanciu et al. **[6]**

- The Gilbert damping, calculated from the FMR mode decay and frequency, showed a decline again at this transition, indicating that the spin-orbit coupling was reduced, corroborating the interpretation of the lattice relaxation time mechanism.

7.3.2 Evidence for Angular Momentum Compensation Temperature

During the ultrafast demagnetization process, a higher temperature critical point was also observed corresponding to a reflectivity value of ~6.25V, which was again consistent across each fluence measurement. This was interpreted as the angular momentum compensation temperature T_{Acomp} and manifested in the following ways:

- The observed phenomenon attributed to the ferromagnetic transient state sharply increased in amplitude above this temperature.

- The time taken for the irradiated area to fully demagnetize peaked at this temperature after which it begins to decrease again. This enhancement of the demagnetization rate is indicative of meeting an energy threshold.

Additionally, the recovery at higher fluences showed three key features corresponding to a turning point at T_{Acomp}:

- The frequency of the FMR mode increased underwent a small but significant increase followed by a decline, consistent with theory. From reports **[6]** it is expected that the frequency diverges around this point and higher fluence resolution might uncover this.

- The exchange mode is observed to quench just below this fluence, before increasing again. As the exchange mode softens, it begins to synchronise with the FMR mode around T_{Acomp} again consistently with literature.

- The Gilbert damping shows the strongest corresponding response, in line with previous reports, confirming that this is in fact T_{Acomp}.

The observation of a strong increase in damping along with a rise in FMR frequency at T_{Acomp} conveys the importance of this material for spintronic application. These characteristics lead to the ability to perform ultrafast reversal of magnetization direction for magneto-optic recording media.

7.4 References

[1] F. Radu, et al., Nature. Comms. **1728**, 1 (2012)

[2] Andrei Kirilyuk, et al. Reviews of Modern Physics, **82** (2010)

[3] J. Åkerman, Science **308**, 508 (2005)

[4] C. Felser, G. h. Fecher, Spintronics: From Materials to Devices (Springer Verlag, Berlin, 2013)

[5] J. Stöhr, H. C. Siegmann, Magnetism, (Solid-State Sciences Springer Verlag, Berlin, 2006)

[6] C. D. Stanciu, et al., Phys. Rev. B, **73**, 220402(R) (2006)

[7] S. Weinholdt, et al., Phys. Rev. B, **88**, 020406(R) (2013)

[8] U. Atxitia, et al., Phys. Rev. B, **87**, 224417 (2013)

[9] I. Radu, et al., Nature (London) **472**, 205 (2011)

Chapter 8

Conclusions & Further Work

Both of the materials studied in this project, half-metallic Fe_3O_4 (magnetite) and the rare-earth transition metal alloy GdFe represent important aspects of spintronic research **[1] [2]**. Each material contains its own set of unique challenges and opportunities.

8.1 Discussion of Post-Oxidized Fe_3O_4

8.1.1 Discussion of Results

In this work, the nature of post-oxidized Fe films has been explored with a particular interest in the depth and quality of the oxidation process and the phase of iron oxide produced. It is noteworthy that the growth mechanism appears to produce the Fe_3O_4 inverse spinel structure with ease and that the formation of APB defects is functionally identical to that of a more standard island growth process.

This investigation would imply that single crystal Fe_3O_4 can be produced by this method and in fact benefits from a short oxidation time. Further oxidation rather than extending the depth of the film results in replacing the B site Fe ions, explaining the poor magnetic performance by inhibiting the ferromagnetic exchange and superexchange interactions between the Fe^{2+} and Fe^{3+}. This is confirmed by the relatively low disorder observed in (001) cross-section HRTEM, compared to much higher disorder observed in (011) cross-section HRTEM, which resolves the B site ions separate from the oxygen super-lattice.

The observation of periodic defects between the oxidized and unoxidized layers appear as expected for the lattice mismatches of Fe_3O_4 (001)||Fe (011) and for Fe(011)||MgO(001). This shows again how robust this growth process is, with both layers epitaxially related to their under layer, with only 1-2 atomic planes of transition observed. This type of limited depth oxidation has been observed elsewhere **[3]**, however the sharpness of the interface in this case is particularly noteworthy.

This presents a useful method of producing a multilayer material with an Fe||Fe_3O_4 interface, with potential applications in spin injection device tests. The thick Fe layer, exchange-coupled to the thin Fe_3O_4 layer would lower its coercivity and increase its remanence. A current passed through this structure would experience an enhanced spin polarization by the Fe_3O_4 before potentially being injected into a semiconductor.

8.1.2 Further Research

Further research in this field must consider shorter post-oxidation times and observe the lower limit of the oxide formation process. A sweet spot can be identified by the crystallographic and magnetometric techniques detailed in this thesis and Fe||Fe_3O_4 or pure Fe_3O_4 devices can be grown to begin testing of spin injection efficiencies. This was an intended avenue of investigation during this project, but was postponed due to uncontrollable logistics issues with the growth stage.

8.2 Fluence Dependent Magneto-Dynamics in GdFe

8.2.1 Discussion of Results

This investigation has uncovered four key features in the temperature dependent behaviour of a key spintronic material GdFe. **1.** A discontinuity in the ultrafast peak reflectivity with fluence. **2.** An observed transient picosecond timescale magnetic moment recovery. **3.** A relationship between the lattice and spin relaxation rates. **4.** A low frequency exchange mode softening between the compensation temperatures. These manifest from the unique interaction between the antiferromagnetically coupled sublattices. These provide further insight into the energy and angular momentum exchange taking place, as well as a robust methodology for characterizing such materials in future.

At fluences which raise the peak temperature above T_{Mcomp}, a step in the peak reflectivity was observed. In other words, for a proportionally larger energy density, a constant extra level of heat is produced above this point. This would imply that either the specific heat capacity of the lattice has reduced by a fixed value, or that the electron->lattice and electron->spin energy transfer ratios have been altered. The first option is unlikely, but the second is plausible as a result of the swapping of the dominant sublattices. This could also be a result of, and evidence for, the fast coherent phonon spin-lattice exchange, which is allowed by the large 4f spin-orbital coupling, but inhibited by the much smaller 3d value.

The observed picosecond magnetic moment recovery is produced by the transient ferromagnetic state. This is consistent with the spin temperature rapidly transitioning through the magnetization compensation point and reversing the dominance of the field. This has been reported experimentally in XMCD data **[4]** , but not with the clarity observed in this system. It shows a strong agreement with the interpretation of the other features in this dynamic investigation.

The relaxation of the spin and lattice systems have been observed to be strongly interdependent, as a function of fluence. This provides a clear indication of the timescales of energy and angular momentum transfer. As the lattice-environment is stronger than the spin-environment coupling, exchange will predominantly be by transfer out of the spin system and into the lattice. At low fluence the coupling is strong between them, due to the dominance of the Gd sublattice, and energy transfer is limited only by lattice coupling to the environment (at around 400 ps). As the fluence rises, the Fe sublattice takes over dominance and the spin-orbit coupling significantly weakens. This slows the spin-lattice exchange, creating a longer lived elevated energy state in the lattice. Lattice relaxation shows a consistent 200 ps lag behind spin relaxation in this regime. This would imply that spin-environment exchange plays a larger role, which would be consistent with the itinerant nature of the now dominant 3d Fe. A single point in this region shows a 100 ps lag between the lattice and spin relaxation, corresponding to the angular momentum compensation state. These interpretations are based on a variable strength of the spin-orbital coupling, which is consistent with and supported by the independently measured Gilbert damping results.

The observation of a low frequency oscillation is interpreted as the manifestation of the exchange mode. This interpretation can be supported by comparison to that made by Mekonnen et al. **[5]** to assess the validity of this conclusion. In their paper Femtosecond Laser Excitation of Spin Resonances in Amorphous Ferrimagnetic $Gd_{1-x}Co_x$ Alloys the authors quote an exchange mode of the order of ~70 GHz, while this investigation finds a much lower frequency exchange mode ~1.5 GHz. The frequency of the exchange mode is found via the gyromagnetic ratios of each sublattice (γ_{RE}, γ_{TM})and the interatomic exchange coefficient between them λ_{RE-TM}. This is presented by Mekonnen in the form of **equation 3.3**, where x is the relative concentration of the transition metal, TM and $1 - x$is that of the rare earth RE.

$$f_{ex} = \lambda_{RE-TM}\gamma_{RE}\gamma_{TM}[xM_{TM}/\gamma_{TM} - (1-x)M_{RE}/\gamma_{RE}] \qquad (3.3)$$

While this will not be affected by external field strength like the FMR mode, it can be expected that this system will have a weaker exchange mode by comparing Fe to Co. The gyromagnetic ratios ($\gamma/2\pi$) of Fe **[6]** and Co **[7]** are 0.1382 kHz/G and 1.0054 kHz/G respectively, making this an order of magnitude smaller in Fe. So for a GdFe amorphous material, even before concentrations are considered, this frequency will be significantly smaller due to the proportionality, plausibly an order of magnitude smaller. The observation of a competing exchange mode between the T_{Mcomp} and T_{Acomp} has not been previously reported, and shows that the angular momentum compensation may provide an enhancement to the exchange coupling.

8.2.2 Further Research

Further temperature dependent study would help to complete the characterization process detailed here, including environmental temperature variation. This is possible now with the current setup, which has been fitted with a cryostat capable of measurements down to liquid He temperatures. Additional higher fluence measurements would provide further confirmation of the behaviour of the exchange mode.

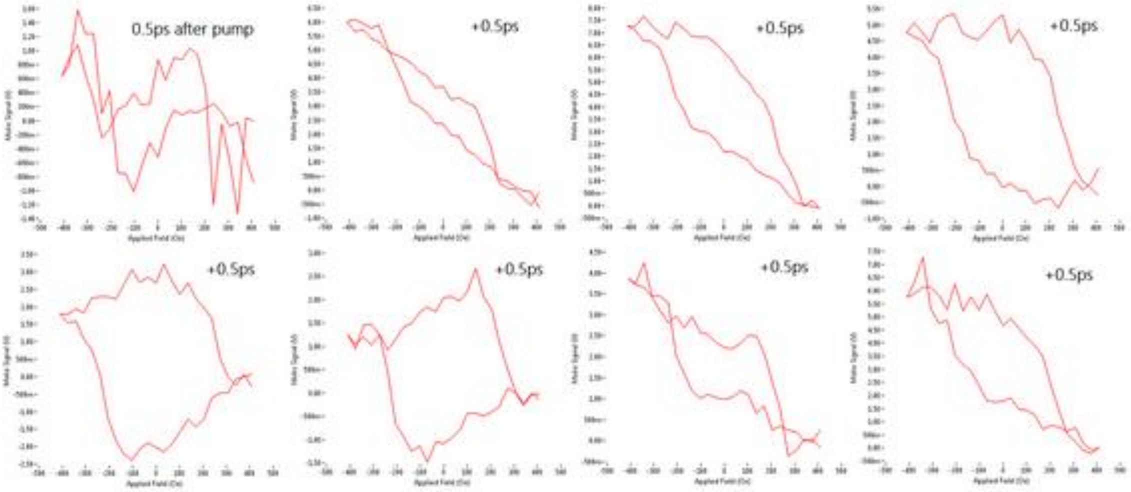

Figure 8.1: Dynamic hysteresis measurements taken at 0.5 ps intervals after pump event

The permanent magnet in the system has been refitted with an electromagnet, to allow field dependent measurements to be carried out. This can help to investigate the ultrafast demagnetization regime, and provide further support for the true nature of the signals observed in the first 15 picoseconds. A system for producing time-resolved hysteresis measurements is in development, with some limited success as shown in **figure 8.1**.

8.3 Concluding Remarks

This thesis has explored and demonstrated a number of experimental techniques capable of characterizing the critical parameters involved in optimizing a material for application in a spintronic device. This has involved preparation and observation of microscopy images as well as the construction and use of a femtosecond pump-probe MOKE apparatus. A number of new and supported observations have been made, which can be used to feedback to growth of improved materials.

8.4 References

[1] S. A. Wolf, et al., Magn. and Mat., **294**, 1488 (2001)

[2] A. Hirohata and K. Takanashi, J. Phys. D: Appl. Phys., **47**, 193001 (2014)

[3] N. Cabrera and N. F. Mott, Rep. Prog. Phys. **12**, 163 (1949)

[4] I. Radu, et al., Nature (London) **472**, 205 (2011)

[5] A. Mekonnen, et al., Phys. Rev. Lett., **107**, 117202 (2011)

[6] G. G. Scott, Phys. Rev., **99**, 1241 (1955)

[7] R. E Walstedt, et al., Phys. Rev., **162**, 301 (1967)

Glossary

Å	Angstrom
AOM	Acousto-Optic Modulator
APB	Anti-Phase Domain Boundary
Ar	Argon
BBO	Barium Borate
Fe	Iron
Fe_3O_4	Magnetite
FFT	Fast Fourier Transform
FMR	Ferromagnetic Resonance
FWHM	Full-Width Half Maximum
Gd	Gadolinium
GMR	Giant Magneto Resistance
GVD	Group Velocity Dispersion
$\hbar$	Planck Constant
H_c	Magnetic Coercivity
HDD	Hard Disk Drive
H_{eff}	Effective Magnetic Field Vector
(HR)TEM	(High-Resolution) Transmission Electron Microscopy
JEOL	Japan Electron Optics Laboratory Company
J_{ex}	Exchange Integral
LBO	Lithium Triborate
LLG	Landau-Lifshitz Gilbert equation
MBE	Molecular Beam Epitaxy
MOKE	Magneto Optic Kerr Effect
M_R	Magnetic Rememance
MRAM	Magnetic Random Access Memory
M_S	Saturation Magnetisation
Nd	Neodymium
O	Oxygen
Oe	Oersted

PSD	Phase Sensitive Detection
RE	Rare Earth Metal
SADIFF	Select-Area Diffraction
SHG	Second Harmonic Generating
Si	Silicon
SNR	Signal to Noise Ratio
TC	Time Constant
Ti	Titanium
TM	Transition Metal
μ_B	Bohr Magneton
VSM	Vibrating Sample Magnetometry
XMCD	X-ray Magnetic Circular Dichroism
YVO	Yttrium Vanadate

Antiferromagnet	A magnetic material whose sublattice moments sit opposite to each other and exactly cancel.
Birefringence	The property of a material causing it to have a refractive index dependent on the polarization and direction of light.
Curie temperature	A phase transition temperature above which magnetic materials undergo a sudden reversible loss of magnetic order.
Exchange	A quantum mechanical effect which occurs only between identical particles and leads to moment alignment required for ferromagnetism.
Fermion	A subatomic particle with half-integer spin.

Ferrimagnet	A magnetic material which exhibits non-perfectly cancelling antiferromagnetism, such that some net moment exists.
Ferromagnet	A material susceptible to magnetization.
Fluence	Radiant energy received by a surface per unit area.
Kerr Effect	A change in the refractive index of a material in response to an applied field.
Magnetic Moment	A property of magnetic materials which interacts with an applied field to produce a mechanical moment.
Magnetoresistance	The extent to which a material’s electrical resistance is modified by an externally applied magnetic field.
Precession	The movement of an axis of rotation around a second axis due to a torque force acting to move the first axis.
Spin	A quantum mechanical intrinsic angular momentum exhibited by a subatomic particles and atomic nuclei.
Spintronic	Spin Transport Electronics (portmanteau).
Ultrafast	Timescales on the order of less than 100 picoseconds.
Voigt Effect	A magneto-optical phenomenon which causes polarized light to rotate and elliptize within an optically active medium.